

# Laser-Induced Forward Transfer of Functional Microdevices

Présentée le 23 janvier 2023

Faculté des sciences et techniques de l'ingénieur  
Laboratoire de microsystèmes 1  
Programme doctoral en microsystèmes et microélectronique

pour l'obtention du grade de Docteur ès Sciences

par

**Zhiwei YANG**

Acceptée sur proposition du jury

Prof. H. Shea, président du jury  
Prof. J. Brugger, directeur de thèse  
Prof. T. Lippert, rapporteur  
Dr M. Despont, rapporteur  
Prof. V. Subramanian, rapporteur



Wings are a constraint that makes  
it possible to fly.  
— Robert Bringhurst

To my parents...  
To my girlfriend...



# Acknowledgements

After experiencing plenty of unique moments for five years at the Laboratory of Microsystems (LMIS1), I finally arrived at the destination of my Ph.D. journey. It is no exaggeration to say that without the support of many people along this journey, I would not be able to arrive at the summit.

First, I would like to express my deepest gratitude to Prof. Jürgen Brugger for giving me this opportunity to carry out the project at LMIS1. During my Ph.D., Juergen is always standing behind me and giving me unwavering guidance, support and encouragement. I still remember that we shared so much time brain-storming and I am grateful when he challenged me to push me to think further about my project. I would like to thank Dr. Giovanni Boero for joining the scientific discussion between Juergen and me. Your valuable advice and critical comments always help me sort out ideas about the project and your enthusiasm for science and your attitude to the students also inspire me.

I want to thank Prof. Thomas Lippert, Prof. Vivek Subramanian, Prof. Herbert Shea and Dr. Michel Despont for accepting my invitation to be the jury members of my oral defense. Your constructive and pointed comments in the report and the oral defense have helped me improve my final thesis.

I am so grateful to join the LMIS1 family and enjoy many joyful moments with my colleagues here. Without their support and the inspiring atmosphere, I would not have been able to complete my Ph.D. work. I want to thank the current lab members, Nicole Bouendin, Hernan Fernando Furci, Xia Liu, Biranche Tandon, André Chatel, Berke Erbas, Reza Farsi, Jongeon Park, Roberto Russo, Nergiz Sahin Solmaz, Qinglan Shan, Pol Torres Vila, Henry Yu and Chenxiang Zhang. In addition, I want to thank the former members, Pierrick Clément, Ana Conde Rubio, Lorenz Hagelüken, Jack Sun, Claudio Gonnlly, Thomas Walger, Séverine Egli, Matthiew Rüegg, Ya Wang, Samuel Howell, Christopher Tse, Jongmoon Jang and Alessandro Matheoud. Especially, I want to thank Henry Yu, Pierrick Clément and Jason Taylor for their proofreading work for my thesis and Thomas Walger for his translation of the thesis abstract into French. Besides, I want to express thanks to my office mates: Christopher Tse, Jack Sun and Roberto Russo. It was a fortune for me that I enjoyed numerous memorable times with them as friends

## Acknowledgements

---

and colleagues.

I thank all the scientists and engineers from the Center of MicroNanoTechnology (CMi) at EPFL for their training and support. Also, I want to thank Remo Widmer and Prof. Johann Michler from the Laboratory for Mechanics of Materials and Nanostructures at Swiss Federal Laboratories for Materials Science and Technology (EMPA) for the scientific collaboration and Ryan van Dommelen and Dr. Danick Briand from Soft Transducers Lab at EPFL for lending us the vibration exciter.

I am so glad that I have developed many friendships outside LMIS1. I had a great time playing football with the Chinese community at EPFL. This not only strengthens my body but also helps me develop good friendships with them. I am also grateful that I made new friends with people from other labs, like Farzad Rezaeianaran, Zhaoyang Wang, Yihui Zuo, etc. Many thanks to all of you for making my Swiss journey meaningful and enjoyable.

Last but not least, I am deeply indebted to my family, which is a source of love and encouragement. My family is a warm harbor helping me weather the storm and I am so grateful they gave me unconditional love and support whenever I needed it. My father, Wenqi Yang, always teaches me to smile and march forward courageously. My mother, Shuying Zhang, shaped my personality with optimism and persistence. I know you are now watching me in another world and I will not let you down. Finally, I would like to show my gratitude to my girlfriend, Bingqin Li. You are a ray of sunlight in my life and help me through many tough times. Met in Beijing and fell in love in Switzerland; I am fully convinced that you are the one I am looking for and thanks for your company in my Swiss and EPFL journey.

*Lausanne, December 21, 2022*

Zhiwei Yang

# Abstract

Laser-induced forward transfer (LIFT) technique is an emerging micro additive manufacturing (AM) technique that has been widely used to print a variety of materials. Distinguished from other nozzle-based AM techniques, LIFT operates without the existence of the nozzle. This unique feature enables the transfer of prefabricated microstructures, and many works demonstrated successful transfers of different microcomponents. However, few studies have investigated the transfer of microstructures with functionality. In addition, no studies have ever explored the transfer of complex or fragile microstructures. Therefore, this thesis aims to tackle these challenges by transferring prefabricated SU-8-supported microdevices and proving their post-transfer functionality. Furthermore, the transfers of two-photon lithography (TPL) fabricated complex and fragile microstructures are demonstrated.

In this thesis, we start by performing the LIFT experiments using pure SU-8 microdisks. Four different variables, including the laser fluence (laser energy), the polyimide (PI) thickness, the SU-8 thickness and the donor-to-receiver gap distance, are systematically studied. Successful and damage-free transfer of SU-8 microdisks with high transfer precision can be achieved with the optimized parametric combination (e.g.,  $\geq 1.6 \text{ J/cm}^2$ , PI thickness of 3 & 5  $\mu\text{m}$ , SU-8 thickness of 50  $\mu\text{m}$ , and small gap distance).

Based on the experimental results in the previous chapter, we take one step further, transferring SU-8-supported functional microdevices. Two types of functional devices, the SU-8-supported metal quick response (QR) codes and temperature sensors, are transferred to different receivers. For the QR codes, their readability is verified after the transfer by the QR scanner. Further analysis of the adhesion between the transferred SU-8-supported QR codes and the receiver demonstrates that SU-8 devices adhere well to the receivers and can survive in harsh conditions. As for the temperature sensors, they are transferred onto receivers with prepatterened electrodes. Our transfer guarantees good electrical contact between the temperature sensor and the electrodes on the receiver, confirmed by the subsequent electrical measurement. Apart from these two functional microdevice transfer demonstrations, we extend LIFT for the realization of large-scale transfer using customized programming codes. A  $40 \times 40$  array of SU-8 microdisks are transferred onto a PDMS-coated 4-inch wafer. Furthermore, SU-8 microdisks are assembled to form three-dimensional (3D) structures and are transferred

## Abstract

---

to different nonplanar surfaces to reveal the non-contact transfer ability of LIFT.

In the end, we extend the transfer to TPL-fabricated microstructures. Microscaffolds with different pore sizes and dimensions are transferred without damage. Moreover, by adding a supporting layer, we achieve the transfer of fragile microscaffolds and large scaffolds. Subsequently, three transfer examples are demonstrated. The first demonstration is the transfer of a T-shape microstructure into the PDMS channel with high precision. In the second example, microscaffolds loaded with Rhodamine B ink are transferred, and the ink release ability is qualitatively assessed. The last demonstration makes use of the ability of LIFT for upscaled transfer, and a  $7 \times 7$  microsccaffold array is placed on a 4-inch wafer.

In conclusion, the methods and results presented in this thesis show the potential of LIFT for transferring functional microdevices & complex and fragile microstructures in a damage-free way and maintaining their functionality after transfer. This work lays a solid foundation for the exploration of transferring other potential microdevices and assembling microstructures in a fully automated manner.

**Keywords:** Laser-induced forward transfer, SU-8, Polyimide, QR code, Temperature sensor, Two-photon lithography



# Résumé

La technique de transfert vers l'avant induit par laser (LIFT) est une technique émergente de fabrication additive. Le LIFT a été largement utilisé pour imprimer une variété de matériaux. Se distinguant des autres techniques de fabrication additive à base de buses, le LIFT fonctionne sans l'existence de la buse. Cette caractéristique unique permet le transfert de microstructures préfabriquées, et de nombreux travaux ont montré des transferts réussis de différents microcomposants. Cependant, peu d'études ont étudié le transfert de microstructures avec fonctionnalité. De plus, aucune étude n'a exploré le transfert de microstructures complexes ou fragiles. Par conséquent, cette thèse vise à relever ces défis en transférant des micro-dispositifs préfabriqués soutenus par du SU-8 et à prouver leur fonctionnalité post-transfert. En outre, les transferts des microstructures complexes et fragiles fabriquées par lithographie à deux photons sont démontrés.

Dans cette thèse, nous commençons par réaliser les expériences LIFT en utilisant des micro-disques de pur SU-8. Quatre différentes variables sont étudiées de manière systématique. Ce sont la fluence laser (l'énergie du laser), l'épaisseur de polyimide (PI), l'épaisseur du SU-8 et la distance entre le donneur et le récepteur. Des transferts réussis et sans dommage des micro-disques de SU8 peuvent être réalisés avec une grande précision de transfert grâce à l'optimisation de la combinaison de paramètres (par exemple, fluence laser  $\geq 1.6 \text{ J/cm}^2$ , épaisseur PI de 3 et 5  $\mu\text{m}$ , épaisseur SU-8 de 50  $\mu\text{m}$ , et petite distance d'écart donneur-récepteur).

Sur la base des résultats expérimentaux, nous allons encore plus loin dans le dernier chapitre en transférant des micro-dispositifs fonctionnels supportés par du SU-8. Deux types de dispositifs fonctionnels supportés par du SU-8 sont transférés sur différents récepteurs : des codes à réponse rapide (QR codes) métalliques et des sondes de température. Pour les codes QR, leur lisibilité est vérifiée après le transfert à l'aide d'un scanner QR. Une plus ample analyse de l'adhérence entre les codes QR (supportés par le SU-8) transférés et le récepteur démontre que de tels appareils en SU-8 adhèrent bien aux récepteurs et qu'ils peuvent survivre dans des conditions difficiles. Quant aux sondes de température, elles sont transférées sur des récepteurs sur lesquels des électrodes avaient été préfabriquées. Notre transfert garantit un bon contact électrique entre la sonde de température et les électrodes sur le récepteur, ce qui est

## Résumé

---

confirmé par test électrique. Outre ces deux démonstrations de transfert de micro-dispositifs fonctionnels, nous développons le LIFT pour la réalisation de transfert à grande échelle en utilisant des codes de programmation personnalisés. Un réseau de  $40 \times 40$  micro-disques SU-8 sont transférés sur une plaquette (wafer) de 100 mm recouverte de PDMS. De plus, des micro-disques de SU-8 sont assemblés pour former des structures tridimensionnelles (3D) et transférés sur différentes surfaces non planes pour révéler la capacité de transfert sans contact du LIFT.

Enfin, nous étendons les transferts aux microstructures fabriquées par lithographie à deux photons. Des micro-échafaudages avec des pores de différentes tailles et dimensions sont transférés sans dommage. De plus, en ajoutant une couche de support, nous réalisons le transfert de micro-échafaudages fragiles et de grands échafaudages. Par la suite, trois exemples de transfert sont présentés. La première démonstration est le transfert d'une microstructure en forme de T dans un canal en PDMS avec une grande précision. Dans le deuxième exemple, des micro-échafaudages chargés d'encre Rhodamine B sont transférés, et la capacité de libération de l'encre est évaluée qualitativement. La dernière démonstration utilise la capacité du LIFT pour un transfert massif, et un réseau de  $7 \times 7$  micro-échafaudages est placé sur une plaquette de 100 mm.

En conclusion, les méthodes et résultats présentés dans cette thèse montrent le potentiel du LIFT pour transférer des micro-dispositifs fonctionnels et des microstructures complexes et fragiles sans dommage tout en maintenant leur fonctionnalité après le transfert. Ce travail pose des bases solides pour l'exploration du transfert d'autres micro-dispositifs et de l'assemblage de microstructures de manière entièrement automatisée.

**Keywords :** Transfert vers l'avant induit par laser, SU-8, Polyimide, Code QR, Sonde de température, Lithographie à deux photons

# List of Figures

|      |  |    |
|------|--|----|
| 1.1  | Schematic illustrations of two approaches for material patterning . . . . .  | 1  |
| 1.2  | Schematic illustrations showing the inkjet printing, EHD printing and LIFT technique . . . . .                               | 2  |
| 1.3  | Schematic illustration of a typical LIFT configuration . . . . .   | 3  |
| 1.4  | Schematic illustrations of four LIFT variations . . . . .  | 4  |
| 1.5  | Laser-based microstructure transfer examples . . . . .   | 10 |
| 1.6  | Four transfer examples using different intermediate layers . . . . .   | 13 |
| 1.7  | Functional device transfer examples using PI as the intermediate layer . . . . .   | 15 |
| 1.8  | Theoretical and experimental analysis of PI blister formation . . . . .  | 19 |
| 1.9  | Simulation of the transfer of microchips . . . . .   | 20 |
| 1.10 | Schematic illustrations of the LIFT process under two cases . . . . .  | 21 |
| 1.11 | Objective of this thesis . . . . .   | 23 |
| 2.1  | LIFT setup . . . . .   | 27 |
| 2.2  | Stencil fabrication . . . . .  | 29 |
| 2.3  | Fabrication process of metal patterned SU-8 microdisks . . . . .   | 30 |
| 2.4  | Influence of laser fluence on the SU-8 transfer result . . . . .   | 32 |
| 2.5  | Representative images presenting transferred SU-8 microdisks under three laser fluences. . . . .                             | 33 |
| 2.6  | PI blister created by 0.96 J/cm <sup>2</sup> laser fluence . . . . .   | 34 |
| 2.7  | Direct comparison of five different PI blisters under different laser fluence conditions . . . . .                           | 35 |
| 2.8  | PI blister profile summary . . . . .   | 36 |
| 2.9  | Blisters created by 0.96 J/cm <sup>2</sup> laser fluence (4 shots) on the free surface of PI . . . . .                       | 39 |
| 2.10 | Direct comparison of five different PI blisters under different laser fluence conditions on the free surface of PI . . . . . | 40 |
| 2.11 | PI blister profile summary created on PI free surface . . . . .  | 41 |
| 2.12 | Simple sketches showing the increase of blister height under different laser pulses . . . . .                                | 42 |
| 2.13 | PI blister comparison with and without the SU-8 microdisk . . . . .  | 43 |
| 2.14 | PI blister profile summary under three situations . . . . .  | 44 |

## List of Figures

---

|   |    |
|---|----|
| 2.15 PI blister created by 3.2 J/cm <sup>2</sup> laser fluence on a 1- $\mu$ m-thick PI film . . . . .                    | 45 |
| 2.16 PI blister created by 3.2 J/cm <sup>2</sup> laser fluence on a 3- $\mu$ m-thick PI film . . . . .                    | 46 |
| 2.17 Direct comparison of six PI blisters created on PI films with different thicknesses                                  | 47 |
| 2.18 PI blister profile summary with different PI thicknesses . . . . .   | 48 |
| 2.19 Direct comparison of six PI blisters created on the free surface of PI films with<br>different thicknesses . . . . . | 49 |
| 2.20 Laser ablation tests on bare float glass wafer . . . . .   | 51 |
| 2.21 Summary of PI blister profiles created on PI surface with different thicknesses .                                    | 52 |
| 2.22 Transfer results of SU-8 microdisks with different SU-8 thicknesses . . . . .  | 53 |
| 2.23 Sketches of different transfer results as the increase of donor-receiver gap distance                                | 55 |
| 2.24 SU-8 transfer result on PDMS receiver with a gap distance of close contact . . .                                     | 55 |
| 2.25 SU-8 transfer results on PDMS receiver with a gap distance of 50, 210 and 370 $\mu$ m                                | 56 |
| 2.26 Summary of the transfer precision of SU-8 microdisks . . . . .   | 57 |
| <br>  |    |
| 3.1 Fabrication of SU-8-supported QR codes . . . . .  | 64 |
| 3.2 Transfer result of five SU-8-supported QR codes . . . . .   | 65 |
| 3.3 Schematic illustrations of the two adhesion tests . . . . .   | 66 |
| 3.4 Experimental results of the two adhesion tests . . . . .  | 66 |
| 3.5 Adhesion test of transferred SU-8 microdisks onto Si receiver . . . . .   | 67 |
| 3.6 Displacement-load curves for SU-8 samples on glass, Cu and PDMS receivers .   | 68 |
| 3.7 SEM images of SU-8 microdisk before and after the adhesion test on different<br>receivers . . . . .                   | 69 |
| 3.8 Adhesion test for SU-8 microdisks on Cu receiver after thermal annealing in DI<br>water . . . . .                     | 70 |
| 3.9 Adhesion test for SU-8 microdisks on glass receiver after thermal annealing in<br>DI water . . . . .                  | 71 |
| 3.10 Adhesion test for SU-8 microdisks on Si receiver after thermal annealing in DI<br>water . . . . .                    | 72 |
| 3.11 Adhesion test for SU-8 microdisks on PDMS receiver after thermal annealing in<br>DI water . . . . .                  | 73 |
| 3.12 SU-8-supported temperature sensor after fabrication . . . . .  | 74 |
| 3.13 SU-8-supported temperature sensor transfer and characterization . . . . .  | 75 |
| 3.14 Measured temperature-resistance curve of the SU-8 supported temperature<br>sensor before annealing . . . . .         | 76 |
| 3.15 Characterization of two additional transferred SU-8-supported temperature<br>sensors . . . . .                       | 77 |
| 3.16 Dense SU-8 microdisk array for large-scale transfer . . . . .  | 79 |
| 3.17 Transfer strategy of SU-8 microdisks from donor to receiver . . . . .  | 81 |
| 3.18 Large-scale transfer of SU-8 microdisks . . . . .  | 82 |

|      |   |     |
|------|---|-----|
| 3.19 | Coordinate calculation and correction for SU-8 microdisks . . . . .   | 83  |
| 3.20 | Large-scale transfer of SU-8 microdisks after rotation correction . . . . .   | 85  |
| 3.21 | 3D assembly of SU-8 microdisks . . . . .  | 87  |
| 3.22 | SU-8 microdisk transfer onto nonplanar surfaces . . . . .   | 87  |
| 3.23 | SU-8 microdisk transfer into concave microstructures . . . . .  | 88  |
| 3.24 | Scratch test of the transferred SU-8 microdisks . . . . .   | 88  |
|      |   |     |
| 4.1  | Two methods to manipulate TPL-fabricated microstructures . . . . .  | 92  |
| 4.2  | Transfer results of microscaffolds on PDMS . . . . .  | 95  |
| 4.3  | Transfer result of microscaffolds with a pore size of 18 $\mu\text{m}$ . . . . .  | 96  |
| 4.4  | Microscaffold size study . . . . .  | 97  |
| 4.5  | Microscaffolds with supporting layers after the transfer process . . . . .  | 99  |
| 4.6  | Transfer of T-shape microstructures into PDMS microchannels . . . . .   | 101 |
| 4.7  | Optical images of transferred of Rhodamine B ink loaded microscaffolds . . . . .  | 102 |
| 4.8  | Rhodamine B ink release experiment after LIFT process . . . . .   | 103 |
| 4.9  | 7 $\times$ 7 microscaffold array on the donor . . . . .   | 104 |
| 4.10 | Transfer result of the microscaffold array . . . . .  | 104 |
|      |   |     |
| 5.1  | Proposed adhesion test of SU-8 microdisks patterned on the donor substrate . . . . .  | 111 |
| 5.2  | Time-resolved imaging of SU-8 microdisk velocity . . . . .  | 112 |
|      |   |     |
| A.1  | Metal number patterned SU-8 microdisk . . . . .   | 113 |
| A.2  | SU-8 microdisk transfer with laser fluence of 0.32 J/cm <sup>2</sup> . . . . .  | 114 |
| A.3  | PI blister created by 1.6 J/cm <sup>2</sup> laser fluence . . . . .   | 115 |
| A.4  | PI blister created by 1.92 J/cm <sup>2</sup> laser fluence . . . . .  | 116 |
| A.5  | PI blister created by 2.56 J/cm <sup>2</sup> laser fluence . . . . .  | 117 |
| A.6  | PI blister created by 3.2 J/cm <sup>2</sup> laser fluence . . . . .   | 118 |
| A.7  | PI blister volume calculation in the presence of the SU-8 microdisk (5 $\mu\text{m}$ thick PI) . . . . .                          | 119 |
| A.8  | Blisters created by 1.6 J/cm <sup>2</sup> laser fluence (2 shots) on the free surface of PI . . . . .                             | 120 |
| A.9  | Blisters created by 1.92 J/cm <sup>2</sup> laser fluence (1 shot) on the free surface of PI . . . . .                             | 121 |
| A.10 | Blisters created by 2.56 J/cm <sup>2</sup> laser fluence (1 shot) on the free surface of PI . . . . .                             | 122 |
| A.11 | Blisters created by 3.2 J/cm <sup>2</sup> laser fluence (1 shot) on the free surface of PI . . . . .                              | 123 |
| A.12 | PI Blisters created by 0.96 J/cm <sup>2</sup> & 1 shot on the free surface of PI . . . . .  | 124 |
| A.13 | PI Blisters created by 0.32 J/cm <sup>2</sup> & 1 shot on the free surface of PI . . . . .  | 125 |
| A.14 | PI Blisters created by 0.32 J/cm <sup>2</sup> & 10 shots on the free surface of PI . . . . .                                      | 126 |
| A.15 | PI blister volume calculation in the absence of the SU-8 microdisk (5 $\mu\text{m}$ thick PI) . . . . .                           | 127 |
| A.16 | PI Blisters created by 0.96 J/cm <sup>2</sup> & 1 shot in the presence of the SU-8 microdisk (1 $\mu\text{m}$ thick PI) . . . . . | 128 |
| A.17 | PI blister created by 3.2 J/cm <sup>2</sup> laser fluence on a 7- $\mu\text{m}$ -thick PI film . . . . .                          | 129 |

## List of Figures

---

|   |     |
|---|-----|
| A.18 PI blister created by 3.2 J/cm <sup>2</sup> laser fluence on a 9- $\mu$ m-thick PI film . . . . .  | 130 |
| A.19 PI blister created by 3.2 J/cm <sup>2</sup> laser fluence on an 11- $\mu$ m-thick PI film . . . . .  | 131 |
| A.20 PI blister volume calculation in the presence of the SU-8 microdisk on different thick PI films . . . . .  | 132 |
| A.21 PI Blisters created by 3.2 J/cm <sup>2</sup> & 1 shot and 0.96 J/cm <sup>2</sup> & 1 shot on the free surface of PI (1 $\mu$ m thick PI) . . . . . | 133 |
| A.22 PI Blisters created by 3.2 J/cm <sup>2</sup> & 1 shot on the free surface of PI (3 $\mu$ m thick PI) . . . . .                                     | 134 |
| A.23 PI Blisters created by 3.2 J/cm <sup>2</sup> & 1 shot on the free surface of PI (7 $\mu$ m thick PI) . . . . .                                     | 135 |
| A.24 PI Blisters created by 3.2 J/cm <sup>2</sup> & 1 shot on the free surface of PI (9 $\mu$ m thick PI) . . . . .                                     | 136 |
| A.25 PI Blisters created by 3.2 J/cm <sup>2</sup> & 1 shot on the free surface of PI (11 $\mu$ m thick PI) . . . . .                                    | 137 |
| A.26 PI blister volume calculation in the absence of the SU-8 microdisk on different thick PI films . . . . .   | 138 |
| A.27 Transfer results of SU-8 microdisks with different SU-8 thicknesses (on the donor) . . . . .   | 139 |
| A.28 Adhesion test for SU-8 microdisks on Cu receiver without thermal annealing in DI water . . . . .   | 140 |
| A.29 Adhesion test for SU-8 microdisks on glass receiver without thermal annealing in DI water . . . . .  | 141 |
| A.30 Adhesion test for SU-8 microdisks on Si receiver without thermal annealing . . . . .   | 142 |
| A.31 Adhesion test for PDMS receiver without thermal annealing in DI water . . . . .  | 143 |
| A.32 G-code script for 40 $\times$ 30 SU-8 microdisk array transfer with pitch distance of 1000 $\mu$ m . . . . .                                       | 144 |
| A.33 SU-8 coordinate in the LIFT setup . . . . .  | 145 |
| A.34 G-code script for 40 $\times$ 40 SU-8 microdisk array transfer with pitch distance of 1000 $\mu$ m . . . . .                                       | 146 |
| A.35 Microscaffold building blocks design . . . . .   | 147 |
| A.36 Microscaffolds with different pore sizes . . . . .   | 148 |
| A.37 Microscaffolds with different sizes . . . . .  | 149 |
| A.38 Microscaffolds with the supporting layer . . . . .   | 150 |
| A.39 Transfer result of a T-shape microstructure into PDMS channel with a tilted angle . . . . .  | 151 |
| A.40 Microscaffold array design . . . . .   | 152 |
| A.41 G-code script for 7 $\times$ 7 microscaffold array transfer with varying pitch distance . . . . .  | 153 |

# List of Tables

|     |   |     |
|-----|---|-----|
| 1.1 | Summary of laser-based transfer of microcomponents . . . . .  | 16  |
| 1.2 | Parameters that influence the successful transfer of a SU-8 microdisk by PI-LIFT . . . . .  | 23  |
| 2.1 | Summary of the transfer result of SU-8 microdisks and the corresponding blisters created on 5 $\mu\text{m}$ thick PI . . . . .      | 38  |
| 2.2 | Summary of blisters created on the free surface of PI (5 $\mu\text{m}$ thick) by different laser fluence . . . . .                  | 43  |
| 2.3 | Summary of the transfer result of SU-8 microdisks and the corresponding blisters created on PI with different thicknesses . . . . . | 50  |
| 3.1 | Summary of the SU-8 microdisk adhesion test results on different receivers in DI water . . . . .                                    | 71  |
| 4.1 | Transfer result of 100 $\mu\text{m}$ large microscaffolds with different pore sizes . . . . .                                       | 96  |
| 4.2 | Transfer result of microscaffolds with the supporting layer . . . . .   | 100 |





# Acronyms

**AFM** Atomic force microscopy

**AM** Additive manufacturing

**CPW** Coplanar waveguide

**DMD** Digital micromirror device

**DRL-LIFT** Dynamic-Release-Layer LIFT

**FEA** Finite-element analysis

**FF-LIFT** Film-free LIFT

**FWHM** Full width at half maximum

**IPA** Isopropanol

**KOH** Potassium hydroxide

**LDT** Laser decal transfer

**LDW** Laser direct-write

**LEAP** Laser-enabled advanced packaging

**LIFT** Laser-induced forward transfer

**LMTP** Laser micro transfer placement

**LPCVD** Low-pressure chemical vapor deposition

**MAPLE-DW** Matrix-assisted pulsed laser evaporation-direct write

**MEMS** Microelectromechanical systems

**MPLLET** Massively parallel laser-enabled transfer

**NQD** Nanocrystal quantum dot

## **Chapter 0. Acronyms**

---

**OLED** Organic light-emitting diode

**PDMS** Polydimethylsiloxane

**PEB** Post-exposure baking

**PEI** Polyethylenimine

**PGMEA** Propylene glycol monomethyl ether acetate

**PI** Polyimide

**PIB** Polyisobutylene

**PLED** Polymer light-emitting diode

**PMMA** Polymethyl methacrylate

**PS** Polystyrene

**QR** Quick response

**SEM** Scanning electron microscopy

**SMP** Shape memory polymer

**TA** Thermal annealing

**TCR** Temperature coefficient of resistance

**TCVS** Trichlorovinylsilane

**tmSLDT** Thermo-mechanical selective laser-assisted die transfer

**TP** Triazene polymer

**TPL** Two-photon lithography

**UV** Ultraviolet

**VSI** Vertical shift interference

**3D** Three dimensional

# Contents

|   |             |
|---|-------------|
| <b>Acknowledgements</b>   | <b>i</b>    |
| <b>Abstract (English/Français)</b>  | <b>iii</b>  |
| <b>List of Figures</b>  | <b>vii</b>  |
| <b>List of Tables</b>   | <b>xi</b>   |
| <b>Acronyms</b>   | <b>xiii</b> |
| <b>1 Introduction</b>   | <b>1</b>    |
| 1.1 Background . . . . .  | 1           |
| 1.2 Laser-induced forward transfer (LIFT) technique . . . . .               | 2           |
| 1.2.1 Introduction of LIFT . . . . .  | 2           |
| 1.2.2 LIFT variations . . . . .   | 3           |
| 1.2.3 LIFT applications . . . . .   | 7           |
| 1.3 LIFT of functional devices . . . . .                                    | 9           |
| 1.3.1 State-of-the-art microcomponent transfer by LIFT . . . . .            | 10          |
| 1.4 Aims and outline of the thesis . . . . .                                | 20          |
| 1.4.1 Aims . . . . .  | 20          |
| 1.4.2 Outline . . . . .   | 23          |
| <b>2 LIFT of SU-8 Microdisks</b>  | <b>25</b>   |
| 2.1 Introduction . . . . .  | 26          |
| 2.2 Materials and methods . . . . .   | 27          |
| 2.2.1 LIFT setup . . . . .  | 27          |
| 2.2.2 SU-8 donor preparation . . . . .                                      | 27          |
| 2.2.3 Stencil fabrication . . . . .   | 28          |
| 2.2.4 SU-8 functional device fabrication . . . . .                          | 29          |
| 2.2.5 Receiver substrate preparation . . . . .                              | 31          |
| 2.2.6 Scanning electron microscopy (SEM) of the transferred SU-8 microdisks | 31          |
|   | xv          |

## Contents

---

|          |   |           |
|----------|---|-----------|
| 2.2.7    | Optical profilometer measurement of the polyimide (PI) blister morphology . . . . . | 31        |
| 2.3      | Results and discussion . . . . .  | 31        |
| 2.3.1    | Influence of laser fluence . . . . .  | 31        |
| 2.3.2    | Influence of PI thickness . . . . .   | 44        |
| 2.3.3    | Influence of SU-8 thickness . . . . .   | 52        |
| 2.3.4    | Influence of donor-to-receiver gap distance . . . . .                               | 54        |
| 2.4      | Conclusion . . . . .  | 58        |
| <b>3</b> | <b>LIFT of SU-8-Supported Functional Devices</b>                                    | <b>61</b> |
| 3.1      | Introduction . . . . .  | 62        |
| 3.2      | Transfer and characterization of SU-8 microdisks with metal QR code . . . . .       | 63        |
| 3.2.1    | Fabrication of donor and receiver . . . . .   | 63        |
| 3.2.2    | Transfer result . . . . .   | 64        |
| 3.2.3    | Adhesion test . . . . .   | 64        |
| 3.3      | Transfer and characterization of SU-8 microdisks with temperature sensor . . . . .  | 73        |
| 3.3.1    | Fabrication and characterization . . . . .  | 73        |
| 3.3.2    | Transfer result . . . . .   | 75        |
| 3.3.3    | Temperature sensor characterization . . . . .                                       | 76        |
| 3.4      | Large-scale transfer of SU-8 microdisks . . . . .                                   | 79        |
| 3.4.1    | Fabrication of SU-8 microdisks and PDMS receivers . . . . .                         | 79        |
| 3.4.2    | Transfer strategy . . . . .   | 80        |
| 3.4.3    | Transfer result . . . . .   | 80        |
| 3.5      | Transfer of SU-8 microdisks onto nonplanar receivers . . . . .                      | 85        |
| 3.5.1    | Nonplanar receiver preparation . . . . .  | 86        |
| 3.5.2    | Transfer result . . . . .   | 86        |
| 3.6      | Conclusion . . . . .  | 89        |
| <b>4</b> | <b>LIFT of Microstructures Fabricated by Two-Photon Lithography (TPL)</b>           | <b>91</b> |
| 4.1      | Introduction . . . . .  | 91        |
| 4.2      | Materials and methods . . . . .   | 93        |
| 4.2.1    | TPL setup . . . . .   | 93        |
| 4.2.2    | TPL donor preparation . . . . .   | 93        |
| 4.2.3    | Receiver substrate preparation . . . . .  | 94        |
| 4.2.4    | Rhodamine B ink preparation . . . . .   | 94        |
| 4.2.5    | SEM characterization of transferred microstructures . . . . .                       | 94        |
| 4.3      | Results and discussion . . . . .  | 94        |
| 4.3.1    | Influence of pore size . . . . .  | 94        |
| 4.3.2    | Influence of TPL structure size . . . . .   | 97        |

|  |            |
|--|------------|
| 4.3.3 Influence of supporting layer . . . . .  | 98         |
| 4.4 LIFT Demonstrations . . . . .  | 100        |
| 4.4.1 Transfer of TPL microstructures into PDMS microchannels . . . . .  | 100        |
| 4.4.2 Transfer of TPL structures filled with liquid ink . . . . .  | 101        |
| 4.4.3 Programmed transfer of TPL structures . . . . .  | 103        |
| 4.5 Conclusion . . . . .   | 105        |
| <br>   |            |
| <b>5 Conclusion and Outlook</b>  | <b>107</b> |
| 5.1 Conclusion . . . . .   | 107        |
| 5.2 Outlook . . . . .  | 110        |
| <br>   |            |
| <b>A An appendix</b>   | <b>113</b> |
| A.1 Metal number patterned SU-8 microdisk . . . . .  | 113        |
| A.2 SU-8 microdisk transfer with a laser fluence of $0.32 \text{ J/cm}^2$ . . . . .  | 114        |
| A.3 PI blister created by $1.6 \text{ J/cm}^2$ laser fluence . . . . .   | 115        |
| A.4 PI blister created by $1.92 \text{ J/cm}^2$ laser fluence . . . . .  | 116        |
| A.5 PI blister created by $2.56 \text{ J/cm}^2$ laser fluence . . . . .  | 117        |
| A.6 PI blister created by $3.2 \text{ J/cm}^2$ laser fluence . . . . .   | 118        |
| A.7 PI blister volume calculation in the presence of the SU-8 microdisk ( $5 \mu\text{m}$ thick PI) . . . . .                          | 119        |
| A.8 Blisters created by $1.6 \text{ J/cm}^2$ laser fluence (2 shots) on the free surface of PI . . . . .                               | 120        |
| A.9 Blisters created by $1.92 \text{ J/cm}^2$ laser fluence (1 shot) on the free surface of PI . . . . .                               | 121        |
| A.10 Blisters created by $2.56 \text{ J/cm}^2$ laser fluence (1 shot) on the free surface of PI . . . . .                              | 122        |
| A.11 Blisters created by $3.2 \text{ J/cm}^2$ laser fluence (1 shot) on the free surface of PI . . . . .                               | 123        |
| A.12 PI Blisters created by $0.96 \text{ J/cm}^2$ & 1 shot on the free surface of PI . . . . .   | 124        |
| A.13 PI Blisters created by $0.32 \text{ J/cm}^2$ & 1 shot on the free surface of PI . . . . .   | 125        |
| A.14 PI Blisters created by $0.32 \text{ J/cm}^2$ & 10 shots on the free surface of PI . . . . .                                       | 126        |
| A.15 PI blister volume calculation in the absence of the SU-8 microdisk ( $5 \mu\text{m}$ thick PI) . . . . .                          | 127        |
| A.16 PI Blisters created by $0.96 \text{ J/cm}^2$ & 1 shot in the presence of the SU-8 microdisk ( $1 \mu\text{m}$ thick PI) . . . . . | 128        |
| A.17 PI Blisters created by $3.2 \text{ J/cm}^2$ & 1 shot in the presence of the SU-8 microdisk ( $7 \mu\text{m}$ thick PI) . . . . .  | 129        |
| A.18 PI Blisters created by $3.2 \text{ J/cm}^2$ & 1 shot in the presence of the SU-8 microdisk ( $9 \mu\text{m}$ thick PI) . . . . .  | 130        |
| A.19 PI Blisters created by $3.2 \text{ J/cm}^2$ & 1 shot in the presence of the SU-8 microdisk ( $11 \mu\text{m}$ thick PI) . . . . . | 131        |
| A.20 PI blister volume calculation in the presence of the SU-8 microdisk on different thick PI films . . . . .                         | 132        |

## Contents

---

|  |            |
|--|------------|
| A.21 PI Blisters created by 3.2 J/cm <sup>2</sup> & 1 shot and 0.96 J/cm <sup>2</sup> & 1 shot on the free surface of PI (1 μm thick PI) . . . . . | 133        |
| A.22 PI Blisters created by 3.2 J/cm <sup>2</sup> & 1 shot on the free surface of PI (3 μm thick PI)   | 134        |
| A.23 PI Blisters created by 3.2 J/cm <sup>2</sup> & 1 shot on the free surface of PI (7 μm thick PI)   | 135        |
| A.24 PI Blisters created by 3.2 J/cm <sup>2</sup> & 1 shot on the free surface of PI (9 μm thick PI)   | 136        |
| A.25 PI Blisters created by 3.2 J/cm <sup>2</sup> & 1 shot on the free surface of PI (11 μm thick PI)  | 137        |
| A.26 PI blister volume calculation in the absence of the SU-8 microdisk on different thick PI films . . . . .                                      | 138        |
| A.27 Transfer results of SU-8 microdisks with different SU-8 thicknesses (on the donor)  | 139        |
| A.28 Adhesion test for SU-8 microdisks on Cu receiver without thermal annealing in DI water . . . . .  | 140        |
| A.29 Adhesion test for SU-8 microdisks on glass receiver without thermal annealing in DI water . . . . .   | 141        |
| A.30 Adhesion test for SU-8 microdisks on Si receiver without thermal annealing in DI water . . . . .  | 142        |
| A.31 Adhesion test for SU-8 microdisks on PDMS receiver without thermal annealing in DI water . . . . .  | 143        |
| A.32 G-code script for 40×30 SU-8 microdisk array transfer . . . . .   | 144        |
| A.33 SU-8 coordinate in the LIFT setup . . . . .   | 145        |
| A.34 G-code script for 40×40 SU-8 microdisk array transfer . . . . .   | 146        |
| A.35 Microscaffold building blocks design . . . . .  | 147        |
| A.36 Microscaffolds with different pore sizes . . . . .  | 148        |
| A.37 Microscaffolds with different sizes . . . . .   | 149        |
| A.38 Microscaffolds with the supporting layer . . . . .  | 150        |
| A.39 Transfer result of a T-shape microstructure into PDMS channel with a tilted angle   | 151        |
| A.40 Microscaffold array design . . . . .  | 152        |
| A.41 G-code script for 7×7 microscaffold array transfer with varying pitch distance .  | 153        |
| <b>Bibliography</b>  | <b>155</b> |
| <b>Curriculum Vitae</b>  | <b>177</b> |

# 1 Introduction

## 1.1 Background

Depositing and patterning materials to form structures with micron/submicron resolution is of great significance in various fields extending from microelectromechanical systems (MEMS), flexible electronics and bioprinting to optoelectronics, etc. To date, the most widely used technique for the realization of materials micropatterning is photolithography. In photolithography, the targeted material is first deposited on the wafer, with subsequent removal steps (e.g., lift-off/etching) to achieve desired patterns. **Figure 1.1a** shows that photolithography operates in a subtractive manner and multi-steps are required. For cases that require a low amount of materials to reduce waste and call for fewer steps for fast prototyping of novel devices, another type of fabrication approach emerges, which is named additive manufacturing (AM) (shown in **Figure 1.1b**)<sup>[1-4]</sup>.

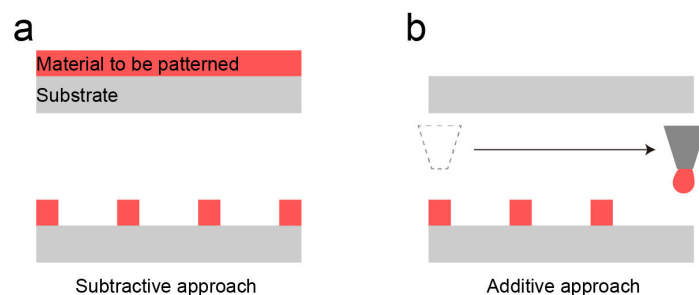


Figure 1.1: **Schematic illustrations of two approaches for material patterning.** (a). The subtractive approach. (b). The additive approach.

Compared to the conventional lithography-based approach, AM technique is famous for its simplicity, flexibility, fast processing time and user customization. Among various AM techniques, there is a family of printing approaches that operate in a drop-on-demand (DOD)

## Chapter 1. Introduction

fashion and are extensively used to pattern a vast diversity of materials. Typical DOD methods include inkjet printing (**Figure 1.2a**) [5–7], electrohydrodynamic (EHD) printing (**Figure 1.2b**) [8,9] and aerosol jet printing [10–12]. However, these DOD schemes have inherent limitations, such as narrow printable windows and nozzle-clogging issues [13,14]. Therefore, the **Laser-Induced Forward Transfer (LIFT)** technique, which uses a laser for selective transfer of materials from a thin film (coated on a donor substrate) to the receiver substrate (**Figure 1.2c**), arises as a strong competitor to other DOD schemes because it is free from the aforementioned limitations. Since its debut in 1986 [15], LIFT has been utilized to print and pattern a series of materials. In all the applications, its ability to transfer prefabricated microstructures due to its nozzle-free nature demonstrates its uniqueness among other AM techniques. Such microstructure transfer ability will be elaborated on in the following sections and it is also our motivation to complete this thesis.

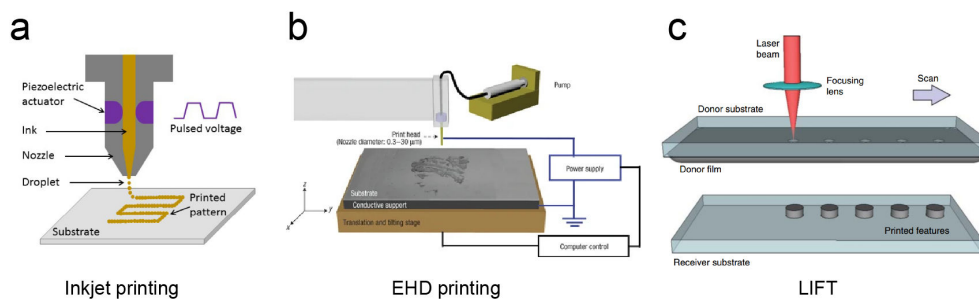


Figure 1.2: Schematic illustrations showing the inkjet printing (a) [16], EHD printing (b) [8] and LIFT technique (c) [17].

## 1.2 Laser-induced forward transfer (LIFT) technique

### 1.2.1 Introduction of LIFT

As mentioned in the "**Background**" section, the term "**LIFT**" is coined in 1986 [15], when Bohandy *et al.* utilized an excimer laser to print metallic lines from a copper (Cu) thin film. Since then, LIFT emerges as a fast-developing AM technique, enabling the printing/transfer of a wide variety of materials/microcomponents [17–24]. The basic operation principle of LIFT is illustrated in **Figure 1.3**. A beam of laser from the laser source is deflected by a mirror and focuses on the interface between the transparent donor substrate and the donor film. By means of laser irradiation, a tiny portion of the donor material will be ejected from the donor film and land on a receiver substrate. This process demonstrates a simple but effective approach to realizing controlled patterning of material on the receiver.

Because of the facile configuration and simple working principle, LIFT is capable of competing with other existing techniques, and it possesses some unparalleled advantages. First, it is a



## 1.2 Laser-induced forward transfer (LIFT) technique

nozzle-free printing technique, which eliminates the adverse effects of nozzle-clogging issues and ink viscosity limitations. This characteristic also makes it compatible with transferring prefabricated microstructures. In addition, LIFT can operate in a non-contact manner. This feature rules out the possibility of contamination of the receiver by the donor materials and broadens the diversity of receiver substrates. Last but not least, the fast laser (pulse width varying from femtosecond to microsecond) enables the printing of materials in a high throughput way, which can find potential in mass production.

In the following parts, the state-of-the-art LIFT technique is reviewed from two aspects: LIFT variations and LIFT applications.

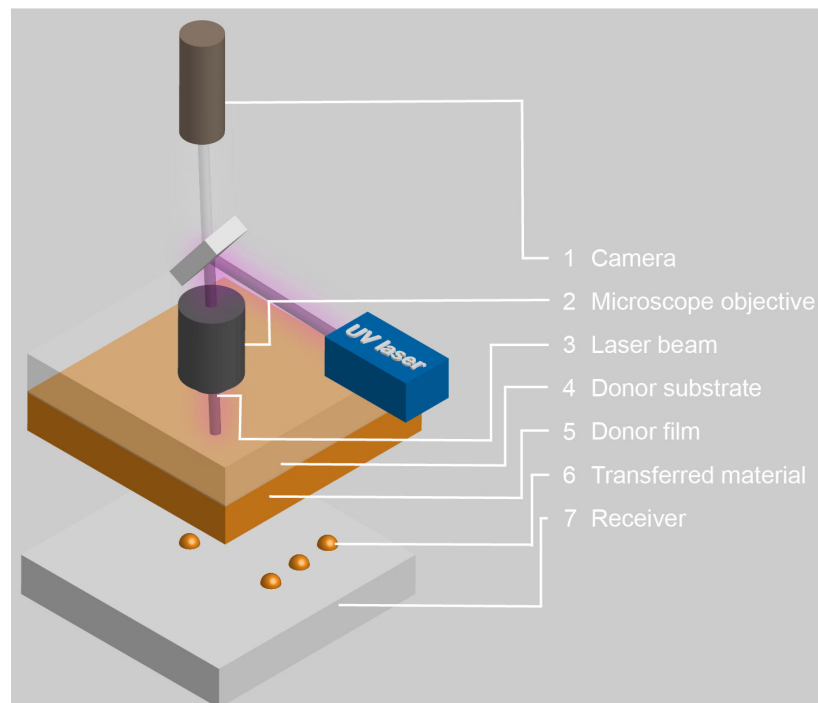


Figure 1.3: **Schematic illustration of a typical LIFT configuration.** In the sketch, the LIFT system consists of a camera, a microscope objective, a laser source, a donor substrate, a thin film of donor material, and a receiver substrate.

### 1.2.2 LIFT variations

The last 40 years have witnessed the rapid development of the LIFT technique, and numerous LIFT variations have been developed in order to print/transfer various materials and address different needs. Below are four types of LIFT variations.

### Matrix-assisted pulsed laser evaporation-direct write (MAPLE-DW)

MAPLE-DW technique is a combination of MAPLE and LIFT. In this technique, the donor material is uniformly embedded into a solvent matrix material with a low evaporation point. Upon absorbing the laser beam, the matrix decomposes into volatile byproducts and then propels the donor material toward the receiver (**Figure 1.4a**). This method features a pyrolytic process only for the matrix material, keeping the donor material uninfluenced by the laser and maintaining its composition and functionality. In the early works<sup>[25–28]</sup>, different materials such as SrTiO<sub>3</sub> (STO), Y<sub>3</sub>Fe<sub>5</sub>O<sub>12</sub> (YIG), BaTiO<sub>3</sub> capacitors and polymer composites as prototypes were printed to prove the feasibility of MAPLE-DW for printing all class of materials.

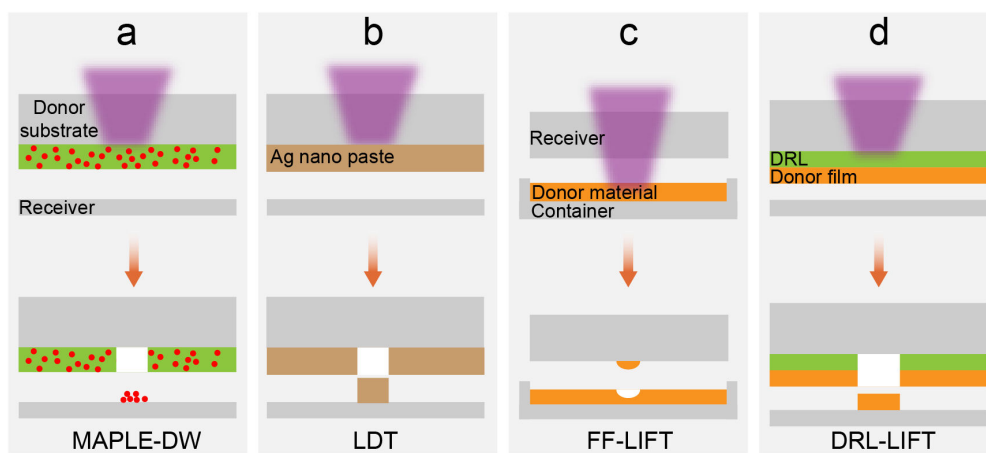


Figure 1.4: **Schematic illustrations of four LIFT variations.** (a). A simple illustration sketches the MAPLE-DW process. (b). A sketch showing the concept of LDT. (c). FF-LIFT process. (d). DRL-LIFT process.

In the meantime, researchers<sup>[29,30]</sup> used ultrahigh-speed optical microscopy to investigate the dynamics of the MAPLE-DW process, and three distinct printing regimes were defined: plume, jetting and sub-threshold regimes, which correspond to high, middle and low laser fluence, respectively.

Due to its flexibility, MAPLE-DW has been employed to print a lot of materials for different applications, including biosensors<sup>[31]</sup>, chemical sensors<sup>[32]</sup>, various cells<sup>[33–36]</sup>, zirconia and hydroxyapatite scaffold materials<sup>[37]</sup>, screen printable inks<sup>[38]</sup>, glycerol-water solution<sup>[35]</sup> and polyethylenimine (PEI) polymers<sup>[39]</sup>.

### Laser decal transfer (LDT)/Congruent LIFT

Congruent LIFT or LDT was first proposed by A. Piqué *et al.*<sup>[40–42]</sup>. Different from conventional LIFT, where evaporation or melting of the donor material is involved in achieving the printing, the LDT process relies on the non-phase transformation of the ink (silver nano-suspensions).

## 1.2 Laser-induced forward transfer (LIFT) technique

---

By capturing the transfer process via high-speed camera<sup>[43,44]</sup>, the transfer mechanism is elucidated, and two parameters, ink viscosity and laser fluence were studied to guarantee the successful transfer of voxels with uniform thickness, sharp edge feature and negligible ink debris (**Figure 1.4b**). With optimized ink viscosity ( $\approx 90,000 - 150,000$  cP) and relatively low laser fluence ( $35-65$  mJ/cm<sup>2</sup>), decals illuminated by the laser separate from the donor film by brittle fracture and fly to the receiver with speed less than 1 m/s, which minimizes the voxel deformation during the transfer and impact with the receiver.

LDT prints structures in a voxel-by-voxel fashion, and the researchers extended this pixelated transfer to complicated structures by placing an aperture with predefined structures on the laser path. But this aperture method has limitations because it requires the frequent change of apertures if one wants to print multiple structures. In order to accomplish dynamic and fast printing of voxel with any geometry, the same team incorporated a real-time reconfigurable digital micromirror device (DMD) into LDT to dynamically modulate the laser<sup>[45-48]</sup>. This novel method can alter the voxel shape from one to the other with a fast speed.

Based on the LDT technique, many applications have been fulfilled such as Ag conductive lines<sup>[40,41]</sup>, freestanding microcantilevers and microbridges<sup>[49,50]</sup>, multilayer scaffold structures and pyramids<sup>[23,51]</sup>, THz metamaterials and meta-antennas<sup>[46,52-54]</sup>, cavity-sealing membranes<sup>[55]</sup>, square grids<sup>[56]</sup>, conformal 3D interconnects<sup>[57]</sup>, checkboard patterns<sup>[47,48]</sup> and coplanar waveguides (CPWs)<sup>[58]</sup>.

### **Film-free LIFT (FF-LIFT)**

The FF-LIFT configuration differs from the conventional LIFT setup, where the donor system is a reservoir containing the liquid to be printed and placed underneath the transparent receiver substrate (**Figure 1.4c**). The laser, being directed either over the receiver or under the donor reservoir, is focused at a short distance (a few hundred  $\mu\text{m}$ ) below the free surface of the liquid. The laser energy is absorbed by the liquid, and if the absorption exceeds the optical breakdown threshold of the liquid, a cavitation bubble will be formed. Its expansion propels a tiny portion of liquid towards the receiver<sup>[59-65]</sup>.

### **Dynamic-Release-Layer LIFT (DRL-LIFT)**

Direct laser-material interaction is a prerequisite for successful printing in the aforementioned complementary LIFT techniques. However, as is often the case, transferred materials are either transparent to the laser or sensitive to laser irradiation/heat. Therefore, direct exposure to the laser may compromise its functionality/performance after the transfer. To tackle this issue, several groups developed a new LIFT variation called DRL-LIFT.

In DRL-LIFT, a sacrificial layer is deposited between the transparent donor substrate and the donor material layer. When the incident laser irradiates on the sacrificial layer, the laser energy will be fully absorbed by this layer, leading to partial/complete vaporization of this layer. As a result, the donor film is kept from being exposed to the laser, and the pressure created by the vapor gives rise to the printing/transfer of the donor material (**Figure 1.4d**). DRL-LIFT is advantageous over the traditional LIFT because it can transfer more delicate materials which are heat-sensitive and prone to be damaged by the laser. Notably, the residues of the DRL can contaminate the donor film if not decomposed completely, so the compatibility of this technique with some materials should be taken into account during the transfer. Based on the nature of the laser-intermediate layer interaction, three types of DRLs (metal, triazene polymer (TP), and polyimide (PI)) have been proposed and widely used for LIFT printing.

The metallic thin-film layer was first investigated as DRL. Its working principle relies on the strong absorption of the laser radiation by the metal layer and the ensuing heat-up and melting/evaporation. This results in the formation of a high-pressure gas bubble and a front jet in the donor material layer. Consequently, a small amount of donor material will be ejected and transferred to the receiver. Different metals have been used for DRL-LIFT. For example, gold (Au) thin film was coated on a transparent carrier to print peptides<sup>[66]</sup>, biomolecules<sup>[67]</sup>, bioink<sup>[68]</sup>. Titanium (Ti) thin film was widely used for printing biomolecules<sup>[69]</sup>, DNAs<sup>[70]</sup>, UV sensitive polymeric glues<sup>[71]</sup>, adhesive fluids<sup>[14]</sup>, sodium alginate-glycerin solution<sup>[72]</sup> and liquid film<sup>[73]</sup>. Silver (Ag) was used for printing cell patterns<sup>[74]</sup>. Besides pure metals, researchers also used metal-oxide film<sup>[33]</sup> and carbon thin film<sup>[75]</sup> as the DRL. The main issue concerning metal-layer DRL is that the melted/evaporated metal will resolidify, mix with donor film and finally contaminate the transferred donor materials, which might be detrimental to delicate materials such as cells.

Aiming at solving the contamination issue, the explosive TP layer is used as an alternative. TP features its low ablation threshold, low decomposition temperature, and high-absorption coefficient at the ultraviolet (UV) spectrum. Upon laser irradiation, the TP will decompose into volatile gases and release N<sub>2</sub>, which provides forward thrust for LIFT printing. In 2001, a Japanese group<sup>[76]</sup> reported the transfer of pyrene-doped polymethyl methacrylate (PMMA) film by a triazeno polymer (TA) film. Then T. Lippert and other researchers proposed to utilize TP as the laser absorbing layer for printing mammalian cells<sup>[77]</sup>. Since then, TP has been extensively investigated as DRL for LIFT printing and various applications have been proven such as organic light-emitting diode (OLED) pixels<sup>[78]</sup>, nanocrystal quantum dot (NQD) emitters<sup>[79]</sup>, Al, gelatine and methylcellulose pixels<sup>[80]</sup>, GdGaO material<sup>[81]</sup>, polystyrene (PS) microbeads<sup>[82]</sup>, polyethyleneimine (PEI) and polyisobutylene (PIB)<sup>[83]</sup>, liposome micropatterns<sup>[84]</sup>, polymer light-emitting diode (PLED) pixels<sup>[85,86]</sup>, organic semiconductor distyryl-quaterthiophenes (DS4T)<sup>[87]</sup>, ferrocene pixels<sup>[88]</sup> and graphene<sup>[89]</sup>.

## 1.2 Laser-induced forward transfer (LIFT) technique

---

Besides metal and TP, another widely used DRL is PI. PI is a commercially available material and the PI thin film preparation is relatively simple, which only requires a spin-coating and curing process. Different from the metal/TP-based DRL-LIFT process, in PI-LIFT, a portion of the PI layer is ablated by the laser. The ablation generates trapped gas with high kinetic energy, thus creating a fast-expanding PI blister. The blister simultaneously exerts an impulse on the donor material, and finally, a small amount of donor material is expelled from the donor substrate and transferred to the receiver. This approach was first developed by C. B. Arnold *et al.* [90] to achieve contamination-free printing of living mammalian embryonic stem cells. Relying on this idea, they further printed light-emitting organic molecules [91] and active organo-metallic material [92]. Other groups printed bio-active detection chemicals [93], bio-active detection chemicals [94], soft material nanolayer [95] and graphene/CuxO nanocomposite [96]. In some cases, a metal thin film is also employed for the LIFT experiments. Different from the metal DRL mentioned above, the metal layer here is deformed by the laser and forms a bump. This bump facilitates the printing of donor materials such as silica nanoparticles and C<sub>60</sub> [97], MoS<sub>2</sub> monolayers [98], single-wall carbon nanotubes [99] and diamond nanoparticles [100].

### 1.2.3 LIFT applications

Due to its excellent characteristics and different variations, LIFT has gained widespread use in a variety of applications. In this part, three main applications are briefly reviewed.

#### LIFT for electronic materials

The diversity of the donor materials makes LIFT exceptionally suitable for printed electronics. In the "DRL-LIFT" part, printing examples of several electronic materials like OLED, PLED and organic semiconductors are mentioned. In recent 10 years, more attention has been paid to printing metal-based inks and other functional electronic materials. Ag ink, a functional material widely used in inkjet printing and screen printing, is printed by LIFT to realize electrical functionality. Ag lines, ring structures, seed layer and interdigital electrodes were printed onto receivers to fulfill different purposes [101–106]. Besides printing such functional structures, Ag pastes were used as interconnects for the chip bonding process as well [107,108]. In addition, other functional inks, including lithium-based cathode ink [109], conductive adhesive [110,111], solder paste [112] and Ag nanowire inks [113,114] were successfully printed for specific applications.

The previous paragraph summarizes the Ag-based ink and other conductive ink printing examples. In the meantime, other metals are employed for LIFT printing. In 2017, zinc (Zn) was printed onto biodegradable polymer substrates for transient electronics [115] and Cu

antennas were printed and sintered by the laser <sup>[116]</sup>. Another group printed ZrPd-based metallic glass microstructures <sup>[117]</sup>. In their subsequent work, they printed continuous lines using CuAgTi and CuBi alloys <sup>[118]</sup>. In 2018, researchers integrated pad-line-pad Cu structures into a glass substrate <sup>[119]</sup> and most recently, the concept of LIFT of liquid metal EGaln was verified <sup>[120]</sup>.

Apart from the metal-based LIFT examples, many more functional electronic materials have been printed, such as graphene <sup>[89, 121]</sup>, graphene oxide <sup>[122]</sup>, single-wall carbon nanotubes <sup>[99]</sup> and poly(3,4-ethylenedioxythiophene)–poly(styrenesulfonate) (PEDOT:PSS) polymers <sup>[123]</sup>.

### LIFT for biomaterials and cells

Biomaterials are essential for developing various fields, including pharmaceutical, bioengineering and sensing applications. To take advantage of biomaterials, the controlled deposition and immobilization of different biomaterials at targeted positions for the realization of miniaturization are of great significance. To achieve this goal, many approaches are employed, such as microcontact printing, photolithography, robotic dispensing and inkjet printing. However, inherent drawbacks like low throughput, cross-contamination, solution viscosity and nozzle clogging hinder their applications, not only in printing biomaterials but also in printing living cells, which are even more sensitive to the above-mentioned drawbacks.

Due to its nozzle-free and contactless characteristics, LIFT has been recognized as an important alternative for bioprinting and there is a term named "laser-assisted bioprinting" (LAB) to emphasize the importance of LIFT. The history of LIFT in bioprinting can date back to the beginning of the 21st century. A group in the USA used LIFT to print pico-liter scale proteins <sup>[124]</sup>. Since then, numerous biomaterials, including DNA & protein microarrays <sup>[69, 125–127]</sup>, biomolecules <sup>[128]</sup>, antibodies <sup>[129]</sup> and bioinks <sup>[68]</sup> have been successfully printed. Besides these biomaterial printing demonstrations, a research team investigated the influence of the laser. Femtosecond and nanosecond lasers were studied for transferring biomolecules and the results turned out that 78 % of biomolecules remained active (femtosecond laser) while the value dropped to 54 % with nanosecond laser <sup>[67, 130]</sup>.

Apart from biomaterials printing, printing living cells by LIFT is even more intriguing because LIFT is capable of eliminating the drawbacks of other printing techniques, which enables the viability of cells after printing. A group started cell printing by LIFT in 2001. In their research <sup>[131]</sup>, Chinese hamster ovaries (CHO) cells were successfully printed and then multiplied over 300 cells. Afterward, a series of cell types appeared in LIFT-related research, including human osteosarcoma cells <sup>[132]</sup>, B35 neuroblasts <sup>[77]</sup>, human adipose-derived stem cells <sup>[133]</sup>, endothelial cells <sup>[134]</sup>, human osteoprogenitor cells <sup>[135]</sup>, fibroblasts <sup>[136]</sup>, Mesenchymal stem

cells <sup>[137]</sup>, B-lymphocyte cells <sup>[94]</sup>. A group moved one step further, developing an *in vivo* bioprinting system to print Nano-hydroxyapatite in the mouse calvaria defect model and proved the possibility of *in vivo* bioprinting <sup>[138]</sup>.

#### LIFT for 3D metallic structures

As reviewed in the "**Laser decal transfer**" part, LIFT is an excellent candidate to print high viscous metallic inks for fabricating 3D structures. Besides using such metallic inks, LIFT is also capable of directly printing metal film due to its nozzle-free characteristic. Such printing starts with the investigation of the printing quality of metals. Typical metals, including aluminum (Al) <sup>[139]</sup>, copper (Au) <sup>[140]</sup> and chromium (Cr) <sup>[141]</sup>, are studied and their droplet size and morphology as a function of laser energy are analyzed.

Based on these results, researchers extend the in-plane printing of metal pixels to out-of-plane printing by stacking each voxel on top of the other. In 2015, a thesis <sup>[142]</sup> studied the printing mechanism of metals using different lasers (femtosecond and nanosecond laser) and defined several printing regimes. In the same year, a group printed multiple Al voxels <sup>[143]</sup> onto receivers to form square slab structures. In other works <sup>[144–146]</sup>, the same group extended the printing to form complex structures such as concentric cylinders and micropillars. Another group made use of the Cu film and printed a long pillar with a high-aspect-ratio (diameter of 6  $\mu\text{m}$  and vertical length of 860  $\mu\text{m}$ ) <sup>[147]</sup>. Apart from the printing of only one metal, researchers performed a sequential printing of Cu and Au <sup>[148]</sup>, and then etched the Cu underneath to obtain the freestanding cantilever structure. In addition, one research team investigated the printing of two metals to form a joint structure as a freestanding thermocouple <sup>[149]</sup>.

In short, all these reviewed examples illustrate that LIFT can be used as a promising micro AM technique to print and pattern various functional materials.

### 1.3 LIFT of functional devices

LIFT is initially developed for printing donor materials consisting of a continuous thin film. However, an intriguing feature of LIFT, distinct from other AM techniques, is that LIFT enables the printing/transfer of prefabricated microstructures/microdevices directly to receivers. In the following section, the state-of-the-art of transferring premachined individual microstructure/microdevice is presented.

### 1.3.1 State-of-the-art microcomponent transfer by LIFT

#### Review of microcomponent transfer examples

The idea of using a laser to transfer individual structures/devices can date back to 1998 [150, 151]. A group from Imperial College in the UK proposed an idea to transfer prepatterned metal structures (Cu and Ni) by an intense pulse of the UV excimer laser, using spin-coated PI as the sacrificial layer. In their metal structure preparation, a layer of 200 nm copper (Cu) was evaporated or sputtered to form the seed layer, followed by a photolithography step to pattern the Cu layer. The electroforming technique was then used to form 50-200  $\mu\text{m}$  thick nickel (Ni) on the Cu layer. The photoresist was then stripped, and the exposed seed layer was etched, producing a Cu/Ni individual pad with the lateral size of  $2 \times 2 \text{ mm}^2$ . **Figure 1.5a** depicts the configuration of the donor system and demonstrates the transfer process.

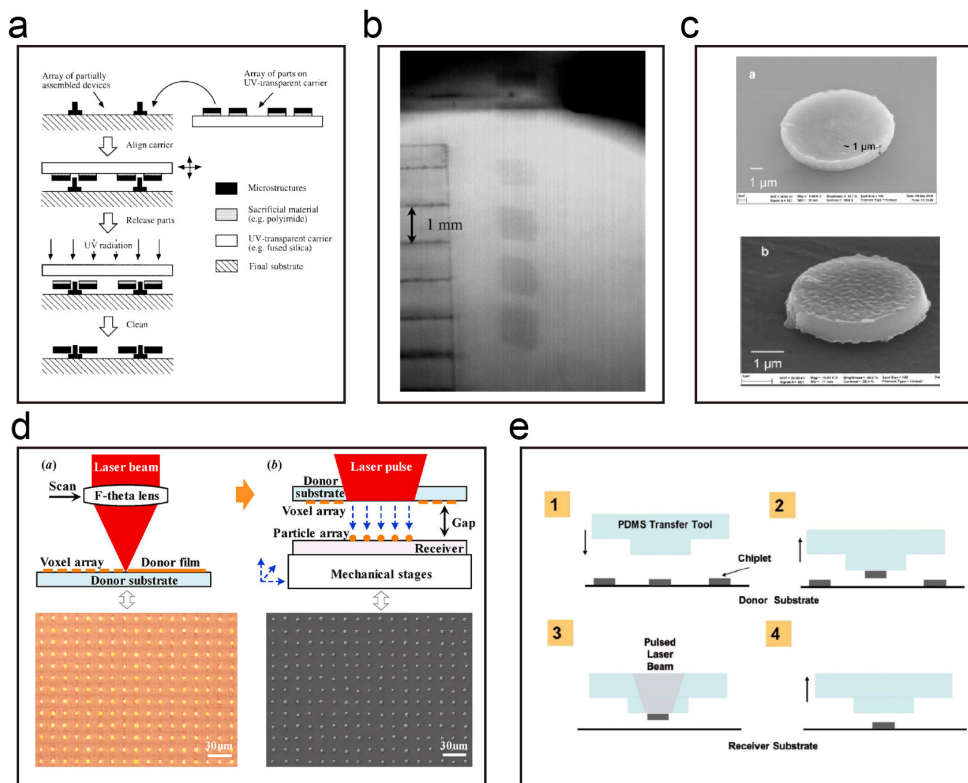


Figure 1.5: **Laser-based microstructure transfer examples.** (a). Basic laser-assisted assembly process [150]. (b). Optical micrograph of 1 mm by 1 mm “dummy” device during transfer [152]. (c). SEM micrographs of 10  $\mu\text{m}$  (a) and 5  $\mu\text{m}$  (b) ZnO pellets printed onto Si and plastic receiver, respectively [153]. (d). Schematic diagram of voxel-based laser-induced forward transfer (VB-LIFT) [154]. (e). Schematics of laser-driven micro-transfer placement using PDMS stamps [155, 156].

Following the idea of the laser-driven release of microcomponents, several groups devel-



oped the transfer process using different DRLs such as adhesive glues and die transfer tapes [152, 157, 158]. Irrelevant to the tape or adhesive glue type, such a DRL layer fulfills two purposes: the miniature electronic components are first picked up by such an adhesive layer. Then upon the laser irradiation on such dummy dies, the topside of the dummy die is heated. Consequently, a portion of the adhesive layer will de-polymerize and decompose, forming gas pressure. The gas pressure exceeds the adhesion force between the adhesive layer and the microcomponents and enables the transfer of such microcomponents (**Figure 1.5b**). Although there are quite a few studies based on this mechanism, one existing issue is the direct interaction between the dummy die chip and the laser, which causes the high temperature on the top surface of the chip. Even if they found the Si bare die release threshold is lower than its thermal damage threshold for the die ( $< 673\text{ K}$ ) [157], the interface temperature is still very high, and one needs to make sure that the microcomponents being transferred can absorb the laser energy.

Besides this idea, other teams take advantage of various approaches to transfer functional microcomponents. One group utilized femtosecond laser to transfer prepatterened piezoelectric material-ZnO pellets, which were micromachined by (focused ion beam) FIB technique [153]. They compared the printing results of ZnO pellets (5 and 10  $\mu\text{m}$  in diameter) with and without FIB preprocessing. A finding was that with the milling process, ZnO voxels with negligible debris were printed on the receiver, whereas debris and splashy deposits were found on the receiver when there is no pretreatment (intact ZnO film), as shown in **Figure 1.5c**. However, the LIFT process requires expensive and time-consuming FIB operation as the prerequisite. Instead of micromachining the donor film, another group patterned Cu interconnects by conventional lithography and Cu wet etching [159]. The first step of the transfer was laser-deforming the center of these interconnects with a laser fluence of  $1100\text{ mJ}/\text{cm}^2$ , while the two ends of the interconnect were pressed by a stencil with apertures. The second step was to remove the stencil and laser transfer the two ends to the targeted positions. As a demonstration, such Cu beams were transferred to connect two capacitors. Recently, another group in China premachined a sputtered Cu film by picosecond laser to form individual voxel arrays. Then they employed a nanosecond laser to print such an array on a large-scale (several millimeter squares by a single pulse) onto receiver [154] (**Figure 1.5d**).

Some researchers removed the dynamic-release layer and exploited micropatterned polydimethylsiloxane (PDMS) as stamps to transfer Si chiplets (laser-driven micro-transfer printing, LMTP). In their research [155, 156], the PDMS stamps are fabricated by soft-lithography. By pressing PDMS stamps on top of prefabricated Si chiplets, these test microstructures are picked up via the strong van der Waal forces between the chiplet and PDMS. Then an incident laser is shined on the interface between the stamp and chiplets, causing a temperature rise. The whole process is shown in **Figure 1.5e**. Benefiting from the huge difference in the coeffi-

cients of thermal expansion between the PDMS (310 ppm/°C) and Si (2.6 ppm/°C), the PDMS deforms and bends more, which decreases the contact area with the Si chiplet. Once the work of adhesion of the PDMS-chiplet interface is surpassed by the energy release rate resulting from the delamination at the interface, the chiplet is released and transferred to the receiver. Relying on a similar configuration, this method was extended to transfer Cu coils<sup>[160]</sup> and Ag nanoink dots<sup>[161]</sup>. Similar to the issues existing for the DRL (glue/tape) based laser transfer, high temperature at the interface is inevitable due to the transfer mechanism.

In order to alleviate temperature-related issues, two other groups found alternative stamps-shape memory polymers (SMP). The working principle of SMP stamps can be simply described as follows: When the temperature exceeds the shape memory transition temperature ( $T_g$ ), SMP stamps deform to a temporary shape with a large contact area with the microcomponents under external pressure. Lowering the temperature to room temperature, these stamps maintain their deformed shape, allowing the pickup of the microcomponents. After shining a laser at the interface of the SMP and chips, the temperature is elevated above  $T_g$  and the SMP-based stamps recover to their undeformed, reverse-pyramid shape, thus decreasing the adhesion and transferring the chips to receivers. In their work<sup>[162]</sup>, the authors successfully picked up Si and GaAs ribbons from growth substrates and transferred them onto PDMS receivers. The second group<sup>[163]</sup> further improved this approach by embedding carbon black (CB) particles into SMP. In their case, the SMP is transparent to near-infrared (NIR) laser, and the absorbing agent is the CB. Via this modification, they avoided the direct interaction between laser and Si inks and minimized the temperature issue from 300°C<sup>[155, 156]</sup> to 80°C. The complete process is illustrated in **Figure 1.6a**. However, these SMP stamps need multiple fabrication steps and the decreased temperature is still much higher than room temperature, which might not be suitable for thermal-sensitive or light-sensitive materials.

To completely address the temperature issues, more groups offered other options. Instead of using glue/tape as DRL, one team used triazene polymer (TP), which has the properties of full decomposition into volatile gas upon UV laser irradiation. A group<sup>[164]</sup> combined LIFT with a magnetic field to guide and align test chips to the targeted location (**Figure 1.6b**). On the microchips, contact pads comprise Ni (5-6 μm thick) and Au (200 nm thick), which makes such chips susceptible to the magnetic field. The results proved that the translational and rotation precision is increased with the aid of a magnetic field. However, the introduction of the magnetic field complicates the whole process. In the meantime, special contact pads (magnetic materials such as Ni by electroplating) are required to guarantee the function of the magnetic field, which might not be practicable for other functional microstructures. Last but not least, even if the UV-absorbable TP DRL can preclude the influence of high temperature, additional process steps and chemicals are required for its preparation (mixing TP with chlorobenzene and cyclohexanone). Recently, a German group used nitrocellulose

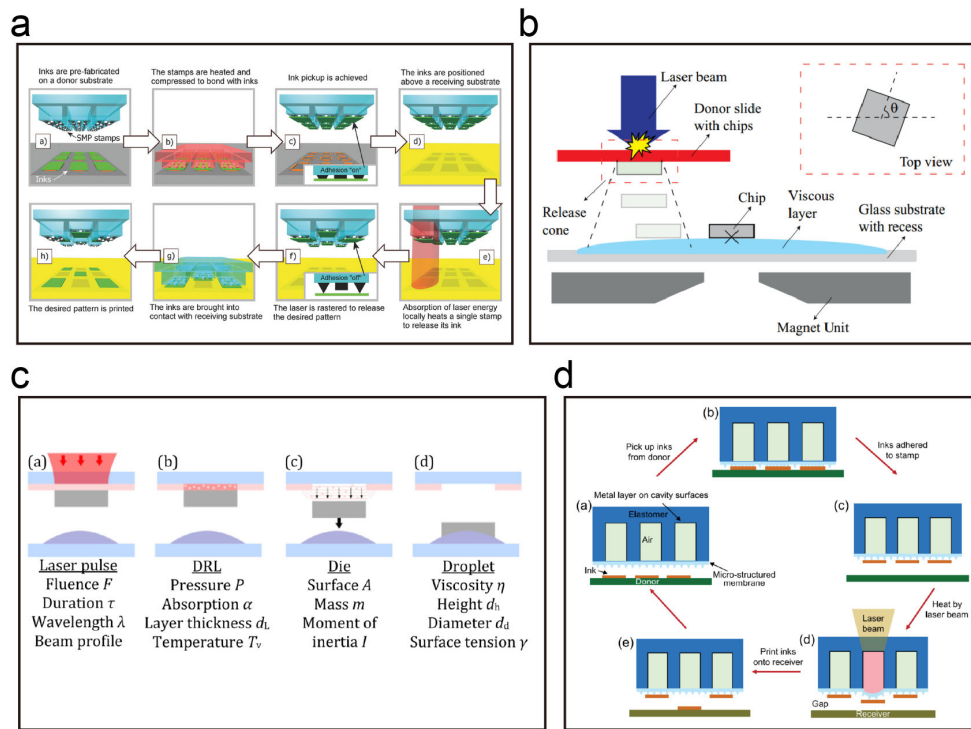


Figure 1.6: **Four transfer examples using different intermediate layers.** (a). The operation of the laser-driven carbon black SMP printing process [163]. (b). Concept of laser dies transfer and magnetic self-assembly [164]. (c). Detailed schematic of laser dies transfer process using the nitrocellulose varnish as the DRL layer [165, 166]. (d). Schematic illustration of the laser-driven programmable non-contact transfer printing process via an active elastomeric microstructured stamp [167].

varnish as the DRL to pick up bare dies and achieve successful transfer of such dies [165, 166], as shown in **Figure 1.6c**. The latest research [167] worked on the fabrication of PDMS-based air cavities as the stamp. Fe particles were coated on the inner surface of the cavity as the laser-absorbing layer, and the cavity was further encapsulated by a thin layer of PDMS with corrugated microstructures. The incident laser is absorbed by the Fe layer and elevates the temperature of the cavity. The gas pressure inside the cavity will increase and deform the encapsulated PDMS layer, hence decreasing the contact area between the PDMS layer and the microdevices and guaranteeing the release of devices (**Figure 1.6d**). Although different transfer examples are demonstrated by this method, the inherent multi-step cleanroom fabrication of the air cavity steps complicates the whole process.

Among all these complementary laser-based transfer techniques, PI-based LIFT stands out as a promising candidate and has evolved fast over the last twenty years for different functional

microcomponents transfer. PI-LIFT is characterized by its excellent features. In the first place, PI is commercially available, and its coating and curing process is mature so that no other chemicals or steps are needed for its thin film preparation. Secondly, its UV absorbable property and small absorption depth ( $<1\ \mu\text{m}$ ) protect the microstructures from laser irradiation, heat/high temperature, and PI contamination from the ablation products. Furthermore, no premachining of the PI (unlike the examples using prefabricated PDMS/SMP as stamps for the transfer) is necessary for transferring microcomponents. The first microcomponent transfer demonstration<sup>[150,151]</sup> using PI as the DRL has been described in the first paragraph of this section. Since then, this approach has successfully transferred various functional singulated devices/structures. In 2008, a Swiss team<sup>[168]</sup> reported the distribution of AFM levers from a source wafer to numerous receiver wafers by LIFT, and the AFM image quality obtained by the transferred AFM lever was comparable with those obtained from commercially available cantilevers. The AFM device transfer demonstration is shown in **Figure 1.7a**. Later, another team explored the transfer (thermo-mechanical selective laser-assisted die transfer, tmSLADT) of Si bare dies<sup>[169,170]</sup> with the aid of a two-layer DRL configuration (PI + adhesive tape). In another research<sup>[171]</sup> from their team, they broadened the application of the LIFT system by laser-machining the flexible substrate and embedding ultrathin dices into such substrates for flexible electronics (laser-enabled advanced packaging, LEAP). **Figure 1.7b** shows its transfer process and a transfer example of a fully functional RFID tag. In 2018<sup>[172]</sup>, they further displayed the potential of PI-LIFT for large-scale  $\mu\text{LED}$  array assembly (massively parallel laser-enabled transfer, MPLET) using "beamlets" originating from a single laser beam (**Figure 1.7c**).

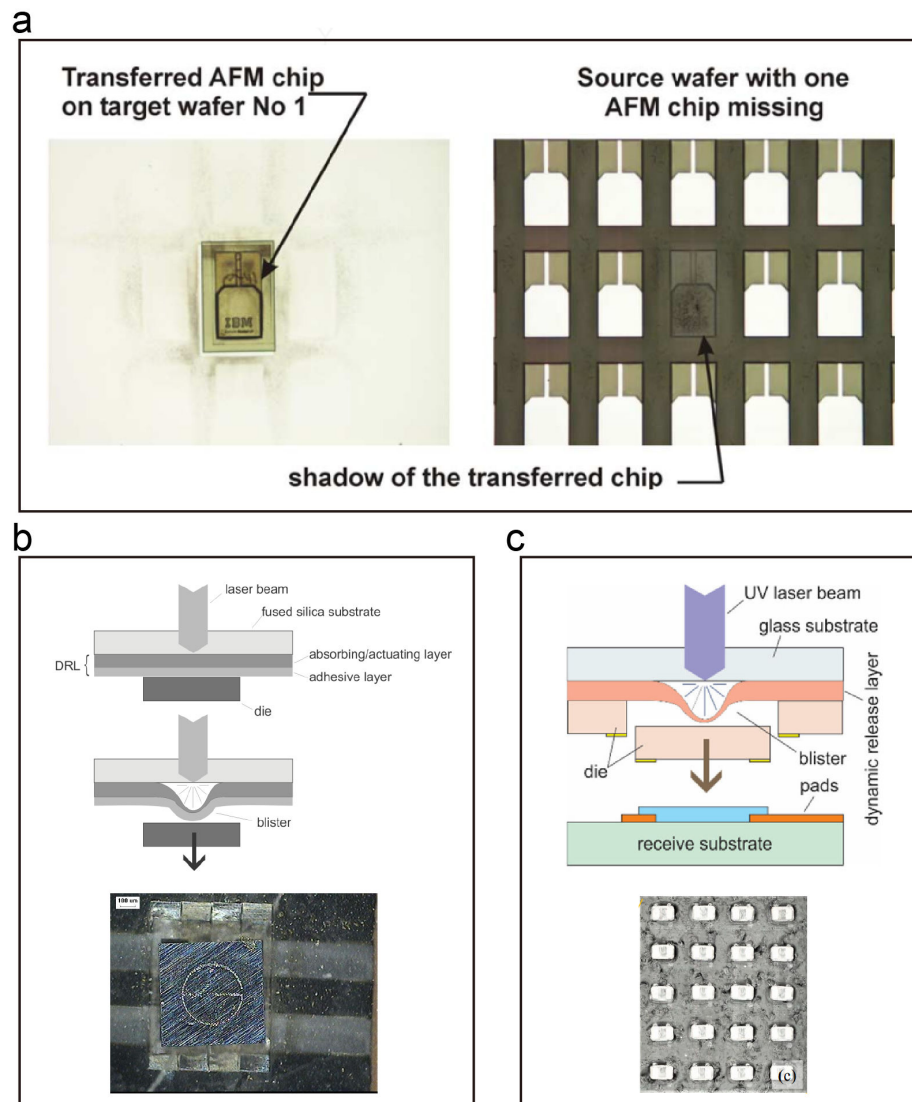


Figure 1.7: **Functional device transfer examples using PI as the intermediate layer.** (a). Optical images of the selectively transferred AFM device and the corresponding source wafer after transfer [168]. (b). A functional RFID chip is placed in a flexible polymer substrate by laser transfer [169]. (c).  $\mu$ LED transfer strategy and one transfer demonstration [172].

To sum up, this section reviews the state of the art of laser-based microstructure transfer using LIFT and its complementary techniques. **Table 1.1** presents all these works in chronological order. Although the variations in the LIFT setup (laser type, with/without DRL, donor substrate type, etc.), all the publications mentioned above show the capability of LIFT to transfer various microcomponents with the size ranging from 0.01 to 10 mm<sup>2</sup>. However, most of these works use Si tiles/chiplets as proof-of-concept demonstration, and fewer functionalities are proved after the transfer. In the meantime, only a few research emphasizes the interaction between the transferred microcomponents and the receiver substrates. Furthermore, one

Table 1.1: Summary of laser-based transfer of microcomponents

| Technique                        | Device                        | Intermediate layer     | Feature size ( $\mu\text{m}^2$ )   | Ref.       |
|----------------------------------|-------------------------------|------------------------|------------------------------------|------------|
| Laser-driven release             | Ni structures                 | PI                     | $2000 \times 2000$                 | [150, 151] |
| Laser die transfer               | Si die                        | PVC                    | $200 \times 200$                   | [157]      |
| Laser releasing and propulsion   | Si die                        | Revalpha tape          | $300 \times 300$                   | [158]      |
| Laser direct-write               | InGaN LED, bare die           | Double stick tape      | $250 \times 250$                   | [152]      |
| Laser selective transfer         | AFM lever                     | PFA foil and PI        | $220 \times 30$                    | [168]      |
| LIFT                             | ZnO pellets                   | N.A.                   | 5 & 10 $\mu\text{m}$ in diameter   | [153]      |
| tmSLADT                          | Si tiles                      | PI + Adhesive layer    | $670 \times 670$                   | [169, 170] |
| LEAP                             | Si dies                       | PI                     | $680 \times 680$                   | [171]      |
| LMTF                             | Si squares                    | N.A.                   | $100 \times 100$                   | [155, 156] |
| Magnetic-field-assisted transfer | Si dies                       | TP                     | $1000 \times 1000$                 | [164]      |
| LDT                              | Cu beam                       | Ag                     | 1000 $\mu\text{m}$ long            | [159]      |
| Laser-driven SMP printing        | Si and GaAs ribbons           | N.A.                   | $400 \times 50$                    | [162]      |
| Laser-driven CBSMP printing      | Si ink                        | N.A.                   | $500 \times 500$                   | [163]      |
| MPLT                             | $\mu\text{LEDs}$              | PI                     | $55 \times 32$                     | [172]      |
| LMTF                             | Cu foil & Ag $\mu\text{dots}$ | N.A.                   | $140 \times 140$ & $5 \mu\text{m}$ | [160, 161] |
| Laser-driven noncontact transfer | Si platelets                  | Iron particles         | $350 \times 350$                   | [167]      |
| LIFT                             | Cu $\mu\text{particles}$      | N.A.                   | 5 $\mu\text{m}$ in diameter        | [154]      |
| LIFT                             | Si square                     | Nitrocellulose varnish | $200 \times 200$                   | [165, 166] |

N.A. in the table represents no intermediate layer is used for LIFT experiments.

more question needs to be answered: is LIFT capable of transferring complex or inherently fragile microstructures? Because all the above-mentioned research focuses on simple and relatively rigid microstructures (e.g., Si square dies).

As for the intermediate layer choice, the PI layer has been proven to be an excellent candidate for microstructure transfer. Its shallow laser absorption depth of  $0.5 \mu\text{m}$  [173] guarantees that the rest of the PI film (e.g.,  $5 \mu\text{m}$  thick) can insulate the transferred microstructures from thermal and mechanical shocks [90], and its preparation process is sufficiently facile. In addition, the mechanical property of the PI film is also favorable for microstructure transfer because the thin PI film has smaller flexural rigidity ( $2.4 \times 10^{-8} \text{ N}\cdot\text{m}$  for  $5 \mu\text{m}$  thick PI) [174, 175], which makes it easy to be deformed by the vapor pressure to form a PI blister. As a result, in our experiments, we make use of PI film as the laser energy-absorbing layer to realize the transfer.

### Transfer mechanism using PI absorbing layer

Since PI film will be used as the intermediate layer to facilitate the transfer, understanding the mechanism of the PI blister formation, expansion, and ensuing microdevice separation process is crucial to optimize the LIFT process and extend it to other functional devices transfer. To date, research has been carried out to investigate the dynamics of the PI-LIFT process, especially the PI blister formation [176–179].

The operation principle of PI-LIFT relies on the laser-PI interaction. PI blister formation and the following blister expansion are initiated by laser irradiation. Upon the irradiation at the

glass/PI interface <sup>[180]</sup>, the laser energy is fully absorbed by a shadow layer of PI because of the opaque property of PI film to the laser (e.g., laser wavelength of 355 nm) <sup>[173, 181–186]</sup>. Once the laser fluence exceeds the ablation threshold of PI, a small portion of PI is ablated, thus generating confined gases between the glass substrate and the nonablated PI.

To deduct the governing equations describing the blister formation process, researchers introduced several assumptions to simplify the theoretical modeling.

1. The heating and vaporization of the PI film are fast enough, and they can be neglected.
2. The establishment of vapor pressure is sufficiently rapid without delay.
3. The vapor pressure that expands because of the laser pulse to deform the remaining PI film can be considered an adiabatic expansion process.
4. The influence of gravity can be ignored with respect to the vapor pressure forward thrust.

Based on the thermodynamic theory, the laser energy is partially converted into thermal energy of the trapped gas, which can be expressed as:

$$\Delta Q = k \int I(t) dt \quad (1.1)$$

where  $\Delta Q$ ,  $k$  and  $I(t)$  denote the increase of thermal energy, the conversion efficiency of laser energy to thermal energy in the trapped gas, and instantaneous laser power over the time step  $dt$ , respectively.

At the start of a time step, the  $\Delta Q$  is added to the trapped gas at constant volume. This gives rise to the increment of the gas temperature, given by

$$\Delta T = \frac{\Delta Q}{m c_v} \quad (1.2)$$

where  $\Delta T$ ,  $m$  and  $c_v$  represent the temperature increase, the mass of the gas, and the specific heat and constant volume, respectively, since **Equation (1.2)** adopts the constant-heat assumption of the ideal gas, the corresponding pressure change  $\Delta P$  is expressed using the general gas equation.

$$\Delta P = \frac{m}{M} \frac{R}{V} \Delta T \quad (1.3)$$

where  $M$ ,  $R$ , and  $V$  are the molar mass of the gas, the universal gas constant, and the volume of the gas, respectively. By substituting **Equation (1.2)** into **Equation (1.3)**, the gas pressure

change can be rewritten as

$$\Delta P = \frac{R\Delta Q}{MVc_v} \quad (1.4)$$

Similarly,  $\Delta Q$  can be replaced by **Equation (1.1)** and therefore,  $\Delta P$  is updated as

$$\Delta P = \frac{kR}{MVc_v} \frac{1}{V} \int I(t)dt \quad (1.5)$$

Based on **Equation (1.1)-(1.5)**, thermal energy stemming from the laser pulse is added to the vapor at the beginning of each time step, then leading to the variation of vapor temperature, vapor volume, and vapor pressure. At the end of the time step, the vapor volumes vary from the initial value  $V_t$  to  $V_{t+\Delta t}$ . Accordingly, the vapor pressure is also updated from  $P_t$  to  $P_{t+\Delta t}$ , given by

$$P_{t+\Delta t} = P_t \left( \frac{V_t}{V_{t+\Delta t}} \right)^{\frac{c_p}{c_v}} \quad (1.6)$$

where  $c_p$  is the specific heat at constant pressure. Combining **Equation (1.5)** and **(1.6)**, the final expression of the blister vapor pressure is given by

$$P_{t+\Delta t} = P_t \left( \frac{V_t}{V_{t+\Delta t}} \right)^{\frac{c_p}{c_v}} + \eta \frac{1}{V_t} \int_t^{t+\Delta t} I(t)dt. \quad (1.7)$$

Here,  $\eta = kR/Mc_v$ . For simplicity,  $\eta$  is assumed to be a static value as a function of laser fluence. After the laser pulse, the second term in **Equation (1.7)** will be zero, and the expression evolves into adiabatic expansion.

The authors utilized the finite-element analysis (FEA) method to simulate PI blister formation and employed PI film with two different thicknesses to verify their model experimentally, and the results are summarized in **Figure 1.8** <sup>[177]</sup>.

1. As the increase of the laser fluence, the PI blister size also increases for both thicknesses. For example, when the PI thickness is 7  $\mu\text{m}$ , the blister height increases from approximately 5  $\mu\text{m}$  to 26  $\mu\text{m}$  when the laser fluence increases from 1.85  $\text{J}/\text{cm}^2$  to 4.75  $\text{J}/\text{cm}^2$ . Accordingly, the conversion efficiency changes from 4.3% to 16.4%.
2. If the laser fluence is unchanged, thicker PI film results in smaller blister height because it is more resistant to plastic deformation. For example, when the laser fluence is 1.85  $\text{J}/\text{cm}^2$ , the blister height corresponding to 7  $\mu\text{m}$ -thick PI is 6  $\mu\text{m}$  while the other is 11  $\mu\text{m}$ .

Another group took one step further and analyzed the modeling in the presence of micro-devices to be transferred <sup>[174]</sup>.



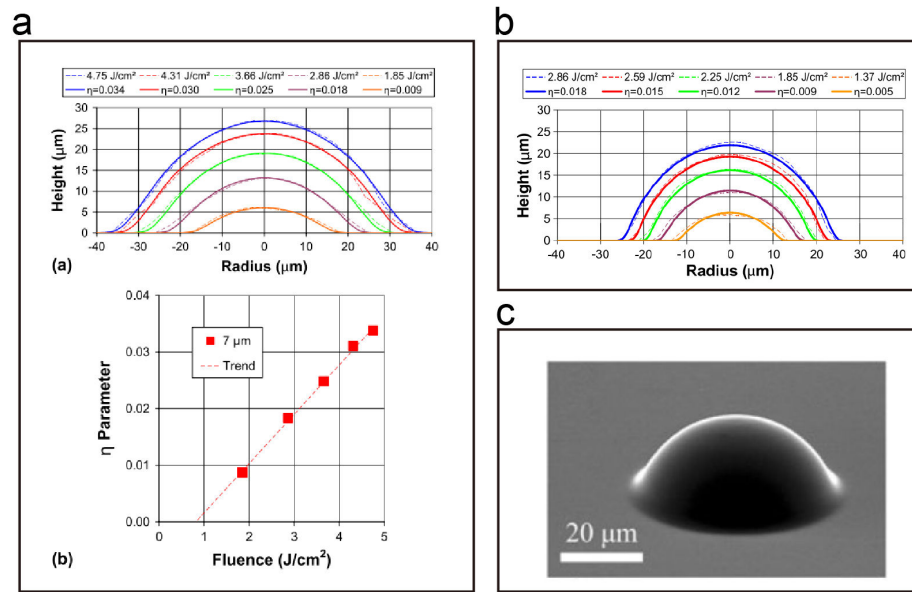


Figure 1.8: **Theoretical and experimental analysis of PI blister formation.** (a). Profile comparison between experiments conducted on a 7- $\mu\text{m}$  PI film and the corresponding simulation. (b). Profile comparison between experiments conducted on a 3- $\mu\text{m}$  PI film and the corresponding simulation. (c). Scanning electron microscopy (SEM) image of the one blister created by a laser fluence of  $2.59 \text{ J}/\text{cm}^2$  [177].

In their model, they divided the LIFT process into two dynamic coupling steps: (a) laser ejecting needle formation and (b) ultrathin chip peeling [175, 187, 188]. The results are summarized in **Figure 1.9**.

Based on their modeling, three important conclusions can be drawn:

1. Laser fluence (laser energy) has a significant influence on the LIFT process and the final transfer result. If the laser fluence is too low, LIFT may fail to peel the microdevices away from the PI layer, whereas high laser fluence can produce a more giant PI blister (laser-ejecting needle). This leads to either chip cracking (transfer with no damage) or local breakage of the chip (transfer with damage).
2. Aspect ratio (length-to-thickness) of the microdevices makes a massive contribution to the successful transfer of microdevices. If the ratio is too large (meaning a device has a larger length compared to its thickness), the device is then highly likely to be damaged because of impact fracture caused by the fast-expanding laser-ejecting needle. When the ratio decreases to a reasonable value, the impact fracture becomes less significant, and device cracking will dominate, which enables the successful transfer of microdevice with minimized damage.
3. The laser fluence, in conjunction with the length-thickness ratio, is two critical parameters determining whether the LIFT process can achieve successful transfer. By optimizing both, a

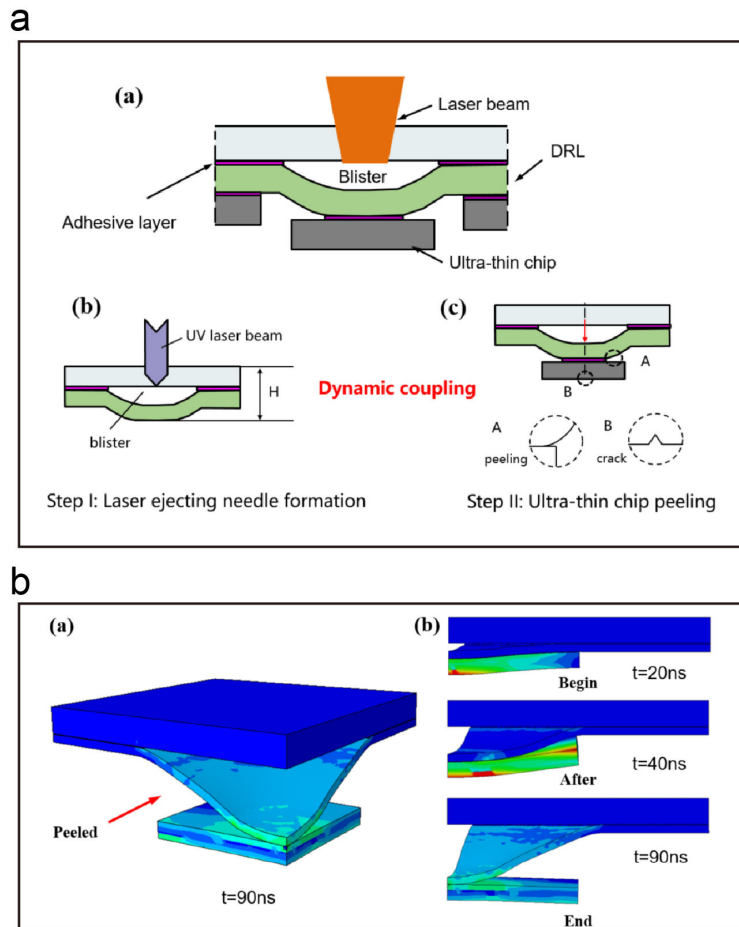


Figure 1.9: **Simulation of the transfer of microchips.** (a). Illustration of the two-step processes: laser ejecting needle formation and ultrathin chip peeling. (b). One simulation result presents the delamination process of the chip from the PI film after the laser shot [174].

transfer window can be defined, which provides us with a guide to extend to other possible functional device transfers.

## 1.4 Aims and outline of the thesis

### 1.4.1 Aims

Although the aforementioned review lists plenty of microcomponent/microdevice transfers, few transferred real functional devices. Many researchers utilize dummy samples, such as Si die, Cu foil, etc., as proof-of-concept examples. Therefore, the first objective of the thesis is to transfer microstructures that have functionality and prove their functionality after the transfer. For functional microdevices, we choose the SU-8 microdisk as the proof-of-concept example because of its mature fabrication approach [189–196] and its compatibility with other techniques

for functionalization, such as stencil lithography technique [197–200]. Before transferring SU-8-supported microdevices, the transfer of pure SU-8 microdisk is required to evaluate the influence of different parameters and obtain the optimized parametric combination, which can guide the transfer of the functional microdevices.

A series of parameters influence the transfer result of microcomponent (SU-8 in our case) by LIFT. Here, I use simple sketches to depict the transfer process and list important parameters that will be investigated in the thesis.

The SU-8 microdisk transfer starts with the laser-PI interaction. The laser ablates a part of the PI film and produces entrapped vapors. In this process, most of the laser energy ( $E_L$ ), denoted as  $E_{abl}$ , is used for laser ablation. After the laser ablation, the rest of the laser energy ( $E_r$ ) is used for the vapor expansion. Depending on whether there is a SU-8 microdisk on the PI layer, the vapor expansion can be categorized into two cases, as illustrated in **Figure 1.10**:

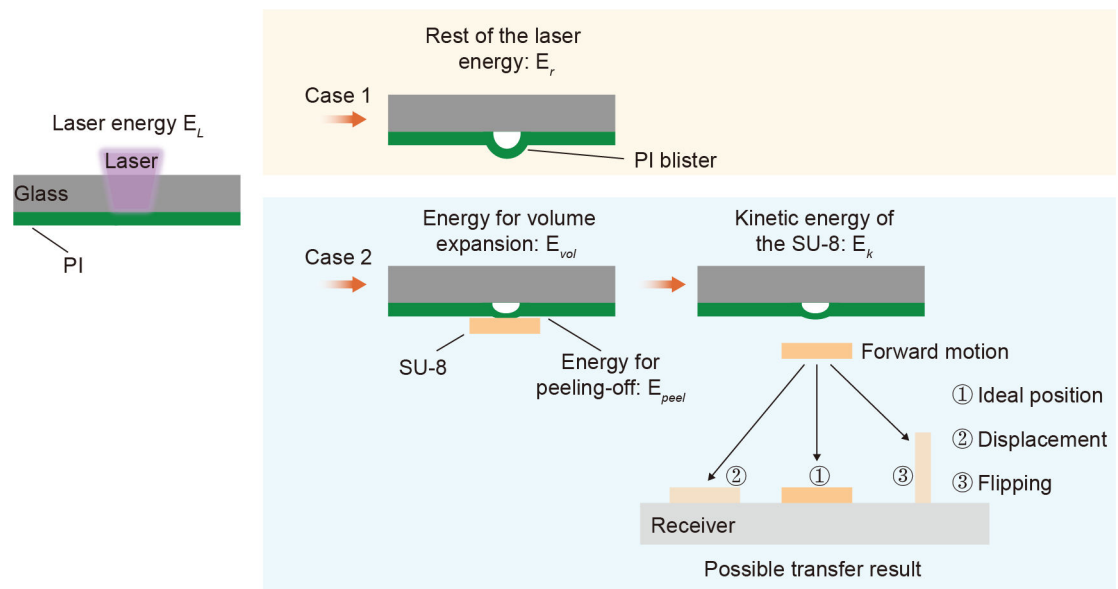


Figure 1.10: **Schematic illustrations of the LIFT process under two cases.** **Case 1:** when there is no SU-8 microdisk to transfer, the laser energy will be completely used for PI ablation and PI blister volume expansion. **Case 2:** when transferring a SU-8 microdisk, the rest of the laser energy (after laser ablation) will be used for PI blister volume expansion, SU-8 microdisk peeling-off and SU-8 microdisk forward motion after separating from the donor substrate.

1. When there is no SU-8 microdisk,  $E_r$  will be completely consumed by the PI blister volume expansion.
2. When there is a SU-8 microdisk, the fast volume expansion of the PI blister exerts the impulse to the SU-8 microdisk, assists the peel-off and completes the transfer of the SU-8 microdisk. In this case,  $E_r$  will only be partially consumed by the PI blister volume expansion

( $E_{vol}$ ). In the meantime, the SU-8 microdisk will peel away from the donor substrate with the assistance of the fast-expanding blister. In this process, a portion of the energy will be used for the peeling-off ( $E_{peel}$ ). Finally, when the SU-8 microdisk separates from the donor substrate, the kinetic energy ( $E_k$ ) sustains its forward motion to the receiver. According to the law of conservation of energy,  $E_r = E_{vol} + E_{peel} + E_k$ . LIFT-related research has proven that given a laser fluence and PI thickness (no SU-8 microdisk to transfer),  $E_r$  has a fixed value. This means the ratio between  $E_r$  and  $E_L$  is also a fixed value. For example, it is reported in one paper that when the PI thickness is 7  $\mu\text{m}$  and the laser fluence reaches 3  $\text{J}/\text{cm}^2$ , the ratio is close to 10 %<sup>[177]</sup>. This value confirms that 90 % laser energy is used for the laser ablation of PI film and 10 % is used for the PI blister volume expansion.

As shown in the example<sup>[177]</sup>, for the successful transfer of SU-8 microdisk, the laser fluence and PI thickness are the first two parameters that need to be investigated. Besides these two parameters, the thickness of the SU-8 microdisk plays an important role because it determines whether the SU-8 microdisk will be damaged during the peel-off process<sup>[175]</sup>. In addition, a successful transfer also requires a high transfer precision, which is directly related to the gap distance between the donor and receiver substrate<sup>[155, 156, 160]</sup> and possible transfer results are listed in **Case 2** depending on different gap distances. Therefore, all these four parameters will be systematically investigated. Last but not least, several parameters are worth probing to complete the picture of the transfer process, such as calculating the PI blister vapor pressure to obtain the work done by the volume expansion, determining the adhesion between the PI and SU-8 microdisk to obtain the peel-off energy and calculating the kinetic energy of the SU-8 microdisk by measuring its velocity via time-resolved imaging.

**Table 1.2** summarizes the parameters that will be investigated in this thesis and several parameters that require further investigation.

Besides the parametric study of the SU-8 microdisk transfer and SU-8-supported microdevices transfer/characterization, investigating the transfer of microstructures with complex geometries is of great interest because the reviewed examples have elementary geometries, such as square shapes. The fragility of the microstructures is also a consideration when transferring them. Taking the complexity and fragility of microstructures into account, the two-photon lithography (TPL) fabricated microstructures are the best option to verify the transfer result. TPL is an enabling technology to fabricate various microstructures/microdevices, and as far as I know, no mature method has been widely explored and designed to transfer TPL-fabricated microstructures/microdevices. Hence, LIFT emerges as a facile but effective approach to transfer such prefabricated structures, and the transfer can be easily extended to realize the massive transfer by using customized programming codes.

Therefore, the objectives of this thesis can be summarized below (**Figure 1.11**):

Table 1.2: Parameters that influence the successful transfer of a SU-8 microdisk by PI-LIFT

| Parameters investigated in this thesis | Parameters to be investigated        |
|--|--------------------------------------|
| Laser fluence                          | PI blister vapor pressure            |
| PI thickness                           | Adhesion of the SU-8 microdisk       |
| SU-8 microdisk thickness               | Kinetic energy of the SU-8 microdisk |
| Donor-to-receiver gap distance         |                                      |

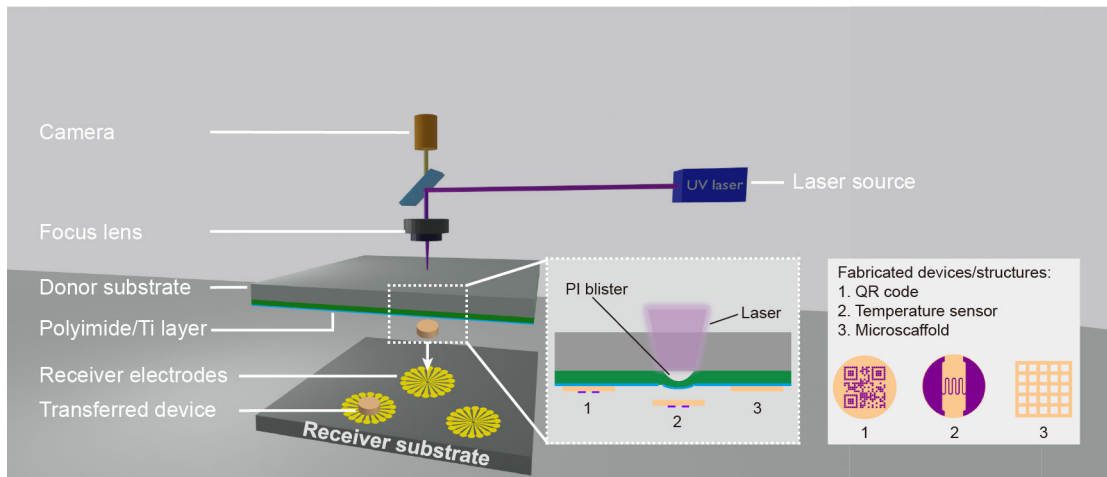


Figure 1.11: **Objective of this thesis.** As illustrated in the figure, this thesis aims to transfer prefabricated microdevices and prove their post-transfer functionality. Transfers of complex and fragile microstructures are also investigated.

1. Quantitatively investigate four variables, including laser fluence, PI thickness, SU-8 thickness and donor-to-receiver gap distance that influence the LIFT of SU-8 microdisks and optimize these variables to achieve non-destructive transfer of SU-8 microdisks with high transfer precision.
2. Perform LIFT demonstrations using SU-8-supported microdevices and assess the post-transfer performance.
3. Extend the transfer to TPL-fabricated microstructures and prove the capability of LIFT to guarantee the transfer of microstructures with complex geometry and fragility.

### 1.4.2 Outline

The thesis is organized as follows:

1. **Chapter 1** introduces the LIFT and its unique advantages as an AM technique. Several LIFT variations, including MAPLE-DW, LDT, FF-LIFT, and DRL-LIFT, are briefly mentioned. Then we summarize the LIFT applications in different fields, including

electronics, biomaterials & cells, and 3D metallic structures. Furthermore, as one of the unique applications enabled by LIFT, the state-of-the-art functional device transfer is reviewed in detail, especially using PI as the DRL. Followed by the review is the introduction of the transfer mechanism of microcomponents by the PI-LIFT. Finally, we present the aims and structure plan of this thesis.

2. **Chapter 2** discusses and analyzes four variables (laser fluence/laser energy, PI thickness, SU-8 microdisk thickness and donor-to-receiver gap distance) that influence the transfer result. The laser fluence experiment is conducted to determine whether the SU-8 microdisk can be transferred under certain laser fluence. Then the effect of the PI thickness is probed to determine the optimal PI thickness for SU-8 microdisk transfer. Based on a similar idea, the influence of SU-8 thickness is also investigated, and an optimal thickness is obtained to achieve damage-free transfer of SU-8 microdisks. This chapter is completed by further studying the influence of the donor-to-receiver gap distance on the SU-8 microdisk transfer precision.
3. In **Chapter 3**, various transfer examples using SU-8-supported microdevices/microstructures are demonstrated. SU-8-supported metal QR codes are transferred onto different receivers, and the QR code readability after the transfer is verified. The second demonstration is the transfer of the SU-8-supported Pt temperature sensor with the subsequent temperature coefficient characterization (TCR) <sup>[201,202]</sup>. Furthermore, the large-scale transfer of SU-8 microdisks using customized programming codes is presented. Finally, we construct 3D structures using such microdisks as building blocks and explore the transfer of SU-8 microdisks onto various non-planar surfaces.
4. **Chapter 4** presents transfers of TPL-fabricated microstructures. Several parameters, such as the pore size of the microscaffolds, the TPL microstructure size, and the supporting layer, are thoroughly discussed. After the parametric study, we present the first transfer demonstration of a T-shape microstructure into PDMS microchannels. A subsequent transfer example of ink-loaded microscaffolds is further provided. Finally, a  $7 \times 7$  microstructure array is transferred onto a PDMS-coated 4-inch wafer.
5. **Chapter 5** summarizes all the works in this thesis and presents an outlook for future plans to continue this project.

## 2 LIFT of SU-8 Microdisks

**Note:** This chapter is adapted from the following manuscript with the permission of all co-authors:

**Z. Yang,** G. Boero, R. Widmer, J. Michler and J. Brugger, "Laser-induced forward transfer of SU-8 supported metallic microdevices", *In preparation*

**My contribution:** conceptualization, design, micro-fabrication, LIFT experiments, characterization, figures, and writing.

### 2.1 Introduction

At the beginning of this chapter, the materials and methods are introduced. LIFT setup for the transfer experiments and demonstrations is detailed. Then, the fabrication processes of the SU-8 microdisks, micro-stencil wafer, SU-8 functional devices, and receivers are discussed. In the end, the methods to characterize the transferred SU-8 microdisks and the PI blisters are introduced.

This chapter is intended to thoroughly investigate LIFT parameters that influence the SU-8 microdisks transfer result. The dependency on laser fluence is first studied as one of the main variables. The SU-8 microdisk transfer results are classified into two regimes based on the magnitude of laser fluence, and the corresponding PI blister morphology is captured and analyzed. In other literature <sup>[176,177]</sup>, the blister morphology has been studied in the absence of the donor device, i.e., on the free surface of PI. In this thesis, PI blister morphology is quantified and discussed in detail in both cases (in the presence/absence of SU-8 microdisks). A significant difference in the PI morphology is observed in the results regarding the height and volume of the blister.

The second parameter being investigated is the PI thickness. PI thicknesses ranging from 1 to 11  $\mu\text{m}$  are employed to determine its influence. The findings show that even thinner PI can generate intact PI blisters without ruptures, whereas it is reported in other literature that such blister ruptures are inevitable under high laser fluence. Following the PI thickness study, the study on the SU-8 thickness is conducted. Four different SU-8 thicknesses are selected for the transfer to sort out successful SU-8 microdisk transfer. It is demonstrated in the experiments that as the diameter-to-thickness ratio of the SU-8 microdisk decreases, such a microdisk can be transferred with its structural integrity well-maintained. At the end of the chapter, the donor-to-receiver gap distance is analyzed to quantify the transfer precision on the receiver. Four gaps allow the SU-8 microdisk transfer with varied transfer results. Slight transfer error, lateral displacement, rotation and flipping of the transferred microdisks are observed.

Based on the analysis of the four variables, transfer parameters are optimized to transfer SU-8 microdisks with minor defects and high precision successfully. The proposed method paves the way towards transferring functional microstructures/microdevices, and all these results substantiate the practicability of large-scale transfer of microdevices.



## 2.2 Materials and methods

### 2.2.1 LIFT setup

LIFT of the functional SU-8 microdisks is achieved by using a pulsed laser ( $\lambda$ : 355 nm, pulse width: 1 ns). The laser beam is converged by a focusing lens to form a minimum laser spot size of approximately 20  $\mu\text{m}$ . A motorized filter is employed to attenuate the laser intensity and tune the laser energy from 1 to 10  $\mu\text{J}$ . In other words, the laser fluence varies from 0.32  $\text{J}/\text{cm}^2$  to 3.2  $\text{J}/\text{cm}^2$ . Two computer-controlled  $xy$  positioning stages serve as the platform to control the movement of the donor system and the receiver substrate with a minimum step of 1  $\mu\text{m}$ . The LIFT system is shown in **Figure 2.1**.

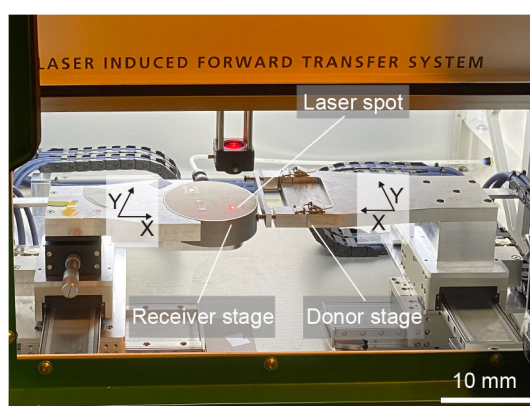


Figure 2.1: **LIFT setup**. The LIFT system consists of a laser, a receiver stage and a donor stage.

### 2.2.2 SU-8 donor preparation

SU-8 is a widely used epoxy-based negative photoresist. In this work, SU-8 is selected as the material to prove the concept of LIFT experiments for the transfer of the functional device owing to the following reasons:

1. SU-8 patterning is a mature microfabrication process to fabricate various microstructures [190–193].
2. SU-8 microstructures have excellent mechanical and optical properties. SU-8 is also compatible with other microfabrication processes, such as stencil lithography, to pattern various functional materials on the SU-8 top surface.
3. SU-8 has been extensively used for microfluidics, MEMS, bioelectronics, lab-on-a-chip applications, etc [190, 191, 194, 195]. This shows the potential of transferring such SU-8-based microdevices for different applications.

The detailed SU-8 microdisk fabrication process is shown below:

Float glass wafers are first cleaned by O<sub>2</sub> plasma (1000 W for 7 mins). Then, glass wafers are primed with a promoter VM-652/isopropanol (IPA) solution (1:200, volume ratio) to increase the adhesion between the wafer and the polyimide (PI) layer. After the priming step, PI (PI 2611, HD Microsystems) is spin-coated on the pre-treated glass wafer to form PI thin film with different thicknesses (from 1 to 11 μm). After the PI coating, the wafers are soft-baked and cured in the oven at 300 °C for 2h. A 5-nm-thick Ti is deposited on the PI film by sputtering (Alliance-Concept DP 650). SU-8 (GM 1060, Gersteltec) is then directly spin-coated on the as-fabricated PI/Ti film with thicknesses of 5, 10 and 20 μm. For a thicker SU-8 (50 μm), another SU-8 (GM 1070, Gersteltec) is used. The SU-8 is soft-baked at 130 °C for 300 s. The following step is UV exposure of the SU-8 with a predesigned mask by a mask aligner (MA6 Gen3). The UV-exposed SU-8 wafers are placed on the hotplate for post-exposure baking (PEB) at the temperature of 85 °C. After the PEB process, SU-8 wafers are developed in propylene glycol monomethyl ether acetate (PGMEA) and rinsed in IPA. The wafers with SU-8 microdisks are dried by a nitrogen gun and are ready for later fabrication processes or LIFT experiments.

### 2.2.3 Stencil fabrication

A Si wafer (thin layer of 500-nm-thick silicon nitride (Si<sub>x</sub>N<sub>y</sub>) grown on both sides of the wafer by low-pressure chemical vapor deposition (LPCVD)) is first coated with a 1-μm-thick AZ ECI 3007 photoresist (MicroChemicals GmbH) by an automatic coater (ACS200 Gen3, Süss MicroTec). Micro-apertures are defined on the photoresist by a direct laser writing system (405 nm, MLA 150, Heidelberg Instruments). For the QR code (21 × 21 pixels), the defined aperture size as one pixel on the Si<sub>x</sub>N<sub>y</sub> layer varies from 4 to 8 μm. For the temperature sensor, the defined line width of the meander structure is 1.5 μm. After the resist exposure process, the wafer is developed (AZ 726 MIF, MicroChemicals GmbH). The Si<sub>x</sub>N<sub>y</sub> is then etched by a C<sub>4</sub>F<sub>8</sub>/H<sub>2</sub>/He atmosphere (SPTS APS). The residual photoresist is stripped by O<sub>2</sub> plasma after the etching step. After defining the micro-apertures, a 5-μm-thick AZ 10XT photoresist (MicroChemicals GmbH) is coated on the backside of the wafer, followed by the backside opening exposure by the direct laser writing. After the development, the backside of the wafer is etched in the SPTS tool with the same parameter mentioned above. The Si is dry-etched from the backside using the Bosch process in SF<sub>6</sub> atmosphere (Alcatel AMS 200 SE) for 1 h. Finally, the remaining Si is etched in a KOH bath (40 %, 14 h) to release the Si<sub>x</sub>N<sub>y</sub> membrane at the front side of the wafer. The entire process flow and corresponding stencil images are provided in **Figure 2.2**.

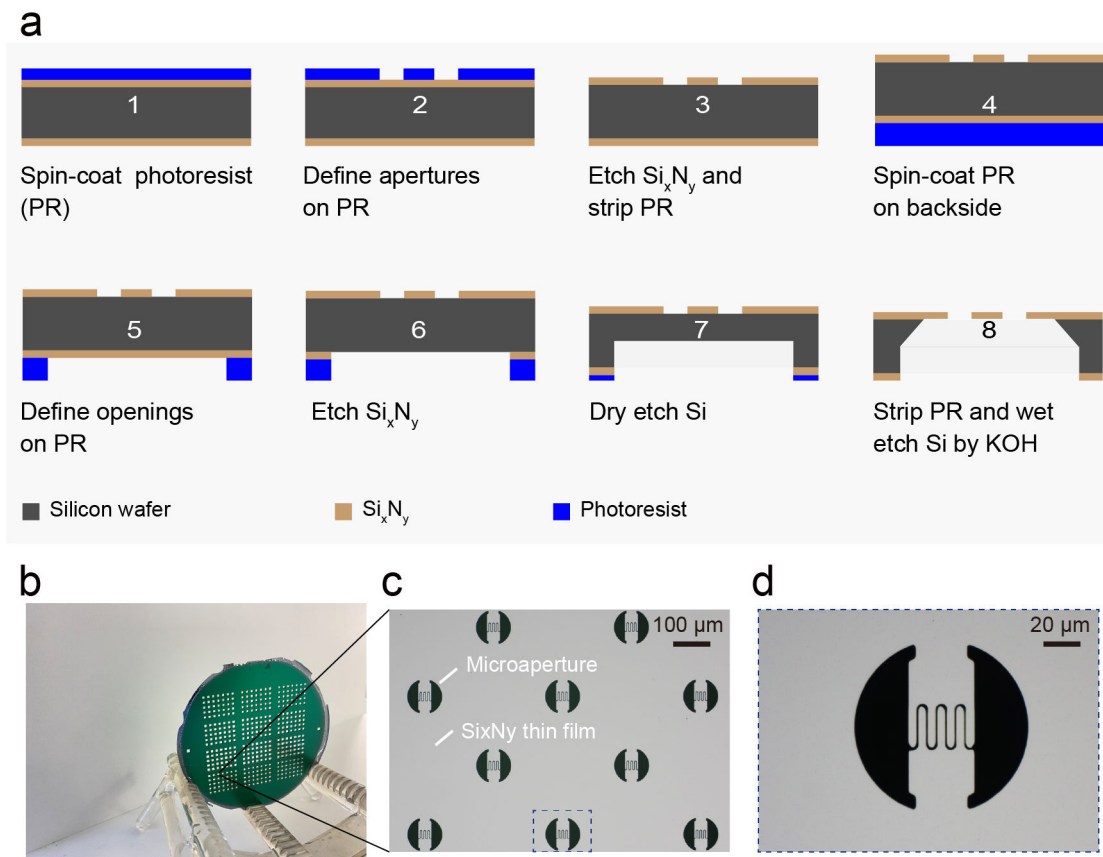


Figure 2.2: **Stencil fabrication.** (a). Process flow of the stencil fabrication. The process starts with patterning and etching the  $\text{Si}_x\text{N}_y$  thin film at the front side of the wafer to obtain desired microstructures. Then the  $\text{Si}_x\text{N}_y$  thin film on the backside of the wafer is etched to expose the Si for Si dry-etching. Subsequently, the wafer is placed in a KOH bath for complete etching of Si and releasing the  $\text{Si}_x\text{N}_y$  membrane at the front side of the wafer. (b). Photograph of one stencil wafer after all the fabrication processes. (c-d). High-magnification images showing one stencil array and one temperature sensor structure, respectively.

#### 2.2.4 SU-8 functional device fabrication

The functional SU-8 microdevices are fabricated by combining conventional UV lithography (SU-8 patterning) and stencil lithography (metal deposition). In this thesis, stencil lithography is utilized instead of the lift-off process because of the following reasons:

1. SU-8 patterned surface is non-planar, making the photoresist spin-coating challenging to achieve a layer with uniform thickness, which deteriorates the laser writing quality. Specifically, in our case, the patterned SU-8 microdisks have a thickness of  $50\ \mu\text{m}$ . This makes laser writing extremely difficult when conducting the lift-off process with the conventional spin-coating process.

2. Stencil lithography is a mature process (using  $\text{Si}_x\text{N}_y$  as the membrane layer), and it has been used as a mask for material deposition, etching, and implantation [197–199]. Previous research works have demonstrated the capability of stencil lithography to pattern metal structures on a surface with a large topographical variation [200].
3. The method can be extended to deposit other functional materials besides typical metals. The solvent-free process makes it compatible with chemical-sensitive or solvent-sensitive materials.

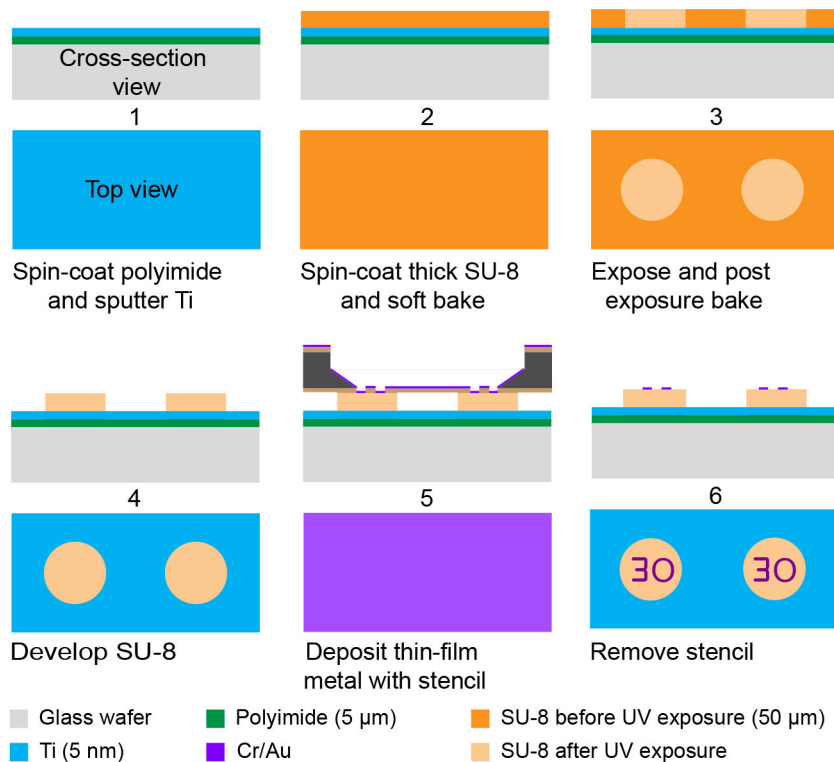


**Figure 2.3: Fabrication process of metal patterned SU-8 microdisks.** Schematic illustration of the detailed process flow, including polyimide coating and Ti sputtering, SU-8 coating and soft baking, SU-8 exposure and post-exposure baking, SU-8 development and thin-film metal deposition through apertures on a stencil wafer.

The fabrication of functional SU-8-supported microdevices begins with aligning the as-fabricated SU-8 microdisks wafer with the micro-stencil wafer by a mask aligner (Süss MicroTec MA6/BA6). The two wafers are brought to close contact (no gap) with a customized chuck to avoid possible blurring effects in the evaporation step. The front side of the stencil wafer is in contact with the SU-8 microdisks. After the alignment, the two wafers are clamped and the customized chuck is assembled into an evaporator (Leybold Optics LAB 600H), where thin layers of Cr/Au (5/50 nm) for metallic numbers are deposited on targeted SU-8 microdisks. The entire process is shown in **Figure 2.3**, and the metallic number patterned SU-8 microdisk

example is provided in **appendix Figure A.1**. Other SU-8-supported microdevices will be discussed in **Chapter 3**.

### 2.2.5 Receiver substrate preparation

PDMS receiver is prepared by mixing the base and the curing agent (Syrgard 184) with a mass ratio of 10:1. The mixture is then degassed in a vacuum desiccator and poured into a petri-dish, followed by a thermal curing process (80 °C for 2 h). After the curing, the PDMS is cut into desired size and shape as the receiver.

### 2.2.6 Scanning electron microscopy (SEM) of the transferred SU-8 microdisks

Before the SEM, SU-8 microdisks samples are first sputtered (Alliance-Concept DP 650) with a thin layer of gold (Au, 10 nm) to avoid the charging effect during the imaging process. SU-8 samples are then assembled on the holder and transferred into the SEM (Zeiss MERLIN) chamber. The acceleration voltage is set to be 3 kV. Two tilted angles are set to take SEM images: 0° and 45°.

### 2.2.7 Optical profilometer measurement of the polyimide (PI) blister morphology

Before performing the surface profile measurements of PI blisters, a thin layer of Au (30 nm) is coated on the blister samples to increase the reflection from the top surface. Then the measurements (Bruker Contour X-200) are performed using vertical shift interference (VSI) mode. After collecting the data, the leveling of the data is done by the "Plane Fit" operation in the software (Vision64).

## 2.3 Results and discussion

### 2.3.1 Influence of laser fluence

Laser fluence (laser energy) is one of the most critical parameters that affect the LIFT process. Much research has revealed that insufficient laser fluence fails to transfer/print donor materials, and excessive laser fluence may negatively influence the transferred materials/devices, such as contamination from the ruptured blister to the donor material <sup>[90]</sup>. Therefore, in the experiments, the influence of laser fluence is studied in the first place. Six magnitudes of laser fluences ranging from 0.32 to 3.2 J/cm<sup>2</sup> (laser energy from 1 to 10 μJ) are employed to transfer SU-8 microdisks with dimensions of 100 μm (diameter) × 50 μm (thickness). In order to ensure the repeatability of experiments, 10 SU-8 microdisks are tested under each laser fluence. For

each microdisk, multiple laser shots are applied if a single laser shot cannot trigger the transfer.

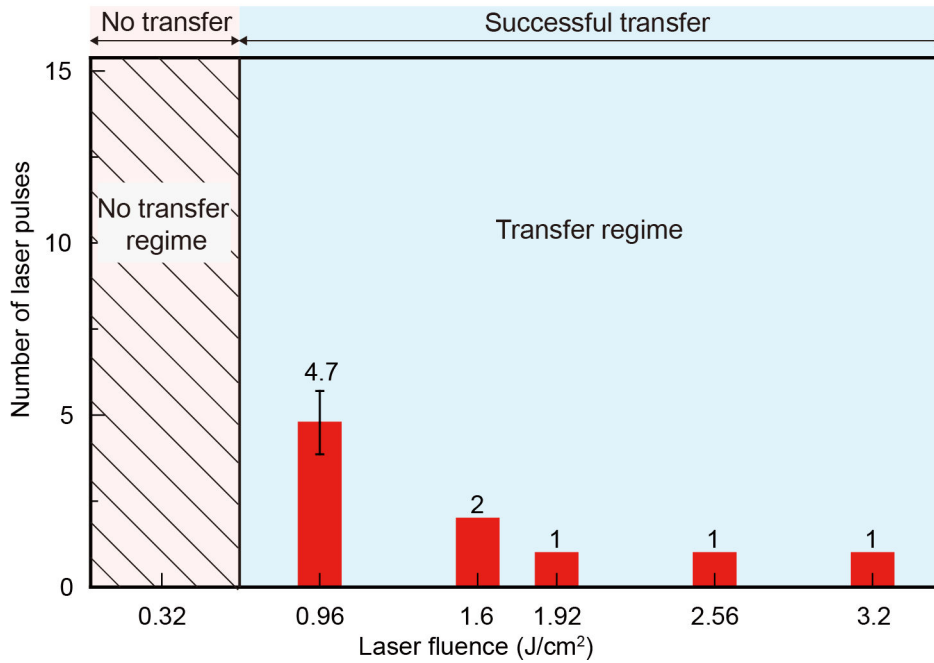
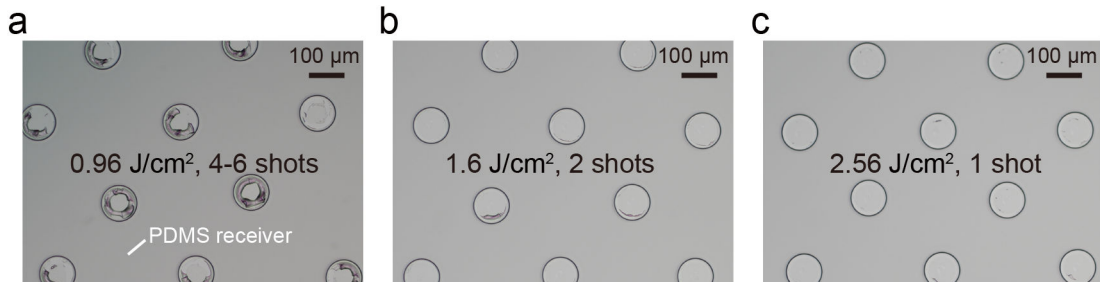


Figure 2.4: **Influence of laser fluence on the SU-8 transfer result.** Transfers of SU-8 microdisks as a function of laser fluence. The vertical value in the plot represents the averaged laser shots needed to transfer one SU-8 microdisk. For each laser fluence, 10 SU-8 microdisks are tested to ensure repeatability.

**Figure 2.4** summarizes the experimental results. The results are categorized into two regimes: no transfer and transfer regime, as indicated by the red and blue background colors. When the laser fluence is too low (e.g., 0.32 J/cm<sup>2</sup>), even multiple shots cannot trigger the transfer. The image displayed in **appendix Figure A.2** confirms this result, where the SU-8 microdisk still stays on the donor with a damaged area in the center, and there are no transferred microdisks on the corresponding PDMS receiver. This phenomenon can be explained by the fact that 0.32 J/cm<sup>2</sup> is below the transfer threshold. The results from other research also support the findings that insufficient laser fluence might fail to form a large blister, and the blister cannot have enough impulse to transfer materials/devices [178]. As the laser fluence increases, the transfer result shifts into the transfer regime. When the laser fluence is lower (i.e., 0.96 and 1.6 J/cm<sup>2</sup>), multiple laser pulses are required for a successful transfer, whereas with higher laser fluence, only one laser pulse is used to trigger the transfer. Three images in **Figure 2.5** present the transfer results under 0.96, 1.6, and 2.56 J/cm<sup>2</sup>, respectively. We observe that the microdisks have been transferred from the donor to the corresponding PDMS receiver. It should be noted that multiple laser shots may damage the SU-8 microdisk, as shown in

**Figure 2.5a** with corresponding laser fluence of  $0.96 \text{ J/cm}^2$ . In **Figure 2.5c**, no evident surface damage is observed when the laser fluence increases to  $2.56 \text{ J/cm}^2$ . The transfer results prove that although multiple laser shots with lower energy guarantee the successful transfer of SU-8 microdisks, such laser conditions are less favorable to realizing damage-free transfer.



**Figure 2.5: Representative images presenting transferred SU-8 microdisks under three laser fluences. (a-c).** Transfer result of ten SU-8 microdisks under each laser fluence with different laser shots. In **a**, obvious defects on the microdisks are observed due to the multiple laser shots.

In **appendix Figure A.2**, it can be seen that the SU-8 center part is damaged by the laser pulse. Such damage is caused by the formation and evolution of the PI blister. To further investigate the influence of PI blister, the blister morphology is characterized by SEM. **Figure 2.6a** shows the tilted SEM image of 10 PI blisters created by  $0.96 \text{ J/cm}^2$  (4 to 6 laser shots). Clearly shown in the image is that the thickness of such blisters is much smaller than the thickness of the SU-8 structure patterned on the donor substrate ( $50\text{-}\mu\text{m}$ -thick). A close-up micrograph (**Figure 2.6b**) shows one magnified PI blister (indicated by the dashed rectangle in **Figure 2.6a**) and demonstrates that the PI blister forms in the center, where the outer trace indicates the existence of the SU-8 microdisk before transfer. The central part of the blister is more identifiable because of the nature of the Gaussian laser beam. Besides the PI blister, SU-8 residues are found on the donor substrates, which further confirms the finding in **Figure 2.5a**. In order to yield essential information about the PI blister profile, optical profilometer characterization is employed to generate the blister contour graph, as displayed in **Figure 2.6c**. From the legend, it can be observed that the maximum height of the blister is  $1.8 \mu\text{m}$ , whereas the SU-8 residue has a larger value. In **Figure 2.6d**, we plot the blister's cross-sectional profile by extracting the data orthogonally (both in X and Y direction), as indicated by the arrows in **Figure 2.6c** (this applies to all the blister profiles shown later). The solid and dashed lines denote the blister profiles in the X and Y direction. As shown in the plot, the blister profile is located in the center, while in the outer region, two peaks are found. These two peaks are attributable to the SU-8 residues, which can also be confirmed by the green and red areas shown in the contour map.

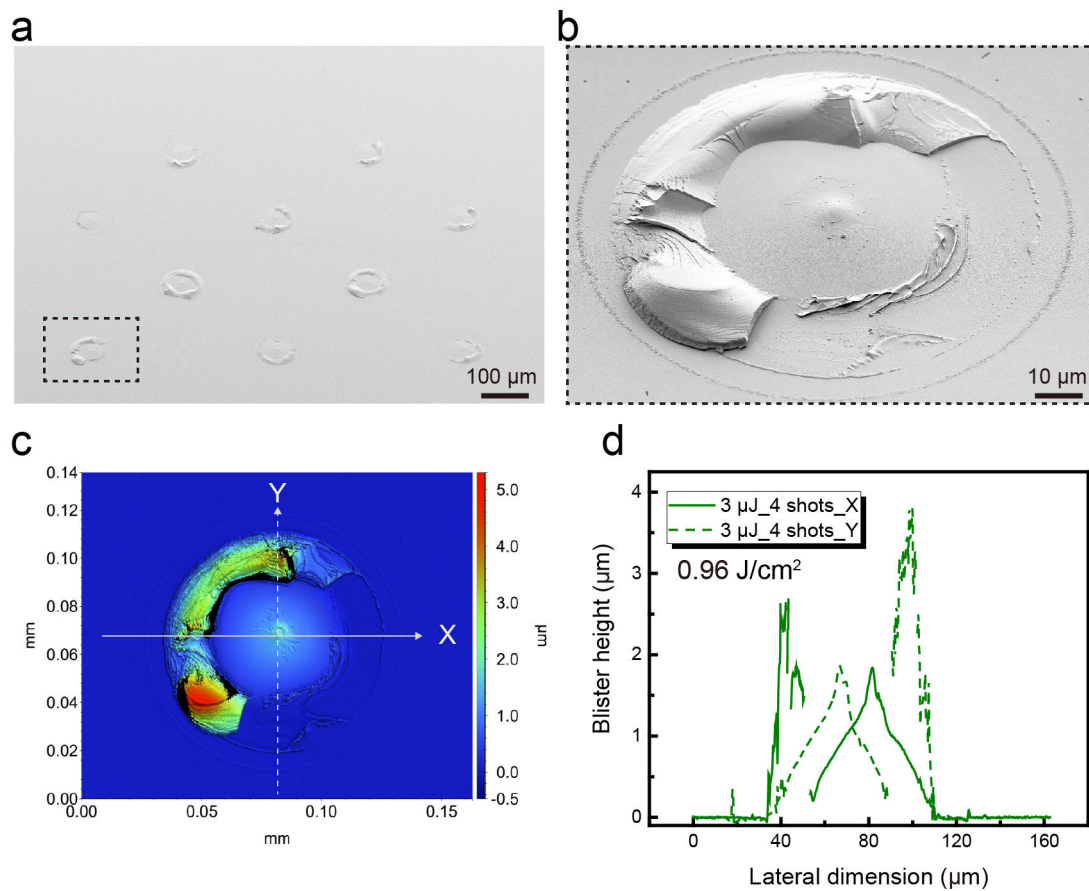


Figure 2.6: **PI blister created by  $0.96 \text{ J/cm}^2$  laser fluence.** (a). SEM image of ten blisters after the transfer process. (b). Magnified SEM image of one blister in (a). (c). Contour map of the PI blister. The X and Y arrows indicate the scanning directions when extracting data to plot the blister’s cross-sectional profiles. (d). The cross-sectional profile of the PI blister.

Apart from the analysis presented in **Figure 2.6**, **appendix Figure A.3** to **A.6** display representative blister characterization results corresponding to laser fluence of 1.6, 1.92, 2.56 and  $3.2 \text{ J/cm}^2$ , respectively. The magnified PI blisters under different laser fluence conditions are then shown in **Figure 2.7** for direct comparison. As laser fluence increases, the blister height increases accordingly. Meanwhile, the amount of SU-8 residues on the donor substrate decreases dramatically. Different from the cross-section profile shown in **Figure 2.6d**, only blister peaks are found in the cross-sectional profiles when the laser fluence exceeds  $0.96 \text{ J/cm}^2$  (from **appendix Figure A.3d** to **A.6d**).

With all the profiles obtained, we summarize them in **Figure 2.8a**. For better comparison, the blister profiles on the Y-direction are removed because a cylindrical symmetry is observed. It can be seen that as laser fluence is increased, the blister height increases monotonically.

In order to further quantify the blister height, we average the height value of 10 blisters under



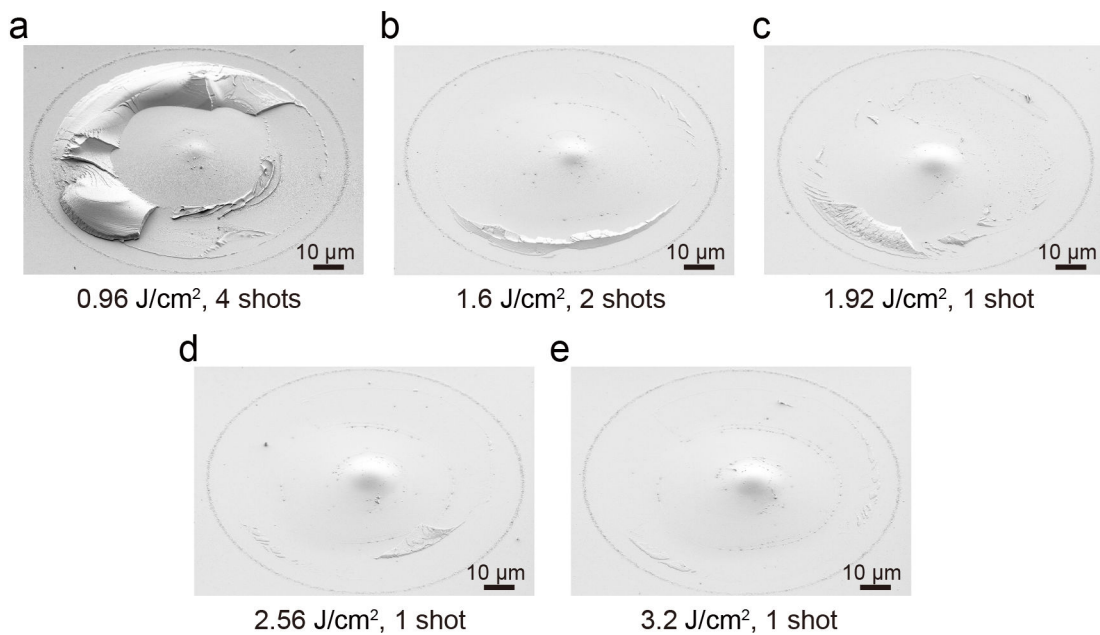


Figure 2.7: **Direct comparison of five different PI blisters under different laser fluence conditions.** (a-e). SEM images of magnified PI blisters when the laser fluence increases from 0.96 to 3.2 J/cm<sup>2</sup>. Blisters are more evident as the increase of laser fluence.

each laser fluence, as shown in each SEM image from **appendix Figure A.3a to A.6a**. The blister height with an error bar is plotted in **Figure 2.8b** in black. The blister height varies from 1.9 to 3.5 µm. To present a complete picture of the blister, their widths under each laser fluence are summarized in **Figure 2.8b** as well. Distinct from the monotonic increase in the blister height, an abrupt drop of the blister width from 67 µm (1.6 J/cm<sup>2</sup>, 2 shots) to 55 µm (1.92 J/cm<sup>2</sup>, 1 shot) is found. This can be explained by the fact that the total energy delivered to the PI layer to trigger SU-8 microdisk transfer is 3.2 J/cm<sup>2</sup> when using a 1.6 J/cm<sup>2</sup> laser pulse. Although the blister height is slightly smaller, more laser fluence is absorbed to facilitate the ablation of the PI film and consequently enhance the delamination of the PI film from the glass substrate. Therefore, the blister width expands to have a larger value. To compare the blister width under 0.96, 1.6, and 1.92 J/cm<sup>2</sup>, we sort out their blister profiles (in the X-direction), as shown in **Figure 2.8c**. Despite that the profile in blue color (1.92 J/cm<sup>2</sup>) has the highest peak, its waist and bottom parts are comparatively narrower than those in purple (1.6 J/cm<sup>2</sup>) and green color (0.96 J/cm<sup>2</sup>). The zoom-in plot shows the difference in the blister profiles. This difference is also confirmed by comparing the SEM images shown in **Figure 2.7a-c**. The top parts of the PI blister in **Figure 2.8a-b** are smaller than that in **Figure 2.8c** because their waist parts are broader and flatter. Even if the area for two blisters (0.96 and 1.92 J/cm<sup>2</sup>) looks similar, the blister volume may differ greatly considering the position of such differences. The blister's upper part produces less volume than the lower part.

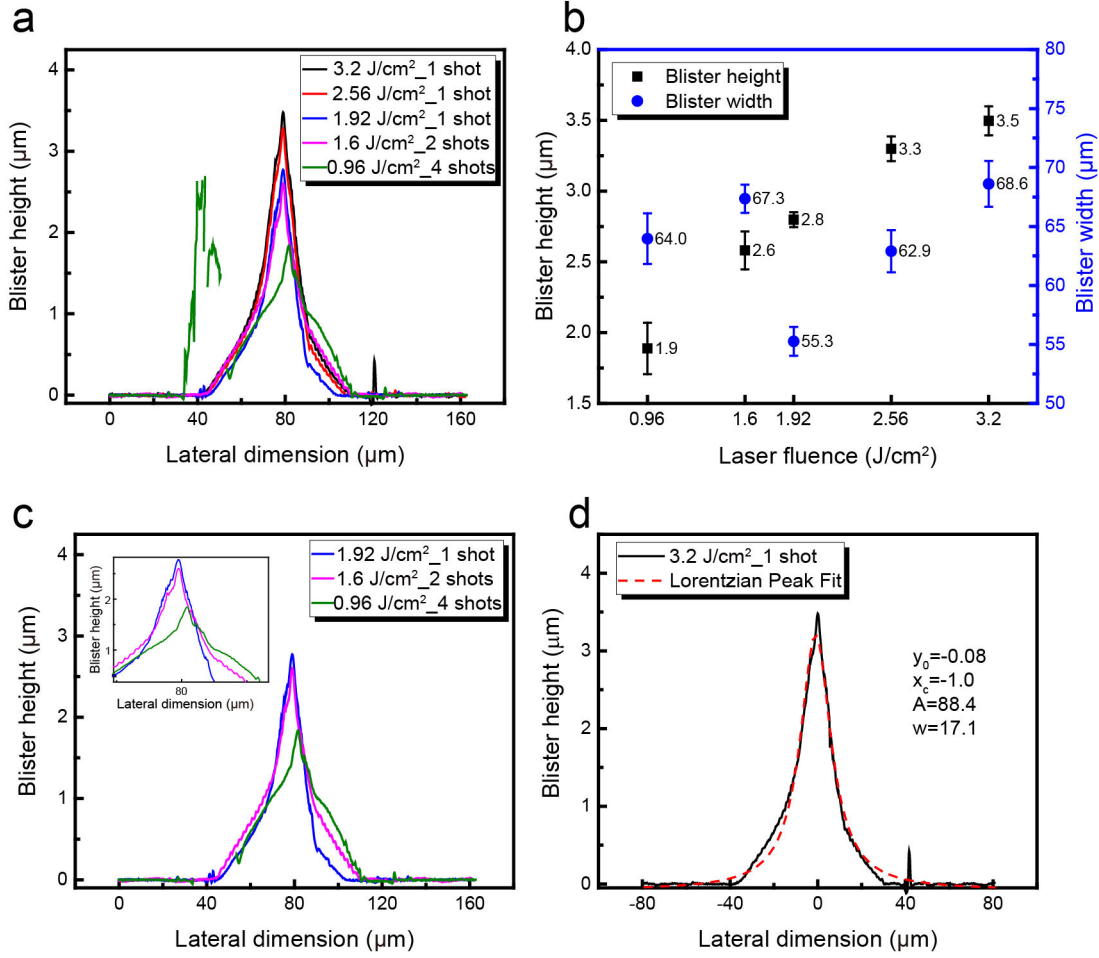


Figure 2.8: **PI blister profile summary.** (a). Summary of all the five types of PI blister created by different laser fluences. (a) only presents the results in the X-direction, considering the symmetric nature of the blister. (b). Blister height and blister width summary. (c). Blister profile comparison among three different laser fluences: 0.96, 1.6, and 1.92 J/cm<sup>2</sup>. (d). Lorentzian fitting of one blister profile (3.2 J/cm<sup>2</sup>).

As introduced in **Chapter 1**, the volume expansion of the entrapped hot gases leads to the formation of the blister. For the purpose of comparing the final blister volume among a series of blisters, we fit the blister profiles using the single-peak fit to simplify the calculation process. Displayed in **Figure 2.8d** is one fitting example with the laser fluence of 3.2 J/cm<sup>2</sup>. The corresponding formula of the fitting is represented as:

$$y = y_0 + \left(\frac{2 \times A}{\pi}\right) \times \frac{w}{4 \times (x - x_c)^2 + w^2} \quad (2.1)$$

where  $y$ ,  $y_0$ ,  $A$ ,  $w$ ,  $x$ , and  $x_c$  denote the  $y$  coordinate, offset, area, full width at half maximum (FWHM) of the blister profile,  $x$  coordinate of the blister, and the central position of the blister peak, respectively. The red dashed curve represents the Lorentzian fitting, and the  $R^2$  value of

this fitting is as high as 98.6 %. After the fitting, the blister volume is obtained by integrating the blister profile using the following equation (detailed calculation steps and codes are provided in **appendix Figure A.7**):

$$V = \pi \times (|\int_a^0 x \times y dx| + |\int_0^b x \times y dx|) \quad (2.2)$$

where V, a, and b represent the blister volume and the left and right border of the blister, respectively. For instance, the corresponding value of  $y_0$ , A, w, and  $x_c$  for 10  $\mu\text{J}$  laser created blister is -0.08, 88.4, 17.1, and -1.0, respectively. Then the final volume of this blister is calculated to be 1870  $\mu\text{m}^3$ .

To examine the accuracy of the calculation, volume statistics provided by the software (Vision6.4, Bruker) are used as a reference. Here, the blister volume from the software is 1979  $\mu\text{m}^3$ . This discrepancy between the two volumes partially results from the fitting. SU-8 residue left on the donor substrate is another factor that causes such a difference. As displayed in the SEM image (**Figure A.6b**), as well as the contour map, a tiny portion of SU-8 (bottom-left in the image) contributes to the final volume. This phenomenon is more prominent when the laser fluence decreases and multiple laser pulses are needed for transfer, e.g., **Figure 2.6c**. Therefore, the volume calculation from the blister fitting is of great significance to quantifying the blister and removing the influence of the SU-8 residues. In this case, the fitting curve is in good agreement with the blister profile, and the calculated volume from the fitting reasonably reflects the actual blister volume.

Similar to the PI blister height trend in **Figure 2.8b**, the calculated blister value drops from 1610  $\mu\text{m}^3$  (2.56  $\text{J}/\text{cm}^2$ ) to 1180  $\mu\text{m}^3$  (1.92  $\text{J}/\text{cm}^2$ ). An interesting finding is that in the case of less laser fluence (0.96 and 1.6  $\text{J}/\text{cm}^2$ ), the calculated values (1635  $\mu\text{m}^3$  for 1.6  $\text{J}/\text{cm}^2$  and 1606  $\mu\text{m}^3$  for 0.96  $\text{J}/\text{cm}^2$ ) are larger than the one created by 2.56  $\text{J}/\text{cm}^2$  laser pulse and are comparable with the blister created by 2.56 and 3.2  $\text{J}/\text{cm}^2$ . Such a finding substantiates the previous claim that multiple laser pulses with lower energy can expand the blister's bottom part, thus causing an increase in the blister volume. In both cases (1.6  $\text{J}/\text{cm}^2$  & 2 shots; 0.96  $\text{J}/\text{cm}^2$  & 4 shots), the total laser fluence is higher than 1.92  $\text{J}/\text{cm}^2$ .

**Table 2.1** summarizes all the transfer results of SU-8 microdisks and the corresponding blister heights & volumes. From all the data shown in **Figure 2.8** and **Table 2.1**, we find that the maximum blister height is close to 3.5  $\mu\text{m}$ , which is much smaller compared with the results in other literature <sup>[176,177]</sup>. For example, in one research <sup>[177]</sup>, a laser with a beam diameter of 21  $\mu\text{m}$  was used for experiments, and the measured blister height varies from 10 to 20  $\mu\text{m}$  and the blister width from 50 to 80  $\mu\text{m}$ . In our case, the laser beam size is similar, around 20  $\mu\text{m}$ . Although the final width of the blisters is comparable with the counterparts in that research, the value of the final height is much lower. The significant reduction of blister height

Table 2.1: Summary of the transfer result of SU-8 microdisks and the corresponding blisters created on 5  $\mu\text{m}$  thick PI

| Laser parameter                     | Transfer result | Blister result | Blister height    | Blister volume       |
|-------------------------------------|-----------------|----------------|-------------------|----------------------|
| 0.32 J/cm <sup>2</sup> & > 30 shots | No transfer     | No blister     | N.A.              | N.A                  |
| 0.96 J/cm <sup>2</sup> & 4-6 shots  | Transfer        | Intact blister | 1.9 $\mu\text{m}$ | 1635 $\mu\text{m}^3$ |
| 1.6 J/cm <sup>2</sup> & 2 shots     | Transfer        | Intact blister | 2.6 $\mu\text{m}$ | 1606 $\mu\text{m}^3$ |
| 1.92 J/cm <sup>2</sup> & 1 shot     | Transfer        | Intact blister | 2.8 $\mu\text{m}$ | 1180 $\mu\text{m}^3$ |
| 2.56 J/cm <sup>2</sup> & 1 shot     | Transfer        | Intact blister | 3.3 $\mu\text{m}$ | 1610 $\mu\text{m}^3$ |
| 3.2 J/cm <sup>2</sup> & 1 shot      | Transfer        | Intact blister | 3.5 $\mu\text{m}$ | 1870 $\mu\text{m}^3$ |

N.A. in the table means that PI blister height and volume cannot be calculated.

can be tentatively ascribed to the existence of the SU-8 microdisk. After the laser ablation of PI film, much of the rest energy (for PI blister volume expansion) is consumed by the SU-8 peeling process, as well as converted into the kinetic energy of the SU-8 microdisk to sustain its forward motion after the separation from the donor substrate.

To assess the difference between blister profiles in the presence/absence of the SU-8 microdisk, we shine laser pulses on the free surface of the PI/Ti film and measure the blister profiles. Here the influence of the Ti film can be reasonably ignored because the thickness of the PI layer is three orders of magnitude larger than the Ti thickness (5 nm). The laser parameter employed here is the same as the experiments shown in **Figure 2.4**.

The corresponding results are presented in **Figure 2.9** and **appendix Figure A.8** to **A.11**. The first finding is that the blister corresponding to 0.96 J/cm<sup>2</sup> laser fluence is more evidently shown in SEM images (**Figure 2.9a-b**). The blister height is then quantified in **Figure 2.9c-d** as 10  $\mu\text{m}$ , which is a five-fold increase compared with the counterpart (1.8  $\mu\text{m}$ ) formed in the presence of the SU-8 microdisk. When the laser fluence is beyond 0.96 J/cm<sup>2</sup>, PI blister rupture happens. The SEM image (**appendix Figure A.8a-b**) demonstrates that the blister top breaks after the laser shot. The rupture formation has been discussed by one group as a result of the excessive laser fluence <sup>[177]</sup>. Owing to the presence of the rupture, the discontinuity of the blister profiles at the peak region is measured in the contour maps (**appendix Figure A.8c-A.11c**).

Nevertheless, we can observe that the maximum height of the PI blister is close to 14  $\mu\text{m}$  when the laser fluence is 3.2 J/cm<sup>2</sup>, which is four times higher than the case with the SU-8 microdisk (**appendix Figure A.6**). The measured blister height is also comparable with those in literature <sup>[176,177]</sup>. Similar to the **Figure 2.7**, all the SEM images corresponding to these five types of blisters are summarized in **Figure 2.10**. It can be observed that in the absence of the SU-8 microdisks, the blister size is much larger than those displayed in **Figure 2.7**.

After the direct comparison, all five types of blister profiles (created on the free surface of PI)

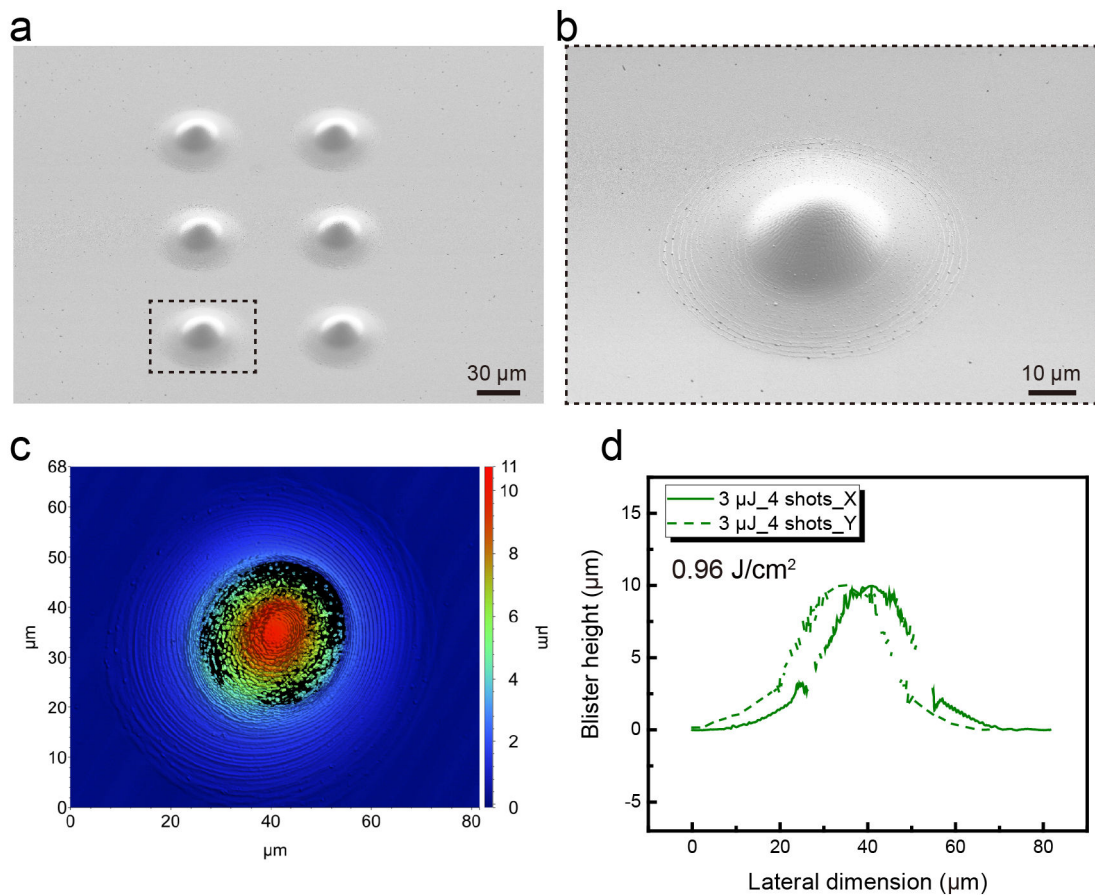


Figure 2.9: **Blisters created by  $0.96 \text{ J/cm}^2$  laser fluence (4 shots) on the free surface of PI.** (a). SEM image presenting the six blisters. (b). Magnified SEM image of one blister. (c). Contour map of the PI blister. (d). Cross-section profile of the PI blister.

are plotted into one figure, as shown in **Figure 2.11a**. A finding in the plot is that in the center of the blister, a height value of approximately  $-5 \mu\text{m}$  appears in the curve (when blister rupture happens). This corresponds to detecting the substrate surface underneath the  $5\text{-}\mu\text{m}$ -thick PI film. Similar phenomena are also found in the SEM images when reducing laser fluence to  $2.56$ ,  $1.92$ , and  $1.6 \text{ J/cm}^2$ , but the rupture size decreases. One research has investigated the formation of ruptured PI blisters due to high laser fluence <sup>[177]</sup>. Under high laser fluence, the entrapped high-pressure gas causes high plastic deformation at the top of the blister. The significant plastic deformation creates overstrained region and leads to crack formation and propagation on the top, thus producing volcano-like fracture geometry. This further substantiates the assumption that in the presence of the SU-8 microdisk, no ruptured blister is observed because much of the remaining energy (after laser ablation of PI film) is consumed to assist the separation of the SU-8 microdisk from the donor substrate. However, when the SU-8 microdisk is absent, the entire remaining energy is consumed by the blister volume

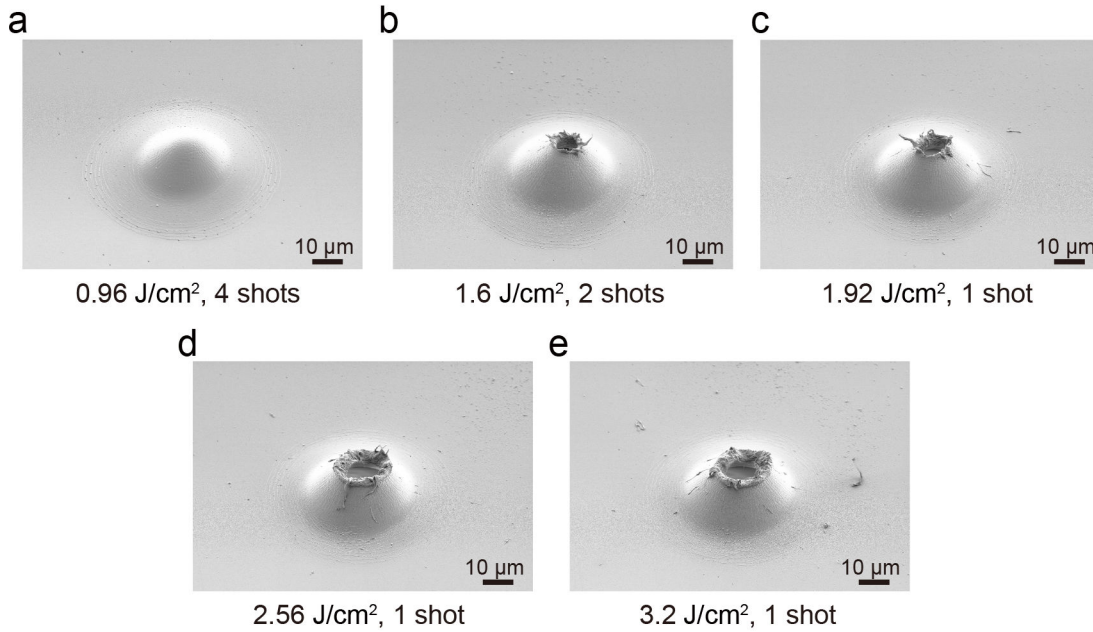


Figure 2.10: **Direct comparison of five different PI blisters under different laser fluence conditions on the free surface of PI. (a-e).** SEM image of magnified PI blisters when the laser fluence increases from 0.96 to 3.2 J/cm<sup>2</sup>. Blister rupture happens when the laser fluence exceeds 1.92 J/cm<sup>2</sup>.

expansion and blister rupture processes.

As shown in **Figure 2.4**, for 0.32 J/cm<sup>2</sup> laser pulse, even multiple laser shots cannot transfer SU-8 microdisks. Such laser shots damage only the centric part of SU-8. To complete the laser fluence experiments on the free surface of PI with all the available laser fluences in the LIFT system, tests with 0.96 J/cm<sup>2</sup> & 1 shot, 0.32 J/cm<sup>2</sup> & 1 shot, and 0.32 J/cm<sup>2</sup> & 10 shots are performed as well. The results are shown from **appendix Figure A.12** to **A.14**. When comparing the results between **Figure 2.9** and **appendix Figure A.12**, it can be observed that their height difference is not as evident as their width difference. SEM images in **Figure 2.9** shows that the blister is widened after 4 laser shots, compared with the blister in **appendix Figure A.12** created by 1 laser pulse. Similar results are presented in **appendix Figure A.13** and **A.14**, where single and 10 laser shots are used to create PI blisters. The blister heights corresponding to 0.32 J/cm<sup>2</sup> & 1 shot and 0.32 J/cm<sup>2</sup> & 10 shots are approximately 3.2 and 2.5 µm, respectively. Because of the widening effect created by multiple laser shots, the blister created by 0.32 J/cm<sup>2</sup> & 10 shots looks like being formed on a bumped PI surface. To summarize the experiments, all the blister profiles corresponding to 0.32 and 0.96 J/cm<sup>2</sup> are merged and re-plotted in (**Figure 2.11b**) to compare the blister size directly. On the whole, these experimental results further validate the previous hypothesis that multiple laser shots lead to a blister with larger bottom and waist parts, both in the presence/absence of SU-8 microdisks. And the non-linear increase

in the blister height can be tentatively explained by several reasons.

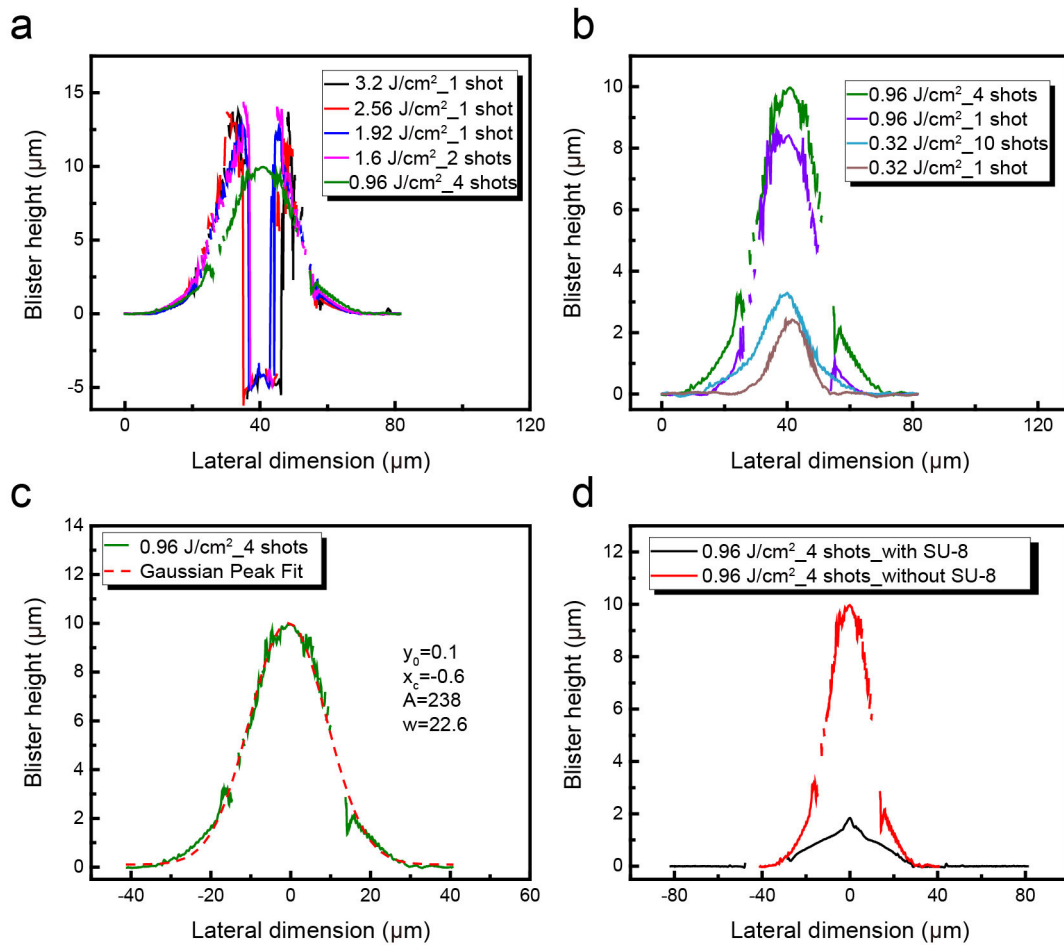


Figure 2.11: **PI blister profile summary created on PI free surface.** (a). Summary of all the five types of PI blister created by different laser fluences on PI free surface. (a) only presents the results in the X-direction, considering the symmetric nature of the blister. (b). Blister profile comparison under four different cases: 0.96 J/cm<sup>2</sup> & 4 shots, 0.96 J/cm<sup>2</sup> & 1 shot, 0.32 J/cm<sup>2</sup> & 10 shots, and 0.32 J/cm<sup>2</sup> & 1 shot. (c). Gaussian fitting of one blister profile (0.96 J/cm<sup>2</sup>, 4 shots). (d). Blister profile (0.96 J/cm<sup>2</sup>, 4 shots) comparison with/without the presence of SU-8 microdisk.

In **Figure 2.12**, the PI blister formation process is divided into multiple steps since, in total, four laser pulses with the fluence of 0.96 J/cm<sup>2</sup> are used to trigger the blister expansion. After the first laser shot, a blister with a height of approximately 8 μm is formed, as displayed in **Figure 2.11a**. This means that the PI blister will delaminate from the glass substrate surface. When the second laser pulse arrives at the substrate surface (after 1 s), the laser-PI interaction is unlike the first laser pulse and only a portion of the PI film that still adheres to the glass substrate will be ablated. In the meantime, after the first laser ablation, laser-induced carbonization

happens, and such carbonaceous materials (on the PI blister, shown in the inset of **Figure 2.12**) have a higher ablation threshold than PI [185, 186]. This will suppress the further ablation of the PI blister (not like the first laser pulse). All these phenomena give rise to less volume expansion of the PI blister starting from the second laser pulse. Therefore, a non-linear increase in the blister height after the first and the fourth laser shot can be observed.

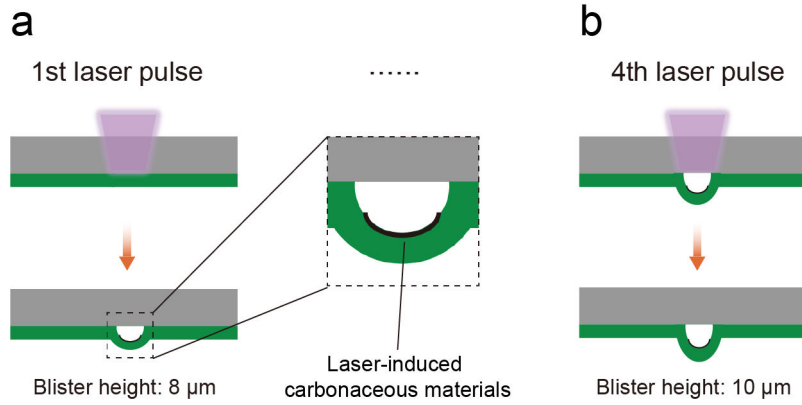


Figure 2.12: **Simple sketches showing the increase of blister height under different laser pulses. (a-b).** The two sketches correspond to the blister formation when the laser condition is  $0.96 \text{ J/cm}^2$  and 1&4 shots (each laser shot is triggered after 1 s of the previous laser shot) without the SU-8 microdisk. The black area in the inset represents the carbonaceous materials formed on the PI blister after the laser ablation.

**Table 2.2** summarizes the blister results created on the free surface of PI by different laser fluences. It can be concluded that when the laser fluence drops to  $0.96$  and  $0.32 \text{ J/cm}^2$ , fully intact PI blisters are formed without a rupture at the peak. However, the discontinuity in the curve corresponding to  $0.96 \text{ J/cm}^2$  (**Figure 2.11b**) is found, and we re-plot the blister profile ( $0.96 \text{ J/cm}^2$  & 4 shots) in **Figure 2.11c**. Different from the curves corresponding to higher laser fluence, in this case, discontinuity happens not at the top but at the waist part of the blister. The SEM image in **Figure 2.9a-b** proves that no rupture occurs at the waist part of the blister. The possible reason is insufficient data collected during the optical profilometer measurement process. Nevertheless, the profile in **Figure 2.11c** can be fitted by single-peak fitting using a Gaussian peak with an  $R^2$  value of 99.3 %, and a fitting formula is expressed as follows:

$$y = y_0 + \frac{A}{w \times \sqrt{\frac{\pi}{4 \times \ln(2)}}} \times e^{\frac{(-4 \times \ln(2) \times (x-x_c)^2)}{w^2}} \quad (2.3)$$

where  $y$ ,  $y_0$ ,  $A$ ,  $w$ ,  $x$ , and  $x_c$  represent the  $y$  coordinate, offset, area, width,  $x$  coordinate of the blister, and central position of the blister peak, respectively. One set of values is extracted from the fitting and shown in **Figure 2.11c**. After the profile fitting, the volume of the blister is obtained by the same integration method presented in **Equation (2.2)**. The calculated



Table 2.2: Summary of blisters created on the free surface of PI (5  $\mu\text{m}$  thick) by different laser fluence

| laser fluence          | Laser shots | Blister result   |
|------------------------|-------------|------------------|
| 0.32 J/cm <sup>2</sup> | 10          | Intact blister   |
| 0.96 J/cm <sup>2</sup> | 4           | Intact blister   |
| 1.6 J/cm <sup>2</sup>  | 2           | Ruptured blister |
| 1.92 J/cm <sup>2</sup> | 1           | Ruptured blister |
| 2.56 J/cm <sup>2</sup> | 1           | Ruptured blister |
| 3.2 J/cm <sup>2</sup>  | 1           | Ruptured blister |

value is 6145  $\mu\text{m}^3$ , while the reference value from the software is 5438  $\mu\text{m}^3$  (the calculation step is provided in **appendix Figure A.15**). The discrepancy between the two values can be well-explained by the dark area in the contour map, which indicates no collected data. Consequently, less blister volume is obtained from the software. Compared with the blister volume of 1606  $\mu\text{m}^3$  created by 0.96 J/cm<sup>2</sup> & 4 shots in the presence of SU-8 microdisk, the volume of PI blister created on the free surface is almost three times larger. **Figure 2.11d**, together with the corresponding SEM images in **Figure 2.13**, also confirms the huge difference in blister profiles with and without the SU-8 microdisk using the same laser parameters. Such a considerable difference in blister size further underpins that the existence of SU-8 suppresses the volume expansion of the blister, and much of the remaining laser energy (after laser ablation) is consumed by the peeling process of the SU-8 from the donor substrate and the ensuing kinetic energy of the SU-8 microdisk.

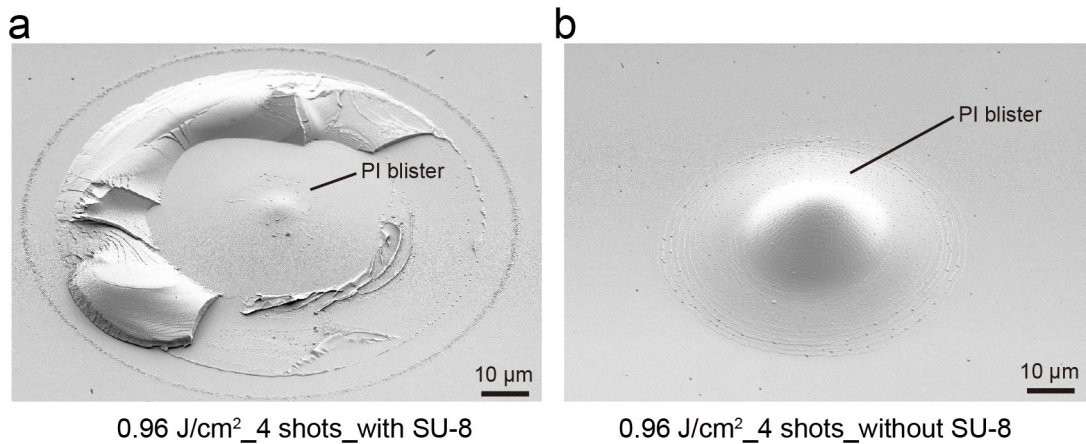


Figure 2.13: **PI blister comparison with and without the SU-8 microdisk.** (a). A PI blister formed with the existence of SU-8. (b). A PI blister formed on the free surface of the PI film.

In this section, we analyze the influence of laser fluence on the SU-8 microdisk transfer and the corresponding blister profiles. **Figure 2.14** summarizes three different cases. When the SU-8 is present, laser fluence 1 (e.g., 0.96 J/cm<sup>2</sup> & 4 shots) leads to the generation of a PI blister

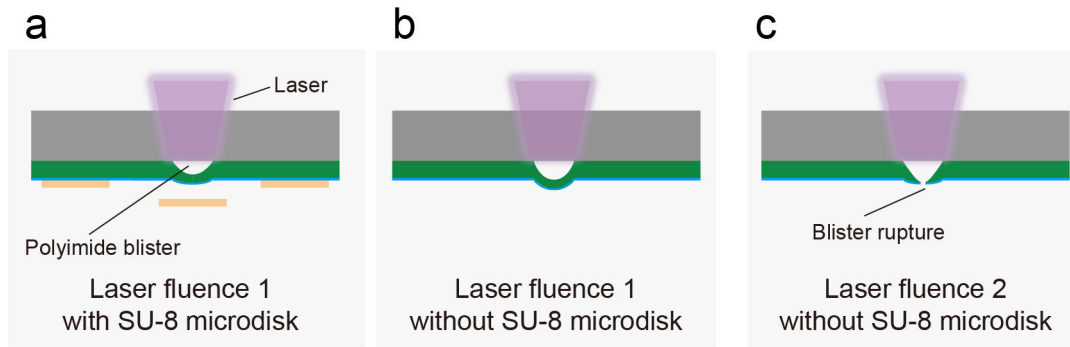


Figure 2.14: **PI blister profile summary under three situations.** (a). A PI blister formed with the existence of the SU-8 microdisk. (b). A PI blister formed on the free surface. The energy is the same as in (a). (c). A PI blister formed on the free surface. The laser fluence is higher than that in (c).

with a small size (**Figure 2.14a**). When the SU-8 microdisk is absent, the PI blister created by the same laser parameter utilized in **Figure 2.14a** has a much larger size. If the laser fluence is higher than the laser fluence 1, blister rupture happens, as shown in **Figure 2.14c**.

Also, it is worth mentioning that because the laser spot size in the LIFT setup is a fixed value (20  $\mu\text{m}$ ), the corresponding PI blister size is limited by this dimension, as shown in the summary of the blister profiles. The largest blister width is no greater than 70  $\mu\text{m}$  and this value also limits the SU-8 microdisk size that can be transferred by the LIFT setup. This is why we choose the SU-8 microdisk with a diameter of 100  $\mu\text{m}$  for the transfer. In addition, it motivates us to overcome this laser spot size limitation and transfer larger microstructures, which will be elaborated on in **Chapter 4**.

### 2.3.2 Influence of PI thickness

The laser fluence study in the previous section proves that in the presence of a SU-8 microdisk, the PI blister has a much smaller size, and no rupture of the PI layer happens. In **Chapter 1**, it has been discussed that in order to transfer thermal-sensitive devices or to avoid contamination, PI rupture should be completely avoided. This blister size reduction analyzed in the previous section is a good sign of fulfilling such a purpose. Based on these results, the PI thickness can be further decreased to realize more efficient laser fluence conversion (from laser fluence to the kinetic energy of SU-8 microdisk) without concerning the blister rupture.

In this section, we prepare PI thin films with different thicknesses while keeping the SU-8 parameters unchanged. We investigate the transfer of SU-8 microdisks and PI blister formation under different thicknesses.

PI samples with various thicknesses (1, 3, 7, 9, and 11  $\mu\text{m}$ ) are prepared following the same

process as the preparation for 5- $\mu\text{m}$ -thick PI. In order to ensure that even with the thickest PI film, the LIFT system can trigger successful transfer, we utilize the maximum laser fluence of  $3.2\text{ J/cm}^2$  for all the experiments in this section. Ten SU-8 microdisks are transferred onto the PDMS receiver to guarantee the repeatability of experiments for each thickness. After the transfer, PI blisters are characterized by SEM and the optical profilometer, respectively.

**Figure 2.15** and **appendix Figure A.16** to **A.19** summarize the characterization results of the blisters created on 1, 3, 7, 9, and 11  $\mu\text{m}$  thick PI in the presence of SU-8 microdisks, respectively. **Figure 2.15** show that the blisters are much larger than those displayed in **appendix Figure A.6a-b** when the PI thickness is 5  $\mu\text{m}$ . Another stark difference between these two experimental results is that a rupture on the blister top can be observed in **Figure 2.15**. This phenomenon can be well explained by the fact that thinner PI film can be more easily ablated by a laser pulse, especially considering the PI thickness is only 1  $\mu\text{m}$  while the absorption depth is close to 0.5  $\mu\text{m}$  <sup>[173]</sup>.

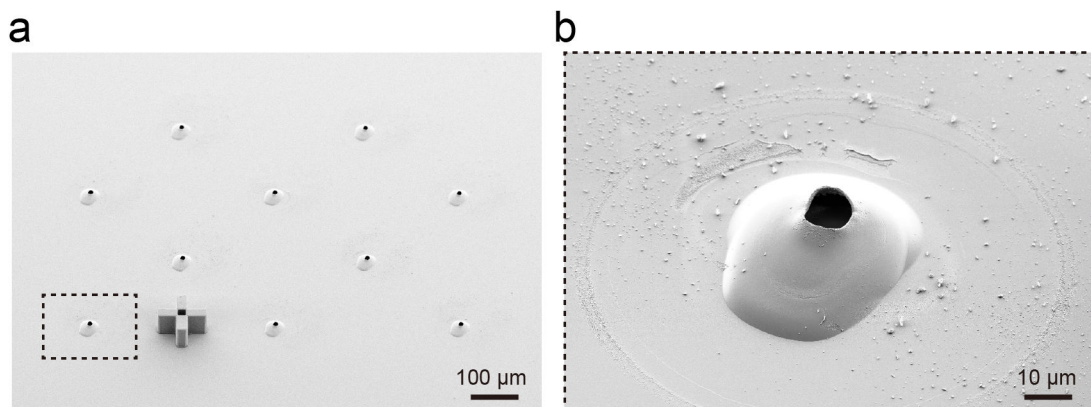


**Figure 2.15: PI blister created by  $3.2\text{ J/cm}^2$  laser fluence on a 1- $\mu\text{m}$ -thick PI film. (a).** SEM image presenting the ten blisters. **(b).** Magnified SEM image of one blister.

Since  $3.2\text{ J/cm}^2$  exceeds the threshold to lead to blister rupture on 1- $\mu\text{m}$ -thick PI, we decrease the laser fluence to  $0.96\text{ J/cm}^2$  and check the result. As shown in **appendix Figure A.16**, the phenomenon of blister rupture is observed as well. The difference lies in the size of the blister. Compared with the result displayed in **Figure 2.15b**, the blister size in **appendix Figure A.16** is smaller, which can be reasonably attributed to lower laser fluence. Raising the laser fluence results in more PI ablated and greater energy stored in the blister. Such energy will finally be dissipated in the PI film delamination and SU-8 microdisk transfer processes. Therefore, a larger dimension of the blister (height and width) is seen. As introduced in **Chapter 1**, PI blister rupture may release hot gases, which is detrimental to heat-sensitive donor material/device. In the meantime, hot gases may carry debris from the PI film, which can contaminate the SU-8 microdisk. The debris is distributed around the blister after the transfer, as shown in **Figure**

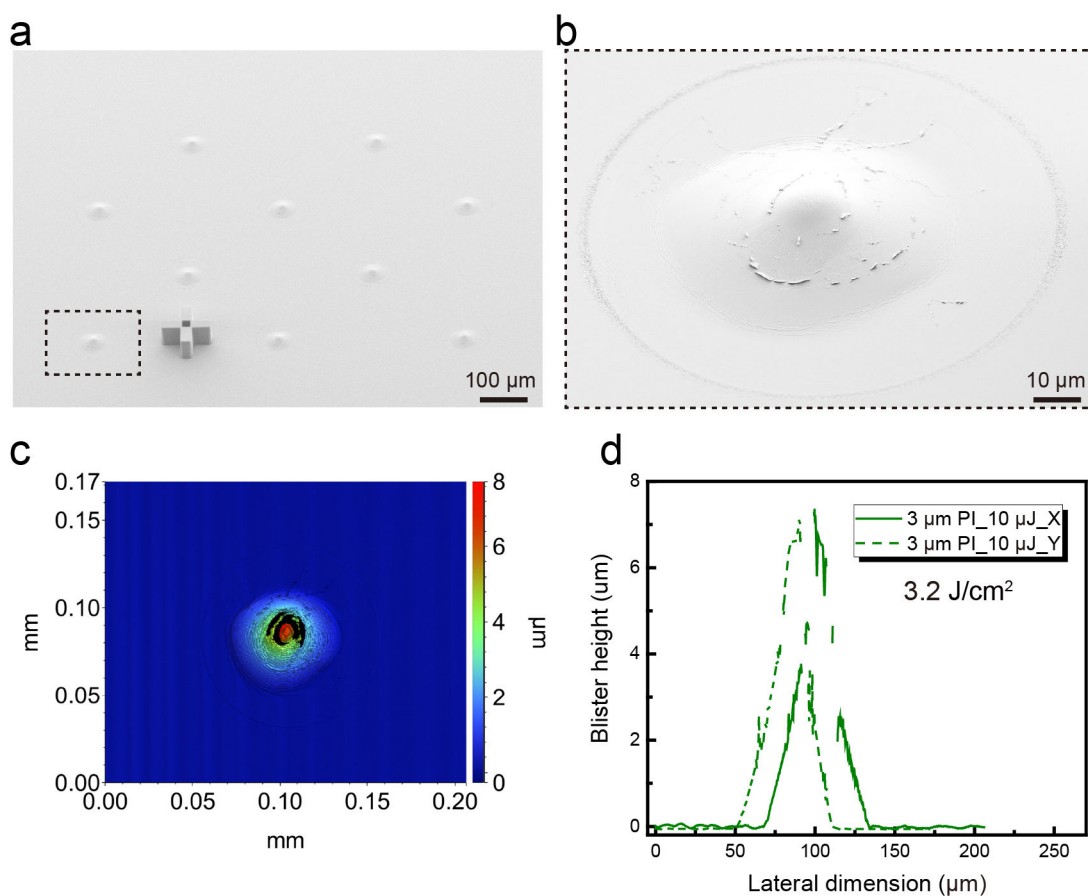


Figure 2.16: **PI blister created by  $3.2 \text{ J/cm}^2$  laser fluence on a  $3\text{-}\mu\text{m}$ -thick PI film.** (a). SEM image presenting the ten blisters. (b). Magnified SEM image of one blister. (c). Contour map of the PI blister. (d). Cross-section profile of the PI blister.

**2.15b.** On the contrary, such debris is absent in **Figure appendix A.6b**. This result proves that although  $1 \mu\text{m}$  thick PI film guarantees successful transfer of the SU-8 microdisk, even at a lower energy ( $0.96 \text{ J/cm}^2$ ), the side effect originating from the byproduct contamination precludes the possibility of considering it an ideal thickness for the SU-8 microdisk transfer.

As we continue increasing the PI thickness and conduct the transfer experiments under constant laser fluence ( $3.2 \text{ J/cm}^2$ ), such blisters become less and less visible in SEM images. By directly comparing blisters created on different thick PI films (**Figure 2.17**), we can conclude that blisters are almost invisible when PI thicknesses reach  $9$  and  $11 \mu\text{m}$ . This blister height decreasing trend is prominently presented in **Figure 2.16d** and from **appendix Figure A.17d** to **appendix Figure A.19d**. In all these cross-sectional profiles, the scale range on the y-axis is unchanged ( $8 \mu\text{m}$ ). Therefore, an obvious decline in blister height as the increase of the PI thickness is observed. This trend can be attributable to the mechanical resistance of the thicker PI film to the laser pulse. With fixed laser fluence, the thicker PI film is more resistant

to the impulse of the laser because it has a larger flexural rigidity <sup>[175]</sup> and a relatively larger portion of the PI film is uninfluenced by the laser.

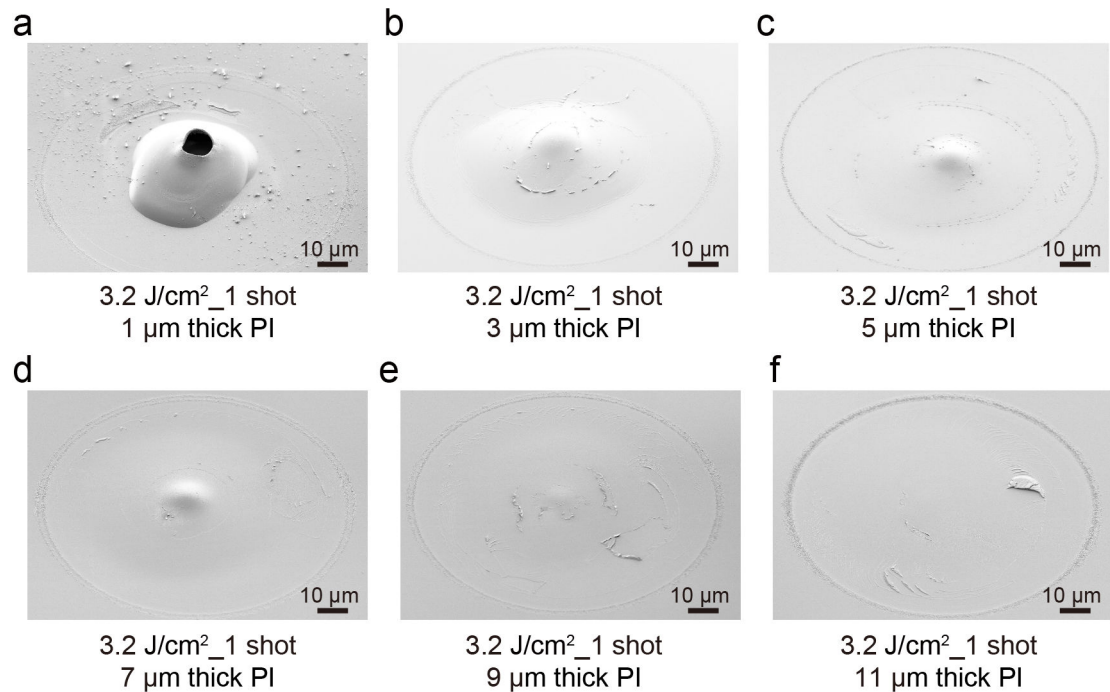


Figure 2.17: **Direct comparison of six PI blisters created on PI films with different thicknesses. (a-f).** SEM image of magnified PI blisters when the PI thickness increases from 1 to 11 μm. Blisters are less evident as the increase of PI thickness.

After the characterization, all the blisters' profiles are plotted in **Figure 2.18a**. As the increase of the PI thickness, the blister height drops dramatically. When the PI thickness reaches 11 μm, the blister height is only 0.3 μm. Then, the blister height data is extracted from **Figure 2.18a** and re-plotted in **Figure 2.18b**. A monotonic decrease in blister height is shown in the plots, which coincides with the observation from the SEM images. In addition, changes in blister width as a function of PI thickness are plotted. The PI blister width first increases from 60.5 μm (3-μm-thick PI) to 69.2 μm (7-μm-thick PI) and then decreases to 56 μm (11-μm-thick PI).

In order to capture the blister volume, such blisters are fitted by the Lorentzian peak fit method (moving the x coordinate of the peak to zero). One example of the fitting is presented in **Figure 2.18c**. The fitting formula is the same as **Equation (2.1)** but with different coefficients, which are listed in **Figure 2.18c**. After the profile fitting, the volume is calculated by the same formula as shown in **Equation (2.2)** and a detailed calculation process is provided in **appendix Figure A.20**. The final volumes corresponding to five different PI thicknesses are plotted in **Figure 2.18d**. A huge decline in blister volume from 5314 μm<sup>3</sup> to 467 μm<sup>3</sup> is shown in the plot. This finding, together with the data summarized in **Table 2.3**, shows a positive correlation between the blister height and the blister volume. As the PI thickness increases, a decreasing trend is

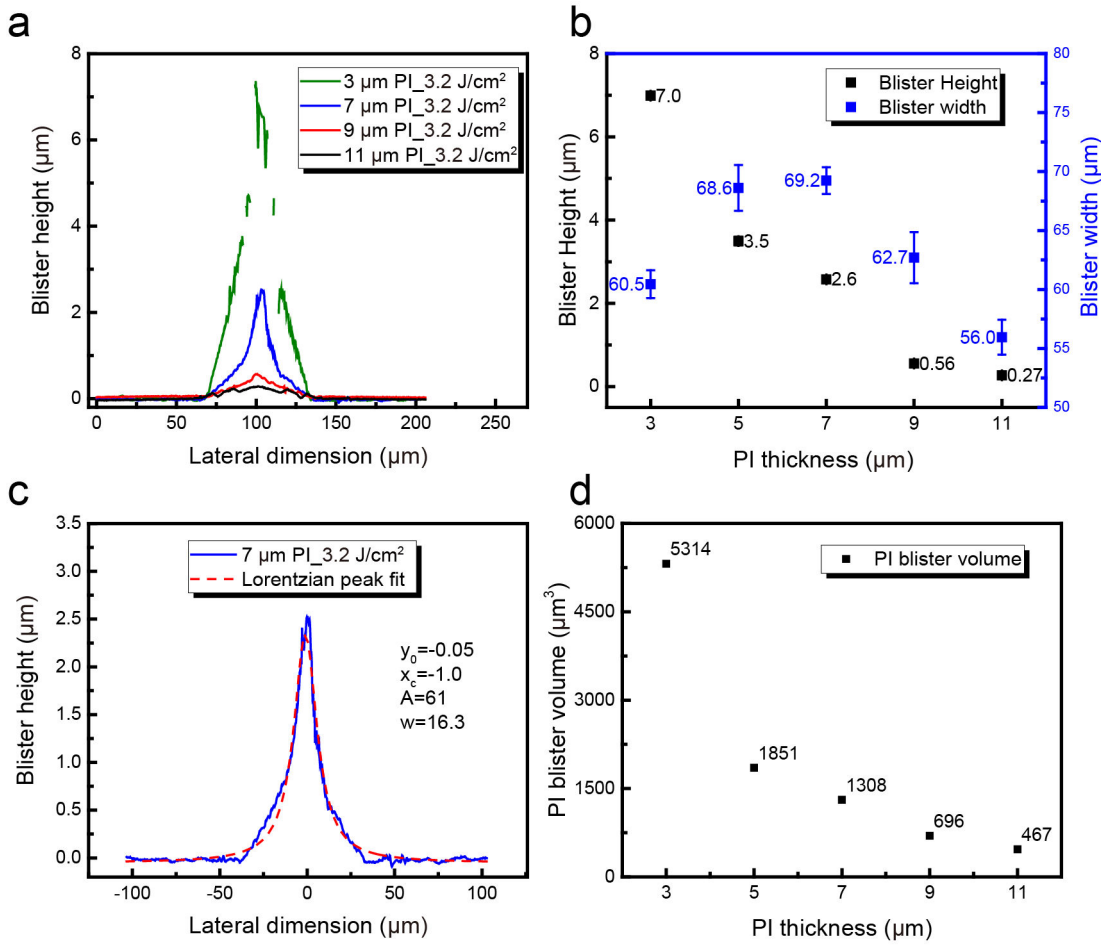


Figure 2.18: **PI blister profile summary with different PI thicknesses.** (a). Summary of all the PI blisters created on different thick PI films. (b). Blister height and blister width summary. (c). Lorentzian fitting of one blister profile (7- $\mu\text{m}$ -thick PI, 3.2 J/cm<sup>2</sup>). (d). PI blister volume change as a function of PI thickness.

found both in the blister height and volume. This effect has been explained before due to the mechanical resistance of the thicker PI film (e.g., 9 and 11  $\mu\text{m}$  thick PI) to the laser pulse.

Similar to the experiments conducted on the free surface of 5  $\mu\text{m}$  thick PI (in the absence of SU-8 microdisks), we investigate the PI blister morphology created on free surfaces of PI with various PI thicknesses. **Appendix Figure A.21 to A.25** show a series of characterization results of the PI blisters. In **appendix Figure A.21a** and **A.21c**, six blisters are formed on 1- $\mu\text{m}$ -thick PI surface with two different laser fluences: 3.2 and 0.96 J/cm<sup>2</sup>. **Appendix Figure A.21b** and **A.21d** are two corresponding magnified images showing details of the blisters. In both cases, the cap area of the blisters is completely removed, whereas in other cases (**appendix Figure A.23b**), blisters have a cone-shaped structure, and their sizes are comparably smaller than those formed on 3 to 11  $\mu\text{m}$  thick PI. The blister width in **appendix Figure A.21** is approximately 30

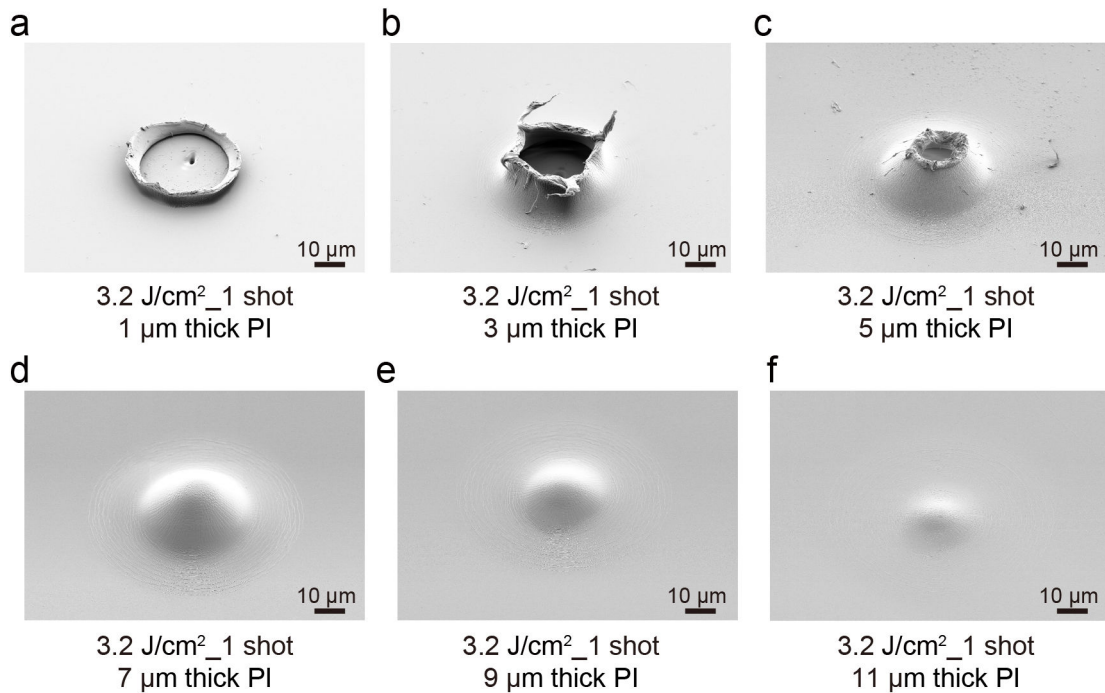


Figure 2.19: **Direct comparison of six PI blisters created on the free surface of PI films with different thicknesses. (a-f).** SEM image of magnified PI blisters when the PI thickness increases from 1 to 11 μm. Blister rupture happens when the PI thickness varies from 1 to 5 μm and intact blisters are formed when the PI thickness continues to increase from 7 to 11 μm.

μm, close to the laser spot size (20 μm). To summarize all the blisters for direct comparison, six PI blisters corresponding to PI films with different thicknesses are presented in **Figure 2.19**.

The removal of the blister cap can be attributed to the thin thickness of the PI film. As mentioned before, the absorption depth of PI using a 355 nm laser is close to 0.5 μm. This value is slightly smaller than the thickness of the PI film (1 μm). Since the laser fluence dramatically exceeds the ablation threshold, meaning that the PI film is completely ablated along the PI thickness direction. Therefore, less expansion of the trapped gas would be anticipated because the trapped gas is quickly released due to the rupture of the blister.

Another phenomenon is that an ablated hole is found on the glass substrate for both laser fluence. As the decrease of the laser fluence (from 3.2 to 0.96 J/cm<sup>2</sup>), the hole becomes shallow. The formation of such ablated holes is tentatively ascribed to the slight absorption of the laser by float glass. One study <sup>[180]</sup> has proved that at a wavelength of 355 nm, the absorbance by the float glass reaches 10 % of the total intensity of the incident light. This part of absorbed laser fluence, in combination with the high temperature created by the laser ablation process, will locally heat and melt the float glass surface.

Table 2.3: Summary of the transfer result of SU-8 microdisks and the corresponding blisters created on PI with different thicknesses

| PI thickness     | Transfer result | Blister result  | Blister height     | Blister volume       |
|------------------|-----------------|-----------------|--------------------|----------------------|
| 1 $\mu\text{m}$  | Transfer        | Rupture blister | N.A.               | N.A.                 |
| 3 $\mu\text{m}$  | Transfer        | Intact blister  | 7.0 $\mu\text{m}$  | 5314 $\mu\text{m}^3$ |
| 5 $\mu\text{m}$  | Transfer        | Intact blister  | 3.5 $\mu\text{m}$  | 1851 $\mu\text{m}^3$ |
| 7 $\mu\text{m}$  | Transfer        | Intact blister  | 2.6 $\mu\text{m}$  | 1308 $\mu\text{m}^3$ |
| 9 $\mu\text{m}$  | Transfer        | Intact blister  | 0.56 $\mu\text{m}$ | 696 $\mu\text{m}^3$  |
| 11 $\mu\text{m}$ | Transfer        | Intact blister  | 0.27 $\mu\text{m}$ | 467 $\mu\text{m}^3$  |

N.A. in the table means that PI blister height and volume cannot be calculated.

In order to verify the hypothesis that the partial absorption of the laser by the donor substrate and the high temperature created by the PI ablation process jointly contribute to the formation of such "craters", we experiment using a bare float glass wafer in the absence of the PI film. The laser is focused on the bottom surface (meaning the laser penetrates through the wafer) of the wafer, and a single laser shot (from 0.32 to 3.2 J/cm<sup>2</sup>) is adopted for the experiment.

**Figure 2.20** summarizes the results. **Figure 2.20a** shows the complete ablation tests on the glass substrate and **Figure 2.20b-d** presents three magnified SEM images, showing three "craters" created by different laser fluences. The first conclusion is that if the laser fluence is too small (e.g., 0.32-1.6 J/cm<sup>2</sup>), there are no such "craters", indicating that such laser fluence fails to reach the ablation threshold to ablate the substrate. As the increase of laser fluence from 1.92 to 3.2 J/cm<sup>2</sup>, larger and deeper "craters" form on the bottom surface of the wafer. In addition, no ablation areas are found on the top surface of the wafer, which confirms that the glass wafer is almost transparent to the laser and can absorb only a small portion of laser energy. Therefore, this slight absorption by the glass wafer does not play an important role in the PI film ablation and subsequent blister formation processes, and it can be reasonably ignored.

For the unruptured PI blisters formed on the thicker PI films (7, 9, and 11  $\mu\text{m}$ ), the blister characterization is individually presented from **appendix Figure A.23** to **A.25**. The SEM images show a decreasing trend of blister height, which is also confirmed by the optical profilometer measurement results (**appendix Figure A.23c-d** to **A.25c-d**). The profiles of the blister shown in **appendix Figure A.23d** to **A.25d** are re-plotted in **Figure 2.21a** for direct comparison. Similar to the blister height and width analysis shown in **Figure 2.18**, we quantify the two parameters of the blister. The blister height drops from 9.2  $\mu\text{m}$  (7- $\mu\text{m}$ -thick PI) to 2.7  $\mu\text{m}$  (11- $\mu\text{m}$ -thick PI). This decreasing trend in blister height resembles that found in **Figure 2.18b**, where the SU-8 microdisk is present but with a much smaller blister height. This difference has been analyzed in the previous section due to the absence of the SU-8 microdisk. The blister width decreases from 73.5  $\mu\text{m}$  (7- $\mu\text{m}$ -thick PI) to 69.5  $\mu\text{m}$  (11- $\mu\text{m}$ -thick PI), which agrees well with the finding



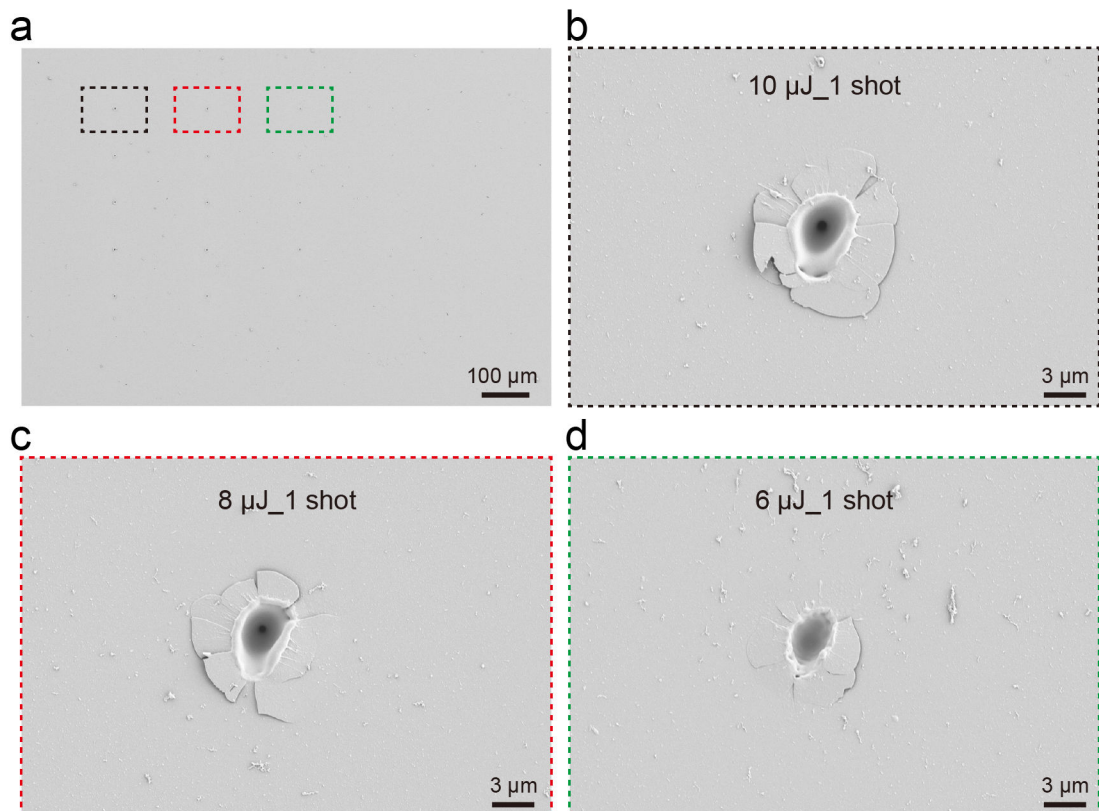


Figure 2.20: **Laser ablation tests on bare float glass wafer.** (a). Summary of the ablation tests. (b). One ablated area on a glass wafer created by a laser pulse of  $3.2 \text{ J/cm}^2$ . (c). One ablated area on a glass wafer created by a laser pulse of  $2.56 \text{ J/cm}^2$ . (d). One ablated area on a glass wafer created by a laser pulse of  $1.92 \text{ J/cm}^2$ .

in **Figure 2.18b** when there are SU-8 microdisks.

After the blister height and width analysis, the result of blister fitting by the Gaussian peak is shown in **Figure 2.21c**, and the corresponding coefficients are listed as well. Consequently, PI blister volumes (Detailed calculation is provided in **appendix Figure A.26**) corresponding to 7, 9, and 11  $\mu\text{m}$  thick PI film are calculated and plotted in **Figure 2.21d**. A decreasing trend in blister volume can be observed, similar to **Figure 2.18d**.

In short, PI thickness influences the blister formation and ensuing SU-8 microdisk transfer. Although thicker PI film (e.g., 11  $\mu\text{m}$ ) enables the transfer of SU-8 microdisk, the optimal PI thicknesses obtained from the discussion above are 3 and 5  $\mu\text{m}$ , where less laser fluence is required to guarantee the successful transfer while ensuring that no blister rupture happens (unlike the results corresponding to 1  $\mu\text{m}$  thick PI).

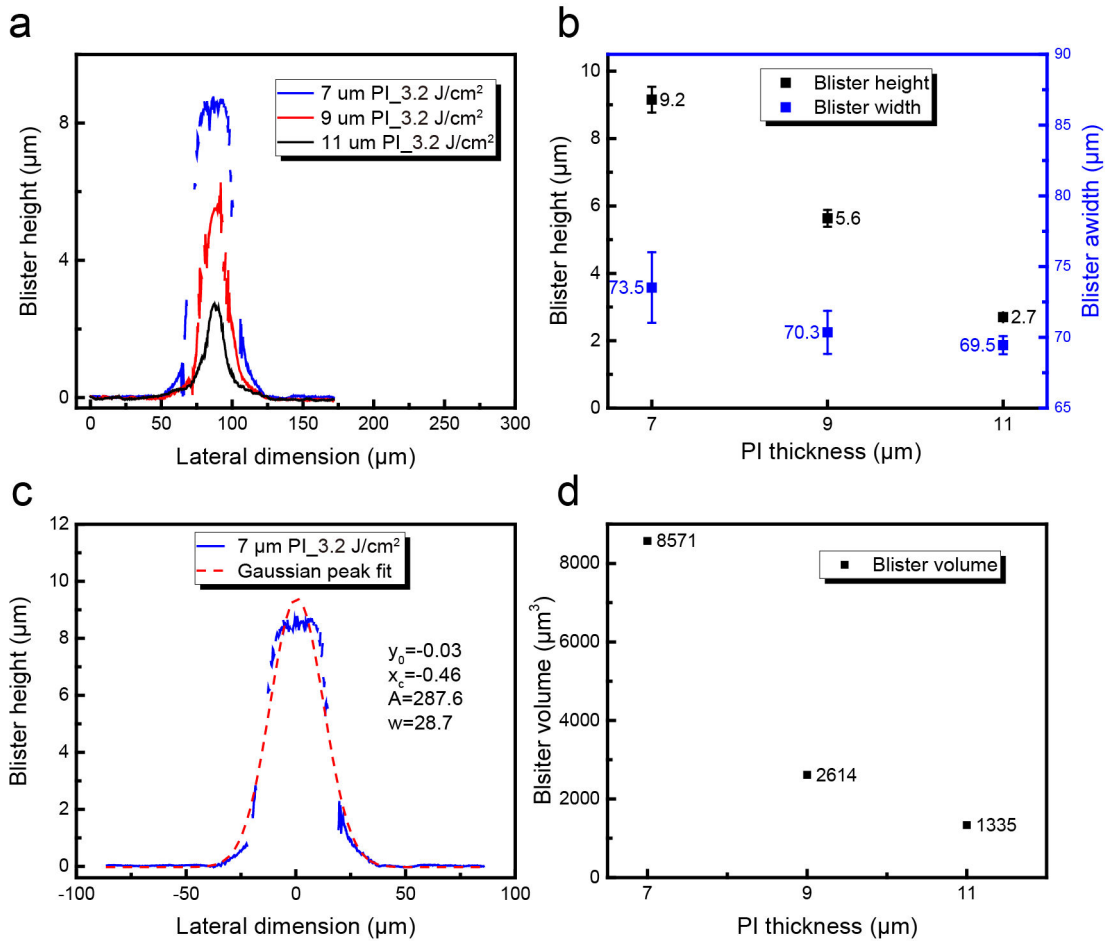


Figure 2.21: **Summary of PI blister profiles created on PI free surface with different thicknesses.** (a). Blister profiles corresponding to the PI thickness from 7 to 11 μm. (a) only presents the results in the X-direction, considering the symmetric nature of the blister. (b). Blister height and blister width summary. (c). Gaussian fitting of one blister profile (7-μm-thick PI, 3.2 J/cm<sup>2</sup>). (d). PI blister volume change as a function of PI thickness.

### 2.3.3 Influence of SU-8 thickness

In this section, we evaluate the relationship between SU-8 thickness and SU-8 structural integrity after transfer.

Four SU-8 donor samples are fabricated with increased thicknesses (5, 10, 20, and 50 μm). For each SU-8 thickness, five SU-8 microdisks (100 μm in diameter) are transferred onto the PDMS receiver (1.6 J/cm<sup>2</sup>, 2 shots). The optical images displayed in **Figure 2.22** demonstrate that SU-8 thickness does influence the transfer result. When SU-8 thickness is 5 μm, only SU-8 debris is found on the PDMS receiver. Fragmented and cracked SU-8 microdisks are observed on PDMS receivers with SU-8 thicknesses of 10 and 20 μm (**Figure 2.22b-c**), respectively. All these results indicate that the PI blister impulse is too strong to enable damage-free transfer.

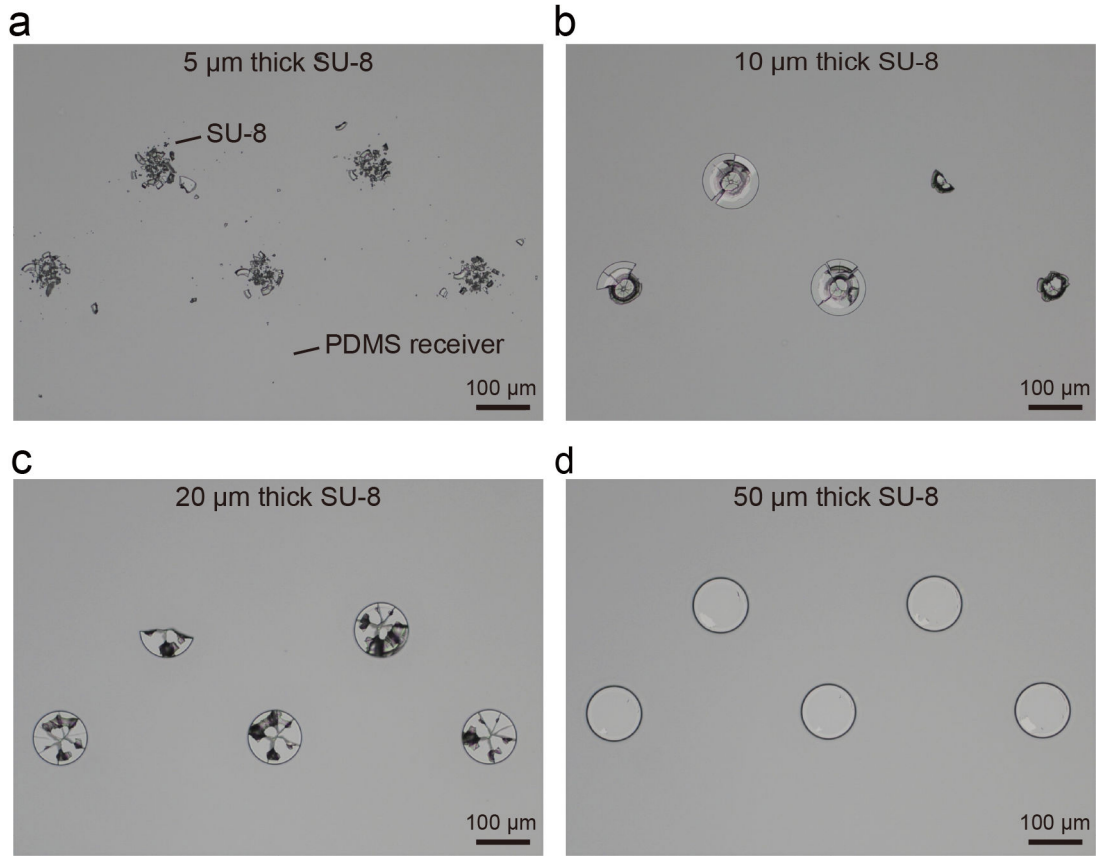


Figure 2.22: **Transfer results of SU-8 microdisks with different SU-8 thicknesses. (a-d).** SU-8 microdisks transferred onto PDMS receivers. SU-8 thickness increases from 5 ((a)) to 50  $\mu\text{m}$  ((d)).

However, when the thickness increases to 50  $\mu\text{m}$ , transferred SU-8 microdisks are free from such defects. **Figure 2.22d** shows the result of the five intact SU-8 microdisks. All these findings are supported by other theoretical and experimental research [174, 175, 187, 188]. It has been proven that the length-thickness ratio of an ultra-thin chip influences the transfer result. A larger length-thickness ratio indicates the chip is more vulnerable to damage because of the transient impulse of the expanding blister and a smaller flexural rigidity ( $D$ ) of the chip. Besides, the stress concentration lies in the center of the free surface (interface between the air and the chip). The chip will fracture once its stress reaches a critical value, leading to the breakage. In our case, the length (diameter) of the SU-8 microdisk is a fixed value. Therefore, the thickness of the SU-8 microdisk plays an important role because the flexural rigidity of the SU-8 is expressed as:

$$D = \frac{E \times h^3}{12 \times (1 - \nu^2)} \quad (2.4)$$

where  $E$ ,  $h$  and  $\nu$  are Young's Modulus, thickness and Poisson's ratio of the SU-8. From

the formula, we can conclude that the flexural rigidity increases with the cubic of the SU-8 thickness. Comparing the flexural rigidity of SU-8 microdisks with two different thicknesses: 5 and 50  $\mu\text{m}$ , their flexural rigidity difference is 1000 times larger ( $5 \times 10^{-8}$  and  $5 \times 10^{-5}$  N·m for 5 and 50  $\mu\text{m}$  thick SU-8, respectively). Thinner SU-8 microdisks have smaller flexural rigidity and prefer to undergo bending deformation with the PI blister instead of peeling away from the PI film. This can be ascribed to the small mismatch of the flexural rigidity between the thinner SU-8 and the PI film (5  $\mu\text{m}$  thick, the flexural rigidity of  $2.4 \times 10^{-8}$  N·m). When the SU-8 and PI have the same thickness (5  $\mu\text{m}$ ), their flexural rigidity is in the same order of magnitude. Therefore, thinner microdisks suffer from larger bending stress and are more easily damaged. At the same time, thicker SU-8 (50  $\mu\text{m}$ ) can survive the peeling-off process because it can be considered a rigid object with respect to the thinner deformable PI film.

In our case, the length-thickness ratio of the SU-8 decreases from 20 to 2 as the SU-8 thickness increases from 5 to 50  $\mu\text{m}$ . When the ratio is too large (e.g., 20, corresponding to SU-8 thickness of 5  $\mu\text{m}$ ), the transfer results in **Figure 2.22a** only show SU-8 debris in the center. Most of the SU-8 parts still stay on the donor substrate, as presented in **appendix Figure A.27a**. As the increase of the SU-8 thickness (length-thickness ratio of 10 and 5), more SU-8 microdisk parts are transferred to the PDMS receiver; however, breakage and cracks are observed. When the ratio is sufficiently small (SU-8 thickness of 50  $\mu\text{m}$ ) and the flexural rigidity is large enough, intact SU-8 microdisks are transferred to the PDMS receiver. On the corresponding donor substrate only 5 PI blisters are found on the donor substrate with negligible SU-8 debris (**appendix Figure A.27d**). Therefore, a minimum thickness of 50  $\mu\text{m}$  is required to realize a successful transfer that can guarantee the structural integrity of SU-8 microdisks. This is of great significance if functional SU-8-supported microdevices need to be transferred by LIFT. Unless otherwise specified, all the experiments discussed below and in **Chapter 3** adopt this optimal thickness (50  $\mu\text{m}$ ).

### 2.3.4 Influence of donor-to-receiver gap distance

The fourth parameter we investigate is the gap distance between the donor and receiver. In many cases, the gap distance is an important process parameter determining the transfer precision. Several groups have reported that with the increase of gap distance, transfer results can shift from high transfer precision to lateral displacement, rotation, and flipping. In 2012, one group investigated the influence of standoff height on the precision in placement<sup>[155]</sup> of Si chipllets. The standoff height varies from 5 to 300  $\mu\text{m}$ , and the conclusion is that the lateral placement error increases dramatically when the height reaches 300  $\mu\text{m}$ . Such placement error becomes insignificant when the height is lower than 20  $\mu\text{m}$ . Another group probed the experiments of Cu foils transfer and obtained similar results<sup>[107]</sup>. Other research also investigated the transfer precision with a fixed gap distance<sup>[166, 169, 170]</sup> and the results

indicate the random distribution of such transferred microcomponents within a certain range. Different results can happen during the transfer process, including small displacement, angle rotation, and flipping. **Figure 2.23** summarize all the possible transfer results.

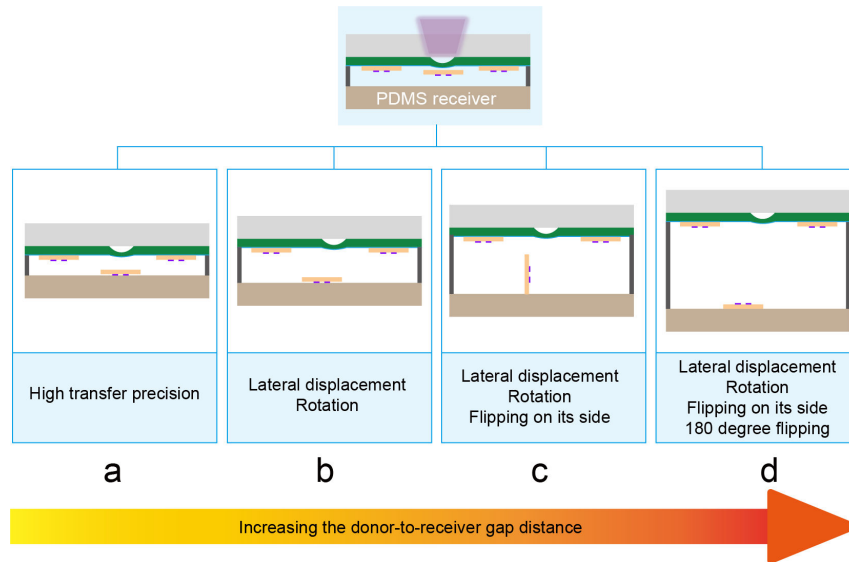


**Figure 2.23: Sketches of different transfer results as the increase of donor-receiver gap distance. (a-d).** Transfer results vary from high-precision transfer to lateral displacement, rotation, flipping on its side, and 180-degree flipping when the gap distance is sufficiently large.

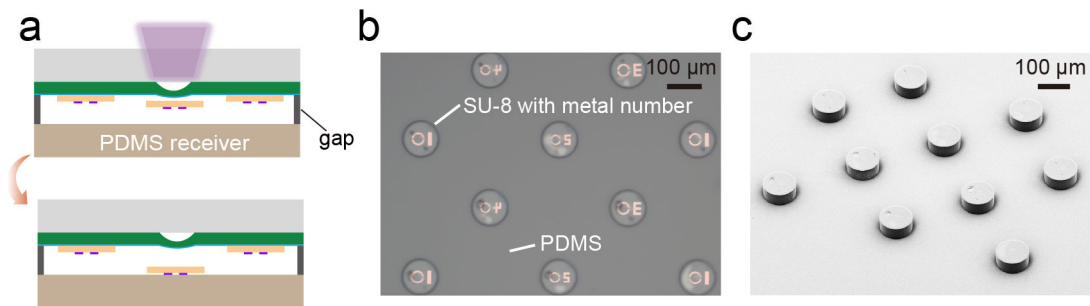


**Figure 2.24: SU-8 transfer results on PDMS receiver with a gap distance of close contact. (a).** Sketch of the transfer process of SU-8 microdisks on PDMS receiver with a gap. **(b).** Transfer result of 10 SU-8 microdisks with the gap distance to be close contact. **(c).** Corresponding SEM image of the 10 SU-8 microdisks.

We begin the experiments by placing spacers with known thicknesses between the donor and the PDMS receiver. This helps quantify the relation between the gap distance and the transfer precision of SU-8 microdisks, as illustrated in **Figure 2.24a**. Four different gap distances: close contact (i.e., directly placing the SU-8 donor substrate on the PDMS receiver), 50, 210, and 370  $\mu\text{m}$  are investigated. **Figure 2.24b** shows the transfer result of ten SU-8 microdisks (diameter:

100  $\mu\text{m}$ , thickness: 50  $\mu\text{m}$ ) with labels of metal number when the gap distance is close contact. Here the label helps determine whether the flipping of the SU-8 microdisk happens during the transfer process. The optical image shows that the SU-8 array is well-aligned, and the tilted SEM image further confirms the high transfer precision. Another finding from the SEM image is that no metal numbers are observed, thus precluding the possibility of SU-8 flipping. Similar results are also found in **Figure 2.25a-b**, where the gap distance increases to 50  $\mu\text{m}$ . The two groups prove that the transfer displacement is insignificant at a small gap distance. When the gap distance increases to 210 and 370  $\mu\text{m}$ , more distinct phenomena such as displacement, rotation, and flipping are found in **Figure 2.25c-f**. Three microdisks in **Figure 2.25c-d** are flipped on their side surfaces, and 180-degree flipping happens in **Figure 2.25e-f**. The flipped SU-8 microdisks in **Figure 2.25f** are distinguishable from those in **Figure 2.25b** and **2.25d** due to the metal labels. If no flipping happens during the transfer, the metal label side will face down (in contact with the PDMS receiver); therefore, no labels will be observed in the SEM image.

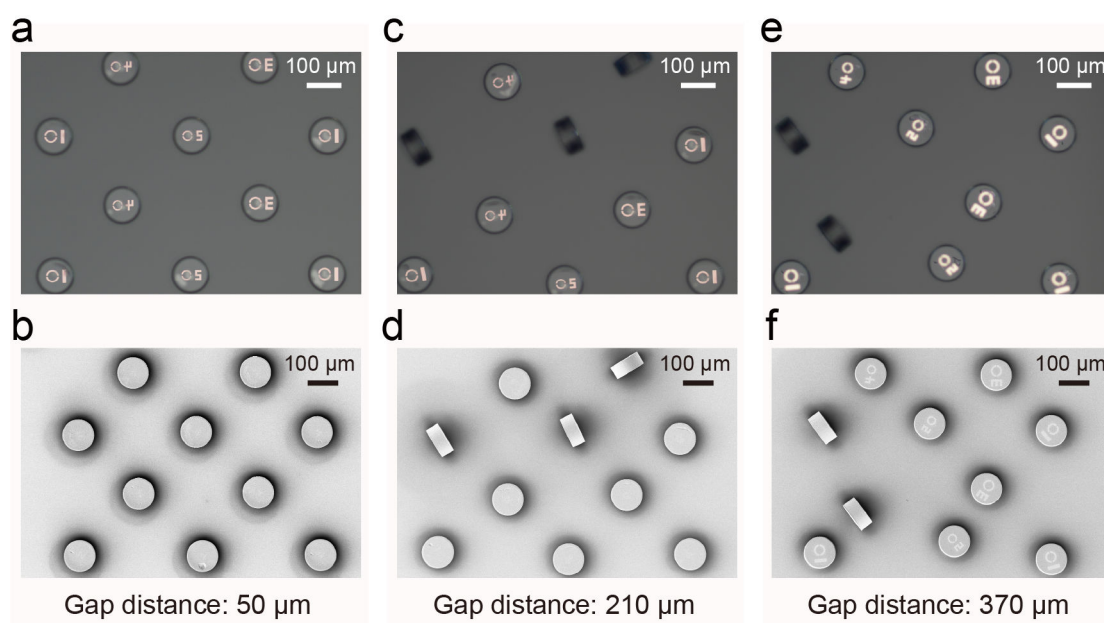


**Figure 2.25: SU-8 transfer results on PDMS receiver with a gap distance of 50, 210 and 370  $\mu\text{m}$ .** (a-b). Optical and SEM images of transferred SU-8 microdisk with a gap distance of 50  $\mu\text{m}$ . No obvious lateral displacement or rotation is found. (c-d). Optical and SEM images of transferred SU-8 microdisk with a gap distance of 210  $\mu\text{m}$ . Lateral displacement and rotation of the transferred SU-8 can be found. Three microdisks flip on its side. (e-f): Optical and SEM images of transferred SU-8 microdisk with a gap distance of 370  $\mu\text{m}$ . Lateral displacement, rotation, flipping on its side, and 180-degree flipping of transferred SU-8 microdisks are observed.

To better evaluate the transfer results corresponding to different gap distances, the coordinates

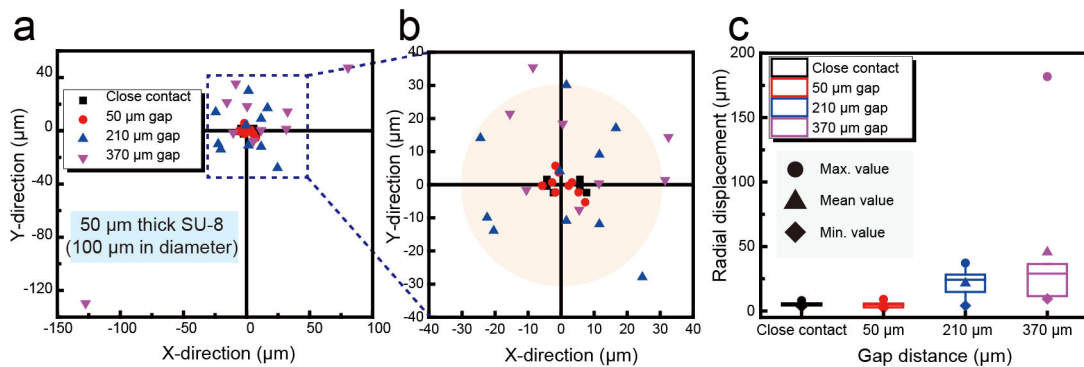


Figure 2.26: **Summary of the transfer precision of SU-8 microdisks.** (a). XY scatter plot of transferred SU-8 microdisks on PDMS receiver, showing the lateral displacement distance with respect to the microdisks' initial position on the donor (the original point). Four groups of SU-8 microdisks with different gap distances are included in the plot: close contact, 50, 210, and 370  $\mu\text{m}$  gap. (b). Zoom-in plot of (a) when removing the bottom left and top right SU-8 microdisks. The majority of the SU-8 is located in a range of  $\pm 30 \mu\text{m}$ , as indicated by the transparent orange circle. (c). Box plot of the radial displacement of transferred SU-8 as a function of gap distance.

of these transferred microdisks (taking the position of the corresponding SU-8 microdisk on the donor as the origin point) are recorded and plotted in **Figure 2.26a**. Except that two data points are located in the bottom left and top right corner, all remaining data points are located in a region enclosed by a dashed square. A zoom-in scatter plot (**Figure 2.26b**) shows the distribution of position shifts of these transferred SU-8 microdisks. The position shift of most SU-8 microdisks does not exceed  $30 \mu\text{m}$ , as indicated by the orange circle. All these SU-8 microdisks are randomly distributed around the origin point. The radial displacement of each group having various gap distances is then calculated, and the result is summarized in a box plot (**Figure 2.26c**).

It should be noted that because of the existence of the PI blister, the actual gap distance in the four cases is smaller than the four values. However, since the measured blister height is around  $2.6 \mu\text{m}$  under  $1.6 \text{ J/cm}^2$  laser fluence (2 shots) and also considering that the maximum blister height is approximately 1.2 times larger than the final blister height because of the elastic property of the PI <sup>[177]</sup>, such value (around  $3 \mu\text{m}$ ) is relatively small than the three gap distances (50, 210 and  $370 \mu\text{m}$ ). We can reasonably use 50, 210 and  $370 \mu\text{m}$  as the gap distances. As shown in **Figure 2.26c**, for the first two groups (close contact and  $50 \mu\text{m}$ ), the radial displacement (transfer error) averages less than  $10 \mu\text{m}$ . As a comparison, the averaged radial displacement values for the latter two groups are much larger than those of the first two groups, which are under  $50 \mu\text{m}$ .

The reduced transfer precision of SU-8 microdisks depends on a series of factors, including

the vibration of the donor stage, laser spot size, the precise centering of the laser beam on the SU-8 microdisks and the ambient atmosphere. In the experiments, three main factors negatively affect the transfer precision. The first one is the back housing and the front door of the LIFT setup. After assembling the rear housing and closing the front door for laser operation, the laser's position is shifted a few micrometers. This leads to the misalignment between the laser center and the SU-8 microdisk center. The second factor is the vibration of the donor stage during a continuous operation. This contributes another few micrometers to the misalignment. The last factor is the determination of the SU-8 microdisk center by our naked eyes. The visual observation can lead to a disk-to-disk observer error when aligning the laser with the SU-8 microdisk. All these accumulated misalignment increases the likelihood of undesired transfer results, such as large displacement, rotation, and flipping.

In our experiments, the influence of the first factor has been eliminated. During the LIFT experiments, the back housing is not assembled, and the front door is open, precluding their influences. However, the other two factors contribute to deteriorated transfer precision and cannot be ignored. Improvements in transfer precision require further efforts and studies to eliminate these negative factors.

## 2.4 Conclusion

This chapter investigates four variables, laser fluence (laser energy), PI thickness, SU-8 thickness, and donor-to-receiver gap distance, to quantify their influence on SU-8 microdisk transfer.

The first variable being studied is laser fluence. Six different laser fluences are used to transfer SU-8 microdisks, and the transfer results are split into two regimes: no transfer ( $0.32 \text{ J/cm}^2$ ) and successful transfer ( $\geq 0.96 \text{ J/cm}^2$ ). Subsequent observation of the transferred SU-8 microdisks proves that although lower fluence with multiple shots ( $0.96 \text{ J/cm}^2$ , 4-6 shots) guarantees the transfer, surface damage of the SU-8 microdisk is unavoidable, and high laser fluence is more favorable to achieving damage-free transfer. The PI blister, which plays a crucial role in transferring SU-8 microdisks, is systematically investigated. Three types of blister are classified from all the experiments. When transferring the SU-8 microdisk with specific laser fluence, the formation and expansion of the blister are suppressed by the existence of the SU-8 microdisk, thus leading to a PI blister having a small size. If there is no SU-8 microdisk, the same laser fluence can generate a much larger blister since no energy is consumed by the microdisk for the separation and forward motion. Finally, if the laser fluence is sufficiently large, blister rupture happens, which should be entirely avoided during an ideal transfer process.

After studying the laser fluence, we probe the influence of PI thickness. A series of PI films (1,



3, 7, 9, 11  $\mu\text{m}$  thick) are prepared and tested. It is observed that for thin PI film (1  $\mu\text{m}$  thick), PI blister rupture happens even with the presence of the SU-8 microdisks. As for thicker PI film (3, 7, 9, 11  $\mu\text{m}$  thick), such blister rupture phenomenon disappears. In the meantime, the blister height drops dramatically from 7.0  $\mu\text{m}$  (3- $\mu\text{m}$ -thick PI) to around 0.27  $\mu\text{m}$  (3- $\mu\text{m}$ -thick PI), which can be reasonably ascribed to the mechanical resistance and larger flexural rigidity of the thicker PI film. When testing these PI films without the SU-8 microdisks, it is observed that much larger blisters are formed on the PI surface (e.g., 7  $\mu\text{m}$  thick PI), and blister ruptures are more evidently shown when the PI thickness is small (1, 3, and 5  $\mu\text{m}$ ). This can be explained by the fact that for the thinner PI film (1, 3 and 5  $\mu\text{m}$ ), the nonablated part is relatively small, whereas for the thicker PI films (7, 9 and 11  $\mu\text{m}$ ), the nonablated part is sufficiently thick. This difference leads to two distinguished phenomena: ruptured blister and intact blister.

Subsequently, the experimental study regarding the SU-8 microdisk thickness is performed. Four SU-8 microdisk samples with different thicknesses (5, 10, 20, and 50  $\mu\text{m}$ ) are tested. Representative transfer results are obtained. When the SU-8 thickness is relatively small, such as 5  $\mu\text{m}$ , only SU-8 debris is found on the receiver, while most of the SU-8 microdisk stays on the donor. When increasing the SU-8 thickness to 10 and 20  $\mu\text{m}$ , only fragmented and cracked microdisks are observed on the receiver. The last tested sample is 50  $\mu\text{m}$  thick SU-8, and the five transferred SU-8 microdisks confirm that the structural integrity of the SU-8 microdisk can be maintained due to negligible SU-8 debris left on the donor substrate.

Finally, the dependence of gap distance on the transfer precision of SU-8 microdisks is studied. Four different gap distances (close contact, 50, 210, and 370  $\mu\text{m}$ ) are created by customized spacers. For the first two groups (close contact and 50  $\mu\text{m}$ ), optical images and SEM micrographs confirm that the transferred SU-8 microdisks are well-aligned on the receiver without apparent rotation. As the increase of the gap distance (210 and 370  $\mu\text{m}$ ), large displacement and rotation of such microdisks are observed. Besides these two phenomena, we find SU-8 microdisks flipping on their side surfaces (gap: 210  $\mu\text{m}$ ) and also flipping 180 degrees (gap: 370  $\mu\text{m}$ ). Quantitative analysis of the displacement distance (transfer error) as a function of gap distance is further summarized. It can be seen that the transfer errors corresponding to the gap distance of close contact and 50  $\mu\text{m}$  are less than 10  $\mu\text{m}$ , whereas the other two gap distances (210 and 370  $\mu\text{m}$ ) result in much larger transfer errors (close to 50  $\mu\text{m}$ ).



# 3 LIFT of SU-8-Supported Functional Devices

**Note:** This chapter is adapted from the following manuscript with the permission of all co-authors:

**Z. Yang,** G. Boero, R. Widmer, J. Michler and J. Brugger, "Laser-induced forward transfer of SU-8 supported metallic microdevices", *In preparation*

**My contribution:** conceptualization, design, micro-fabrication, LIFT experiments, characterization, figures, and writing.

### 3.1 Introduction

In **Chapter 2**, the influences of four different parameters on the final transfer result of SU-8 microdisks are elaborated upon. In this chapter, the optimal parameter combination based on the previous chapter's study is employed to fulfill one of the ultimate goals of this thesis: transferring functional SU-8 microdevices to various targeted receivers and proving their post-transfer functionalities. In contrast to other works using Si dummy dies <sup>[155–157]</sup> as LIFT demonstrations, in our work SU-8 functional microdevices are first fabricated and then transferred by the LIFT setup. Post-transfer characterization proves the functionalities are well-preserved without causing damage during the transfer process.

As a first demonstration, SU-8 microdisks with metal QR codes are transferred. To assess the QR code readability after the transfer, optical images are taken, and the QR code is scanned by the camera. The scanning results demonstrate that metal QR codes on the SU-8 microdisks are readable. As an important metric for the potential application of such microscale QR codes, adhesion between the SU-8 microdevice and receivers is quantified by a variety of methods, such as spinning tests, shaking tests, and adhesion force measurements. All these tests illustrate promising results regarding strong adhesion on different receivers. Another study is the adhesion experiments in deionized (DI) water. Metal QR code patterned SU-8 samples are transferred onto a series of receivers and immersed in DI water to simulate harsh conditions for these SU-8 microdisks. After a certain amount of time, SU-8 samples are taken out of DI water and examined under an optical microscope to determine how long transferred SU-8 microdisks can remain attached when immersed in DI water.

Besides the metal QR code, SU-8 microdisks with thin-film temperature sensors are transferred and characterized to demonstrate the electrical functionality of the device. The high-precision transfer of the temperature sensor to the targeted position on the electrode-patterned receiver ensures that electrical contact is created between the temperature sensor and the electrodes. Subsequent electrical characterization of the temperature sensor records the resistance change at different temperatures. The as-obtained temperature-resistance curve shows a high degree of linearity. The extracted temperature coefficient of resistance (TCR) approximates the value obtained from the Pt100 reference sensor.

The aforementioned two functional microdevices are transferred on a small scale. In order to show the potential of our LIFT system for wafer-scale functional device array transfer, a customized g-code program is developed to enable the transfer of a  $40 \times 30$  microdisk array on a PDMS-coated 4-inch wafer. The influences of dwelling time and donor substrate rotation angle during the transfer are explored. After optimizing these two parameters, a  $40 \times 40$  array is transferred onto a wafer with a constant pitch of  $1000 \mu\text{m}$ . The second transfer demonstration with improved dwelling time control and rotational correction produces a

## 3.2 Transfer and characterization of SU-8 microdisks with metal QR code

---

higher yield rate, where the number of flipped SU-8 microdisks is significantly reduced. This means our approach is able to meet the high demand for the assembly of ultrathin microcomponents/microsystems in a fully automated fashion.

All experiments discussed previously are carried out by transferring SU-8 microdisks onto planar receivers. As a printing technique that enables contactless transfer, LIFT has the ability to transfer functional microdevices onto non-planar surfaces and make use of microscale building blocks to realize 3D assembly. This attribute makes it possible for LIFT to find potential applications in the rapidly developing field of flexible/stretchable electronics. Therefore, in this section, various transfer examples demonstrate transfers onto non-planar receivers. Such demonstrations strongly confirm that the LIFT technique does not rely on the physical/geometrical properties of the receivers.

### 3.2 Transfer and characterization of SU-8 microdisks with metal QR code

#### 3.2.1 Fabrication of donor and receiver

##### Fabrication of SU-8 microdisk with metal QR codes

The fabrication of functional SU-8-supported micro QR codes follows the same process mentioned in **Chapter 2 ("SU-8 functional device fabrication")**. To overcome the issue of closed-loop patterns, each pixel in the QR code is isolated by introducing microbridges. **Figure 3.1a** illustrates one design with such microbridges. The QR code consists of  $21 \times 21$  pixels. The pixel size is  $4 \mu\text{m}$ , and the bridge is  $1 \mu\text{m}$  wide, as indicated in the high-magnification image. Therefore, a  $3 \times 3 \mu\text{m}^2$  area will be patterned with metal, as indicated by the purple square. **Figure 3.1b** shows the corresponding SU-8 supported QR codes (Cr/Au, 5/50 nm) after the fabrication. The SU-8 microdisk has a diameter of  $130 \mu\text{m}$  and a thickness of  $50 \mu\text{m}$ .

##### PDMS, PI, Si, Cu, and glass receiver substrates preparation

PDMS receiver is fabricated by mixing the base and the curing agent (Syrgard 184) with a mass ratio of 10:1. The mixture is degassed in a vacuum desiccator and poured into a petri-dish, followed by a thermal curing process ( $80 \text{ }^\circ\text{C}$  for 2 h). After the curing, the PDMS is cut into the desired size and shape as the receiver. The PI receiver fabrication process follows the same steps discussed in the previous chapter ("**SU-8 donor preparation**"). The glass slide size is  $26 \times 26 \text{ mm}^2$ , and the PI thickness is  $3 \mu\text{m}$ . Si and glass receivers are rinsed in IPA and ultrasonically cleaned for 5 mins. They are then cleaned in deionized (DI) water and dried with a nitrogen gun. Thin film Cu (100 nm thick) is sputtered on Si substrate to serve as a Cu

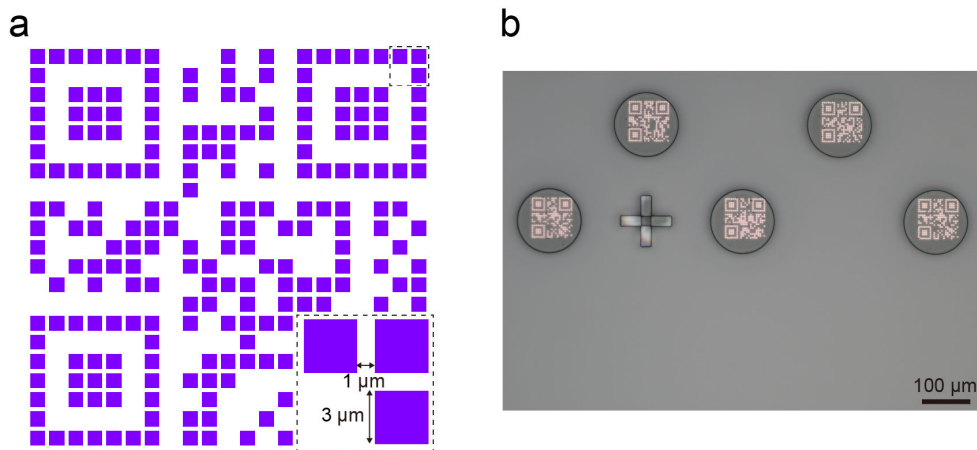


Figure 3.1: **Fabrication of SU-8-supported QR codes.** (a). One representative QR code design. The zoom-in image shows the detail of the bridge design. (b). A SU-8 microdisk array after the metallic QR code fabrication.

receiver.

#### 3.2.2 Transfer result

The LIFT experiment begins with transferring a  $130\ \mu\text{m}$  (diameter)  $\times$   $50\ \mu\text{m}$  SU-8 array on a PDMS receiver. Each SU-8 microdisk is transferred by several laser pulses ( $1.6\ \text{J}/\text{cm}^2$ , 3-6 shots), and in total, five SU-8 microdisks are transferred. After the transfer, both the structural integrity and QR readability can be verified from the optical image (**Figure 3.2**). The inset images show two SU-8 microdisks with metal QR codes. The information contained within the codes (Chinese characters "Laser-induced forward transfer" (left QR code) and "Microsystems laboratory" (right QR code)) is easily accessible by the QR scanner.

#### 3.2.3 Adhesion test

Adhesion between the transferred SU-8 microdisks and the receiver is of great importance for potential applications. For example, microscale anti-counterfeiting can be realized by transferring the SU-8 microdisk with a metal QR code (containing certain information like the serial number of a product) onto the desired surface. The feasibility of this application relies on the adhesion between the SU-8 and the surface. Since the SU-8 microdisk may experience extreme conditions such as collision (with objects, other people, etc.) and fall on the ground, the microdisk may be subject to high accelerations and be separated from the receiver. Quantitative analysis is required to determine the adhesion force between the two.

### 3.2 Transfer and characterization of SU-8 microdisks with metal QR code

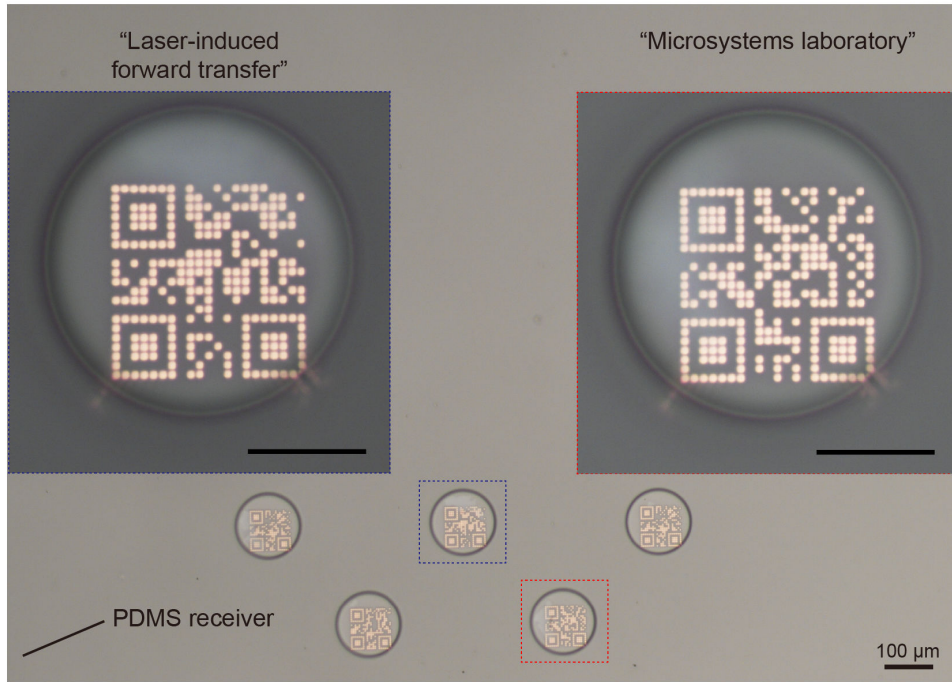


Figure 3.2: **Transfer result of five SU-8-supported QR codes.** An array of SU-8 microdisks with metal QR codes transferred on the PDMS receiver. The QR codes are readable after the transfer. Insets: two magnified images of SU-8 with the QR code, and the QR code contains Chinese characters for: “laser-induced forward transfer” and “microsystems laboratory”, respectively. Scale bar in the insets: 50 μm.

#### Rotation and shaking test

We first perform two adhesion experiments, as sketched out in **Figure 3.3**. Before testings, 130 μm (diameter) × 50 μm thick SU-8 microdisks with metal QR code (1.6 J/cm<sup>2</sup>, 3-6 pulses) are first transferred onto different receivers (Si, PDMS, glass, and PI) and then vacuum annealed (120 °C, 2 h). The four receivers with transferred SU-8 samples are attached to the edge of a 4-inch wafer with adhesive tape. This ensures that the distance between the SU-8 and the wafer center is around 50 mm. Then the wafer is placed on a spin-coater and centrifuged at various angular velocities (up to 5000 rpm) for 30 s. As a result, the centrifugal force is obtained by the following equation (**Equation 3.1**):

$$F = m\omega^2 r \quad (3.1)$$

where  $F$ ,  $m$ ,  $\omega$ , and  $r$  represent the centrifugal force, the mass of the SU-8 microdisk, angular velocity (rpm), and radius, respectively. The maximum force exerted on the SU-8 microdisks is calculated to be around 12 μN. **Figure 3.4b** shows the SU-8 microdisk after the rotation test.

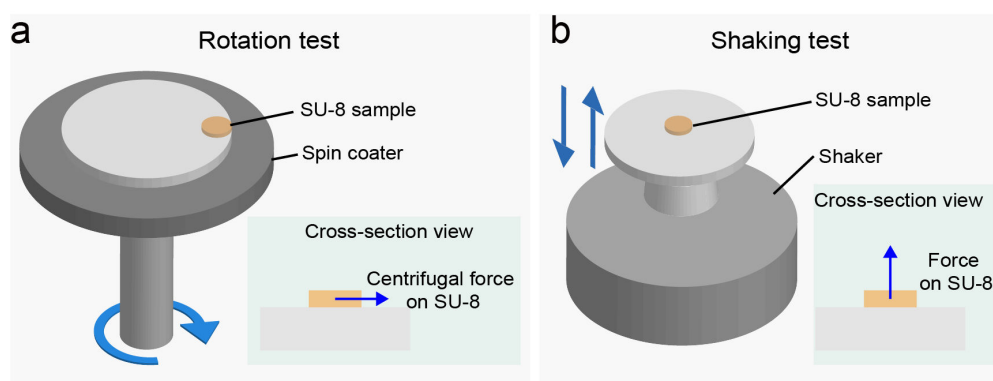


Figure 3.3: **Schematic illustrations of the two adhesion tests.** (a). Simple sketch of the rotation test. The angular speed increases from 1000 to 5000 rpm. (b). Sketch of the shaking test. The acceleration is up to 50 g.

Compared with the image showing the SU-8 microdisk after the transfer (**Figure 3.4a**), the SU-8 microdisk still stays on the Si receiver, proving strong adhesion between the SU-8 and the Si receiver under high centrifugal acceleration.

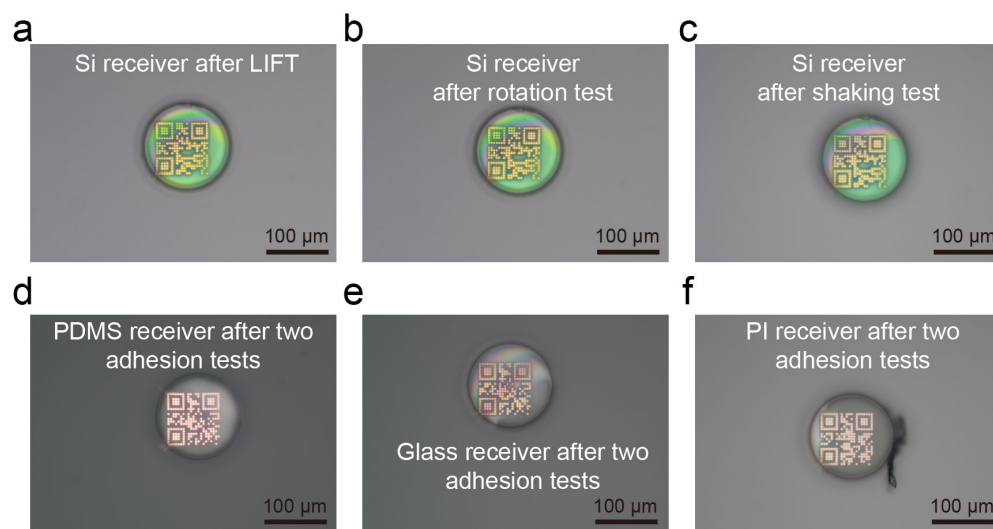


Figure 3.4: **Experimental results of the two adhesion tests.** (a-c). Optical images showing the SU-8 microdisk after LIFT, rotation test and shaking test on the Si receiver, respectively. (d-f). Optical images of SU-8 samples after the two adhesion tests corresponding to different receivers. (d): SU-8 on PDMS. (e): SU-8 on glass. (f): SU-8 on PI.

After the rotation test, we employ a vibration exciter to apply vertical acceleration on SU-8 samples. Receivers with SU-8 samples are glued onto an acrylic plate mounted on the shaker platform. The SU-8 microdisk samples are tested in two modes: the SU-8 facing up with an acceleration of 50 g for 30 s and the SU-8 facing down with an acceleration of 30 g for 30 s.



### 3.2 Transfer and characterization of SU-8 microdisks with metal QR code

All receivers are then checked by an optical microscope. As clearly seen in **Figure 3.4c**, the transferred SU-8 microdisks still adhere to the Si receiver after the shaking test. Similar results for other receivers can be found in **Figure 3.4d-f**, which further confirms the strong adhesion between the transferred SU-8 microdisks and the other three receivers (PDMS, glass, and PI).

#### Adhesion quantification by a micro-mechanical test system

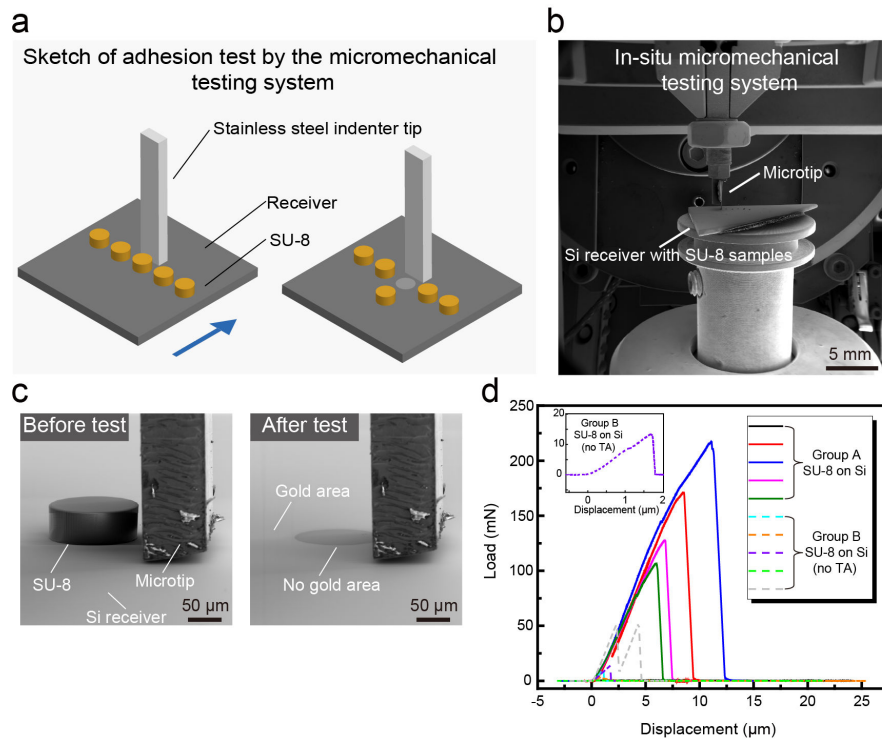


**Figure 3.5: Adhesion test of transferred SU-8 microdisks onto Si receiver.** (a). Simplified sketch of the micromechanical testing system. (b). SEM image of the in-situ micromechanical testing system with SU-8 samples on Si receiver. (c). SEM images of one SU-8 microdisk before and after the adhesion test. This sample corresponds to the purple dashed curve shown in (d). (d). Displacement-load curves for all SU-8 samples on Si receiver. Group A denotes SU-8 samples with vacuum thermal annealing (TA) at 120 °C for 2h and Group B represents SU-8 samples without TA treatment.

In order to further quantify the adhesion strength between the SU-8 microdisk and different receivers, micropillar lateral force tests are performed. **Figure 3.5a** shows a simplified view of the measurement process. The receiver moves laterally, and the SU-8 samples on the receiver approach a stainless steel microtip (tip width of 300  $\mu\text{m}$ ). Upon contacting the fixed microtip, the tip exerts a lateral force on the SU-8 sample, and the displacement-load curve of the SU-8 microdisk sample will be recorded. Four different types of receivers (Si, glass, Cu, and PDMS) are prepared for the test. On each receiver, 5 SU-8 microdisks are transferred by LIFT (1.6

J/cm<sup>2</sup>, 3-6 shots) and thermally annealed in a vacuum (120 °C, 2 h). The thermally annealed samples are categorized into Group A. A control group (Group B) is also prepared to investigate whether the annealing process influences the adhesion, where SU-8 microdisks are transferred to the four receivers by LIFT without further treatment.

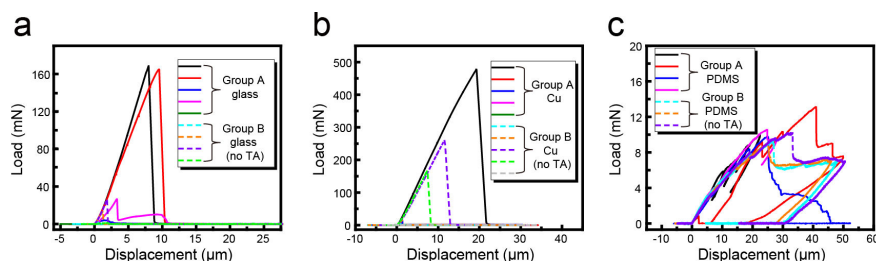


**Figure 3.6: Displacement-load curves for SU-8 samples on glass, Cu and PDMS receivers. (a-c).** Curves for SU-8 on glass, Cu, and PDMS receivers, respectively. Group A denotes SU-8 samples with vacuum thermal annealing (TA) at 120 °C for 2h, and Group B represents SU-8 samples with no TA treatment.

**Figure 3.5b** displays the measurement system with a Si receiver sample mounted on the holder. **Figure 3.5c** presents two SEM photographs showing a representative adhesion test result. The SU-8 microdisk separates from the Si substrate upon reaching the maximum adhesion force, and the region without gold indicates the location of the microdisk in the right SEM image. In **Figure 3.5d**, all displacement-load curves quantify the adhesion force of the SU-8 microdisk on the Si receiver. The first conclusion that can be reached from all these curves is that the shear load increases rapidly to a maximum value (as can be seen from curves corresponding to other receivers in **Figure 3.6**). The slope in the displacement-load curve can be tentatively ascribed to the fact that the microtip is compliant and is deflected by a given load. When the force reaches a maximum value corresponding to the adhesion force between the SU-8 microdisk and the receiver, the SU-8 microdisk either separates from the receiver or slides on it. Sliding examples are provided in **Figure 3.7**, and the sliding distances are measured accordingly. As a result, the shear load either drops to zero or decreases to a stable value to maintain the sliding of the SU-8 microdisk on the receiver surface.

Another finding is that the adhesion force is larger after TA because the TA treatment increases the adhesion between the SU-8 and the receiver. Nevertheless, in both cases (with/without TA), all of the measured values are larger than those obtained from the rotation test (around 12  $\mu$ N when the rotation speed is 5000 rpm). Another interesting phenomenon is displayed in **Figure 3.6c**, where the curves seem irregular compared with **Figure 3.5d** and **Figure 3.6a-b**. This results from the fact that the PDMS receiver is soft, and it can deform while the load applies to the SU-8 microdisk. The crack formation also appears on the PDMS with the applied load, as marked in **Figure 3.7f**. All of these factors contribute to the repeated increase/decrease of the shear load value and lead to inaccurate adhesion force measurement. Therefore, the

### 3.2 Transfer and characterization of SU-8 microdisks with metal QR code

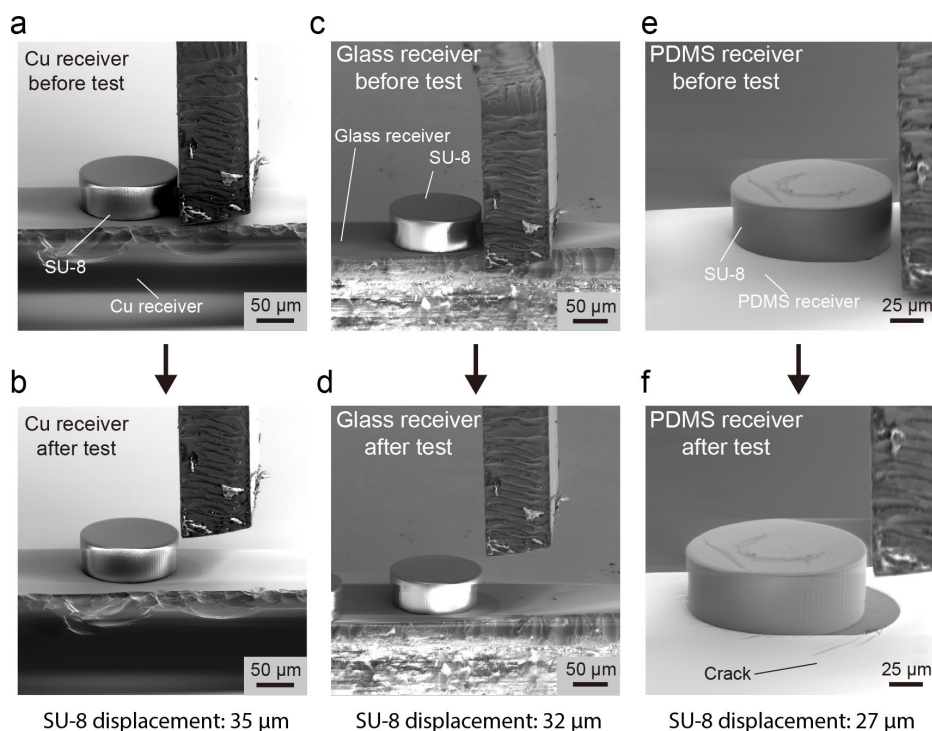


Figure 3.7: **SEM images of SU-8 microdisk before and after the adhesion test on different receivers.** (a-b). Adhesion test result on a Cu receiver. Upon the application of a lateral load, the SU-8 slides on the glass surface, leaving a trace as shown in (b). (c-d). Adhesion test results on a glass receiver. A similar trace can be found in (d). (e-f). Adhesion test results on a PDMS receiver. In addition to the trace left by the SU-8 microdisk, cracks are observed on the PDMS after the test.

maximum load from **Figure 3.6c** is much smaller than those from the other three receivers. However, even if the measured load value is relatively small, SU-8 microdisks remain on the PDMS receiver after the adhesion tests, thus proving good adhesion between the transferred SU-8 and the PDMS receiver.

#### Adhesion test in DI water

The aforementioned rotation and shaking tests have proven that transferred SU-8 microdisks can survive in high acceleration conditions. To examine whether the transferred QR code patterned SU-8 microdisks can survive under other harsh conditions, like rinsing in water, we conduct the adhesion test by placing different receivers with transferred SU-8 microdisks into DI water and evaluate the survival of such microdisks.

Similar to the two groups of SU-8 microdisk samples prepared in the previous section, we transfer SU-8 microdisks with metal QR codes onto four receivers and categorize them into

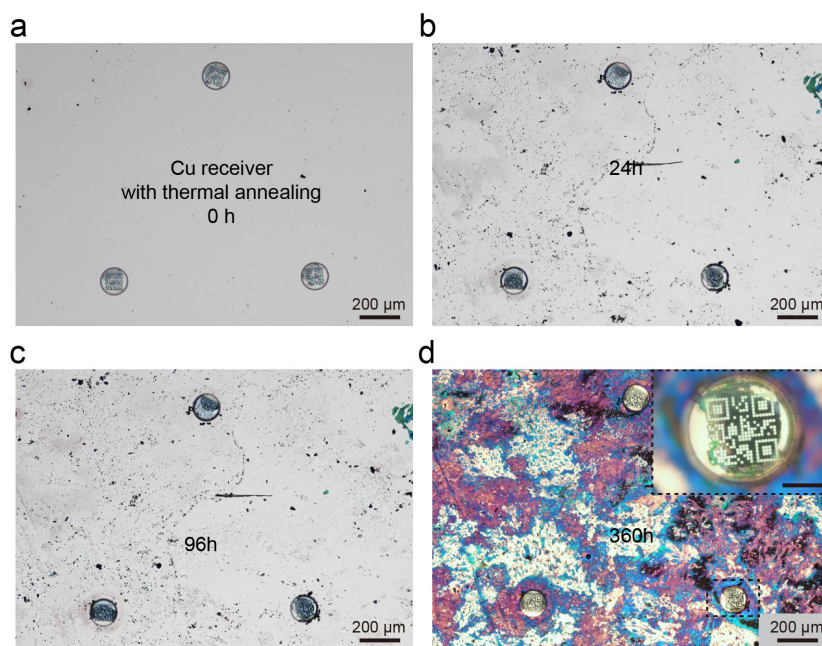


Figure 3.8: **Adhesion test for SU-8 microdisks on Cu receiver after thermal annealing in DI water.** (a). Image of three transferred SU-8 microdisks after thermal annealing. (b-d). Images of the SU-8 microdisks after being immersed in DI water for 24, 96, and 360 h. The color change is due to the corrosion of Cu in DI water after 360 h. The magnified image in d displays that the SU-8 microdisk still adheres to the Cu receiver. Scale bar in the inset: 50 μm.

two groups (Group A and Group B). After the thermal annealing for Group A (the same thermal annealing process as discussed in the previous section), SU-8 samples in Group A and Group B are immersed in DI water. After a specific time interval (8, 24, 48, 96, 144, and 360 h), all the receiver samples are placed under a fume hood for drying. Then SU-8 microdisk samples are examined under an optical microscope.

**Figure 3.8** to **Figure 3.11** summarize the adhesion tests of SU-8 microdisk samples in Group A in DI water. For all these four figures, the first images represent the SU-8 samples after thermal annealing, as indicated by 0 h. From **Figure 3.8b** to **3.8c**, it can be observed that the Cu receiver is contaminated with impurities (probably the ink from the marker pen), and it is corroded after immersing in DI water for 360 h. Even if so, the transferred three SU-8 microdisks with the metallic QR code still adhere to the receiver. A high magnification image displayed in **Figure 3.8d** demonstrates that the QR code on the SU-8 is still readable by a QR code scanner (the QR code contains the text of "laser-induced forward transfer"). This confirms that even under harsh conditions (e.g., immersing in DI water), the functional SU-8 microdisk with a QR code can survive and maintain its readability. In **Figure 3.9**, it is found that all three SU-8 microdisks separate from the glass receiver after 8 h, indicating the SU-8 microdisk is less resistant to DI water. Similar results are found in **Figure 3.10** and **Figure 3.11**,

### 3.2 Transfer and characterization of SU-8 microdisks with metal QR code

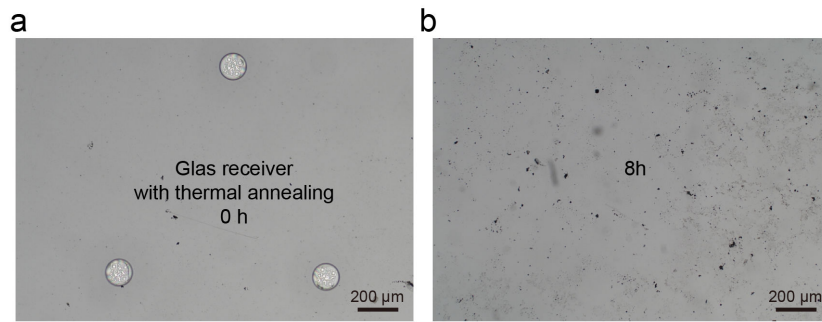


Figure 3.9: **Adhesion test for SU-8 microdisks on glass receiver after thermal annealing in DI water.** (a). Image of three transferred SU-8 microdisks after thermal annealing. (b). Image of the glass receiver immersed in DI water for 8 h. No SU-8 microdisks are observed on the receiver.

Table 3.1: **Summary of the SU-8 microdisk adhesion test results on different receivers in DI water**

| Receiver type | TA treatment | SU-8 attachment time | QR code readability |
|---------------|--------------|----------------------|---------------------|
| Cu            | ✓            | 360 h                | Readable            |
| Cu            | ×            | 360 h                | Readable            |
| Glass         | ✓            | < 8 h                | Readable            |
| Glass         | ×            | 24 h                 | Readable            |
| Si            | ✓            | 96 h                 | Readable            |
| Si            | ×            | 96 h                 | Readable            |
| PDMS          | ✓            | 360 h                | Readable            |
| PDMS          | ×            | 360 h                | Readable            |

✓ and × in the table denote with and without TA treatment, respectively.

where the SU-8 samples can survive in DI water for at least 96 h (Si receiver) and 360 h (PDMS receiver), respectively.

In addition to the analysis of the results in Group A, we examine the results obtained from the adhesion tests of Group B, where all of the SU-8 samples are transferred by LIFT without further treatment. The optical images shown in **appendix Figure A.28** (Cu receiver) look similar to **Figure 3.8**. All three SU-8 microdisks survive 360 h in the DI water, and the magnified image in **appendix Figure A.28d** displays the QR code on the SU-8 microdisk. The text of "Microsystems Laboratory" is easily accessible via a QR scanner.

The SU-8 microdisk samples on glass and Si receivers are then examined. From **appendix Figure A.29a-b**, it can be seen that one SU-8 microdisk has separated from the glass receiver surface after 8 h, and the remaining two microdisks also change their positions on the receiver. After 24 h, the two SU-8 microdisks stay on the receiver, but their positions change further. Notwithstanding the translocation of the receivers, the high-magnification image in **appendix**

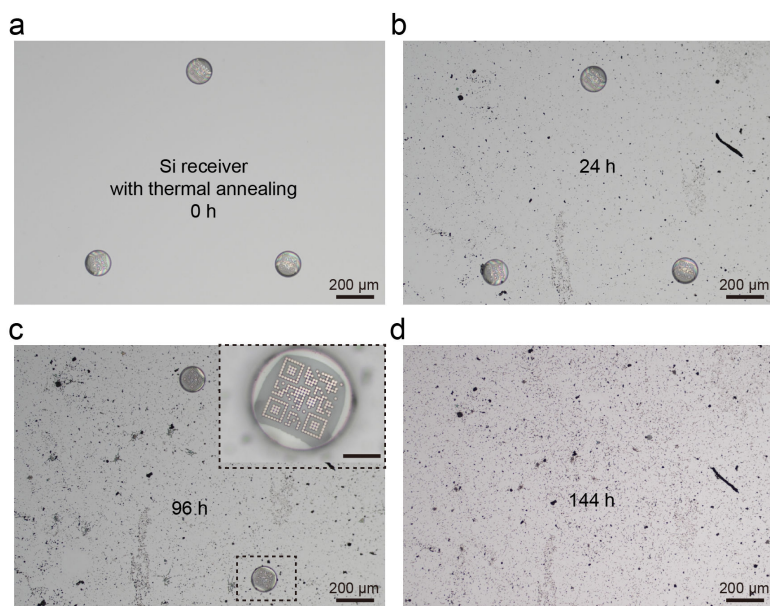


Figure 3.10: **Adhesion test for SU-8 microdisks on Si receiver after thermal annealing in DI water.** (a). Image of three transferred SU-8 microdisks after thermal annealing. (b-d). Images of the SU-8 microdisks after being immersed in DI water for 24, 96, and 144 h. Scale bar in the inset: 50 μm.

**Figure A.29c** still confirms that the QR code remains readable. Despite such position shifts also being observed in **appendix Figure A.30**, the three SU-8 microdisks still adhere to the Si receiver after 96 h. The last sample features the SU-8 microdisks on a PDMS receiver without the thermal annealing treatment (**appendix Figure A.31**). After 360 h, the four SU-8 microdisks are still present on the receiver, and no obvious movement is observed for these microdisks.

From **Figure 3.8-3.11** (Group A) to **appendix Figure A.28-A.31** (Group B), it can be concluded that for different types of receivers, transferred SU-8 microdisks tend to have different attachment capabilities to the receivers in DI water. Furthermore, the thermal annealing process does not influence the adhesion of microdisks in DI water. **Table 3.1** summarizes the adhesion tests for the direct comparison of the attachment time of SU-8 microdisks to different receivers and also for the verification of the QR code readability.

From all of the images and **Table 3.1**, it can be concluded that SU-8 microdisks transferred to Cu and PDMS receivers can stay on the receivers for at least 360 h. The reason for such a phenomenon on the PDMS receiver can be inferred from the fact that the PDMS is adhesive, and transferred SU-8 microdisks can adhere firmly to the PDMS surface. A similar phenomenon for the Cu receiver can be tentatively ascribed to the corrosion of Cu in DI water after a long period of time, but this requires further investigation.

In summary, all of these LIFT experiments of functional SU-8 microdisks with metal QR codes,

### 3.3 Transfer and characterization of SU-8 microdisks with temperature sensor

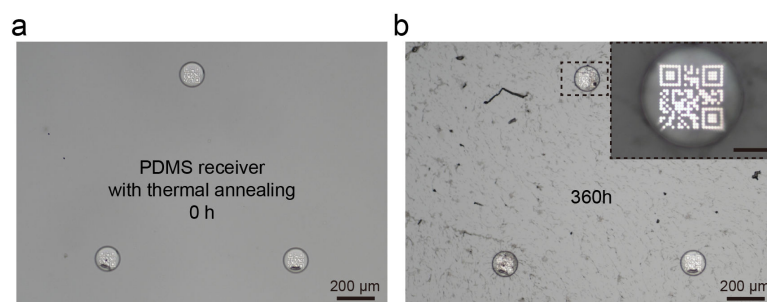


Figure 3.11: **Adhesion test for SU-8 microdisks on PDMS receiver after thermal annealing in DI water.** (a). Image of three transferred SU-8 microdisks after thermal annealing. (b). Image of the SU-8 microdisks after being immersed in DI water for 360 h. The magnified image in **b** proves that the SU-8 adheres to the PDMS receiver and the QR code is still readable. Scale bar in the inset: 50  $\mu\text{m}$ .

substantiate the idea of making use of the transferred SU-8 microdisks with QR codes as a novel method for potential microscale anti-counterfeiting or QR code authentication.

### 3.3 Transfer and characterization of SU-8 microdisks with temperature sensor

In the previous section, we investigate the transfer of SU-8 microdisks with optical functionality (metal QR code). The post-transfer evaluation, together with the adhesion tests, proves the feasibility of distributing SU-8 microdisks to different surfaces while maintaining the readability of the QR code. In this section, we take the research one step further, explore the transfer of the SU-8-supported temperature sensors and assess the electrical functionality. SU-8-supported temperature sensors are transferred onto receivers (with prepatterned electrodes), and electrical contact is created between the contact pads of the temperature sensor and receiver electrodes. The electrical performance of the temperature sensor is evaluated by conducting the temperature-resistance measurement and calculating the TCR of the temperature sensor.

#### 3.3.1 Fabrication and characterization

##### Fabrication of SU-8 microdisk supported temperature sensor

The fabrication of functional SU-8-supported temperature sensors follows the same process outlined in Chapter 2 ("**SU-8 functional device fabrication**"). As shown in **Figure 3.12a**, the SU-8 has a diameter of 100  $\mu\text{m}$  and a thickness of 50  $\mu\text{m}$ . The thin-film temperature sensor on top of the SU-8 microdisk is made of Cr/Pt (5/130 nm) and composed of a meander structure

(width: 1.5  $\mu\text{m}$ ) in the center and two large contact pads at two ends. **Figure 3.12a** shows one array of such microdevices after fabrication, and the close-up image in **Figure 3.12b** shows more details of the meander structure.

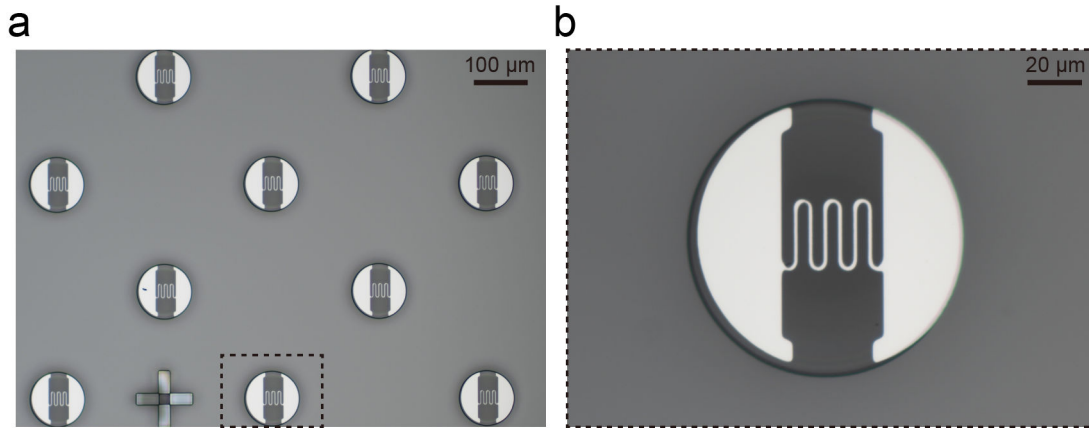


Figure 3.12: **SU-8-supported temperature sensor after fabrication.** (a). Image of an array of SU-8 supported temperature sensors (b). Magnified image of one temperature sensor.

#### Fabrication of electrode-patterned Si/SiO<sub>2</sub> receiver

A Si/SiO<sub>2</sub> wafer (SiO<sub>2</sub> thickness: 500 nm) is first coated with a LOR 5A (Micro Resist Technology)/AZ 1512 HS (MicroChemicals GmbH) double layer (0.7/1.5  $\mu\text{m}$ ). The photoresist is then patterned by a laser writer (MLA 150). After developing the photoresist, a thin layer of Cr/Au (5/150 nm) is deposited on the wafer by sputtering. Then the wafer is placed in Remover 1165 for lift-off (48 h). After the lift-off process, the wafer is rinsed in IPA and dried by a nitrogen gun. Finally, the wafer is cleaved to the desired size for LIFT experiments. The as-fabricated electrodes can be seen in **Figure 3.13a-b**.

#### Temperature sensor measurement

The temperature sensor measurement setup consists of a hotplate, a microscope, a camera and computer, a multimeter, a source meter, a thermocouple, a Pt100 sensor and one micro-probe station, as illustrated in **Figure 3.13c**. Two needles of the micro-prober system contact the targeted receiver electrodes. To guarantee the temperature condition for the temperature sensor, the Pt100 sensor and the thermocouple are the same. The Pt100 sensor and the thermocouple are also placed on Si/SiO<sub>2</sub> substrates. The temperature varies from room temperature to 100  $^{\circ}\text{C}$ , with an increment of 5  $^{\circ}\text{C}$  for each step. At each temperature, the Pt100 sensor and SU-8 temperature sensor resistances are recorded when the temperature readout of the thermocouple has been stabilized for 20 s.



### 3.3 Transfer and characterization of SU-8 microdisks with temperature sensor

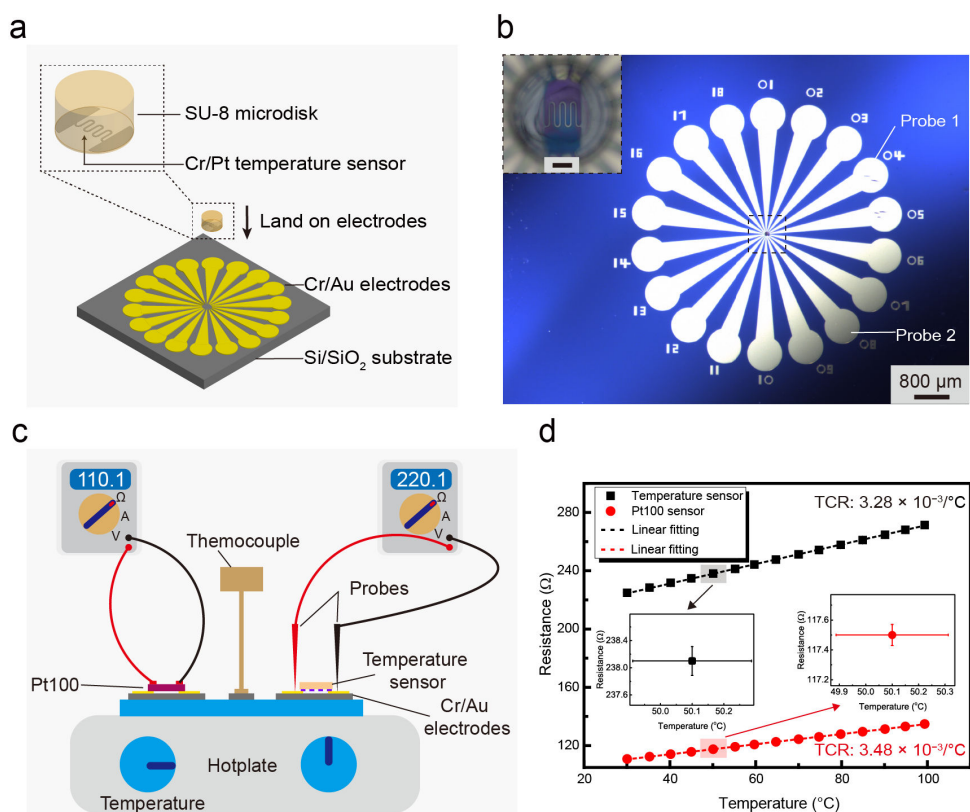


Figure 3.13: **SU-8-supported temperature sensor transfer and characterization.** (a). Exploded view of a temperature sensor transferred onto radial-electrode-patterned Si/SiO<sub>2</sub> receiver. (b). Optical image of one transferred temperature sensor onto the electrodes. The SU-8 microdisk size is 100 μm in diameter and 50 μm in thickness. Two probes are in contact with electrodes 04 and 08 when measuring the resistance. Inset: magnified image showing the meander structure of the temperature sensor. Scale bar: 20 μm. (c). Sketch of the temperature sensor characterization system. (d). Measured temperature-resistance curves of the temperature sensor and the Pt100 reference sensor. The TCRs of the temperature sensor and Pt100 sensor are extracted from the curves and shown in the plot.

#### 3.3.2 Transfer result

We utilize LIFT ( $1.6 \text{ J/cm}^2$ , 2 shots) to transfer SU-8-supported temperature sensors and conduct the post-transfer performance assessment (Figure 3.13). The temperature sensor consisting of Cr/Pt meander microstructures (exploded-view displayed in Figure 3.13a) is transferred onto radial Cr/Au electrodes. As seen from Figure 3.13b, combining the radial electrode design with multiple electrodes increases the likelihood of the temperature sensor contacting the Cr/Au electrodes underneath electrically. Even if small displacements and large rotations can be introduced during the transfer process, such a design guarantees successful electrical contact between the transferred temperature sensor and receiver electrodes. The top-left inset image proves that the transfer precision of the temperature sensor is high, where

the meander structure of the temperature sensor is located in the center of these electrodes.

### 3.3.3 Temperature sensor characterization

After transfer, the temperature sensor is thermally annealed (200 °C, 2h) considering the degradation temperature of SU-8 is 380 °C [189]. The SU-8 temperature sensor, together with a commercial Pt100 sensor and a thermocouple, is placed on the same hotplate for the electrical measurement. The Pt 100 sensor is a reference temperature sensor, and the thermocouple monitors the temperature. **Figure 3.13d** summarizes the measurement results of the SU-8-supported temperature sensor and the reference Pt100 sensor. For each sensor (both the SU-8 temperature sensor and Pt100 sensor), five measurements are conducted to ensure repeatability of measurement. The scattered dots, in combination with the trend line, confirm that the resistance of the temperature sensor shows a high degree of linearity as a function of temperature. The temperature-resistance measurement is also conducted before the annealing process and the measurement result is provided in **Figure 3.14**. Similar linearity is also observed from this figure, thus proving the transfer of the SU-8 temperature sensor by LIFT enables good electrical contact between the sensor and the receiver electrodes, even without thermal annealing.

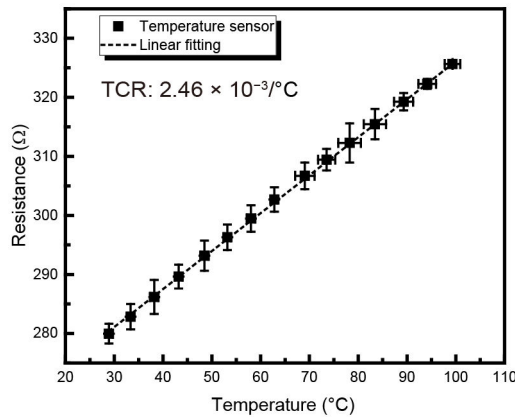


Figure 3.14: **Measured temperature-resistance curve of the SU-8 supported temperature sensor before annealing.** The TCR of the temperature sensor is extracted from the curves and shown in the plot.

The error bar in the two inset images in **Figure 3.13d** shows the data extracted from the five measurements, and the small magnitudes of the standard deviation indicate slight variations of resistance among the five measurements. This further demonstrates the excellent repeatability of the temperature sensor characterization. Furthermore, we obtain the TCR of the temperature sensor and Pt100 sensor by the following equation:

$$TCR = (R_2 - R_1) / (R_1 \times (T_2 - T_1)) \quad (3.2)$$

### 3.3 Transfer and characterization of SU-8 microdisks with temperature sensor

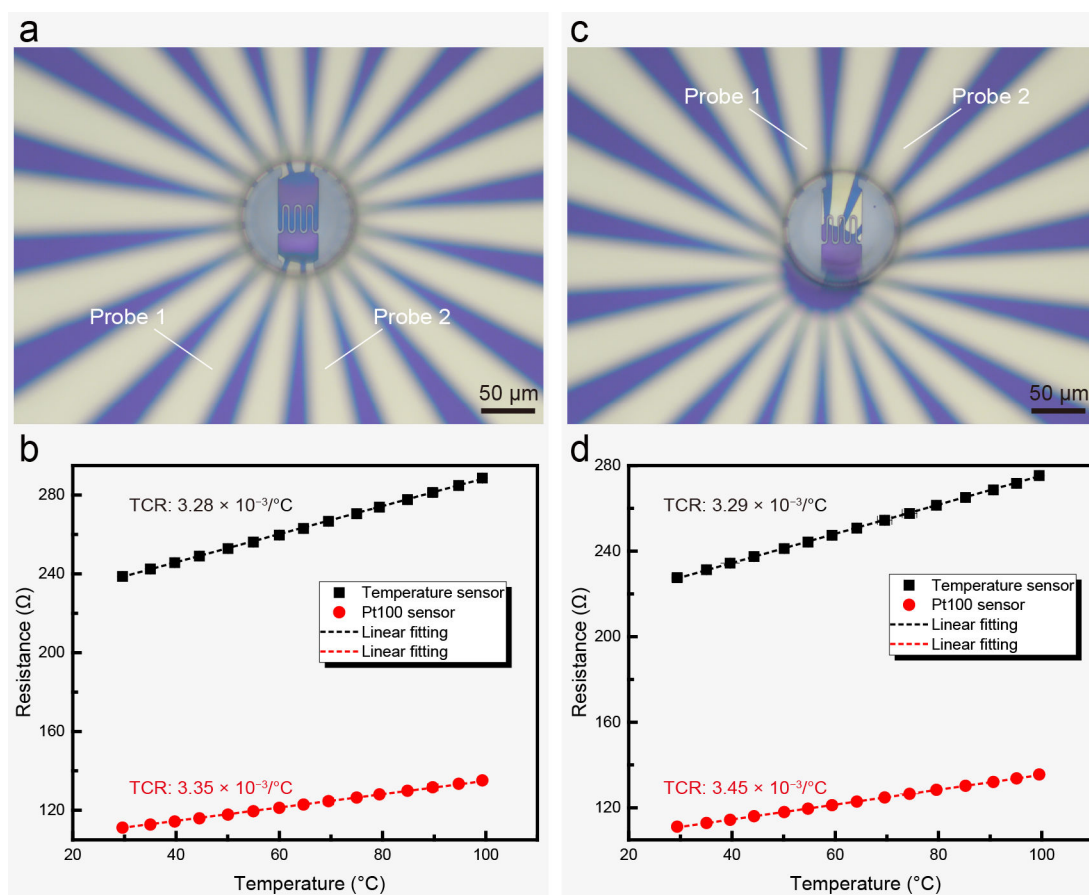


Figure 3.15: **Characterization of two additional transferred SU-8-supported temperature sensors. (a-b and c-d).** Optical image and the corresponding temperature-resistance curves for two temperature sensors. The Pt100 sensor is used as a reference. The TCR of the temperature sensor and Pt100 sensor are extracted from the curves and shown in the plot.

where  $R_2$  and  $R_1$  represent the resistances of the temperature sensor at the temperature of  $T_2$  and  $T_1$ , respectively. The TCR values for the temperature sensor (after annealing) and Pt100 sensor are  $3.28 \times 10^{-3}/^{\circ}\text{C}$  and  $3.48 \times 10^{-3}/^{\circ}\text{C}$ , respectively. In addition, we obtain the TCR value of the temperature sensor before thermal annealing, which is  $2.46 \times 10^{-3}/^{\circ}\text{C}$ . Such difference in the TCR values of the temperature sensor before/after the annealing process is because thermal annealing produces big-size grains and reduces the resistivity. These measured TCR values are typical for thin-film Pt temperature sensors [201,202]. Moreover, we perform the temperature-resistance measurement for an additional two temperature sensors transferred by LIFT, with the corresponding optical images shown in **Figure 3.15**. High linearity and excellent repeatability are revealed in **Figure 3.15b** and **3.15d**, and the TCR values of the SU-8 temperature sensor extracted from **Figure 3.15b** and **3.15d** are  $3.28 \times 10^{-3}/^{\circ}\text{C}$  and  $3.29 \times 10^{-3}/^{\circ}\text{C}$ , respectively, which are close to the TCR value obtained from **Figure 3.13d**.

It should be noted that for the two types of SU-8-supported microdevices (QR code and temperature sensor), the functional metallic layer is not influenced by the transfer process, as proven by their post-transfer functionality evaluation. This can be explained by the following three hypotheses:

1. The first hypothesis is that the PI film used in the experiments is 5  $\mu\text{m}$  thick while the absorption depth of the laser by the PI film is 0.5  $\mu\text{m}$  <sup>[173]</sup>. The shallow absorption depth guarantees the rest of the PI film remains intact after the laser ablation and the transfer process is based on the PI volume expansion, and no thermal stress is exerted on the SU-8 microdisk <sup>[90]</sup>.
2. The second hypothesis is that the SU-8 is thick enough (50  $\mu\text{m}$ ) and has a large flexural rigidity ( $5 \times 10^{-5}$  N·m). Compared to the 5  $\mu\text{m}$  thick PI used for the transfer, which has a flexural rigidity of  $2.4 \times 10^{-8}$  N·m, the SU-8 can be viewed as a rigid microdisk <sup>[174,175]</sup>. Therefore, the mechanical stress caused by the peel-off process of the SU-8 cannot damage the metallic structure and impact the functionality of the microdevices.
3. The last hypothesis is that the landing velocity of the SU-8-supported microdevices guarantees the functionality of the device is well-maintained. Other research has proven that the landing velocity of microcomponents transferred by LIFT averages less than 30 m/s <sup>[157,158,165]</sup>. In our case, we can estimate the velocity of the transferred SU-8-supported microdevices by using the parameters in one research <sup>[92]</sup>.

As mentioned in **Chapter 1**, in one research studying the PI blister, they concluded when the laser fluence reaches  $3 \text{ J/cm}^2$ , only 10 % laser energy is used for PI blister volume expansion. In our case, since the SU-8-supported microdevice is present, it means the 10 % laser energy will be consumed by the PI blister expansion, the peeling-off of SU-8 from the donor substrate and the forward motion of the SU-8 towards the receiver. An estimation of the landing velocity of SU-8 can be made when considering an extreme condition: the total 10 % laser energy (in our case,  $3.2 \text{ J/cm}^2$  laser fluence corresponds to  $10 \mu\text{J}$  laser energy) is converted into the kinetic energy of SU-8. Since the gap distance for such transfer is relatively small (less than 20  $\mu\text{m}$ ), air friction can be ignored. The calculated velocity of the SU-8 reaches 65 m/s. In reality, this 10 % laser energy will only be partially converted to the kinetic energy of the SU-8. For example, considering only 10 or 50 % of the rest of the laser energy is used for the forward motion of the SU-8, the calculated velocity is 21 and 47 m/s, respectively. These two values are close to those obtained from other research (less than 30 m/s) and if the air friction is taken into account, the calculated velocity is even smaller. These landing velocities prevent a violent impact of the SU-8 on the receiver and maintain the functionality of the SU-8-supported microdevices.

It is noteworthy that one can further decrease the influence of the landing velocity of SU-8-supported microdevices by patterning electrodes on the receiver using viscous conductive

liquids such as die-attach adhesive <sup>[164, 166]</sup> and conductive epoxy <sup>[159]</sup>. The viscous conductive liquids serve as a "cushion" and the microdevice lands on these electrodes with less impact.

### 3.4 Large-scale transfer of SU-8 microdisks

The previous two demonstrations illustrate the capability of the LIFT setup for functional microdevice transfer. Nevertheless, in each case, only a single or a few microdevices are transferred to receivers, with the LIFT experiment performed manually. In order to explore the potential of the LIFT system to complete the scalable transfer of functional SU-8 microdevices, we utilize the g-code programming method to control the movement of the donor and receiver stage in an automated fashion. To simplify the experiment, we utilize SU-8 microdisks as test samples, but such transfer can be extended to functional microdevices, as shown in the previous two sections (QR code and temperature sensor).

#### 3.4.1 Fabrication of SU-8 microdisks and PDMS receivers

The fabrication of SU-8 microdisks follows the same process mentioned in Chapter 2 ("SU-8 donor preparation"). SU-8 microdisks are patterned in high density. **Figure 3.16a** presents the smallest SU-8 microdisk area, consisting of a  $10 \times 10$  array with a pitch distance of  $200 \mu\text{m}$  (**Figure 3.16b**). Each SU-8 has a diameter of  $130 \mu\text{m}$  and a thickness of  $50 \mu\text{m}$ . In this case, the inner edge-to-edge distance of two consecutive SU-8 microdisks is  $70 \mu\text{m}$ . This distance can be further decreased to achieve higher SU-8 array density.

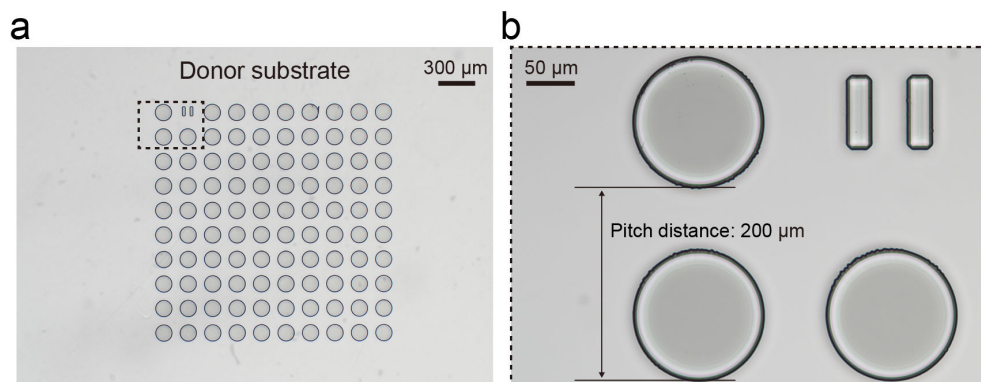


Figure 3.16: **Dense SU-8 microdisk array for large-scale transfer.** (a). One array consisting of  $10 \times 10$  SU-8 microdisks. (b). High-magnification image of the array. The pitch distance is  $200 \mu\text{m}$ .

The receiver substrate is prepared by coating a thin layer of PDMS onto a 4-inch Si wafer. The rotation speed for the coating is set to 1900 rpm. After placing the PDMS-coated wafer in the

ambient environment for 20 mins, the wafer is cured in an oven at 80 °C for 2 h.

### 3.4.2 Transfer strategy

The large-scale transfer of SU-8 microdisks is realized by controlling the movement of the donor and receiver substrate using the g-code programming. To prove that our LIFT is capable of adjusting the pitch distance according to our need, we increase the pitch distance of the SU-8 microdisks on the donor substrate (200  $\mu\text{m}$ ) to 1000  $\mu\text{m}$  on the PDMS receiver. The programmed transfer is executed by running a g-code file, which is provided in **appendix Figure A.32**. The commands in the g-code file control the movement of two stages (the donor and receiver stage) and the operation of the laser. Different parameters can be fine-tuned in the file, such as laser energy, laser focus, X and Y coordinates, dwelling time of the stages, etc.

The transfer strategy is shown in a simple schematic illustration in **Figure 3.17**. (**Figure 3.17a**) sketches one array on the donor substrate, as detailed in the "**Fabrication of SU-8 microdisks and PDMS receivers**" part. The first 10 SU-8 microdisks in the green dashed rectangle are transferred (first column with the green label "1", from the bottom to the top of the array) to the corresponding area on the receiver (green dashed rectangle in **Figure 3.17b**). The donor stage then moves to the bottom of the second column, repeating the transfer process. After transferring the first four columns (corresponding to the first row on the receiver wafer shown in **Figure 3.17b**), the receiver stage moves back to the initial position with a shift in the Y-direction. The transfer of SU-8 microdisks on the fifth column then commences. The donor stage can move to a new SU-8 array area after transferring all the SU-8 microdisks. Multiple SU-8 microdisk array areas are required to fulfill the mass transfer process.

### 3.4.3 Transfer result

Based on the g-code programming, a  $40 \times 30$  SU-8 array is transferred ( $3.2 \text{ J/cm}^2$ , 1 shot) onto the PDMS-coated 4-inch wafer, covering an area of  $40 \times 30 \text{ mm}^2$ . In comparison, the same 1200 SU-8 microdisks occupy an area of approximately  $48 \text{ mm}^2$  on the donor substrate, which is only one-twenty-fifth of that on the receiver. The ratio (one-twenty-fifth) can be further decreased/increased by tuning the pitch distance of SU-8 microdisks on the donor/receiver.

**Figure 3.18a** displays an image of the 4-inch receiver with the transferred SU-8 array. The  $40 \times 30$  arrays can be classified into three categories: the region without a SU-8 microdisk, the region with SU-8 microdisks flipped on their side surfaces and regions with unflipped microdisks. Representative images of these three regions are displayed from **Figure 3.18b** to **3.18d** (Region 1 to Region 3), respectively. In **Figure 3.18b**, twelve SU-8 microdisks are aligned on the PDMS receiver, forming  $4 \times 3$  arrays. In **Figure 3.18c**, four SU-8 microdisks in

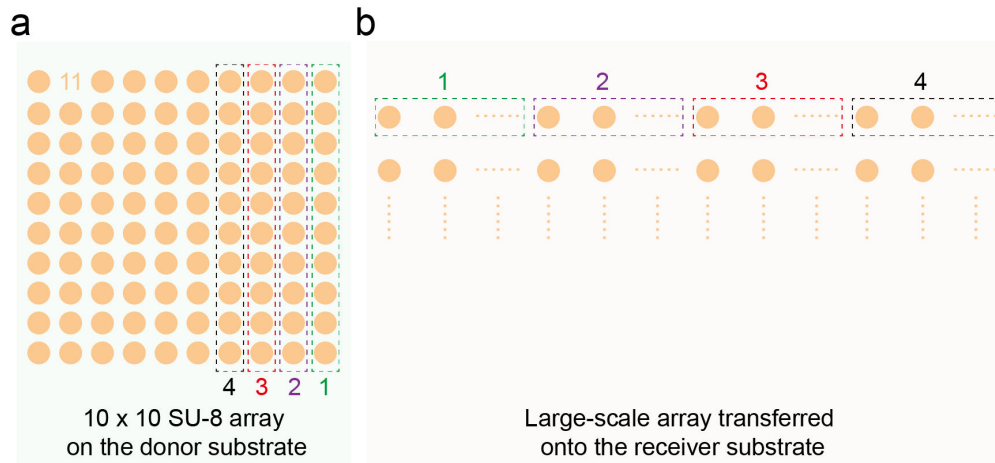


Figure 3.17: **Transfer strategy of SU-8 microdisks from donor to receiver (a).** Illustration of the array on the donor. The four numbers with corresponding dashed rectangles indicate the transfer sequence. **(b).** Illustration of SU-8 microdisks transferred onto the receiver. The numbers correspond to those shown in **a**, and the pitch distance can be fine-tuned.

the middle are missing, leading to incomplete transfer. This phenomenon can be ascribed to the pulse-to-pulse variation of the laser. **Figure 3.18d** corresponds to the transfer result where flipped SU-8 microdisks (dark area) are found. As revealed previously, the flipping arises from inaccurate centering of the laser spot to the SU-8 center. Even slight misalignment may lead to asymmetric momentum transferred to the microdisk. Since the gap distance is large enough (more than 300  $\mu\text{m}$ ), the SU-8 has the chance to land on its side.

We count the number under each category to analyze the yield rate ( $Y$ ) of the SU-8 transfer (defined as SU-8 microdisks successfully transferred onto PDMS without flipping). Here,  $N_n$ ,  $N_f$ , and  $N_s$  denote the number of SU-8 microdisks that stay on the donor (without transfer), flip on its side surface, and land on the receiver without flipping. Therefore, the yield rate can be expressed as:

$$Y = \frac{N_s}{N_s + N_f + N_n} \quad (3.3)$$

For the  $40 \times 30$  array, the counted number corresponding to  $N_n$ ,  $N_f$ , and  $N_s$  is 24, 250, and 926, respectively. Therefore, the calculated  $Y$  value is 77 %.

As explained previously, inaccurate centering of the laser spot with respect to the SU-8 center is the main reason for such a low yield rate. After the first transfer process, two parameters are explored and optimized to improve the centering and enhance the yield rate. The first parameter is the dwelling time. Dwelling time in our g-code file is defined as the stage moving to another position and stopping for a certain amount of time to stabilize the stage. Dwelling

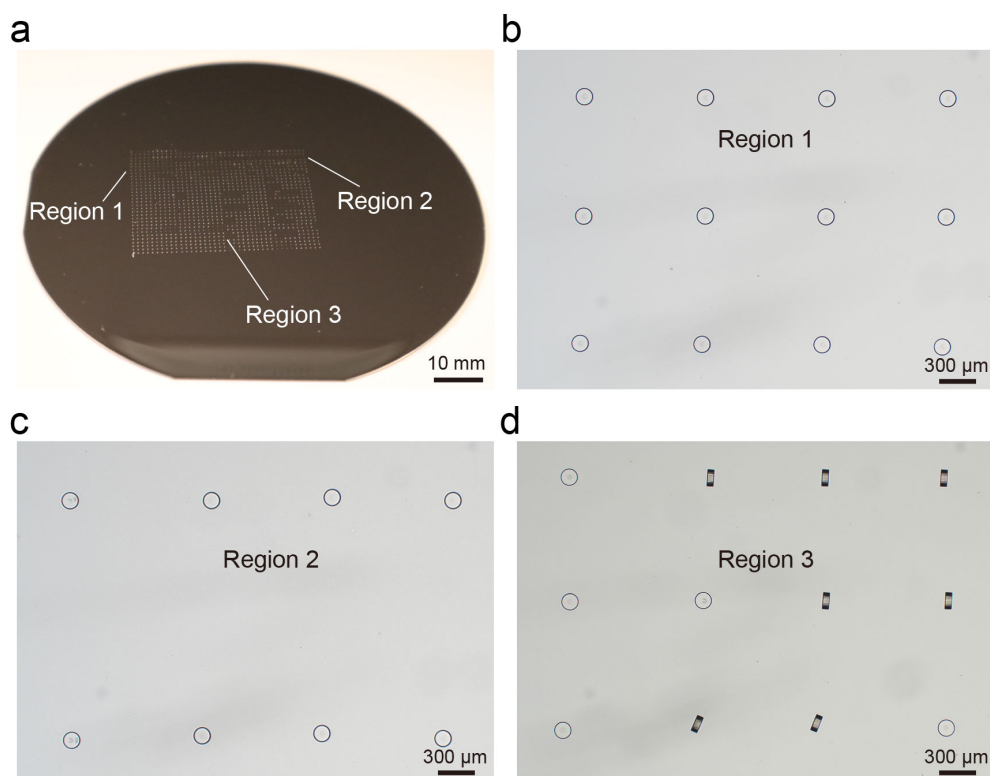


Figure 3.18: **Large-scale transfer of SU-8 microdisks.** (a). The transfer result of a  $40 \times 30$  SU-8 microdisk array onto PDMS coated 4-inch wafer. The pitch distance is  $1000 \mu\text{m}$ . (b-d). High-magnification images show three regions of SU-8 microdisks that land on the receiver. Region 1 shows a well-aligned  $4 \times 3$  SU-8 arrays. In (c), four SU-8 microdisks in the center are missing, and seven flipped SU-8 microdisks are observed from (d).

time is of great importance because it enables the stage to move to and remain in the correct position before the laser shot. In our experiments, the first twenty rows are transferred with a dwelling time of 0.4 s, while the last ten rows are transferred with a dwelling time of 0.8 s. As a result, fewer flipped SU-8 microdisks are found in the last ten rows, as displayed in **Figure 3.18a**.

The second factor that influences the final yield rate is the wafer rotation when mounting the donor wafer onto the donor stage. Even if such rotation is small (e.g., a few milliradians), it can accumulate and become sufficiently large to worsen the precision of the laser, thus lowering the yield rate. Therefore, coordinate correction for each SU-8 microdisk is necessary and completed by rewriting the g-code file.

The coordinate correction process is illustrated in **Figure 3.19**. The XY-plane represents the coordinate system of the stages, and the yellow circles represent the distribution of a  $10 \times 10$  SU-8 microdisk array on the donor. As sketched, the whole array globally rotates at an angle. Hence, the x-coordinate for the SU-8 microdisk in the dashed red square cannot be expressed



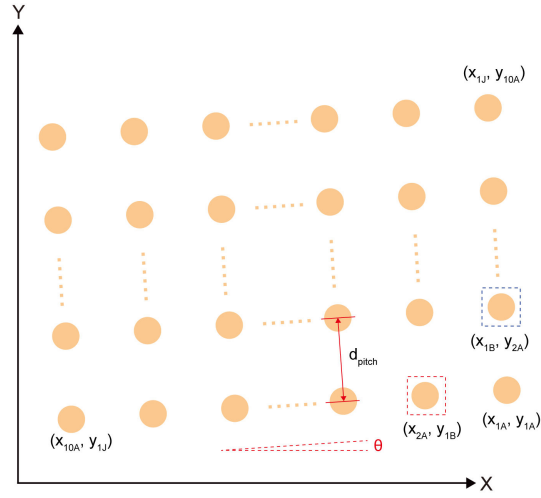


Figure 3.19: **Coordinate calculation and correction for SU-8 microdisks.** The schematic illustration demonstrates the case when the SU-8 microdisk array has a rotation angle with respect to the donor stage. The rotation angle can be calculated and the corresponding coordinate for each microdisk can be deduced.

as:

$$x_{2A} = x_{1A} - d_{pitch} \quad (3.4)$$

Instead, the corrected coordinate for this SU-8 microdisk is expressed as:

$$x_{2A} = x_{1A} - d_{pitch} \times \cos\theta \quad (3.5)$$

The small rotation angle is calculated from the formula:

$$\tan\theta = \frac{y_{1A} - y_{1J}}{x_{1A} - x_{10A}} \quad (3.6)$$

Here we use the coordinates of the first and the last SU-8 microdisks (in the first row) to minimize the error caused by our visual observation. The y-coordinate of the SU-8 is written as:

$$y_{1B} = y_{1A} - d_{pitch} \times \sin\theta \quad (3.7)$$

A similar result can be obtained for SU-8 in the blue dashed square in **Figure 3.19**:

$$x_{1B} = x_{1A} - d_{pitch} \times \sin\theta \quad (3.8)$$

$$y_{2A} = y_{1A} + d_{pitch} \times \cos\theta \quad (3.9)$$

Based on the coordinate correction, the coordinate for any individual SU-8 microdisk in the array can be summarized as:

$$x_M = x_{1A} - d_{pitch} \times \cos\theta \times (M - 1) - d_{pitch} \times \sin\theta \times (N - 1) \quad (3.10)$$

$$y_N = y_{1A} + d_{pitch} \times \cos\theta \times (N - 1) - d_{pitch} \times \sin\theta \times (M - 1) \quad (3.11)$$

where M and N denote the M row and N column, respectively. We apply **Equation 3.6** to our LIFT system and calculate the small rotation angle. **Appendix Figure A.33** shows two micrographs of the SU-8 arrays. In **Figure A.33a**, the coordinate for the SU-8 in the dashed square is (-32.592, 41.775), and the other one in **Figure A.33b** is (-34.385, 41.783). Therefore, the rotation angle is calculated to be -4.5 mrad. Given that  $x_{1A} = y_{1A} = 0$ , it can be calculated that  $(x_{2A}, y_{1B})$  and  $(x_{1B}, y_{2A})$  are approximately (-200, -0.87) and (0.87, 200), respectively (pitch distance of 200  $\mu\text{m}$  in our case).

From the calculations performed, we can draw the conclusion that when the stage moves along Y-axis, for two consecutive SU-8 microdisks, the x-coordinate will increase by approximately 1  $\mu\text{m}$  (considering the minimal step for the donor stage is 1  $\mu\text{m}$ ). A similar trend can be concluded from the movement along the X-axis. Although such increments (1  $\mu\text{m}$ ) are small, the accumulated value can strongly influence the final yield rate. Consider moving the stage along the Y-direction; if we ignore introducing the x-coordinate shift (1  $\mu\text{m}$  per SU-8 microdisk), it is only 1  $\mu\text{m}$  that the laser spot misaligns with the second SU-8 microdisk. However, such misalignment will approach 9  $\mu\text{m}$  for the tenth SU-8 microdisk, which accounts for 7 % of the SU-8 diameter. Such misalignment will lead to the SU-8 microdisk flipping on its side. As a result, the coordinate adjustment is applied to a while loop in the g-code to guarantee that the coordinate shift adjustment of the donor stage (1  $\mu\text{m}$ ) is executed for every SU-8 microdisk.

**Figure 3.20** demonstrates the transfer of a 40  $\times$  40 SU-8 array after the coordinate correction. The g-code command is improved with the corrected coordinates (The g-code file is provided in **appendix Figure A.34**). Simultaneously, the dwelling time is kept at 0.8 s to make the transfer process more stable. Clearly shown in **Figure 3.20a** is an overview of the whole SU-8

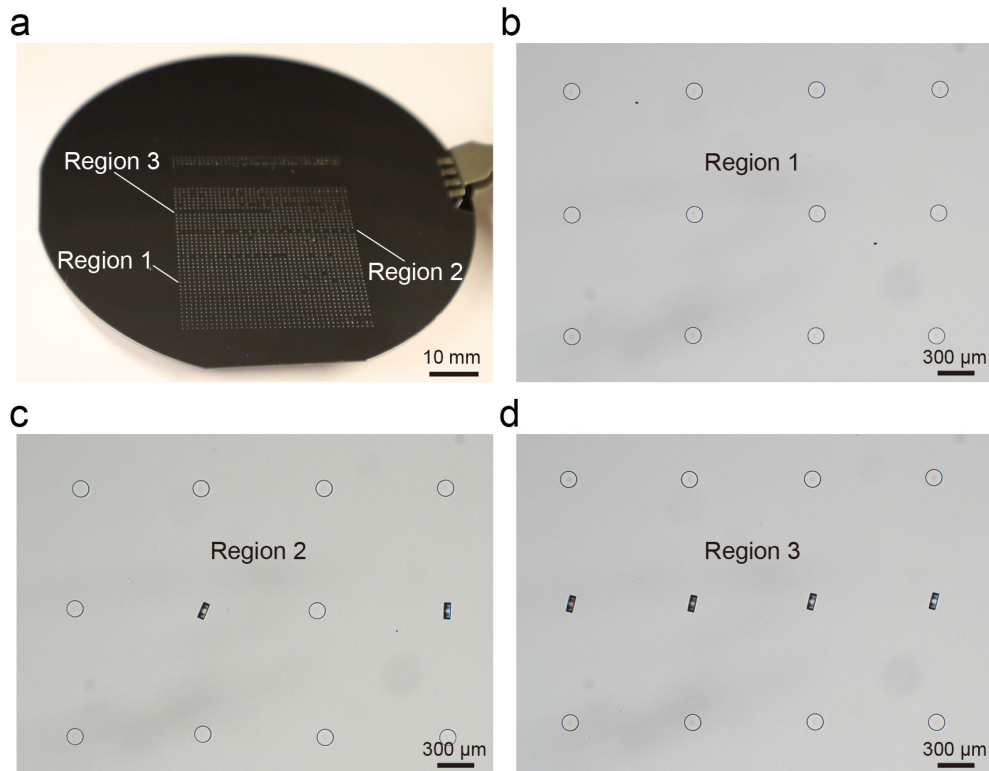


**Figure 3.20: Large-scale transfer of SU-8 microdisks after rotation correction.** (a). The transfer result of a  $40 \times 40$  SU-8 microdisk array onto a PDMS-coated 4-inch wafer. The pitch distance is  $1000 \mu\text{m}$ . (b-d). Magnified images showing three regions of SU-8 microdisks that land on the receiver. (b) shows a well-aligned  $4 \times 3$  SU-8 arrays. In (c) and (d), two and four SU-8 microdisks flipped on their side surfaces.

array on the receiver. Compared to **Figure 3.18a**, fewer dark regions in the array are observed, indicating fewer SU-8 are flipped on their sides. It is worth noting that all of the 1600 SU-8 microdisks land on the receiver, while 24 SU-8 microdisks in **Figure 3.18a** are missing (still on the donor).  $N_n$ ,  $N_f$ , and  $N_s$  are 0, 162, and 1438, respectively and therefore, the yield rate of the transfer is approximately 90 %, where a 17 % improvement of the yield rate is achieved by fine-tuning the dwelling time and the coordinates of the SU-8 microdisks.

In conclusion, our experiments demonstrate that the transfer of SU-8 microdisks has good scalability using our LIFT system, and it is promising to extend such transfer to other functional microsystems.

### 3.5 Transfer of SU-8 microdisks onto nonplanar receivers

Each transfer demonstration shown above shares a common feature: all the receivers have a planar surface. However, due to the noncontact feature of LIFT, such transfers can be

extended to non-planar surfaces and used to realize the assembly of 3D microstructures. In this section, we perform several transfer experiments on various non-planar surfaces to explore this possibility.

### 3.5.1 Nonplanar receiver preparation

First, 4- $\mu\text{m}$ -thick AZ 10XT photoresist is coated on two Si wafers, followed by the patterning of desired microstructures with the laser writer (MLA 150). After the development, the two wafers are etched in an  $\text{SF}_6$  atmosphere with controlled time to form 70 and 140  $\mu\text{m}$  deep structures. Then the two Si wafers are treated with oxygen plasma (1000 W for 1 min). A layer of trimethylsilyl chloride silane (TMCS, Sigma-Aldrich) is coated on the wafers in a desiccator. The PDMS is poured on the wafer and degassed in a desiccator. After these steps, the PDMS is cured for 2 h (80  $^\circ\text{C}$ ) in an oven and peeled off from the Si wafers.

### 3.5.2 Transfer result

#### 3D assembly of SU-8 microdisks

In the first demonstration (**Figure 3.21**), 5 and 7 SU-8 microdisks (diameter: 130  $\mu\text{m}$ , thickness: 50  $\mu\text{m}$ ) are sequentially transferred (1.6  $\text{J}/\text{cm}^2$ , 3-6 shots) onto the PDMS receiver to form two-layer and three-layer pyramid-like structures. For all the transfers, the SU-8 donor substrate is in close proximity to the receiver substrate to guarantee high transfer precision, as discussed in **Chapter 3**. The manufactured pyramid-like structures show the ability of our technique in 3D constructions using functional SU-8 microdisks as building blocks. This demonstration also proves that LIFT is capable of distributing functional devices to targeted surfaces with high density, compared to the low-dense array prepatterned on the donor substrate. In our case, two consecutive SU-8 microdisks have a pitch distance of 400  $\mu\text{m}$  on the donor substrate, while the transferred SU-8 has a much smaller pitch distance (110  $\mu\text{m}$ , **Figure 3.21**).

#### SU-8 microdisk transfer onto nonplanar surface and pre-structured receivers

To extend the transfer onto non-planar surfaces by LIFT, the sequential transfer of two 100  $\mu\text{m}$  (diameter)  $\times$  50  $\mu\text{m}$  (thickness) SU-8 microdisks on the tip of a freestanding stainless steel needle is shown in **Figure 3.22a**, which might not be easily accessible via other printing techniques. Furthermore, two additional receivers with different features are fabricated and tested. SU-8 microdisks are transferred onto PDMS micropillars of smaller widths (width: 50 and 70  $\mu\text{m}$ , height: 140  $\mu\text{m}$ ) compared to the SU-8 microdisk diameter (**Figure 3.22b**). SU-8 microdisks with a diameter of 100 and 130  $\mu\text{m}$  are transferred onto such PDMS pillars without falling off. For all the transfers, the gap distance between the SU-8 donor substrate and the

### 3.5 Transfer of SU-8 microdisks onto nonplanar receivers

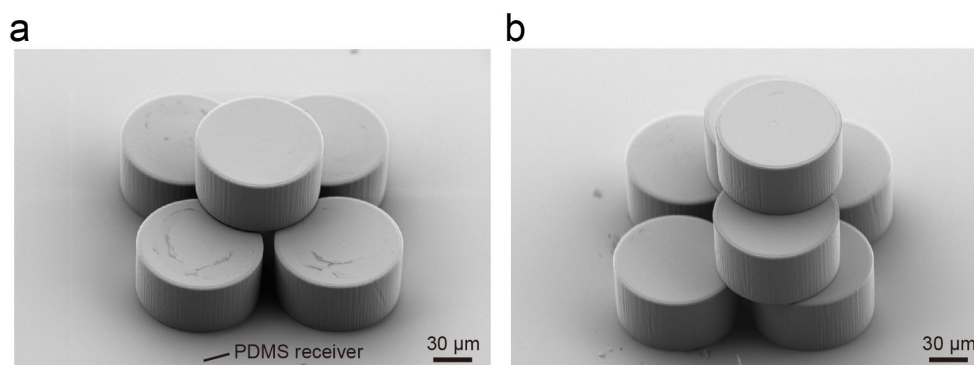


Figure 3.21: **3D assembly of SU-8 microdisks.** (a). SEM images of two-layer pyramid-like structures made of sequentially transferred SU-8 microdisks. (b). SEM images of three-layer pyramid-like structures made of sequentially transferred SU-8 microdisks.

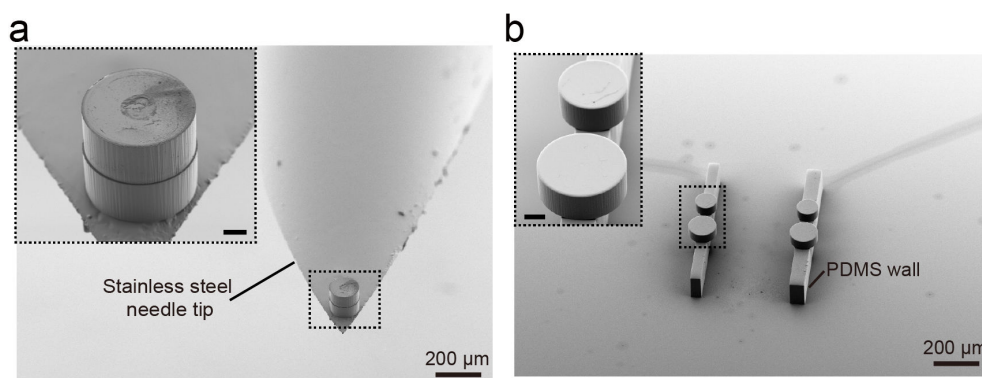


Figure 3.22: **SU-8 microdisk transfer onto nonplanar surfaces.** (a). SEM image of the transfer of two stacked SU-8 microdisks on the tip of a freestanding needle. Scale bar in the inset: 20 μm. (b). SEM image of the transfer of two SU-8 microdisks on 50- and 70-μm wide PDMS micropillars. The two SU-8 microdisks have a diameter of 130 and 100 μm, respectively. The height of the PDMS pillar is 140 μm. Scale bar in the inset: 30 μm.

receiver substrate is kept in close proximity to increase the transfer precision.

**Figure 3.23** demonstrates the transfer of the SU-8 array into PDMS concave structures that have a depth (70 μm) slightly larger than the thickness of the SU-8 microdisk (50 μm). Compared with the diameter of the SU-8 microdisk (100 μm), the PDMS microwell has a larger diameter (150 μm). This design allows the transfer of SU-8 microdisks into these microwells. **Figure 3.23a** sketches the cross-section view of the transferred SU-8 microdisks in the PDMS microwells, where the top side of the SU-8 is below the top surface of the PDMS. An experiment is detailed in **Figure 3.24** to show that transferred microdisks can be protected from surface scratches by microwells. The scratch test is conducted using a leveling applicator, as illustrated in **Figure 3.24a**. SU-8 microdisks in the microwells cannot be reached by the leveling applicator, whereas the microdisk on the top surface of the PDMS can be moved when

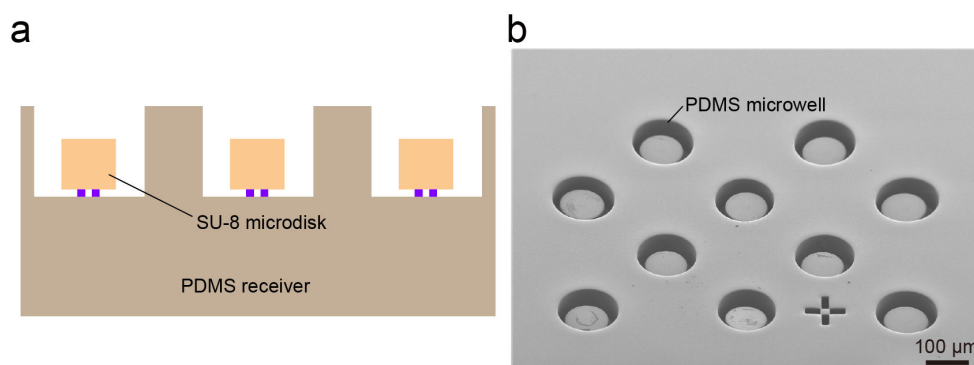


Figure 3.23: **SU-8 microdisk transfer into concave microstructures (a)**. A simple sketch showing the transferred SU-8 microdisks in PDMS microwells. **(b)** SEM image showing the transfer of an array of SU-8 microdisks into PDMS microwells. The height of the recess is approximately 70 μm, and the lateral dimension is 150 μm in diameter.

scratched by the applicator. **Figure 3.24b-c** display the transferred SU-8 microdisks before and after the scratch test. In these two micrographs, five SU-8 microdisks are transferred into microwells, and one SU-8 microdisk is placed on the PDMS top surface by LIFT, as indicated by the dashed white square. After the scratch, the positions of the five microdisks remain unchanged, while the SU-8 microdisk in the dashed white square has been moved along the scratch direction.

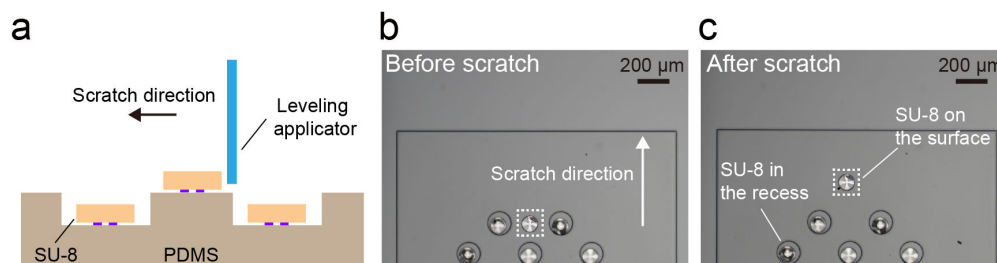


Figure 3.24: **Scratch test of the transferred SU-8 microdisk. (a)** Sketch of the scratch test using a leveling applicator. The bottom surface of the applicator is set to be approximately 20 μm above the PDMS top surface. **(b-c)** Experimental results before and after the scratch. The dashed square indicates the SU-8 microdisk is transferred onto the PDMS surface while the remaining five SU-8 microdisks are located within PDMS microwells. The PDMS microwell has a diameter of 150 μm and a depth of 70 μm. The position shift of the SU-8 microdisk in the dashed square demonstrates that the SU-8 microdisks transferred into recesses are uninfluenced by the scratch.

All these demonstrations reveal the potential of LIFT to precisely assemble and transfer microscale SU-8 microdisks onto receivers having very different physical and geometrical properties. Furthermore, by controlling the gap distance discussed in **Chapter 2**, the transfer precision can be further improved to fulfill potential applications that require high precision.

### 3.6 Conclusion

The LIFT demonstrations reported in this chapter substantiate the idea of transferring SU-8-supported microdevices to various receivers while maintaining their functionality. As proof-of-concept examples, the LIFT setup transfers two types of microdevices: a SU-8-supported QR code and a temperature sensor. The metallic QR code's readability is verified after the transfer, and the adhesion between transferred SU-8 microdisks and receivers is also evaluated. The rotation and shaking tests are first performed to examine the adhesion under high acceleration scenarios. SU-8 microdisks on different receivers after these high acceleration experiments support our assumption of strong adhesion. Quantitative characterization of the adhesion force by an in-situ micromechanical testing system records the lateral force applied to the transferred SU-8 microdisks. The displacement-load curve determines the maximum load corresponding to the adhesion force. The results indicate that the adhesion force can be as high as several tens/hundreds of millinewton, depending on the type of receivers and thermal annealing treatment. The adhesion experiments in DI water further confirm that transferred SU-8 microdisks can survive such harsh conditions for a long time, especially SU-8 samples on Cu and PDMS receivers.

Furthermore, large-scale transfer of SU-8 microdisks using g-code programming is also implemented. Two parameters, the dwelling time and the donor wafer rotation, are investigated and optimized. By extending the dwelling time to 0.8 s and introducing coordinate shift (1  $\mu\text{m}$ ), the yield rate of the transferred SU-8 microdisks increases from 77% (1200 SU-8 microdisks in total) to 90% (1600 SU-8 microdisks in total). In the last experiment, we explore the capability of LIFT to transfer SU-8 microdisks onto nonplanar surfaces through several demonstrations. The sequential transfer of SU-8 microdisks to construct multi-layer pyramid-like structures makes the 3D assembly of such microstructures possible. The transfer of SU-8 microdisks onto a freestanding needle tip and onto PDMS micropillars verifies the claim that the LIFT process is independent of the geometrical properties of the receivers. The last example reveals that SU-8 microdisks can be precisely transferred into PDMS microwells and the subsequent scratch test by a leveling applicator demonstrates that microdisks in the microwells are unperturbed by the incoming applicator.





# 4 LIFT of Microstructures Fabricated by Two-Photon Lithography (TPL)

## 4.1 Introduction

**Chapter 3** summarizes the transfer of functional SU-8 microdevices, consisting of simple SU-8 microdisks and layers deposited on top of them. Even if these simple microstructures are successfully transferred, the LIFT technique is not limited to this and can transfer more complex geometries. As a fast-evolving technique, two-photon lithography (TPL) is widely used to fabricate microstructures/devices with complex geometries, notably as micro-mixers [203], helical micromachines [204], microscaffolds [205,206], micromeshes [207], microcages [208], micro-rockets [209] and microwalkers [210]. All these fabricated microstructures have been widely used in microfluidics [203], drug delivery [204,210], cell study [205–208] and micro-robots [210], etc.

There are three main scenarios after the 3D printing of the microstructure on a surface: First, the microstructure can be used without further modification [203,205–207]. Second, it is required to move it to on the surface without precise location by simple detachment methods such as manual transfer [211], scratching the substrate surface [212] or using sacrificial layer to release devices [213–215]. Finally, the microstructures need to be transferred to targeted positions and possibly different substrates. However, up to date, there are few reports about their precise placement/transfer. One group reported transferring micro-rockets into an acrylic-based container by the micro-manipulation system [209]. Another one used microwalkers to assemble microcontainers in a stacked way, as shown in **Figure 4.1a**. A Japanese team employed AFM tip to place magnetic helix microstructures into microchannels [216] (**Figure 4.1b**). Nevertheless, these three demonstrations have inherent disadvantages, hindering the applications. First, the micro-manipulation system is operated under a "pick-and-place" mode to transfer prefabricated functional microstructures, so is the atomic force microscope (AFM) tip placement. This process requires a slow and delicate operation to avoid misalignment. Moreover, the AFM tip placement approach demands the helix structure to have thin supporting legs, which

the tip can more easily detach, but it complicates the design and fabrication step. Therefore, less efficient operations lead to a low throughput rate and prevent them from the large-scale transfer of functional microstructures with high throughput.

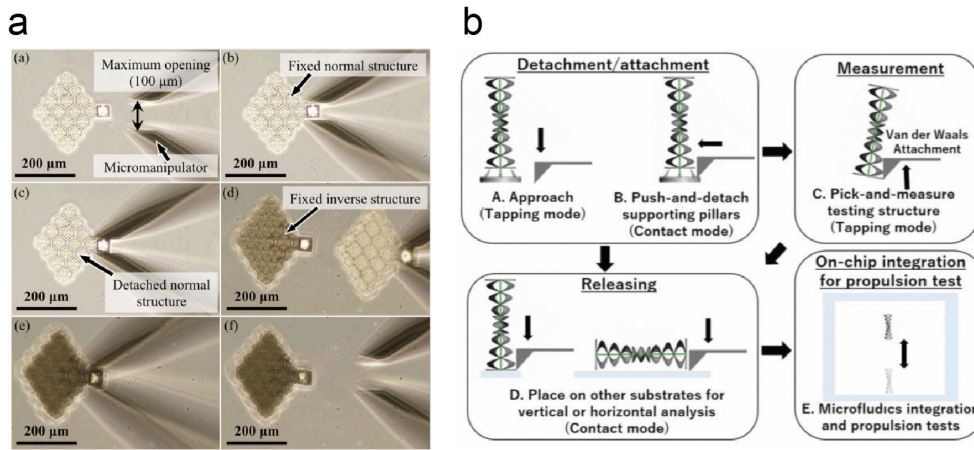


**Figure 4.1: Two methods to manipulate TPL-fabricated microstructures. (a).** Microstructure stacking by microtweezers [208]. **(b).** 3D helical microswimmers manipulated by an AFM tip [216].

As an alternative approach, LIFT has some unparalleled advantages. A laser pulse transfers microdevices, and consequently, direct contact with the micro-manipulator or AFM tip can be avoided, lowering the chance of damaging such microdevices by mechanical force. Furthermore, the throughput rate is much higher due to the shift from the conventional "pick-and-place" to a "lase-and-place" process by programming the transfer process. In the previous study, the throughput rate is close to 1 pcs/s, which can be further improved. As a result, LIFT is a powerful method to transfer TPL-fabricated microstructures with complex geometries; meanwhile, the structural integrity and throughput rate can be maintained simultaneously.

In this chapter, we systematically analyze the transfer of TPL-fabricated microstructure as test samples. The pore size is first investigated to quantify the threshold to guarantee the damage-free transfer of such microstructures. Then we explore the influence of the structure size and determine the upper limit of the current LIFT setup for transfer. Finally, the size range is considerably broadened by incorporating a supporting layer without increasing the laser fluence and spot size. The maximum size that has been transferred reaches 880 μm and is 44-fold larger than the laser spot size.

After the parametric study, several proof-of-concept demonstrations are presented. The first example shows the transfer of a T-shape microstructure into a targeted PDMS microchannel with high alignment. In the second demonstration, microstructures loaded with inkjet-printed Rhodamine B ink are transferred by LIFT, and the subsequent characterization helps verify the

capability to release liquid inks. To show the potential for large-scale transfer of TPL structures, a  $7 \times 7$  micro scaffold array is prepared on a donor substrate and then transferred onto a PDMS-coated 4-inch Si wafer with varying pitch distances.

## 4.2 Materials and methods

### 4.2.1 TPL setup

The TPL microstructures are fabricated by a commercial TPL system (Photonic Professional GT, Nanoscribe GmbH). It is equipped with a femtosecond-pulsed infrared laser ( $\lambda=780$  nm) and four different objectives (10X, 20X, 25X, and 63X) to provide different magnifications and resolutions. For example, the 25X objective can achieve a resolution of 600 nm and  $2 \mu\text{m}$  in X-/Y-direction and Z-direction, respectively. A galvanometric scanner and a high-resolution XYZ stage control the movement of the laser focus and the sample substrate, respectively.

### 4.2.2 TPL donor preparation

The TPL microstructures are first designed with COMSOL software. **Appendix Figure A.35** present five different building blocks. The dimension for each building block is  $20 \times 20 \times 20 \mu\text{m}^3$ . The pore size of these building blocks varies from 2, 6, 10, 14, and  $18 \mu\text{m}$  and the building block in **appendix Figure A.35e** has the largest hollow ratio.

As for the donor sample preparation, the first step is the PI film preparation, which has been discussed in Chapter 2 ("**SU-8 donor preparation**"). A thin layer of PI ( $5\text{-}\mu\text{m}$ -thick) is spin-coated on  $26 \times 26$  mm coverslips, with a subsequent curing process at  $300^\circ\text{C}$  for 2h.

One droplet of IP-S photoresist (NanoScribe, GmbH) is placed on the as-prepared substrate, and the substrate is flipped with the photoresist facing downwards. The laser is automatically focused between the interface of PI and photoresist by immersing the  $25\times$  objective lens into the photoresist droplet, and the two-photon laser writing is performed using dip-in laser lithography (DILL) mode.

After the TPL printing process, samples are developed in PEGMA for 15 mins, followed by a rinsing step in IPA for 2 mins. Then the microstructures are gently dried by  $\text{N}_2$  gun and ready for LIFT experiments.

### 4.2.3 Receiver substrate preparation

#### Small PDMS receiver

Similar to the PDMS receiver preparation process in Chapter 2, the base and curing agent is mixed with a mass ratio of 10:1 in a mechanical mixer. The mixture is degassed in a vacuum desiccator and poured into a petri-dish, followed by a thermal curing process (80 °C for 2 h). After the curing, the PDMS is cut into desired size and shape as the receiver.

#### PDMS receiver on 4-inch Si wafer

After degassing in the vacuum desiccator, the mixed PDMS is spin-coated (SCS6800 PDMS coater) onto a 4-inch Si wafer with a spinning speed of 1900 rpm for 40 s. After the coating, the wafer is kept in the ambient environment for 20 mins to homogenize the thickness on the edges. Finally, the wafer is placed into the oven for curing (80 °C for 2 h).

### 4.2.4 Rhodamine B ink preparation

The Rhodamine B ink is prepared by mixing the Rhodamine B (Sigma-Aldrich, 100 mg) with DI water (10 mL). A magnetic stirrer mixes the solution for 30 mins at a rotation speed of 1000 rpm.

### 4.2.5 SEM characterization of transferred microstructures

Before the SEM, TPL-fabricated microstructure samples are first sputtered (Alliance-Concept DP 650) with a thin layer of gold (Au, 10 nm). The samples are then mounted on the holder and transferred into the SEM (Zeiss MERLIN) chamber. The acceleration voltage is set to be 3 kV. Two tilted angles are set to take SEM images: 0° and 45°.

## 4.3 Results and discussion

### 4.3.1 Influence of pore size

The pore size of the TPL microscaffolds is a key factor that can regulate cell behavior, control cell loading and growth, etc. It has been extensively investigated in many cell studies [217–220]. Moreover, the pore size affects the transfer result by LIFT because the microstructure structures may be damaged by the PI blister during the transfer process if the pore size is too large and the backbone beam size is too small.

The experiment uses microscaffolds with five different lateral pore sizes to verify their printabil-

ity. Based on the SU-8 microdisk transfer experiments performed in **Chapter 2** and **Chapter 3**, the lateral dimension for one microsccaffold is designed to be  $100 \times 100 \times 100 \mu\text{m}^3$ . Each scaffold is composed of  $5 \times 5 \times 5$  building blocks and the as-fabricated microsccaffold samples (shown in **appendix Figure A.36**) are mounted on the donor holder, and the PDMS receiver is placed underneath the donor substrate. One single laser shot with a laser fluence of  $0.96$  or  $1.6 \text{ J/cm}^2$  triggers the successful transfer onto the PDMS receiver. SEM images presented in **Figure 4.2** show that the top surface of the microsccaffold adhering to the PI film before the transfer is free from damage after the transfer. This result agrees well with our findings in **Chapter 2**, where we have achieved the damage-free transfer of SU-8 microdisks.

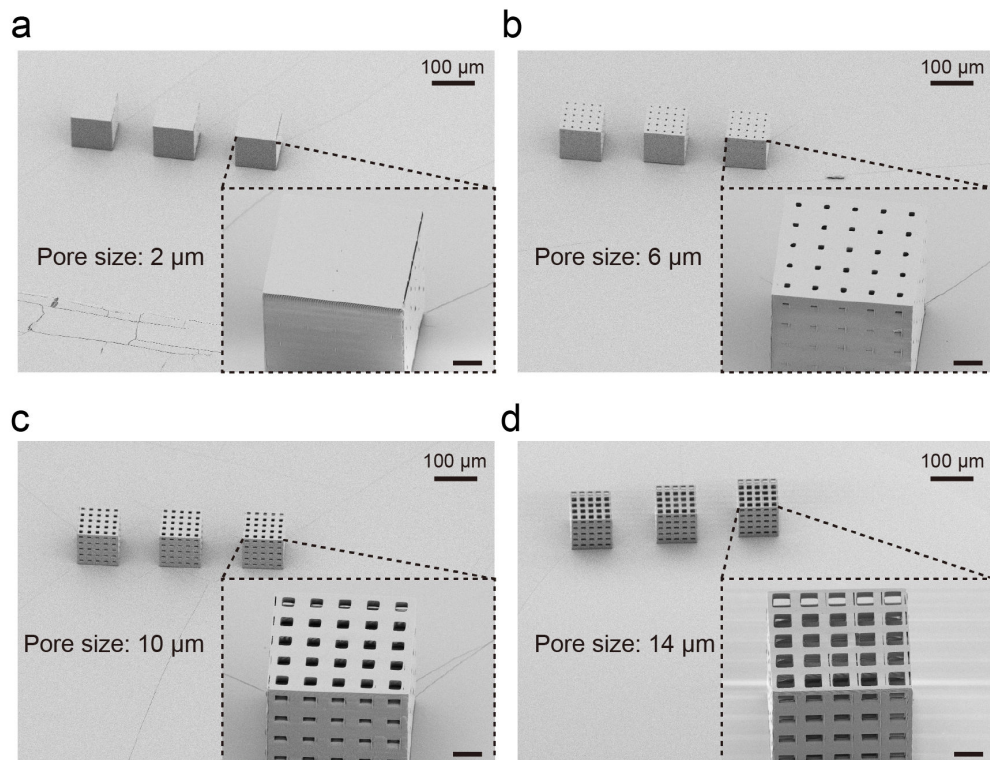


Figure 4.2: **Transfer results of microsccaffolds on PDMS.** From (a-d), the pore size increases from 2 to  $14 \mu\text{m}$ . Insets: High-magnification image of one microsccaffold. Scale bar in all the insets:  $20 \mu\text{m}$ .

It is worth noting that these scaffolds need less laser fluence to be transferred compared to the laser fluence test result discussed before. In **Chapter 2**, we prove that only if the laser fluence is higher than  $1.6 \text{ J/cm}^2$ , a single laser pulse can transfer the SU-8 microdisk. Whereas in this case, only  $0.96$  or  $1.6 \text{ J/cm}^2$  is needed. This variation can be tentatively ascribed to the different adhesion properties between the microsccaffold and PI film, compared with the adhesion property between SU-8 and Ti thin film. Furthermore, unlike the SU-8 microdisk on the donor substrate, the effective contact area of the scaffold with PI film is less due to

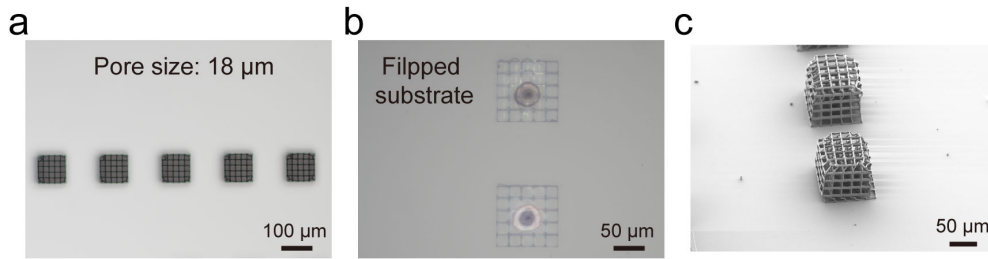


Figure 4.3: **Transfer result of microscaffolds with a pore size of 18  $\mu\text{m}$ .** (a). Optical image of five microscaffolds on the donor. Scale bar: 100  $\mu\text{m}$ . (b). Optical image of two microscaffolds after 10 laser shots. The laser fluence is 0.96  $\text{J}/\text{cm}^2$ . The donor substrate is flipped to visualize the PI blister. Scale bar: 100  $\mu\text{m}$ . (c). SEM image of the same two microscaffolds displayed in (b). Scale bar: 100  $\mu\text{m}$ .

Table 4.1: **Transfer result of 100  $\mu\text{m}$  large microscaffolds with different pore sizes**

| Pore size        | Laser parameter                          | Transfer result |
|------------------|--|-----------------|
| 2 $\mu\text{m}$  | 1.6 $\text{J}/\text{cm}^2$ & 1 shot      | Transfer        |
| 6 $\mu\text{m}$  | 1.6 $\text{J}/\text{cm}^2$ & 1 shot      | Transfer        |
| 10 $\mu\text{m}$ | 0.96-1.6 $\text{J}/\text{cm}^2$ & 1 shot | Transfer        |
| 14 $\mu\text{m}$ | 0.96-1.6 $\text{J}/\text{cm}^2$ & 1 shot | Transfer        |
| 18 $\mu\text{m}$ | 1.6 $\text{J}/\text{cm}^2$ & > 10 shots  | No transfer     |

the presence of pores. For example, the contact area of the scaffold displayed in **Figure 4.2c** only accounts for half of its surface area because the pore size is 10  $\mu\text{m}$ . As this effect is not in the scope of this thesis, this finding is not further investigated. However, further study can be carried out to quantitatively determine the adhesion force, such as using an in-situ microgripper system to measure the adhesion force [221,222].

Besides these four pore sizes, we also investigate the 18  $\mu\text{m}$  pore size microscaffolds transfer result. **Figure 4.3a** presents five microscaffolds before transfer and **Figure 4.3b** shows two scaffolds that have been shot by 0.96  $\text{J}/\text{cm}^2$  laser pulse (10 shots). The two scaffolds still stay on the donor substrate, and this image is captured by flipping the substrate to have better visualization of the blisters under the scaffolds. The SEM image of **Figure 4.3c** further confirms that the two scaffolds remain on the PI layer. Compared with the other four types of scaffolds shown in **Figure 4.2**, it is possible that the scaffolds in **Figure 4.3** are too fragile, and the expanding blister can easily break the center part. Because of the broken backbone beams, the blister fails to further impart forward momentum to the scaffold. Therefore, it can be observed that even if multiple laser shots are used, scaffolds still stay on the donor.

The transfer results of microscaffolds with five types of pore size are listed in **Table 4.1**. This result helps determine the threshold of the pore size, which is 14  $\mu\text{m}$  in our case, to guarantee the damage-free transfer of microscaffolds.

### 4.3.2 Influence of TPL structure size

As mentioned above, the pore size of the scaffold influence targeted applications. For example, one research team <sup>[217]</sup> demonstrated that cells could be more uniformly distributed inside 52- $\mu\text{m}$ -pore-size scaffolds than inside 25- and 12- $\mu\text{m}$ -pore-size scaffolds. Another group fabricated a series of scaffolds with the pore size varying from 10 to 90  $\mu\text{m}$  <sup>[220]</sup>. Their study confirmed that scaffolds with a pore size of 90  $\mu\text{m}$  showed the best cell growth, and cells were densely populated after nine days.

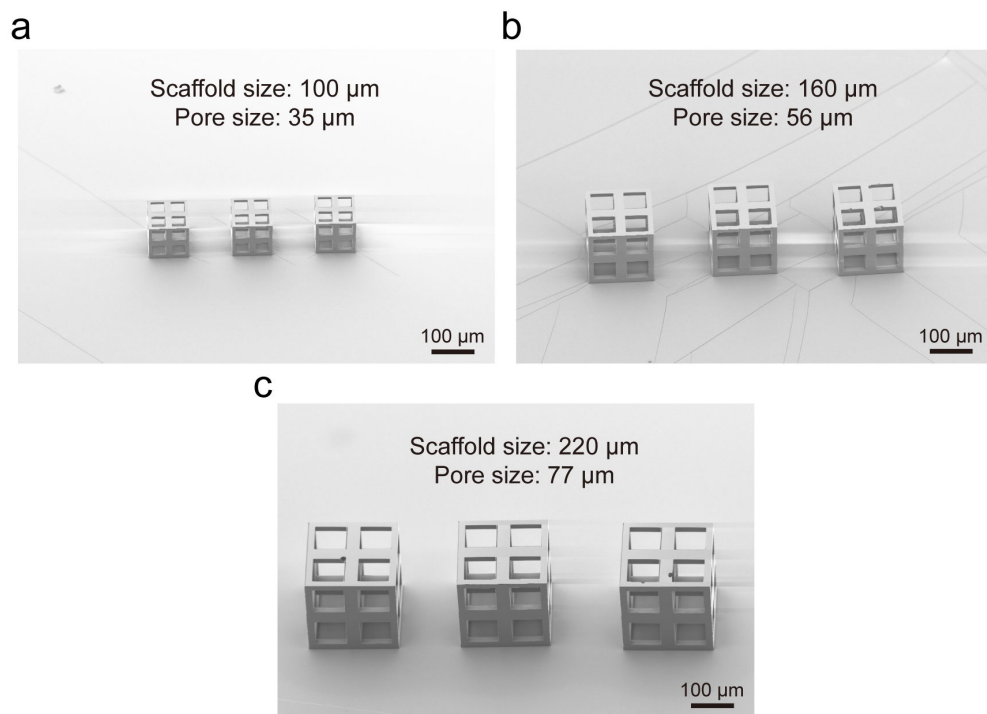


Figure 4.4: **Microscaffold size study.** (a-c). SEM images of 3 microscaffolds transferred on PDMS receiver. Scaffold size increases from 100  $\mu\text{m}$  in (a) to 220  $\mu\text{m}$  in (c).

In the previous section, the maximum pore size investigated is 18  $\mu\text{m}$ , which is smaller with respect to the two works mentioned above. To determine the maximum size of the microscaffold that the current LIFT system can transfer, microscaffolds with three different sizes are fabricated. All the three types of scaffolds consist of  $2 \times 2 \times 2$  building blocks, as presented in **appendix A.37**. The pore-to-backbone-beam ratio is chosen as 0.7 based on the successful transfer of scaffolds in the previous section. This ratio produces pores with the maximum size. Building block size in the three types increases from 50 to 110  $\mu\text{m}$ , thus generating the largest pore size of 77  $\mu\text{m}$ .

All three scaffolds with different pore sizes are successfully transferred onto the PDMS receiver, as shown in **Figure 4.4**. One single shot of 0.96 and 1.6  $\text{J}/\text{cm}^2$  laser fluence is needed to

achieve the transfer of 100- and 160- $\mu\text{m}$ -large microscaffolds while two shots of  $3.2 \text{ J}/\text{cm}^2$  laser fluence is required to trigger the transfer of 220- $\mu\text{m}$ -large microscaffolds. If the scaffold size continues to increase (larger than 220  $\mu\text{m}$ ), the successful transfer is still possible by multiple laser shots. Here, we take the 220- $\mu\text{m}$ -large microscaffold as the upper limit of the LIFT setup for the successful transfer of such structures. Therefore, compared to the pore size study in the previous section (maximum 18  $\mu\text{m}$ ), the LIFT setup is able to transfer microscaffold that has a much larger pore size (around 80  $\mu\text{m}$ ), which is close to the value that is favorable for cell growth and dispersion [217,220].

It should be noted that in the experiments, some defects are found at the top of the surface scaffolds (the right one in **Figure 4.4b** and **Figure 4.4c**) and this is mainly due to bubble formation during the TPL printing process preventing the polymerization of the photoresist. It can be avoided by reducing the laser power during printing. Therefore, one can assume that the LIFT transfer does not or negligibly damages the microscaffolds.

### 4.3.3 Influence of supporting layer

The previous section explores and finds out the upper limit of the LIFT setup to transfer a single microscaffold, but the size is limited to 220  $\mu\text{m}$ . In the meantime, the LIFT system fails to transfer scaffolds with a pore size of 18  $\mu\text{m}$ . Aiming to solve both the size limitation and the fragility of TPL microstructures, a supporting layer is introduced to the TPL microstructures to ease the transfer.

**Appendix Figure A.38** summarizes four types of scaffolds with supporting layer structures fabricated on the donor substrate. **Appendix Figure A.38a** shows three scaffolds that have a pore size of 18  $\mu\text{m}$  (scaffold size of  $100 \times 100 \times 100 \mu\text{m}^3$ ). As proven in the previous section, such a scaffold is unable to be transferred by the LIFT setup. In this design, we add a thin supporting layer centered between the PI film and the scaffold with a lateral dimension of  $40 \times 40 \mu\text{m}^2$ . Scaffolds in **Figure A.38b-c** have the same supporting structure, which has  $100 \times 100 \mu\text{m}^2$  lateral dimensions (pore size of 10  $\mu\text{m}$ ). The last image presents the largest scaffold with a size of 880  $\mu\text{m}$ , and the supporting layer has a length of 220  $\mu\text{m}$ . In all four images, the supporting layer is invisible because it is at the bottom of the scaffolds.

After the LIFT experiment, such supporting layers are visible, as displayed in **Figure 4.5**. **Figure 4.5a** shows the transfer result of 100- $\mu\text{m}$ -large microscaffolds with the supporting layer ( $0.96 \text{ J}/\text{cm}^2$ , 1 shot). This image shows that a damage-free transfer can be achieved because of the presence of this supporting layer. This inspires the transfer of remarkably delicate and fragile microstructures without fearing the damage caused by the transfer process.

**Figure 4.5b-c** demonstrates the capability of the LIFT setup to transfer larger scaffolds without



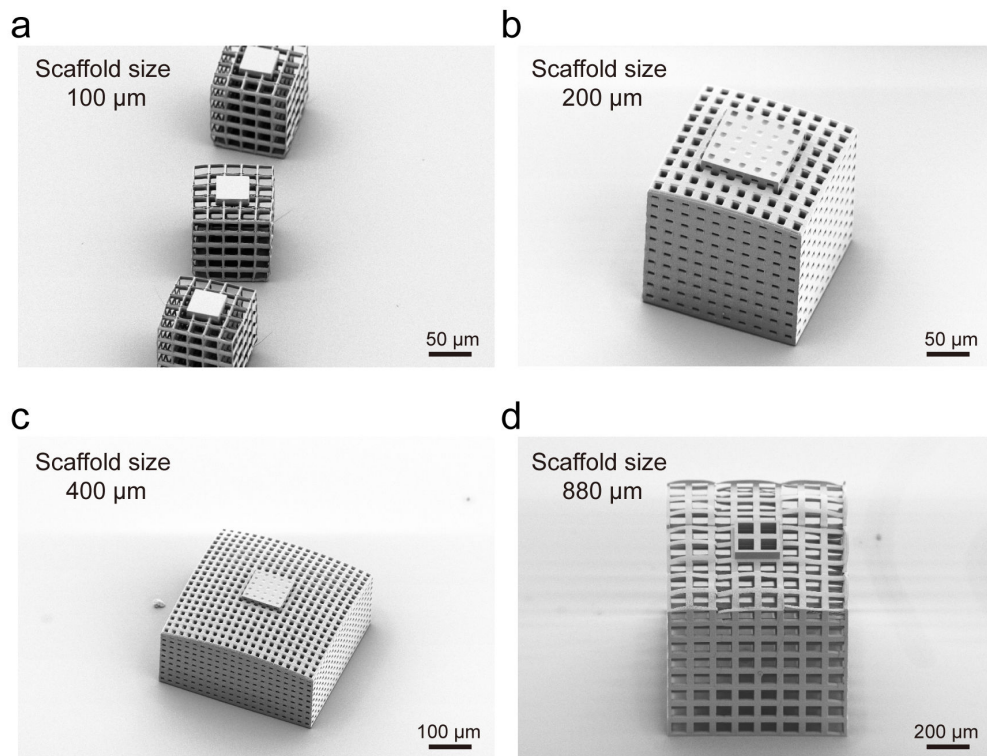


Figure 4.5: **Microcaffolds with supporting layers after the transfer process.** (a). SEM image of 3 microcaffolds transferred on PDMS receiver. The scaffold has a pore size of  $18\ \mu\text{m}$ , and the lateral dimension of the supporting layer is  $40\ \mu\text{m}$ . (b-c). Scaffolds with a lateral dimension of 200 and  $400\ \mu\text{m}$ , respectively. The pore and supporting layer sizes in both cases are 10 and  $100\ \mu\text{m}$ . (d). Scaffold with a lateral dimension of  $880\ \mu\text{m}$ . The pore and supporting layer sizes are 77 and  $220\ \mu\text{m}$ , respectively.

increasing the laser fluence or laser spot size by incorporating the supporting layer. In all cases, incorporating this layer guarantees successful transfer with the currently available laser parameter (single laser shot,  $0.96\text{-}1.6\ \text{J}/\text{cm}^2$  for 200 and  $400\ \mu\text{m}$  large scaffolds). No apparent damage is observed for all these scaffolds. **Figure 4.5d** shows the transfer of an  $880\ \mu\text{m}$  large microcaffold (1-2 shots,  $3.2\ \text{J}/\text{cm}^2$ ), which is close to the millimeter range. The summary of the transfer result of different microcaffolds with the supporting layer is shown in **Table 4.2**. As can be concluded, the strategy of the supporting layer is capable of transferring scaffolds substantially large than the laser spot size (around  $20\ \mu\text{m}$ ), which broadens the size range of structures to be transferred (from microscale level to millimeter scale level).

Table 4.2: **Transfer result of microscaffolds with the supporting layer**

| <b>Scaffold size</b>                               | <b>Laser parameter</b>                   | <b>Transfer result</b> |
|--|--|------------------------|
| 100 $\mu\text{m}$ (pore size of 18 $\mu\text{m}$ ) | 0.96 $\text{J}/\text{cm}^2$ & 1 shot     | Transfer               |
| 200 $\mu\text{m}$                                  | 0.96-1.6 $\text{J}/\text{cm}^2$ & 1 shot | Transfer               |
| 400 $\mu\text{m}$                                  | 0.96-1.6 $\text{J}/\text{cm}^2$ & 1 shot | Transfer               |
| 880 $\mu\text{m}$                                  | 3.2 $\text{J}/\text{cm}^2$ & 1-2 shots   | Transfer               |

## 4.4 LIFT Demonstrations

### 4.4.1 Transfer of TPL microstructures into PDMS microchannels

TPL-fabricated microstructures are often used as microrobots in microfluidic channels. In some cases, instead of laser writing them directly in the channel, microstructures are first fabricated on a donor substrate and followed by the transfer. This fabrication strategy relies upon two considerations. First, the movable microstructures cannot be printed directly in the channel because the development process may wash them away. Furthermore, if the functionalization of the microstructures is required, this strategy can avoid the contamination of the entire microchannel area by completing the functionalization steps on the donor substrate. For example, a research team fabricated helical structures on a source substrate and then deposited Cr/Ni on such structures by sputtering, followed by the final transfer process <sup>[216]</sup>. Some research also investigated surface functionalization of TPL microstructures, including thiol-Michael addition reaction of a thiol <sup>[223]</sup> and trichlorovinylsilane (TCVS) treatment <sup>[224]</sup>.

As a proof-of-concept, this experiment helps to determine the transfer precision on the microchannels with alignment features. T-shape TPL microstructures are fabricated and transferred to the targeted position in the microfluidic channel. The microstructure has two lateral dimensions: 20 and 50  $\mu\text{m}$  (**Figure 4.6**). The transfers of the two microstructures are performed where the gap distance is controlled to be less than 20  $\mu\text{m}$ . For the 20  $\mu\text{m}$  large structure, a single shot with a laser fluence of 0.32  $\text{J}/\text{cm}^2$  enables the transfer. When the laser fluence increases to 0.96  $\text{J}/\text{cm}^2$ , the structure breaks up, indicating that although larger fluence can transfer it, it cannot guarantee damage-free transfer. For the 50  $\mu\text{m}$  large structure shown in **appendix Figure A.39**, one laser shot with a laser fluence of 0.96  $\text{J}/\text{cm}^2$  enables successful transfer. It can be observed that the microstructure does not fit into the channel and tilt against the PDMS wall. This results from the dimensions of the microchannel (21 and 51  $\mu\text{m}$  in **Figure 4.6a** and **4.6b**, respectively) being slightly larger than the microstructures. The 1  $\mu\text{m}$  difference cannot guarantee that the microstructure fits into the channel. However, after pressing by a glass plate, the tilting effect of the microstructure is eliminated, as shown in **Figure 4.6b**, where the microstructure is located at the targeted position as if it is directly printed in the channel by the laser writing system.

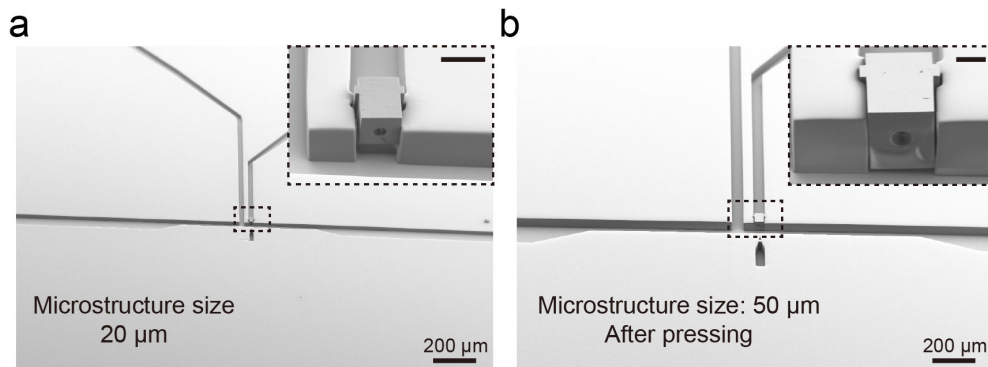


Figure 4.6: **Transfer of T-shape microstructures into PDMS microchannels.** (a). SEM image of a 20 μm large T-shape structure to the targeted position in the channel. Scale bar in the inset: 20 μm. (b). SEM image of a 20 μm large T-shape structure to the targeted position in the channel after pressing. Scale bar in the inset: 20 μm.

Although we only test a few such microstructures, the alignment accuracy of the transferred microstructure and the repeatability of such transfers can be guaranteed because the microstructure and the PDMS microchannel are in close proximity. As discussed in **Chapter 2**, the transfer precision of microstructure can be high under smaller gap distances (e.g., close proximity). For the yield, as discussed in **Chapter 3**, the proper laser fluence enables the transfer of all the microstructures (1600 SU-8 microdisks in **Chapter 3**) onto the receiver.

In short, this demonstration proves that it is practical to transfer microstructures into microchannels. The misalignment between the microstructure and the microchannel can be solved using a wider channel, which does not require perfect fitting between the microstructure and the channels.

#### 4.4.2 Transfer of TPL structures filled with liquid ink

Besides utilizing microscaffolds as a 3D microenvironment for cell growth, TPL microscaffolds are often used as carriers/capsules and filled by inkjet-printed functional inks for delivery systems [225–227]. As a proof-of-concept experiment, microscaffolds filled with liquid Rhodamine B ink are transferred to targeted receivers and the transfer result is characterized. The choice of Rhodamine B dye is motivated by its color, which allows a qualitative visual inspection.

**Figure 4.7a** presents the fabricated scaffolds array. The Rhodamine B ink is printed into microscaffolds by an inkjet printing system. The nozzle diameter for inkjet printing is 60 μm, and each scaffold is loaded with 20 droplets. **Figure 4.7b** displays the same microscaffold array after the ink filling.

After the inkjet printing step, the scaffold sample is mounted on the donor holder in the

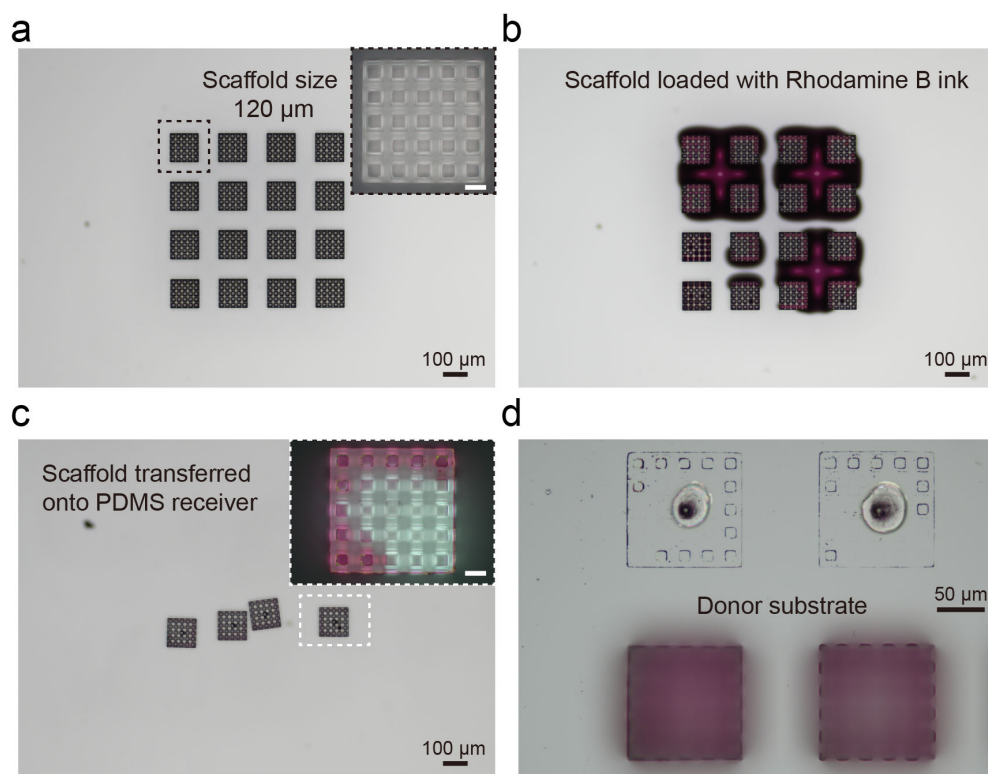


Figure 4.7: **Optical images of transferred of Rhodamine B ink loaded microscaffolds.** (a).  $4 \times 4$  microscaffold arrays. The scaffold has a dimension of  $120 \times 120 \times 120 \mu\text{m}^3$  with a pore size of  $12 \mu\text{m}$ . (b). Same array after inkjet printing of the Rhodamine B ink. (c). Four microscaffolds transferred onto the PDMS receiver. Inset: Magnified image of one microscaffold. The red part indicates the existence of the Rhodamine B ink. Scale bar in the inset:  $20 \mu\text{m}$ . (d). Traces left by the transferred microscaffolds in comparison to the microscaffolds left on the donor.

LIFT system. The LIFT parameter is set to be  $1.6 \text{ J}/\text{cm}^2$  and 1-2 laser shots. In total, four microscaffolds are transferred onto a PDMS receiver, as shown in Figure **Figure 4.7c**. The Rhodamine B ink is not evident in this figure, but from the close-up image, we can identify that the Rhodamine B ink is loaded in the microscaffold, as indicated by the red color. **Figure 4.7d** presents the post-transfer characterization of the donor substrate. The comparison of the transferred and non-transferred microscaffolds further proves that negligible Rhodamine B ink is left on the donor substrate once a microscaffold is transferred. This guarantees no ink loss during the transfer process, which is of great interest for potential drug/functional ink delivery.

Then we conduct the subsequent ink release test, and the results are presented in **Figure 4.8**. A droplet of DI water is placed on top of these four microscaffolds, and images are captured after 2, 6, 10, 20, 40, and 60 mins. From **Figure 4.8a** to **Figure 4.8e**, it can be concluded that the Rhodamine B ink filled in the microscaffolds can be released when immersed in DI water.

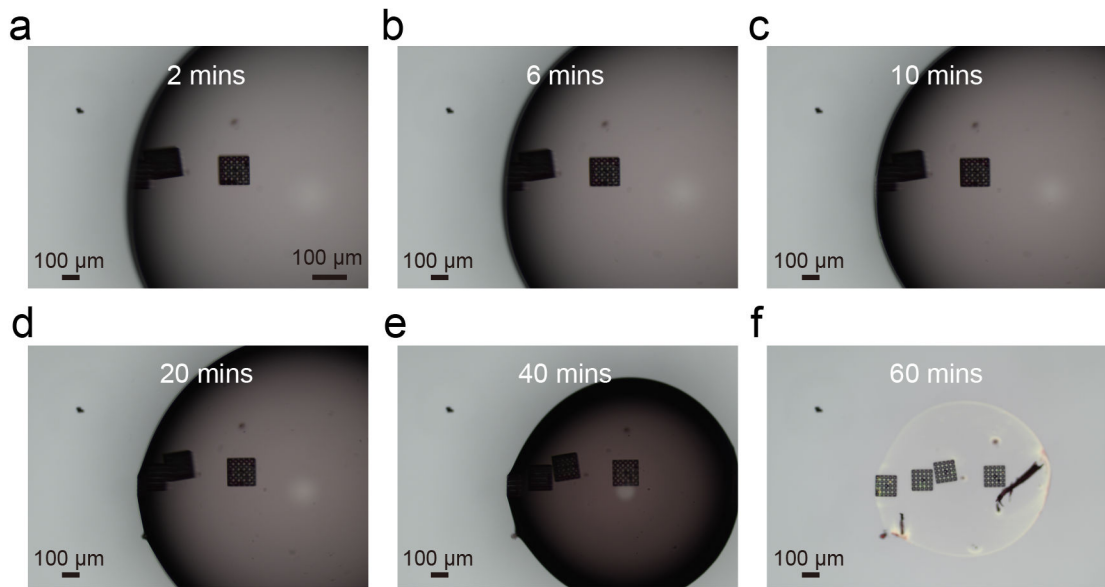


Figure 4.8: **Rhodamine B ink release experiment after LIFT process.** (a-f). Rhodamine B ink release process when placing one droplet of DI water onto these microcaffolds. Images are captured at 2, 6, 10, 20, 40, and 60 mins after placing the DI water. The color change of the DI water indicates the release of the ink. In (f), the water droplet evaporates completely.

At the beginning (2 mins), the droplet has no color. As time evolves, the color of the droplet becomes red, which is a joint result of the ink release and water volume reduction. Finally, the DI water evaporates completely, leaving the microcaffold and the Rhodamine B on the PDMS surface, as shown in **Figure 4.8f**.

This proof-of-concept demonstrates that microcaffolds filled with water-based ink are successfully transferred to another substrate by the LIFT method and be used as a drug/ink delivery system.

#### 4.4.3 Programmed transfer of TPL structures

An array of TPL-fabricated microcaffold structures are successfully transferred. **Figure 4.9** presents the optical image of this  $7 \times 7$  microcaffold array (microcaffold size:  $100 \times 100 \times 100 \mu\text{m}^3$ ) on the donor after the laser writing (structure design shown in **appendix Figure A.40**). The pitch distance for two consecutive scaffolds is  $200 \mu\text{m}$ . Slightly different from the demonstrations in **Chapter 3**, which uses a constant pitch distance of  $1000 \mu\text{m}$ , here we introduce a varying pitch distance strategy to cover a large area with fewer microstructures.

**Figure 4.10a** presents the  $7 \times 7$  microcaffold arrays transferred onto a PDMS-coated 4-inch wafer with a single laser pulse ( $1.6 \text{ J}/\text{cm}^2$ ). The g-code file controlling the transfer process is provided in **appendix Figure A.41** and the whole transfer process is less than 50 s, which shows

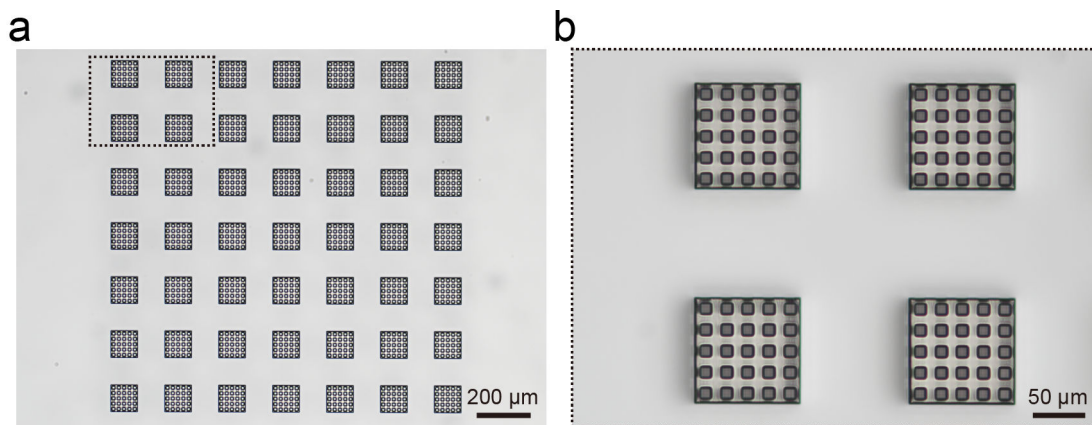


Figure 4.9:  $7 \times 7$  microsccaffold array on the donor. (a). Optical image presenting the microsccaffold array. The pitch distance is  $200 \mu\text{m}$ . (b). The high-magnification image of the dashed area in (a), showing a  $2 \times 2$  arrays. The scaffold has a pore size of  $10 \mu\text{m}$ .



Figure 4.10: **Transfer result of the microsccaffold array.** (a). Simple sketch showing the distribution of the 49 microscavolds on the receiver after transfer. In vertical and horizontal directions, the pitch distance varies from  $2000$  to  $12000 \mu\text{m}$ . (b). Optical image of the 4-inch receiver with all the 49 transferred microscavolds, forming a  $7 \times 7$  array with varying pitch distance. (c). High-magnification image of Region 1. A  $2 \times 2$  scaffold array is displayed in this image with a pitch distance of  $2000 \mu\text{m}$ . (d). High-magnification image of 1 scaffold in (c).

LIFT is an excellent candidate for transferring TPL-fabricated microstructures on a large scale with a high-throughput rate. For each row, the pitch distance increases from  $2000 \mu\text{m}$  to  $12000 \mu\text{m}$  with an increment of  $2000 \mu\text{m}$ , and the pitch distance variation applies to each column as well. As a result, this  $7 \times 7$  array on the wafer accounts for an area of  $42 \times 42 \text{ mm}^2$ , while these 49 microscavolds only cover an area of  $1.4 \times 1.4 \text{ mm}^2$  on the donor substrate. Therefore, programming the transfer process achieves a 900-fold increase in the area. **Figure 4.10b** shows  $2 \times 2$  arrays with a pitch distance of  $2000 \mu\text{m}$ . The slight rotation of the microsccaffold in **Figure 4.10c** is caused by the rotation angle discussed in **Chapter 3**.

## 4.5 Conclusion

In this chapter, we present the transfer of TPL-fabricated microstructures by LIFT. Several parameters are first investigated, including the scaffold pore size, scaffold size, and supporting layer. The pore size investigation reveals that when the pore-to-backbone-beam ratio increases, the scaffold is less likely to be transferred, even with multiple laser shots, due to the fragility of the scaffolds. The maximum ratio for successful transfer is 0.7, and a value of 0.9 (corresponding to a pore size of 18  $\mu\text{m}$  with a backbone beam size of 2  $\mu\text{m}$ ) fails to trigger the transfer. As for the scaffold size experiments, microstructures with three different sizes are prepared and tested. The transfer results indicate that the maximum size of the structure to be transferred by the LIFT setup is 220  $\mu\text{m}$ . To transfer fragile microscaffolds and extend the possible scaffold size range, a smaller supporting layer is introduced. The presented results show that successful transfer is achievable with this additional layer, both for fragile and much larger scaffolds.

Moreover, several demonstrations are provided to show the practicability of LIFT to transfer microstructures. The first example is the transfer of T-shape microcomponents into a PDMS microfluidic channel. The experimental result confirms that precise transfer of the microstructure to the targeted position is achievable, and this example paves the way for placing microstructures that require functionalization into microchannels without influencing the microchannel properties. The following demonstration shows the potential of LIFT to transfer functional ink-filled microscaffolds to targeted receivers while keeping the ink free from leakage. The following ink release tests prove that the loaded ink can be released with proper conditions. In the last, we demonstrate an upscaled transfer of a  $7 \times 7$  array, which proves that LIFT is compatible with the massive transfer of TPL microstructures. All the transfer results reported in this chapter lays a solid foundation for the exploration of transferring complex and fragile microstructures in a damage-free way.





# 5 Conclusion and Outlook

In this chapter, we summarize the main results obtained from the thesis and propose possible research plans for future work.

## 5.1 Conclusion

This thesis starts with a systematic study of four different variables that influence the results of transferring SU-8 microdisks by LIFT. The optimized parametric combination guarantees successful and damage-free transfer of SU-8 microdisks with high transfer precision. Then we functionalize the SU-8 microdisks with metallic QR codes and temperature sensors and perform the transfer, with subsequent functionality verification. Besides transfers of the two functional microdevices, transfer demonstrations, including large-scale transfer of SU-8 microdisks and transfer of SU-8 microdisks onto non-planar receivers, are discussed to reveal the capability of LIFT. Lastly, the transfer is further extended to TPL-fabricated complex and fragile microstructures. Below is the summary of the contribution of this thesis:

### 1. Parametric study of four variables that influence the SU-8 microdisk transfer result

Four variables are studied in detail, including the laser fluence, PI thickness, SU-8 thickness and donor-to-receiver gap distance. Laser fluence experiments define two transfer regimes of SU-8 microdisks: no transfer (lower laser fluence, e.g.,  $0.32 \text{ J/cm}^2$ ) and successful transfer (sufficient laser fluence, e.g.,  $\geq 0.96 \text{ J/cm}^2$ ). Specifically, the difference in the PI blister dimension with/without the SU-8 microdisk is experimentally verified. The results prove that the SU-8 microdisk suppresses the PI blister's volume expansion, and part of the energy for PI blister volume expansion is used for SU-8 peeling-off process and the subsequent forward motion to the receiver substrate. This result also proves that PI blister rupture is less likely to happen with the existence of the SU-8 microdisk.

As for the investigation of PI thickness, a thin PI film (1  $\mu\text{m}$ ) results in a ruptured PI blister, even in the presence of a SU-8 microdisk. PI film thicker than 1  $\mu\text{m}$  enables the successful transfer of SU-8 microdisks without the PI blister rupture, which results from the mechanical resistance of the thicker PI film to the influence of the laser fluence. Subsequently, SU-8 microdisk samples with four different thicknesses are prepared and tested to verify the structural integrity of transferred SU-8 microdisks. The results ascertain that thicker SU-8 microdisks are less susceptible to damage by the LIFT process. When the SU-8 thickness is no larger than 20  $\mu\text{m}$ , no intact microdisks are transferred, whereas successful transfer of damage-free SU-8 microdisks is achieved when the thickness increases to 50  $\mu\text{m}$ . The last variable being explored is the donor-to-receiver gap distance. The results reveal that with a smaller gap distance, SU-8 microdisks are able to be transferred with high precision. When the gap distance reaches a large value (e.g., 370  $\mu\text{m}$ ), distinguishable lateral displacement, rotation and flipping occur. The parametric study in this chapter lays a solid foundation for functional microdevices/microstructures transfer in the following chapters.

### 2. SU-8-supported microdevice transfer demonstrations

With the optimized variable combinations mentioned above, functional microdevices, consisting of SU-8 microdisks and metallic structures on top of them, are transferred to various receivers. The first type of microdevices being tested is SU-8-supported QR codes. These QR codes are transferred onto different receivers by LIFT, and the post-transfer analysis is conducted by checking their readability. Three types of adhesion tests are performed to examine the adhesion force between transferred SU-8 microdisks and a series of receivers. The results reveal that transferred SU-8 microdisks have strong adhesion on receivers, especially after thermal annealing treatment. Another experiment verifies the survival of transferred SU-8 microdisks under harsh conditions, i.e., immersion in DI water. The second demonstration is the transfer of SU-8-supported temperature sensors. The transferred temperature sensor contacts electrically with the prepatterned electrodes on the receiver and the subsequent TCR measurement of the temperature sensor further reveals that the electrical functionality of the temperature sensor is well-preserved. Besides these two single microdevice transfer demonstrations, we broaden the LIFT applications to the massive transfer of these microdisks in an automated prototype. The flipping phenomenon of SU-8 microdisks during the up-scaled transfer process is alleviated by increasing the dwelling time and correcting the wafer rotation. A 90 % yield rate is achieved with a  $40 \times 40$  array transfer demonstration. Finally, the LIFT system is applied to demonstrate transfers of SU-8 microdisks onto non-planar surfaces, highlighting the contactless characteristics and receiver diversity of the LIFT technique. All the results in this chapter confirm that functional microdevice transfers can be accomplished individually and on a large scale, both on conventional

planar surfaces and non-planar receivers.

### 3. TPL-fabricated microstructure transfer demonstrations

As a classical microstructure, microcaffolds with different pore sizes are first transferred. Transfer results reveal that LIFT is able to transfer microcaffolds with various pore sizes. However, if the pore size is too large (e.g., 18  $\mu\text{m}$ , accounting for 90 % percent of the microcaffold size), even multiple laser shots fail to trigger the transfer, which can be ascribed to the breakage of the microcaffold by the PI blister. The dependence of the microcaffold size on the transfer result is then studied. In this experiment, microcaffold size varies from 100 to 220  $\mu\text{m}$ . For 220  $\mu\text{m}$  large microcaffold, several 3.2 J/cm<sup>2</sup> laser pulses are required to guarantee the transfer, which can be taken as the dimension limit of the transferable microcaffold using the LIFT system. To overcome the current size limitations of microcaffolds and transfer fragile microcaffolds, a small supporting layer is added between the donor substrate and the microcaffold. As a result, fragile microcaffolds (pore size of 18  $\mu\text{m}$ ) and large microcaffolds (dimension size of 880  $\mu\text{m}$ ) are successfully transferred without damage. After the parametric study, the LIFT system is applied to transfer a T-shape microstructure into a microchannel. A high transfer precision can be achieved to place the microstructure in the targeted position. In addition, microcaffolds loaded with Rhodamine B ink are transferred onto the PDMS receiver without ink leakage and the subsequent ink release test proves that such inks can be easily released. In the last demonstration, we apply the large-scale transfer strategy to transferring a 7  $\times$  7 microcaffold array onto a 4-inch wafer.

For the first time, our experiments prove that LIFT is a facile but effective and time-saving approach to transfer TPL-fabricated complex and fragile microstructures. Our research also greatly broadens the choice of microstructures to be transferred by LIFT.

In general, the proposed methods and experimental outcomes in this thesis provide guidance for transferring functional microdevices/microstructures in a damage-free way with high precision. The parametric study clarifies the influences of four critical variables. Then the optimized parametric combination is utilized for functional SU-8-supported microdevice transfers. Last, LIFT is extended to transfer complex and fragile TPL-fabricated microstructures. All these prove that LIFT, capable of achieving non-destructive, high-precision and large-scale transfer, offers unparalleled advantages in the realization of the integration of diverse microdevices/microstructures, which has tremendous prospects in various fields such as ultrathin dies bonding and massive  $\mu\text{LEDs}$  placement.

### 5.2 Outlook

#### 1. PI thickness measurement after LIFT experiments

**Chapter 2** has experimentally investigated the formation of PI blister, which is due to the PI ablation process. Simulation results also confirm the reduction in the PI thickness at the laser-ablated area. However, a quantitative study of the thickness is still required. Since the PI blister is relatively thin and small, the focused ion beam (FIB) technique can be used to cut the PI blister and reveal the cross-section profile of a particular blister. Then the thickness of the ablated PI film can be obtained by the SEM image and compared with that corresponding to the nonablated area. This experiment will help determine the influence of laser fluence on the ablation of PI film.

#### 2. Quantifying the adhesion of SU-8 microdisks on the donor substrate

In **Chapter 2**, a thin layer of Ti is first sputtered onto the PI layer, followed by the SU-8 patterning process. The reason for adding the Ti layer is to reduce the adhesion between the SU-8 microdisks and the donor substrate <sup>[228,229]</sup>, which facilitates the SU-8 microdisk transfer. In a previous experiment, we find that when directly patterning SU-8 microdisks on the PI layer, the adhesion is too strong to allow the LIFT system to transfer SU-8 microdisks, even with  $3.2 \text{ J/cm}^2$  laser fluence (multiple laser shots). Therefore, the quantification of adhesion force is of great importance to understanding the SU-8 separation process.

Inspired by the micropillar lateral force tests discussed in **Chapter 3**, the adhesion force measurement on the normal direction can be performed by a microgripper system <sup>[221,222]</sup>. In order to grasp the SU-8 microdisk and apply normal load upon it, a T-shape SU-8 microstructure is supposed to be designed, as shown in **Figure 5.1**. TPL can be utilized to fabricate such a structure and subsequent microtensile testing can be employed to quantify the adhesion force between SU-8 microdisks and the donor substrate. This method also applies to quantifying the adhesion force between TPL-fabricated microscaffolds and the PI layer as mentioned in the previous chapter.

#### 3. Real-time observation of the microdevice separation process

Direct observation of the material/device transfer process is often used in LIFT experiments to understand the transfer dynamics and calculate the velocity of transferred materials/devices <sup>[72,165]</sup>. The proposed method to image the microdevice in the transfer process is shown in **Figure 5.2**. To shed light on the relationship between the laser pulse energy and the velocity of the transferred microdisk, a simple energy model can be established, as expressed below:

$$E_p = E_{ki} + E_{lost} \quad (5.1)$$

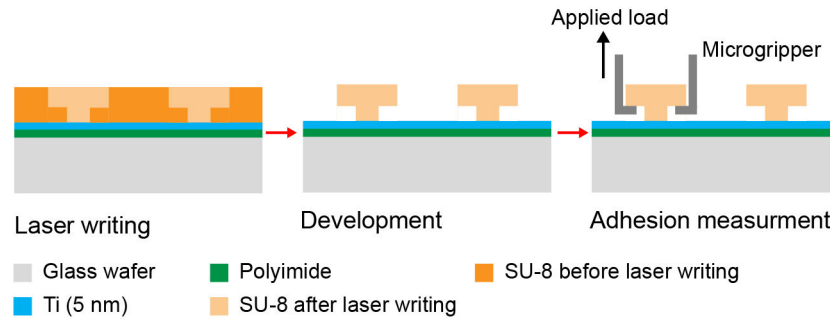


Figure 5.1: **Proposed adhesion test of SU-8 microdisks patterned on the donor substrate.** The adhesion test is performed by fabricating a T-shape SU-8 microstructure and applying normal load by the microgripper to separate it from the donor substrate.

where  $E_p$ ,  $E_{ki}$  and  $E_{lost}$  denote the laser fluence, the kinetic energy of the flying microdisk and the energy consumed by other processes. As discussed before, a series of processes (PI film ablation, PI blister expansion, SU-8 microdisk delamination from the donor substrate, etc.) consume the laser fluence and only a small portion of the laser fluence contributes to the kinetic energy. The kinetic energy of the flying microdisk, as a function of the velocity, can be written as:

$$E_{ki} = \frac{1}{2} \times m \times v^2 \quad (5.2)$$

where  $m$  and  $v$  represent the mass and velocity of the microdisk.

Therefore, with the velocity data obtained by the high-speed camera, the kinetic energy can be calculated. Furthermore, we can determine the efficiency ( $\eta$ ) of the transfer process as follows:

$$\eta = \frac{E_{ki}}{E_p} \quad (5.3)$$

By calculating the efficiency value under different laser energies, the relationship between the efficiency and laser fluence can be plotted, which can offer guidance in choosing the proper laser fluence for microdevice transfer.

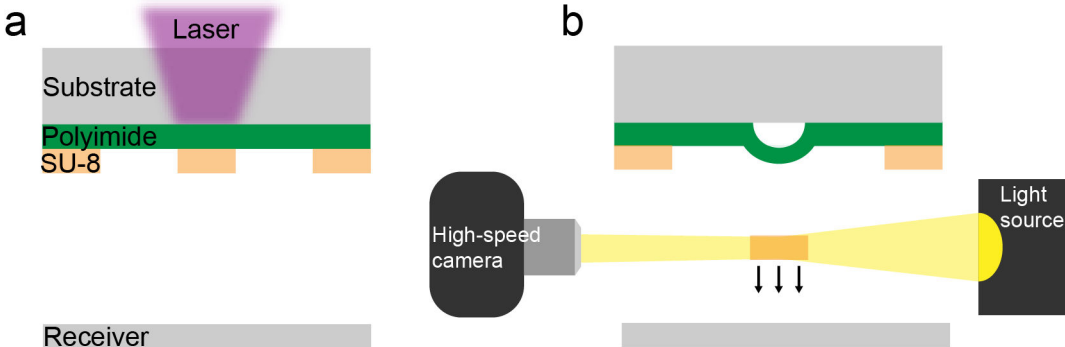


Figure 5.2: **Time-resolved imaging of SU-8 microdisk velocity.** The imaging system consists of a high-speed camera and a light source.

# A An appendix

## A.1 Metal number patterned SU-8 microdisk



Figure A.1: **Metal number patterned SU-8 microdisk.** Ten SU-8 microdisks are shown in the image. Metal numbers (Cr/Au, 5/50 nm) "10", "20", "30", and "40" are patterned on top of the SU-8 microdisks by stencil lithography.

## A.2 SU-8 microdisk transfer with a laser fluence of $0.32 \text{ J/cm}^2$

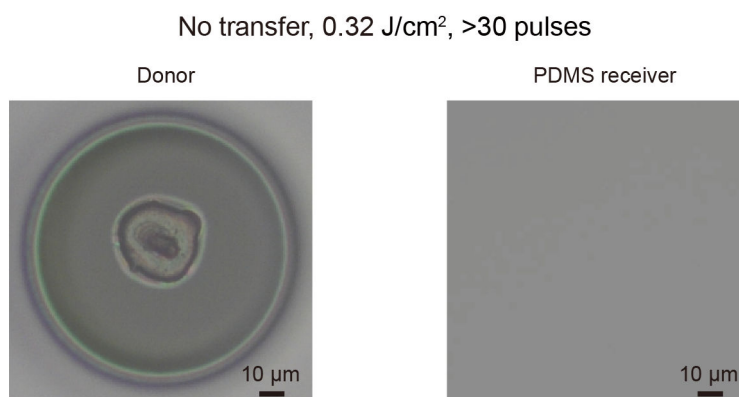


Figure A.2: **SU-8 microdisk transfer with laser fluence of  $0.32 \text{ J/cm}^2$** . The SU-8 microdisk fails to be transferred even with multiple shots. The donor image shows that the center of the SU-8 is damaged by laser shots, and no SU-8 microdisk is transferred onto the corresponding PDMS receiver.



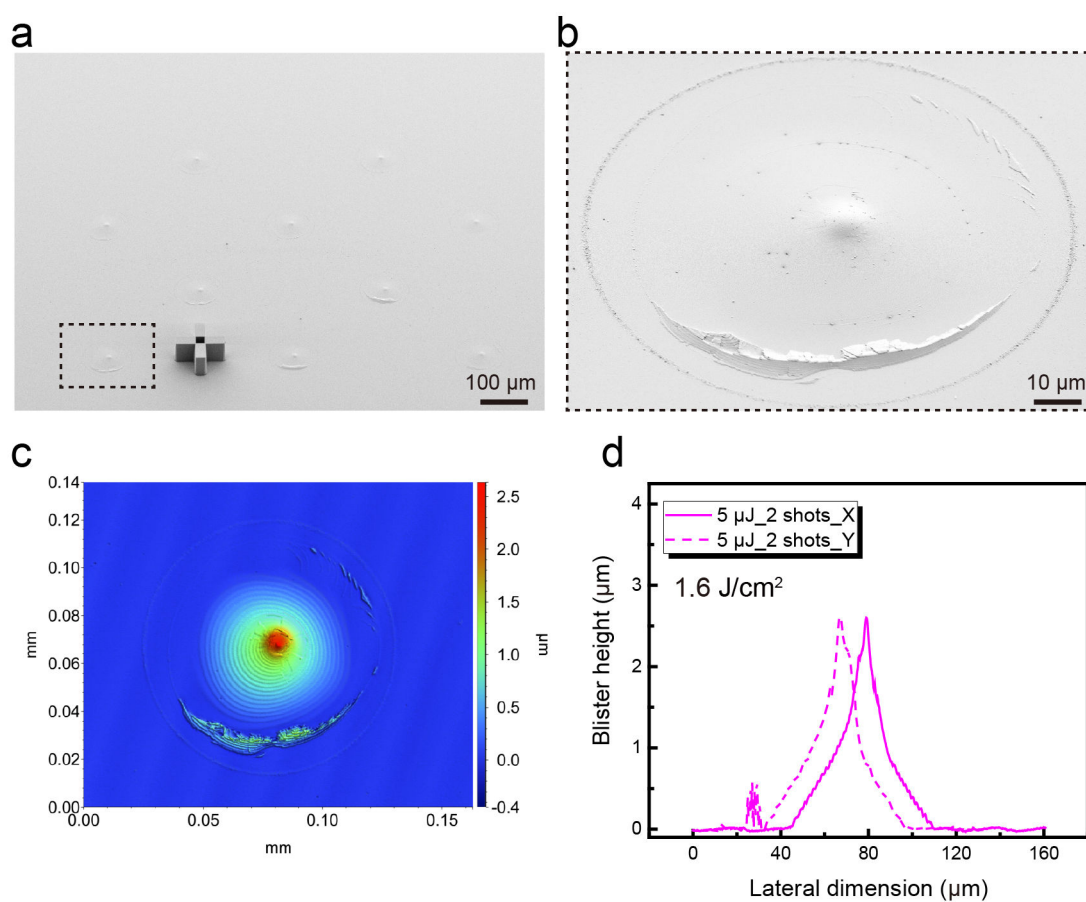
A.3 PI blister created by 1.6 J/cm<sup>2</sup> laser fluence

Figure A.3: **PI blister created by 1.6 J/cm<sup>2</sup> laser fluence.** (a). SEM image of ten blisters after the transfer process. (b). Magnified SEM image of one blister in (a). (c). Contour map of the PI blister. (d). The cross-sectional profile of the PI blister.

### A.4 PI blister created by $1.92 \text{ J/cm}^2$ laser fluence

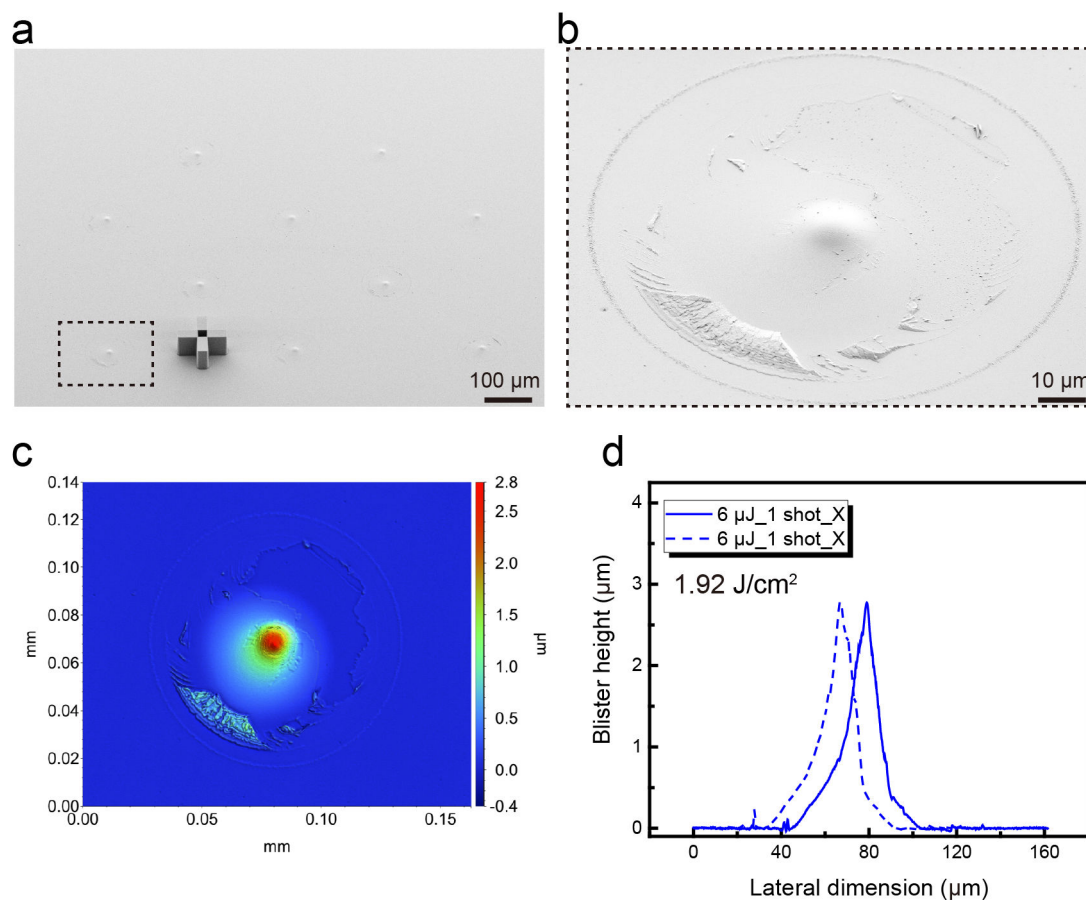


Figure A.4: **PI blister created by  $1.92 \text{ J/cm}^2$  laser fluence.** (a). SEM image of ten blisters after the transfer process. (b). Magnified SEM image of one blister in (a). (c). Contour map of the PI blister. (d). The cross-sectional profile of the PI blister.

A.5 PI blister created by 2.56 J/cm<sup>2</sup> laser fluence

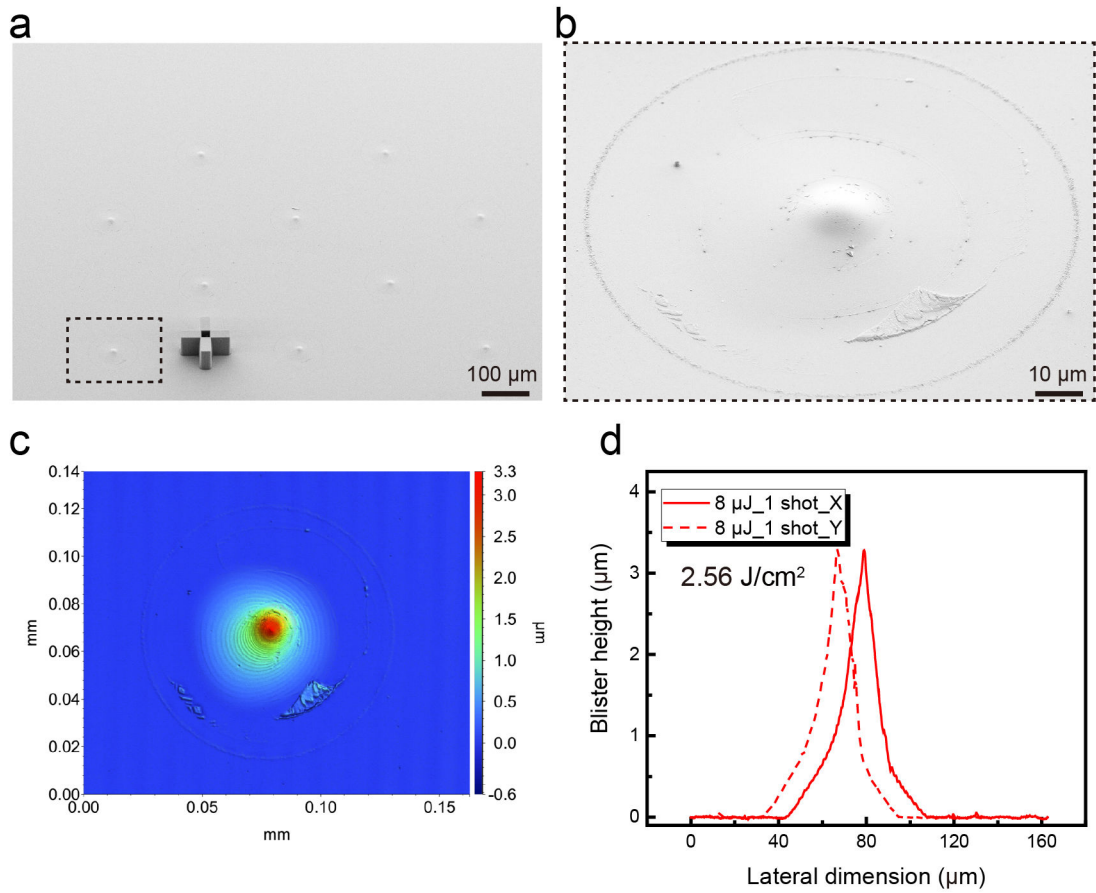


Figure A.5: **PI blister created by 2.56 J/cm<sup>2</sup> laser fluence.** (a). SEM image of ten blisters after the transfer process. (b). Magnified SEM image of one blister in (a). (c). Contour map of the PI blister. (d). The cross-sectional profile of the PI blister.

### A.6 PI blister created by $3.2 \text{ J/cm}^2$ laser fluence

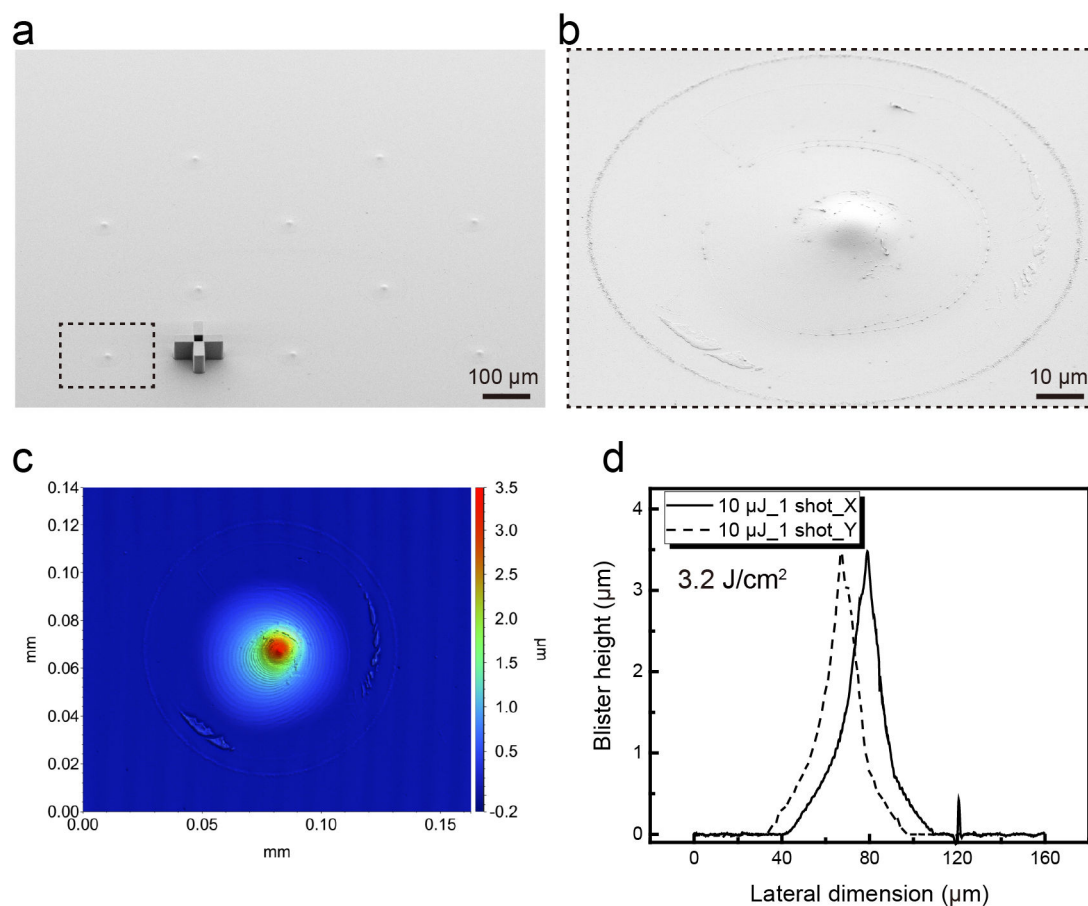


Figure A.6: **PI blister created by  $3.2 \text{ J/cm}^2$  laser fluence.** (a). SEM image of ten blisters after the transfer process. (b). Magnified SEM image of one blister in (a). (c). Contour map of the PI blister. (d). The cross-sectional profile of the PI blister.

## A.7 PI blister volume calculation in the presence of the SU-8 microdisk (5 $\mu\text{m}$ thick PI)

```
In [2]: from scipy import integrate
import math
```

10uJ cal.

```
In [38]: # define the function
# Lorenz distribution

def f(x,y0,xc,w,A):
    return abs(math.pi*x*(y0+(2*A/math.pi)*(w/(4*(x-xc)**2+w**2))))
v,err = integrate.quad(f,-38,30, args=(-0.079,-0.98,17.137,88.358))

print(v)
```

1851.3011682199672

8uJ cal.

```
In [36]: def f(x,y0,xc,w,A):
    return abs(math.pi*x*(y0+(2*A/math.pi)*(w/(4*(x-xc)**2+w**2))))
v,err = integrate.quad(f,-35,30, args=(-0.0729,-1.094,16.198,79.196))

print(v)
```

1590.2123510008391

6uJ cal.

```
In [37]: def f(x,y0,xc,w,A):
    return abs(math.pi*x*(y0+(2*A/math.pi)*(w/(4*(x-xc)**2+w**2))))
v,err = integrate.quad(f,-30,30, args=(-0.0555,-1.242,14.623,60.968))

print(v)
```

1138.1387303380027

5uJ cal.

```
In [11]: def f(x,y0,xc,w,A):
    return abs(math.pi*x*(y0+(2*A/math.pi)*(w/(4*(x-xc)**2+w**2))))
v,err = integrate.quad(f,-35,30, args=(-0.0823,-1.057,21.225,76.562))

print(v)
```

1635.3547494811098

3uJ cal.

```
In [51]: def f(x,y0,xc,w,A):
    return abs(math.pi*x*(y0+(2*A/math.pi)*(w/(4*(x-xc)**2+w**2))))
v,err = integrate.quad(f,-30,30, args=(-0.1364,-1.152,30.847,82.382))

print(v)
```

1606.289656110019

Figure A.7: **PI blister volume calculation in the presence of the SU-8 microdisk (5  $\mu\text{m}$  thick PI).** The blister volume calculation is based on the Lorentzian peak fitting and subsequent integration.

### A.8 Blisters created by $1.6 \text{ J/cm}^2$ laser fluence (2 shots) on the free surface of PI

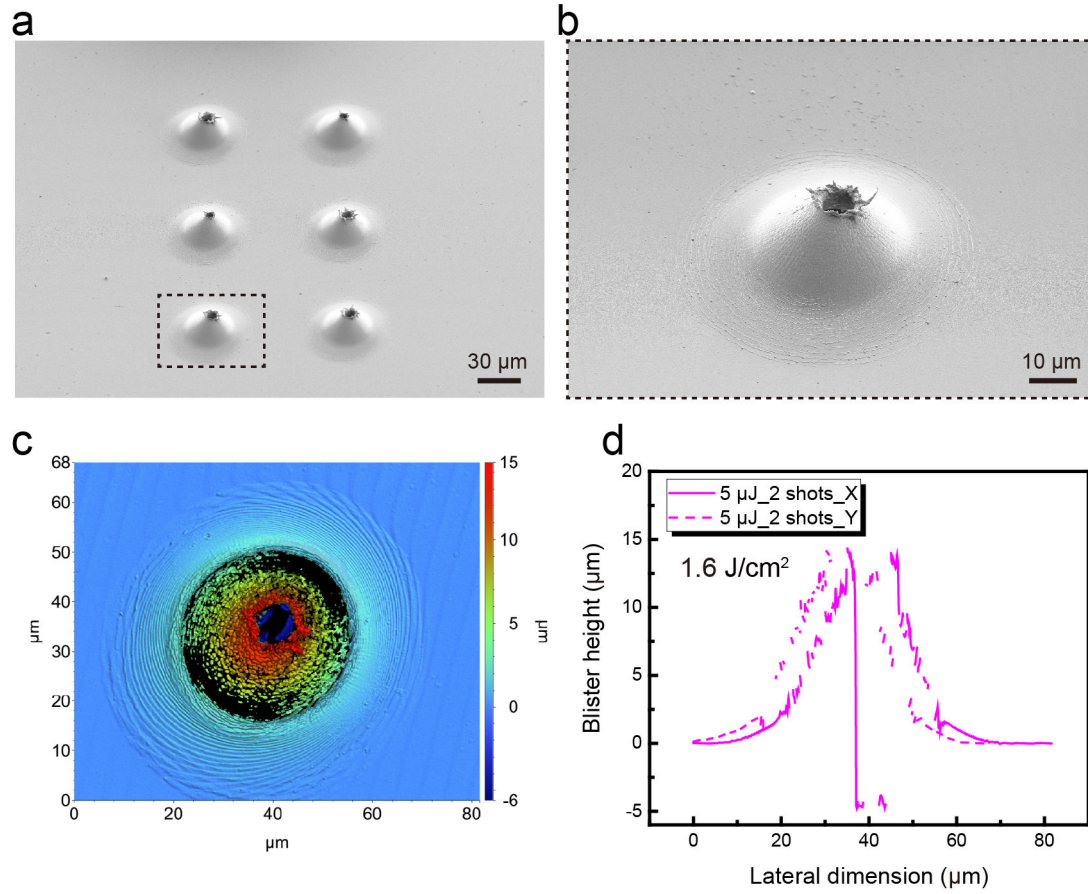


Figure A.8: **Blisters created by  $1.6 \text{ J/cm}^2$  laser fluence (2 shots) on the free surface of PI.** (a). SEM image presenting the six blisters. (b). Magnified SEM image of one blister. (c). Contour map of the PI blister. (d). Cross-section profile of the PI blister.

**A.9 Blisters created by  $1.92 \text{ J/cm}^2$  laser fluence (1 shot) on the free surface of PI**

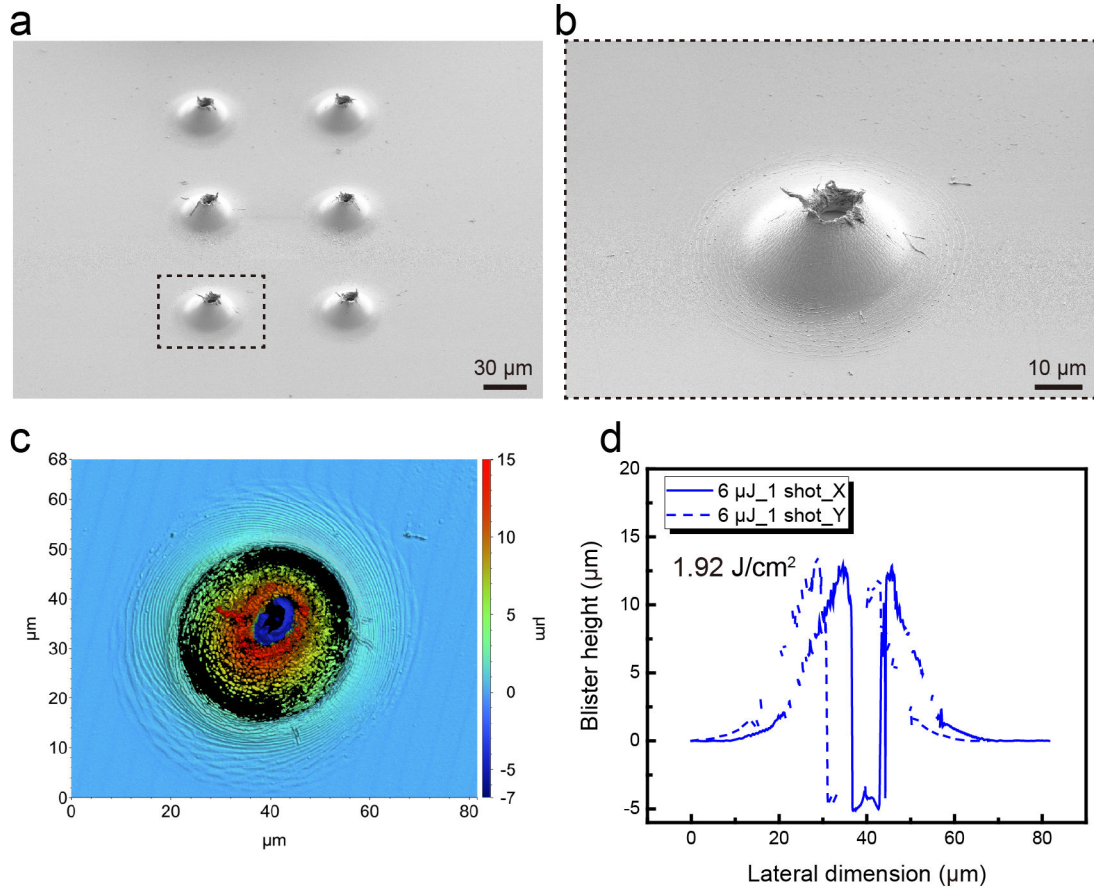


Figure A.9: **Blisters created by  $1.92 \text{ J/cm}^2$  laser fluence (1 shot) on the free surface of PI.** (a). SEM image presenting the six blisters. (b). Magnified SEM image of one blister. (c). Contour map of the PI blister. (d). Cross-section profile of the PI blister.

### A.10 Blisters created by $2.56 \text{ J/cm}^2$ laser fluence (1 shot) on the free surface of PI

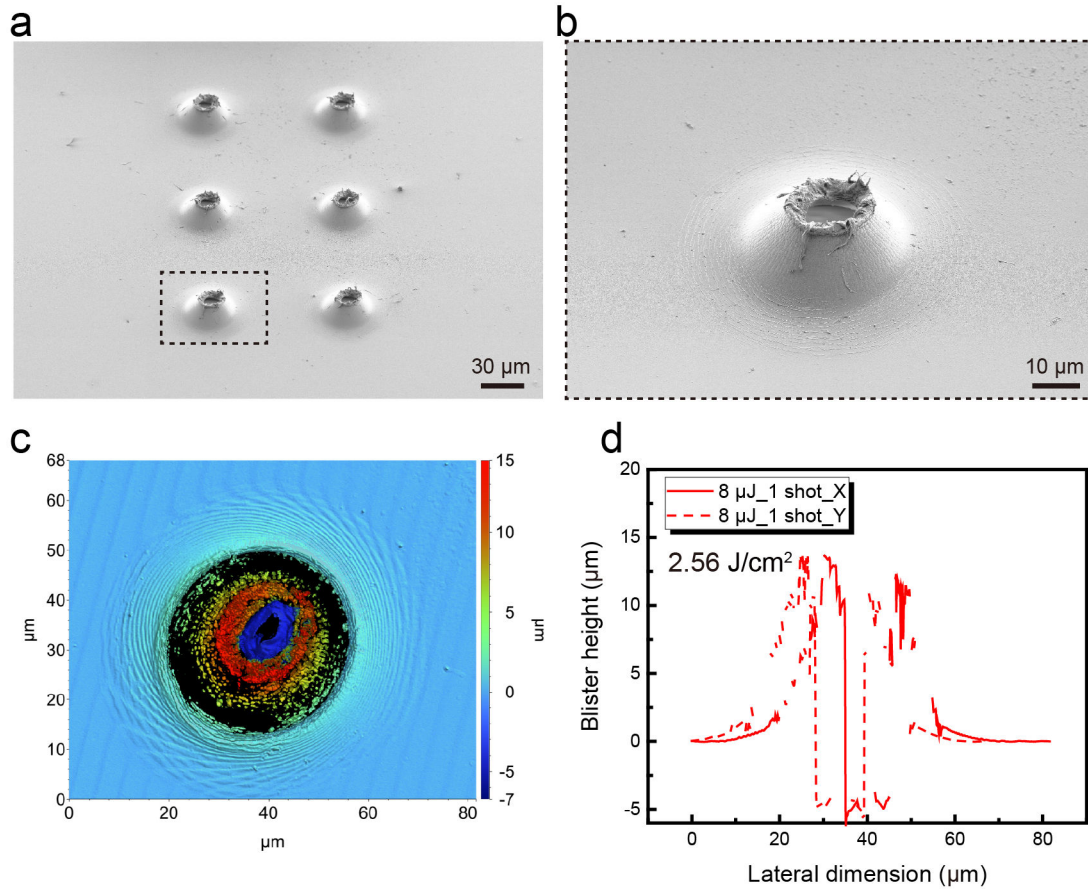


Figure A.10: **Blisters created by  $2.56 \text{ J/cm}^2$  laser fluence (1 shot) on the free surface of PI.** (a). SEM image presenting the six blisters. (b). Magnified SEM image of one blister. (c). Contour map of the PI blister. (d). Cross-section profile of the PI blister.



**A.11 Blisters created by  $3.2 \text{ J/cm}^2$  laser fluence (1 shot) on the free surface of PI**

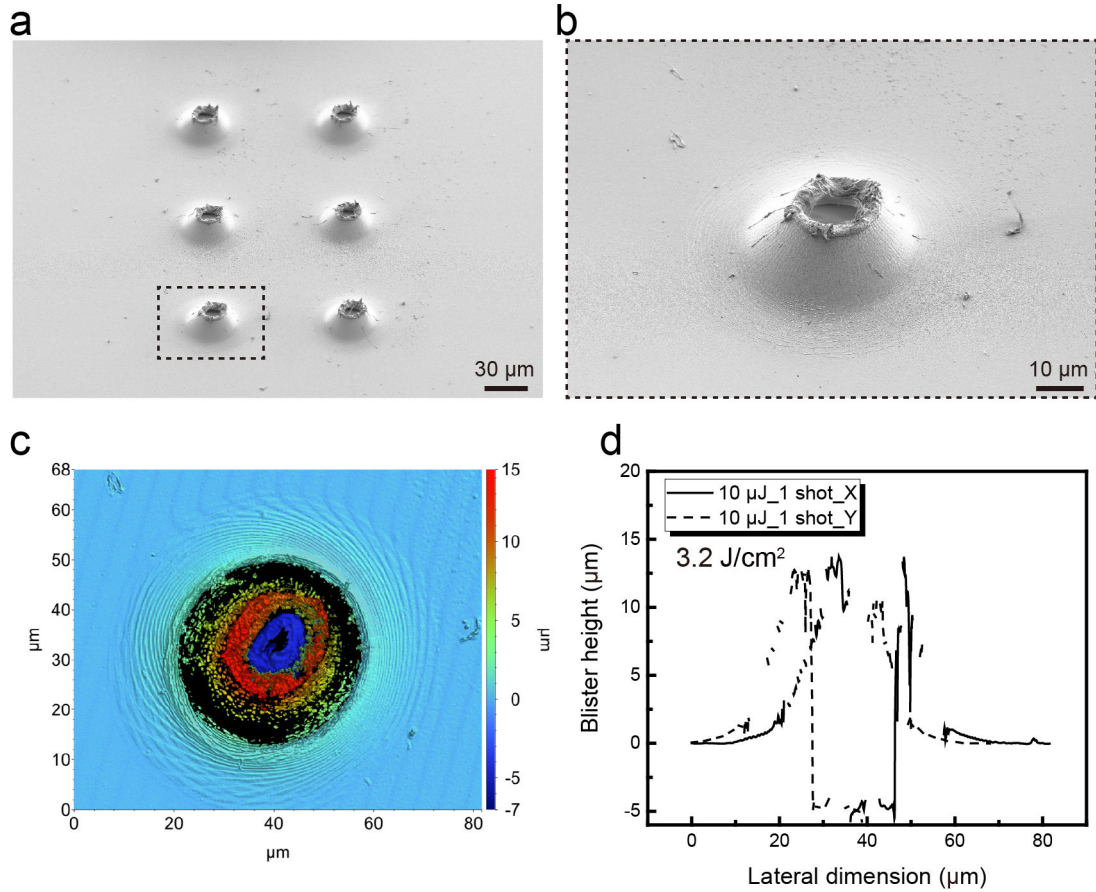


Figure A.11: **Blisters created by  $3.2 \text{ J/cm}^2$  laser fluence (1 shot) on the free surface of PI.** (a). SEM image presenting the six blisters. (b). Magnified SEM image of one blister. (c). Contour map of the PI blister. (d). Cross-section profile of the PI blister.

### A.12 PI Blisters created by $0.96 \text{ J/cm}^2$ & 1 shot on the free surface of PI

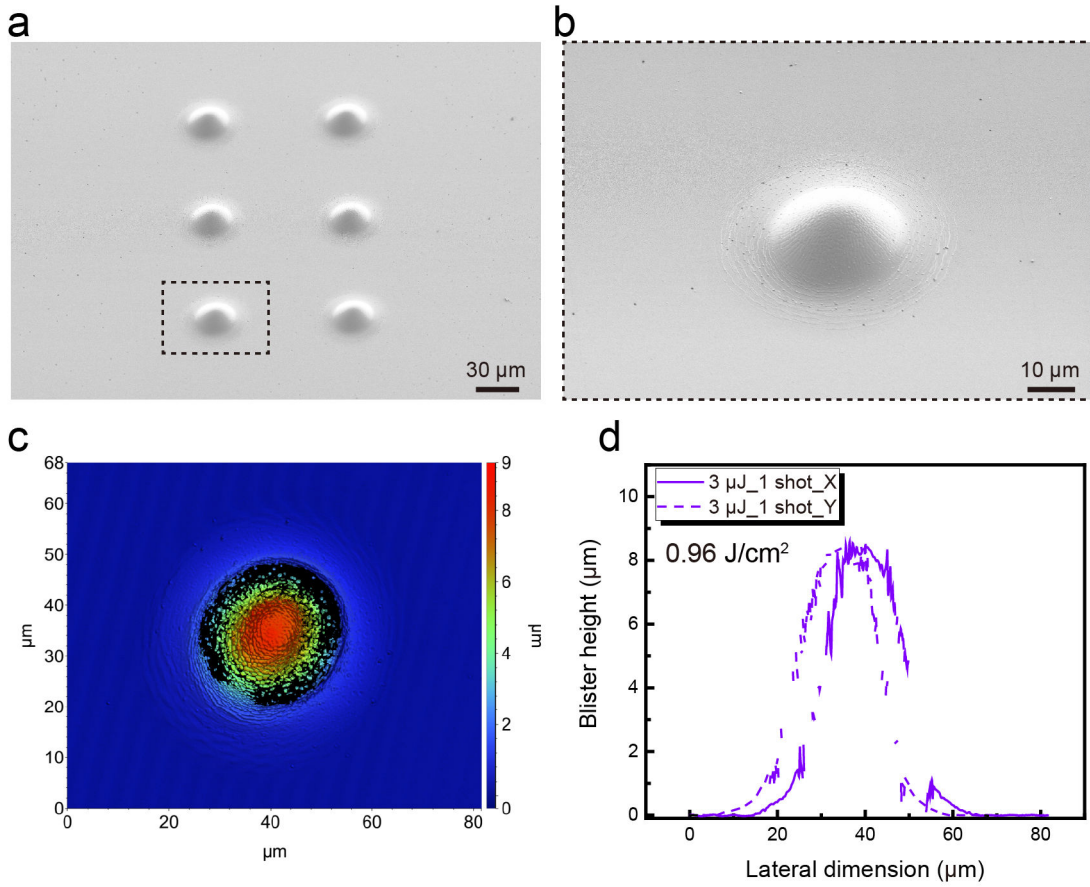


Figure A.12: **PI Blisters created by  $0.96 \text{ J/cm}^2$  & 1 shot on the free surface of PI.** (a). SEM image presenting the six blisters. (b). Magnified SEM image of one blister. (c). Contour map of the PI blister. (d). Cross-section profile of the PI blister.

**A.13 PI Blisters created by  $0.32 \text{ J/cm}^2$  & 1 shot on the free surface of PI**

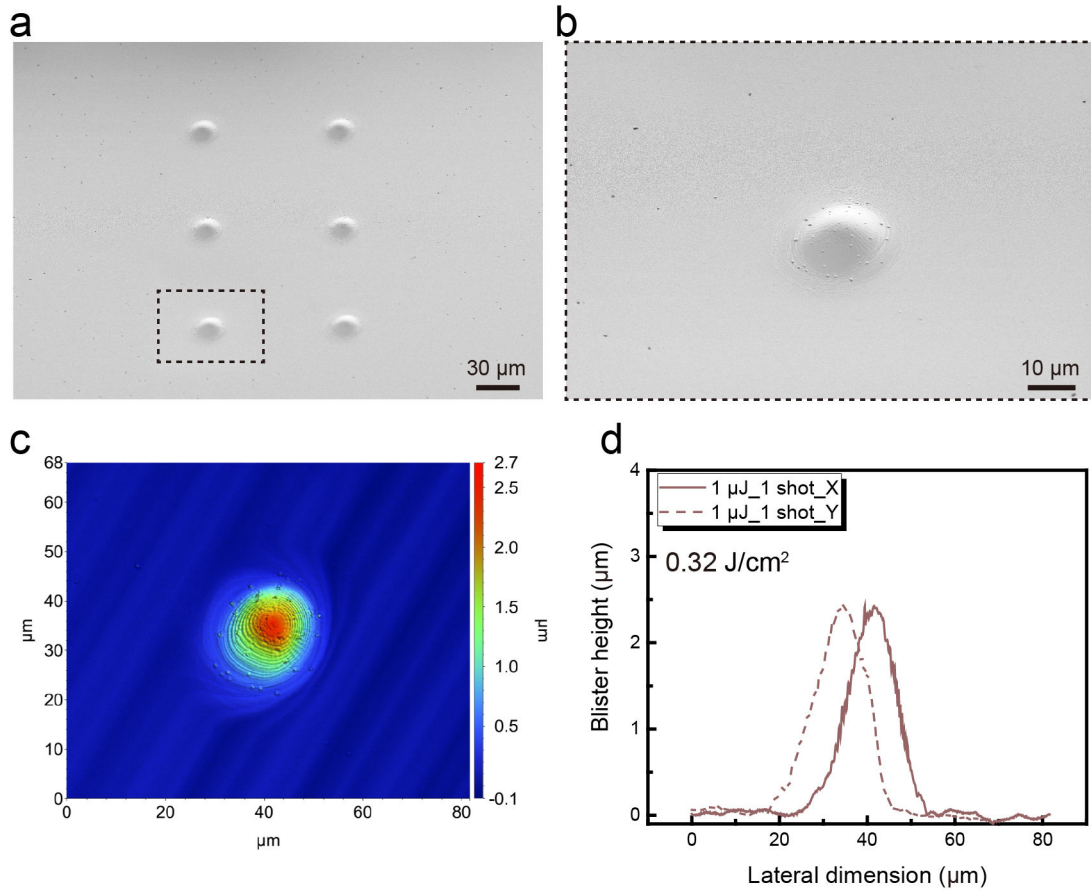


Figure A.13: **PI Blisters created by  $0.32 \text{ J/cm}^2$  & 1 shot on the free surface of PI.** (a). SEM image presenting the six blisters. (b). Magnified SEM image of one blister. (c). Contour map of the PI blister. (d). Cross-section profile of the PI blister.

### A.14 PI Blisters created by $0.32 \text{ J/cm}^2$ & 10 shots on the free surface of PI

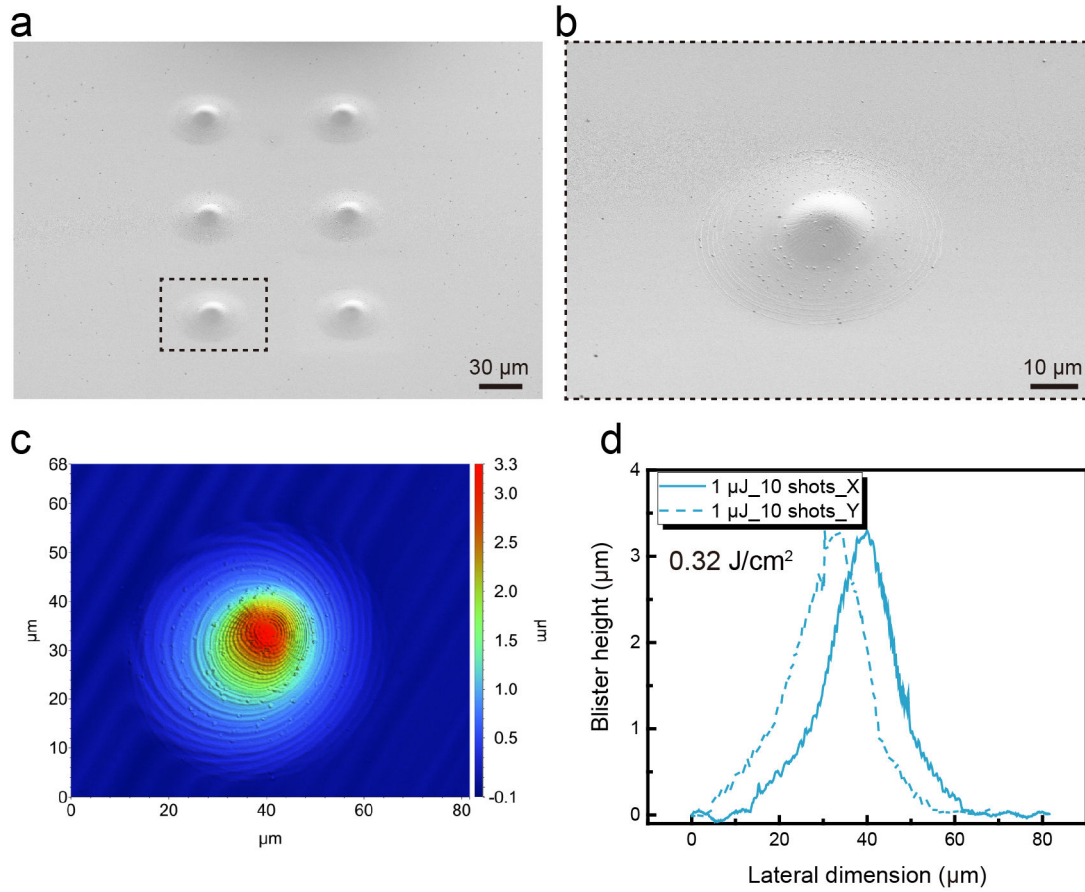


Figure A.14: **PI Blisters created by  $0.32 \text{ J/cm}^2$  & 10 shot on the free surface of PI.** (a). SEM image presenting the six blisters. (b). Magnified SEM image of one blister. (c). Contour map of the PI blister. (d). Cross-section profile of the PI blister.

## A.15 PI blister volume calculation in the absence of the SU-8 microdisk (5 $\mu\text{m}$ thick PI)

```
In [2]: from scipy import integrate
import math
```

**3uJ\_4shots\_cal.**

```
In [7]: # Define the function
# Gaussian distribution

def f(x,y0,xc,w,A):
    return abs(math.pi*x*(y0 + A/(w*math.sqrt(math.pi/(4*math.log(2)))))*math.exp(-4*math.log(
v,err = integrate.quad(f,-35,35, args=(0.106,-0.649,22.605,238.213))
print(v)
6145.2928112810805
```

**3uJ\_1shot\_cal.**

```
In [8]: def f(x,y0,xc,w,A):
    return abs(math.pi*x*(y0 + A/(w*math.sqrt(math.pi/(4*math.log(2)))))*math.exp(-4*math.log(
v,err = integrate.quad(f,-25,25, args=(-0.06,-0.803,19.219,181.971))
print(v)
3587.0786941445053
```

**1uJ\_10shots\_cal.**

```
In [15]: def f(x,y0,xc,w,A):
    return abs(math.pi*x*(y0 + A/(w*math.sqrt(math.pi/(4*math.log(2)))))*math.exp(-4*math.log(
v,err = integrate.quad(f,-25,25, args=(0.068,-1.138,18.375,58.582))
print(v)
1283.9359832526848
```

**1uJ\_1shot\_cal.**

```
In [16]: def f(x,y0,xc,w,A):
    return abs(math.pi*x*(y0 + A/(w*math.sqrt(math.pi/(4*math.log(2)))))*math.exp(-4*math.log(
v,err = integrate.quad(f,-15,15, args=(0.008,-0.467,12.576,32.065))
print(v)
427.9460330324896
```

Figure A.15: **PI blister volume calculation in the absence of the SU-8 microdisk (5  $\mu\text{m}$  thick PI).** The blister volume calculation is based on the Gaussian peak fitting and subsequent integration.

**A.16 PI Blisters created by  $0.96 \text{ J/cm}^2$  & 1 shot in the presence of the SU-8 microdisk (1  $\mu\text{m}$  thick PI)**

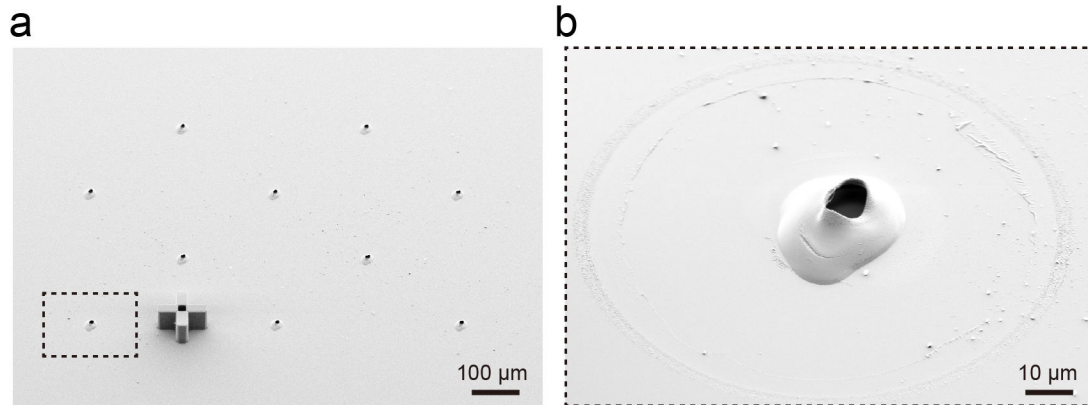
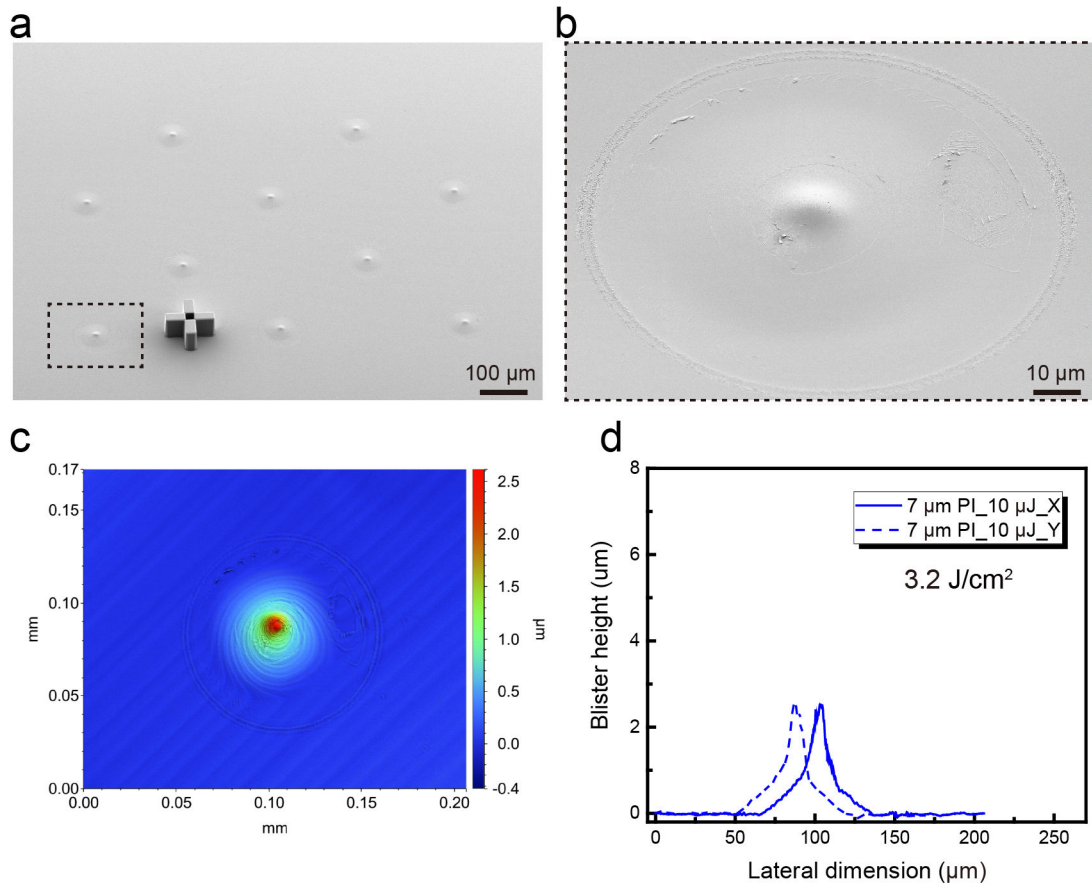


Figure A.16: **PI Blisters created by  $0.96 \text{ J/cm}^2$  & 1 shot in the presence of the SU-8 microdisk (1  $\mu\text{m}$  thick PI).** (a). SEM image presenting the ten blisters. (b). Magnified SEM image of one blister.

**A.17 PI Blisters created by  $3.2 \text{ J/cm}^2$  & 1 shot in the presence of the SU-8 microdisk (7  $\mu\text{m}$  thick PI)**

**A.17 PI Blisters created by  $3.2 \text{ J/cm}^2$  & 1 shot in the presence of the SU-8 microdisk (7  $\mu\text{m}$  thick PI)**



**Figure A.17: PI blister created by  $3.2 \text{ J/cm}^2$  laser fluence on a 7- $\mu\text{m}$ -thick PI film. (a). SEM image presenting the ten blisters. (b). Magnified SEM image of one blister. (c). Contour map of the PI blister. (d). Cross-section profile of the PI blister.**

### A.18 PI Blisters created by $3.2 \text{ J/cm}^2$ & 1 shot in the presence of the SU-8 microdisk (9 $\mu\text{m}$ thick PI)

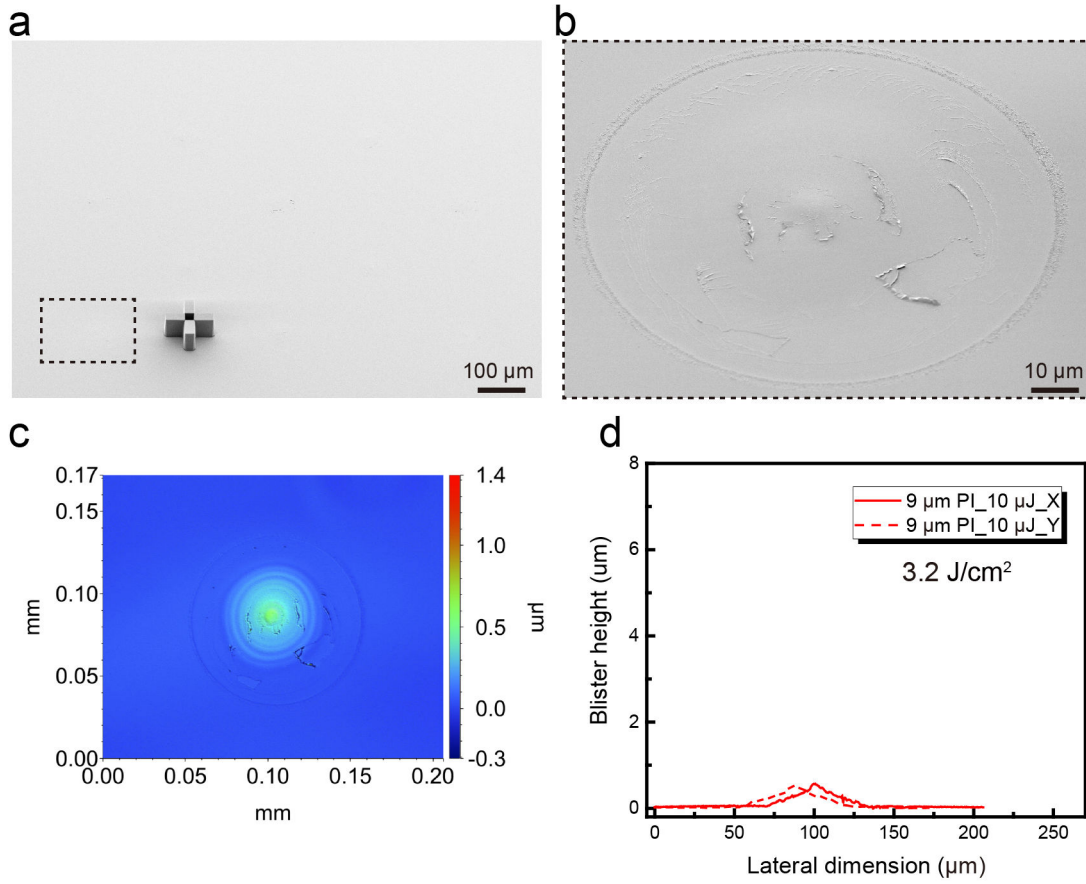


Figure A.18: **PI blister created by  $3.2 \text{ J/cm}^2$  laser fluence on a 9- $\mu\text{m}$ -thick PI film.** (a). SEM image presenting the ten blisters. (b). Magnified SEM image of one blister. (c). Contour map of the PI blister. (d). Cross-section profile of the PI blister.



**A.19 PI Blisters created by  $3.2 \text{ J/cm}^2$  & 1 shot in the presence of the SU-8 microdisk (11  $\mu\text{m}$  thick PI)**

**A.19 PI Blisters created by  $3.2 \text{ J/cm}^2$  & 1 shot in the presence of the SU-8 microdisk (11  $\mu\text{m}$  thick PI)**

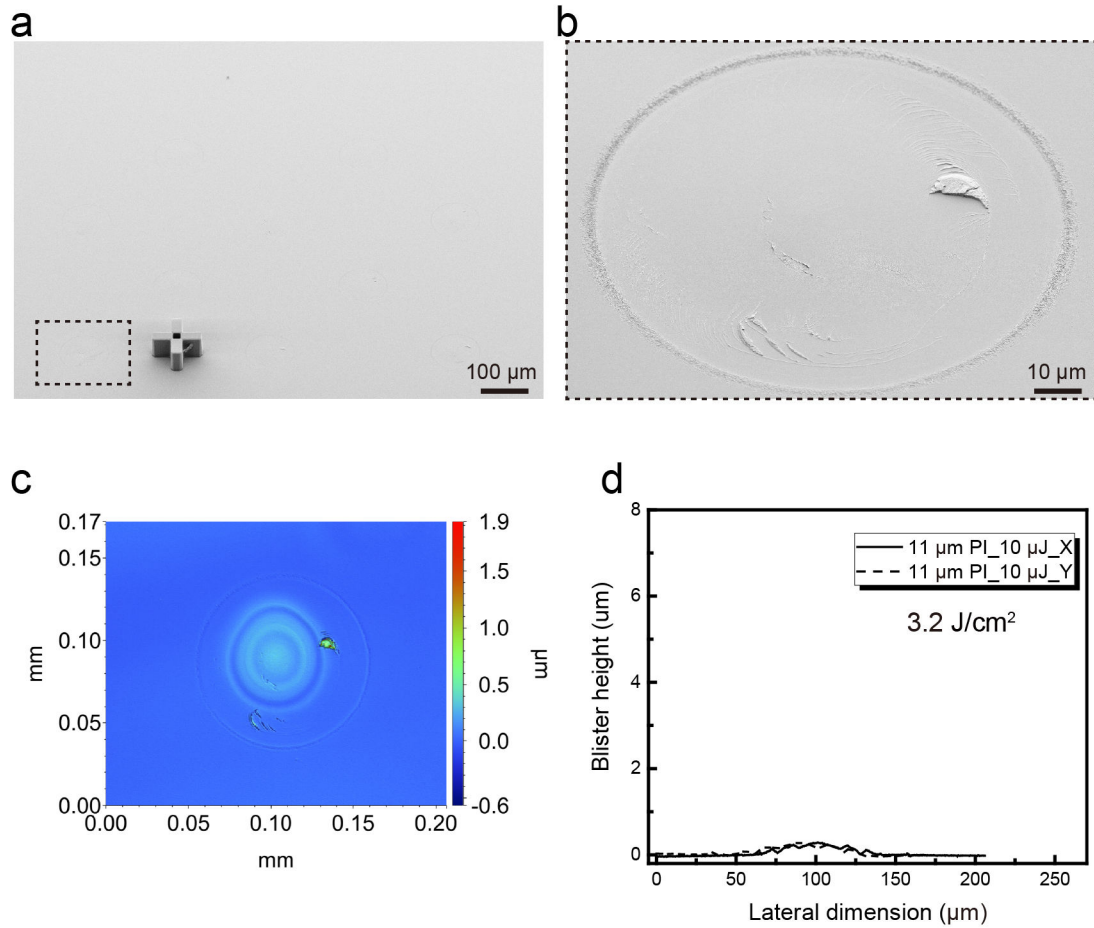


Figure A.19: **PI blister created by  $3.2 \text{ J/cm}^2$  laser fluence on an 11- $\mu\text{m}$ -thick PI film.** (a). SEM image presenting the ten blisters. (b). Magnified SEM image of one blister. (c). Contour map of the PI blister. (d). Cross-section profile of the PI blister.

## A.20 PI blister volume calculation in the presence of the SU-8 microdisk on different thick PI films

```
In [2]: from scipy import integrate
import math
```

10uJ&7um PI cal.

```
In [4]: # define the function
# Lorentz distribution

def f(x,y0,xc,w,A):
    return abs(math.pi*x*(y0+(2*A/math.pi)*(w/(4*(x-xc)**2+w**2))))
v,err = integrate.quad(f,-36.5,36.5, args=(-0.051,-1.04,16.31,60.991))

print(v)

1308.5563514857909
```

10uJ&3um PI cal.

```
In [5]: def f(x,y0,xc,w,A):
    return abs(math.pi*x*(y0+(2*A/math.pi)*(w/(4*(x-xc)**2+w**2))))
v,err = integrate.quad(f,-30.25,30.25, args=(-0.265,-0.47,23.28,254.723))

print(v)

5314.106063298359
```

10uJ&9um PI cal.

```
In [6]: def f(x,y0,xc,w,A):
    return abs(math.pi*x*(y0+(2*A/math.pi)*(w/(4*(x-xc)**2+w**2))))
v,err = integrate.quad(f,-38.1,38.1, args=(0.017,0.345,26.679,20.94))

print(v)

696.259007939116
```

10uJ&11um PI cal.

```
In [9]: def f(x,y0,xc,w,A):
    return abs(math.pi*x*(y0+(2*A/math.pi)*(w/(4*(x-xc)**2+w**2))))
v,err = integrate.quad(f,-39.05,39.05, args=(-0.051,-0.312,46.15,22.79))

print(v)

466.532254454341
```

Figure A.20: **PI blister volume calculation in the presence of the SU-8 microdisk on different thick PI films.** The blister volume calculation is based on the Lorentzian peak fitting and subsequent integration.

**A.21 PI Blisters created by  $3.2 \text{ J/cm}^2$  & 1 shot and  $0.96 \text{ J/cm}^2$  & 1 shot on the free surface of PI ( $1 \mu\text{m}$  thick PI)**

**A.21 PI Blisters created by  $3.2 \text{ J/cm}^2$  & 1 shot and  $0.96 \text{ J/cm}^2$  & 1 shot on the free surface of PI ( $1 \mu\text{m}$  thick PI)**

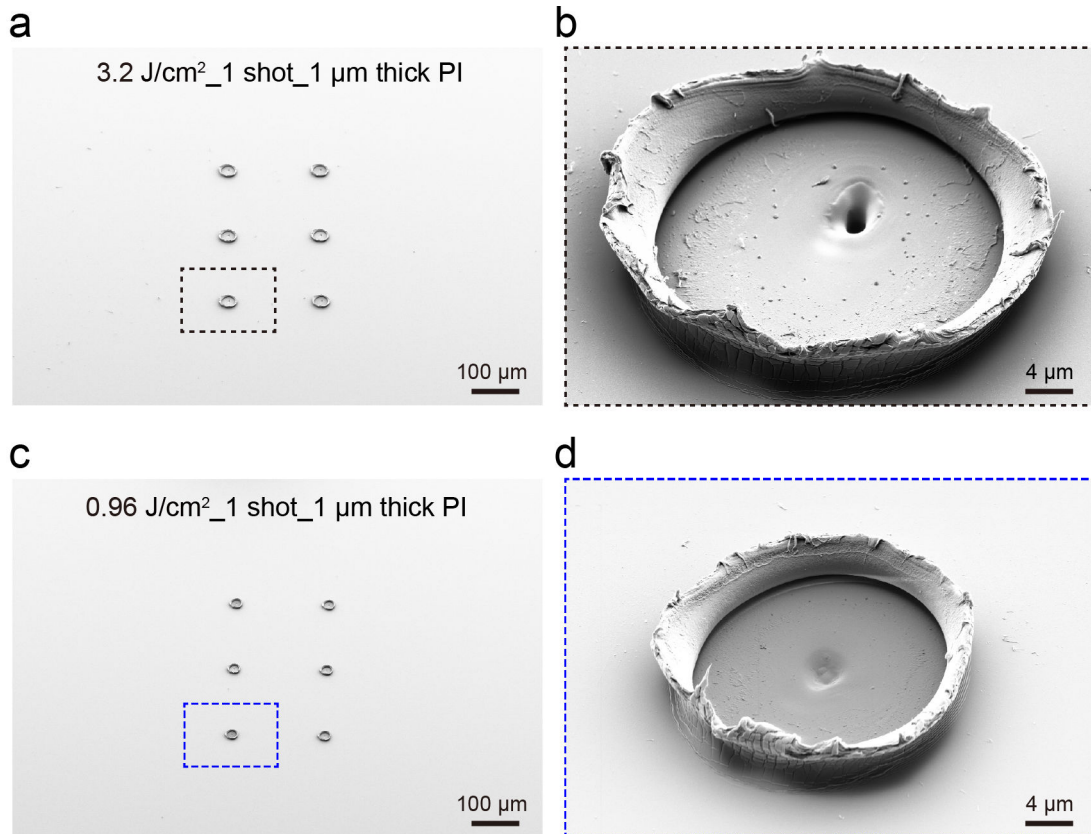


**Figure A.21: PI Blisters created by  $3.2 \text{ J/cm}^2$  & 1 shot and  $0.96 \text{ J/cm}^2$  & 1 shot on the free surface of PI ( $1 \mu\text{m}$  thick PI).** (a). SEM image presenting the six blisters created by  $3.2 \text{ J/cm}^2$  & 1 shot. (b). Magnified SEM image of one blister. (c). SEM image presenting the six blisters created by  $0.96 \text{ J/cm}^2$  & 1 shot. (d). Magnified SEM image of one blister.

## A.22 PI Blisters created by $3.2 \text{ J/cm}^2$ & 1 shot on the free surface of PI ( $3 \mu\text{m}$ thick PI)

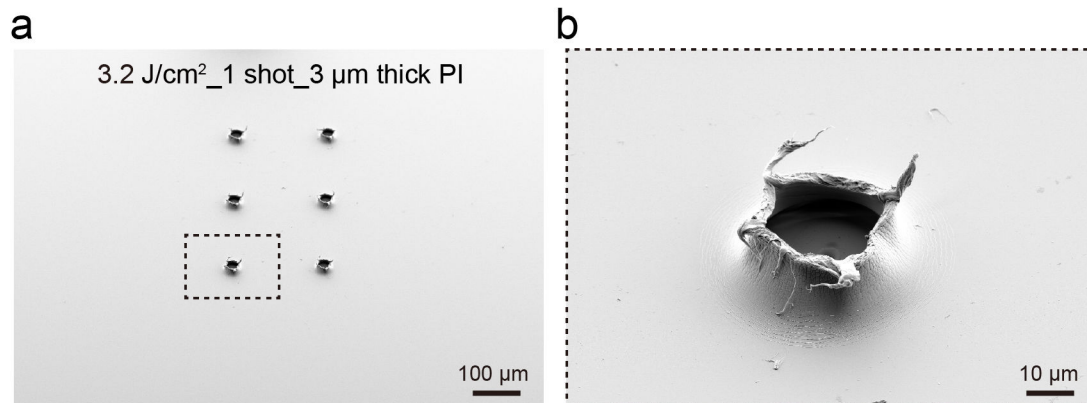


Figure A.22: **PI Blisters created by  $3.2 \text{ J/cm}^2$  & 1 shot on the free surface of PI ( $3 \mu\text{m}$  thick PI).** (a). SEM image presenting the six blisters. (b). Magnified SEM image of one blister.

**A.23 PI Blisters created by  $3.2 \text{ J/cm}^2$  & 1 shot on the free surface of PI ( $7 \mu\text{m}$  thick PI)**

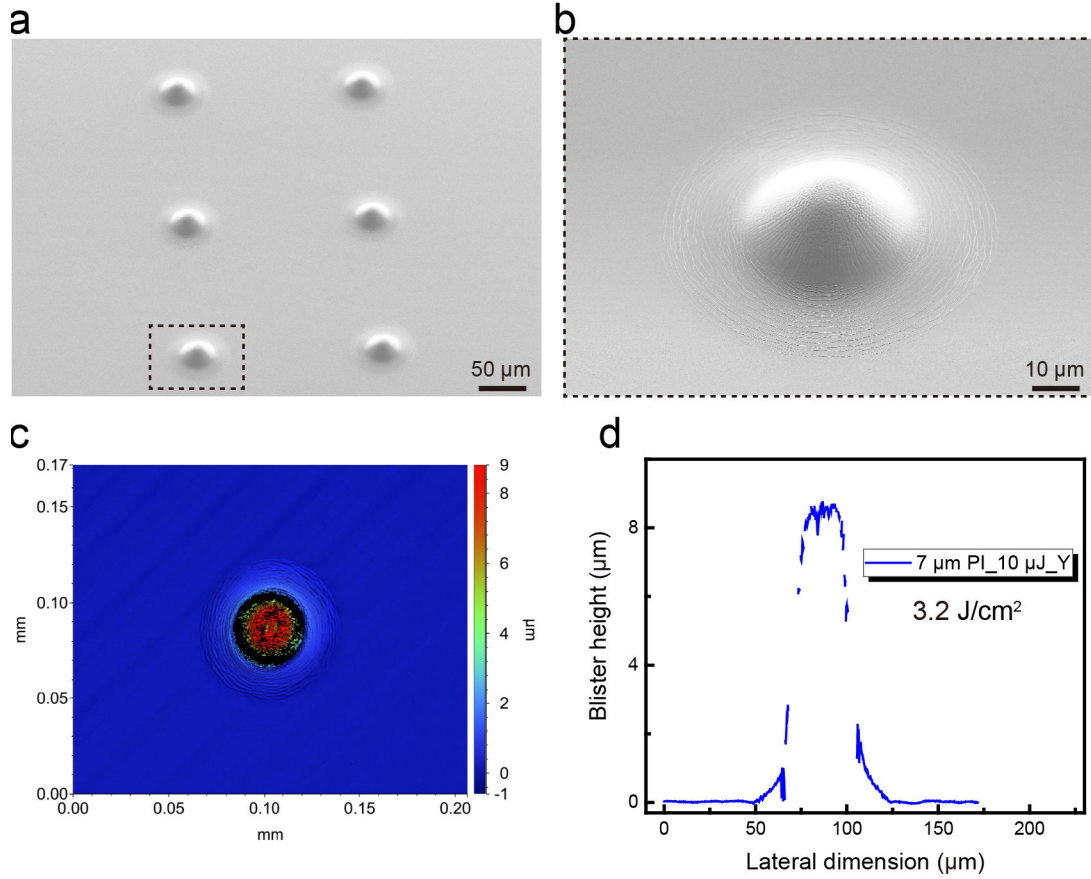


Figure A.23: PI Blisters created by  $3.2 \text{ J/cm}^2$  & 1 shot on the free surface of PI ( $7 \mu\text{m}$  thick PI). (a). SEM image presenting the six blisters. (b). Magnified SEM image of one blister.

**A.24 PI Blisters created by  $3.2 \text{ J/cm}^2$  & 1 shot on the free surface of PI ( $9 \mu\text{m}$  thick PI)**

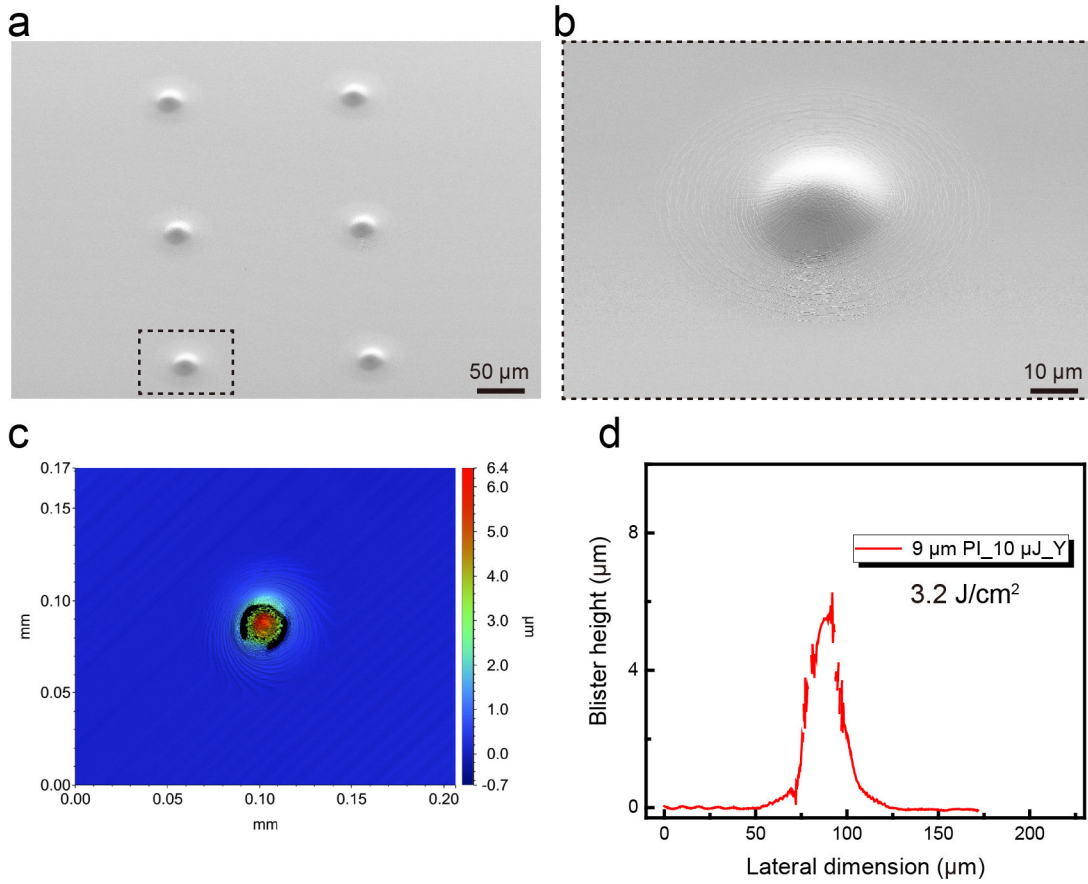


Figure A.24: **PI Blisters created by  $3.2 \text{ J/cm}^2$  & 1 shot on the free surface of PI ( $9 \mu\text{m}$  thick PI).** (a). SEM image presenting the six blisters. (b). Magnified SEM image of one blister.

**A.25 PI Blisters created by  $3.2 \text{ J/cm}^2$  & 1 shot on the free surface of PI ( $11 \mu\text{m}$  thick PI)**

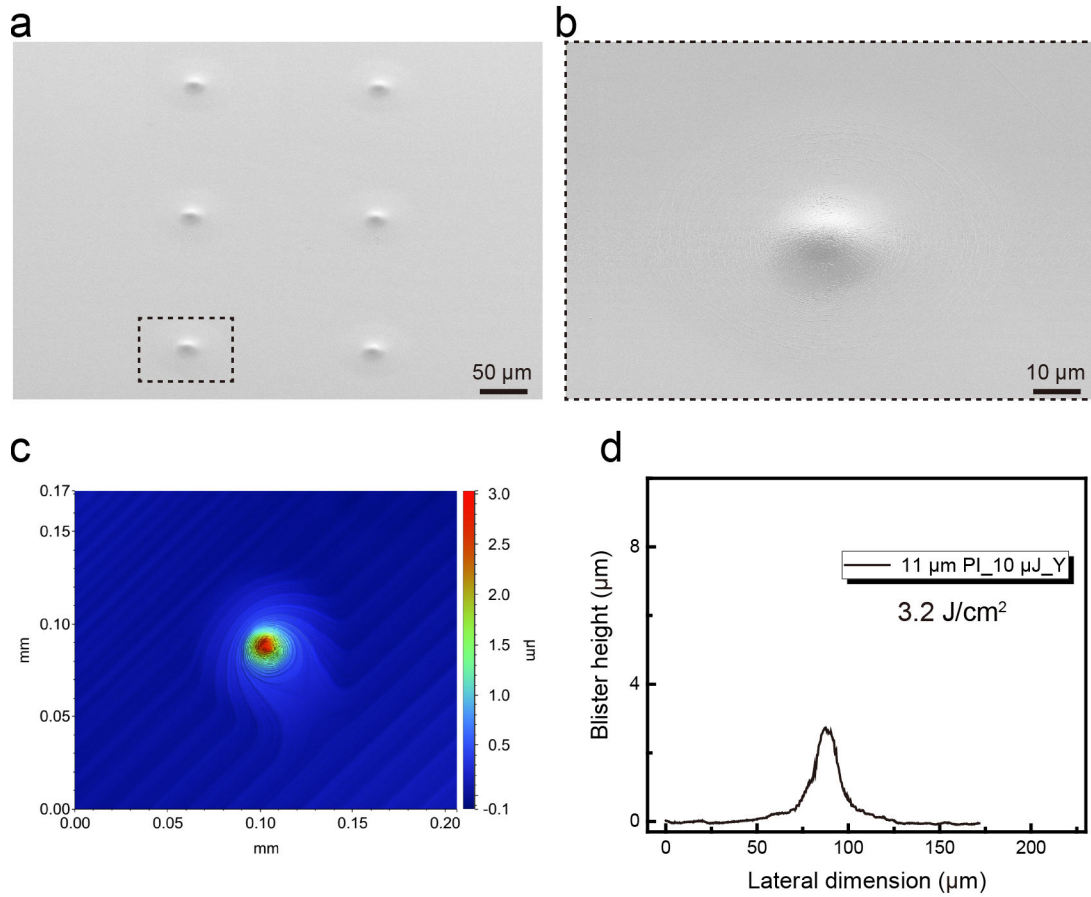


Figure A.25: **PI Blisters created by  $3.2 \text{ J/cm}^2$  & 1 shot on the free surface of PI ( $11 \mu\text{m}$  thick PI).** (a). SEM image presenting the six blisters. (b). Magnified SEM image of one blister.

## A.26 PI blister volume calculation in the absence of the SU-8 microdisk on different thick PI films

```
In [8]: from scipy import integrate
import math
```

10uJ&7um PI cal.

```
In [2]: # Define the function
# Gaussian distribution

def f(x,y0,xc,w,A):
    return abs(math.pi*x*(y0 + A/(w*math.sqrt(math.pi/(4*math.log(2)))))*math.exp(-4*math.log(
v,err = integrate.quad(f,-36.75,36.75, args=(-0.03,-0.46,28.7,287.6))
print(v)
8571.326440812914
```

10uJ&9um PI cal.

```
In [16]: def f(x,y0,xc,w,A):
    return abs(math.pi*x*(y0 + A/(w*math.sqrt(math.pi/(4*math.log(2)))))*math.exp(-4*math.log(
v,err = integrate.quad(f,-38.5,38.5, args=(0.00016,-1.23,20.42,119.08))
print(v)
2614.276807695113
```

10uJ&11um PI cal.

```
In [14]: def f(x,y0,xc,w,A):
    return abs(math.pi*x*(y0 + A/(w*math.sqrt(math.pi/(4*math.log(2)))))*math.exp(-4*math.log(
v,err = integrate.quad(f,-36.75,36.75, args=(0.026,0.70,17.44,46.90))
print(v)
984.8634968170755
```

```
In [17]: # define the function
# Lorentz distribution

def f(x,y0,xc,w,A):
    return abs(math.pi*x*(y0+(2*A/math.pi)*(w/(4*(x-xc)**2+w**2))))
v,err = integrate.quad(f,-36.75,36.75, args=(-0.073,0.785,15.127,67.697))
print(v)
1335.1862299328916
```

Figure A.26: **PI blister volume calculation in the absence of the SU-8 microdisk on different thick PI films.** The blister volume calculation is based on the Lorentzian peak fitting and subsequent integration.



**A.27 Transfer results of SU-8 microdisks with different SU-8 thicknesses (on the donor)**

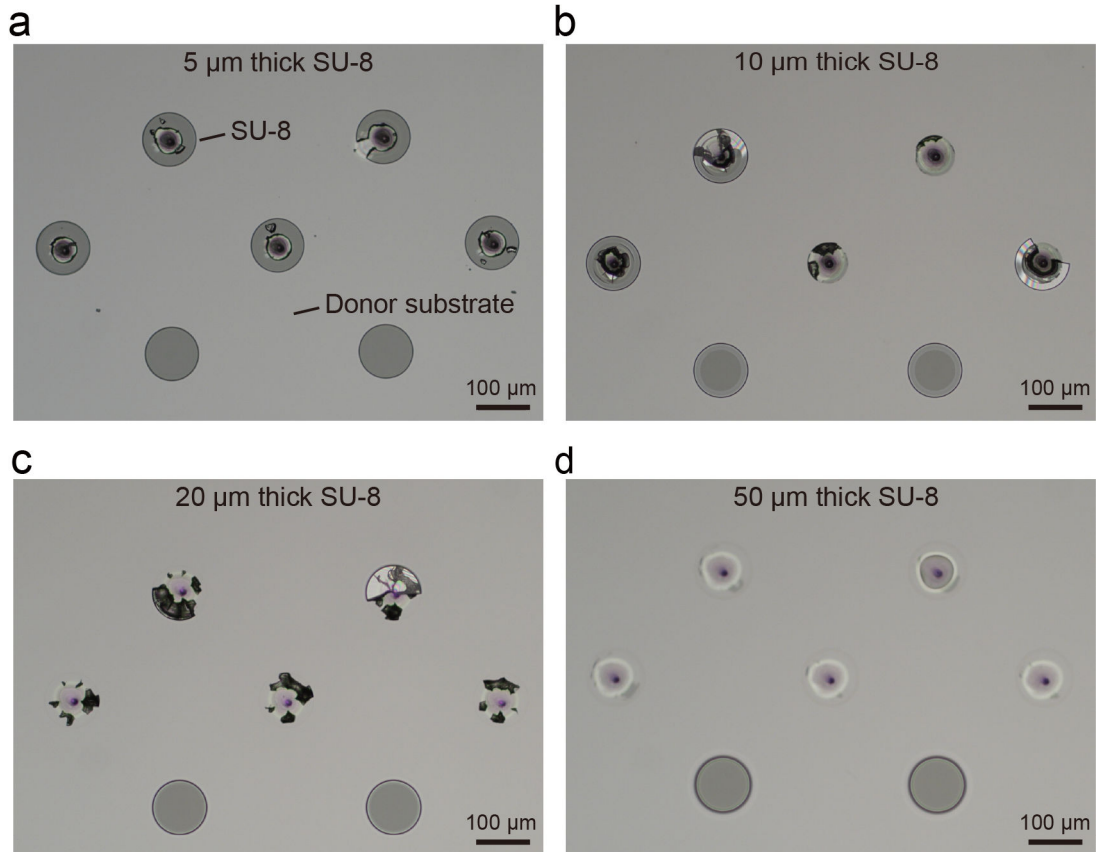


Figure A.27: **Transfer results of SU-8 microdisks with different SU-8 thicknesses (on the donor).** (a-d). SU-8 residues left on the donor substrate after transfer. SU-8 thickness increases from 5 ((a)) to 50 μm ((d)).

**A.28 Adhesion test for SU-8 microdisks on Cu receiver without thermal annealing in DI water**

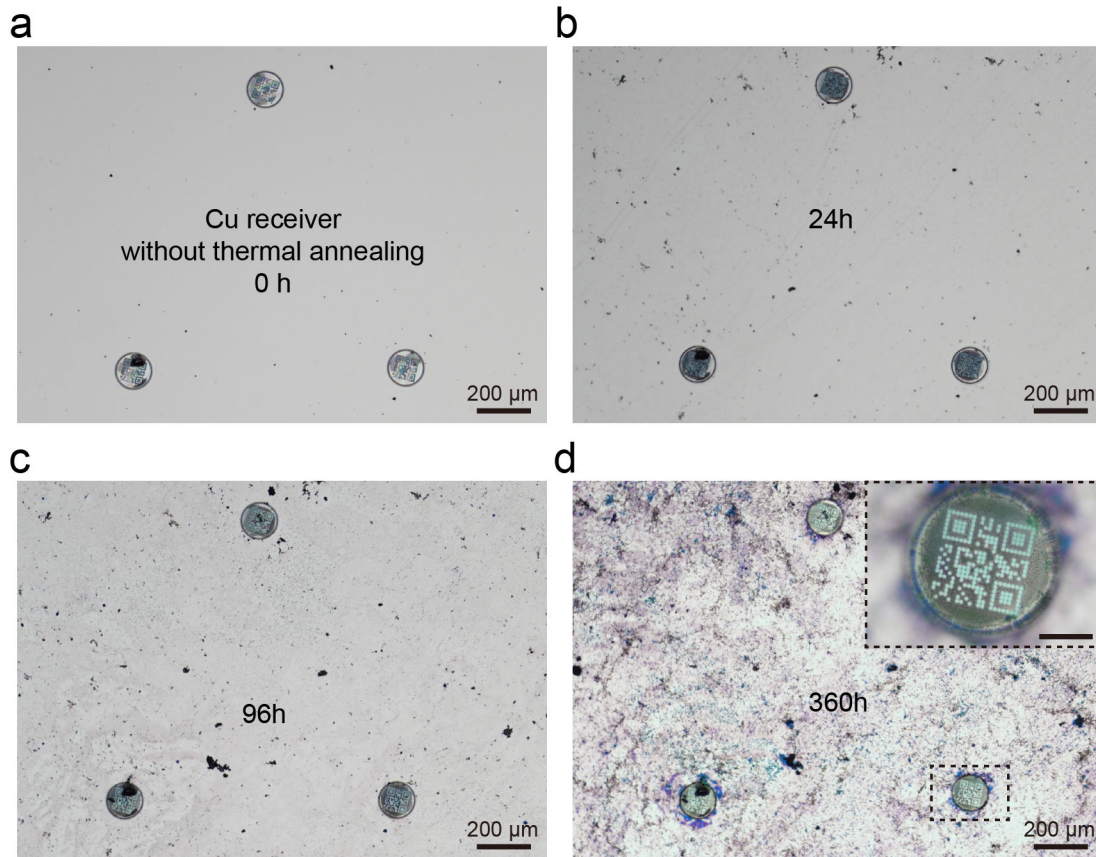


Figure A.28: **Adhesion test for SU-8 microdisks on Cu receiver without thermal annealing in DI water.** (a). Image of three transferred SU-8 microdisks LIFT experiment. (b-d). Images of the SU-8 microdisks after being immersed in DI water for 24, 96, and 360 h. Scale bar in the inset: 50 µm.

**A.29 Adhesion test for SU-8 microdisks on glass receiver without thermal annealing in DI water**

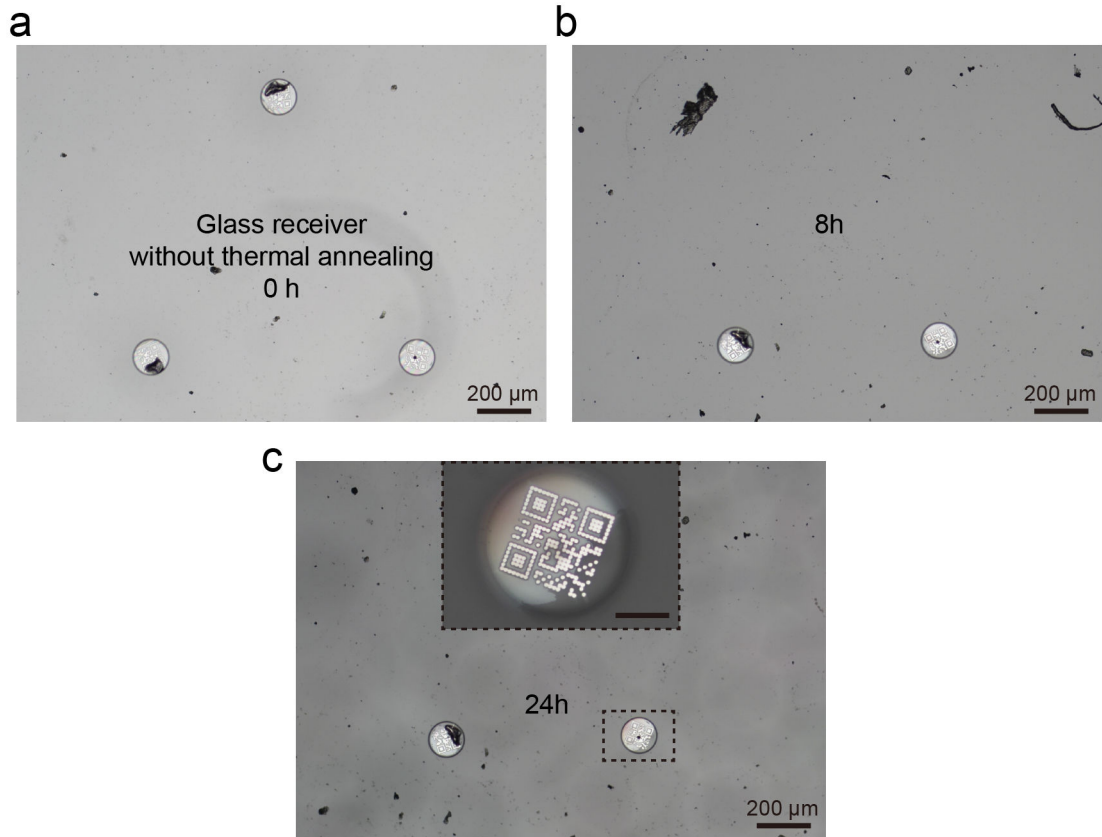


Figure A.29: **Adhesion test for SU-8 microdisks on glass receiver without thermal annealing in DI water.** (a). Image of three transferred SU-8 microdisks LIFT experiment. (b-d). Images of the SU-8 microdisks after being immersed in DI water for 8 and 24 h. Scale bar in the inset: 50 μm.

### A.30 Adhesion test for SU-8 microdisks on Si receiver without thermal annealing in DI water

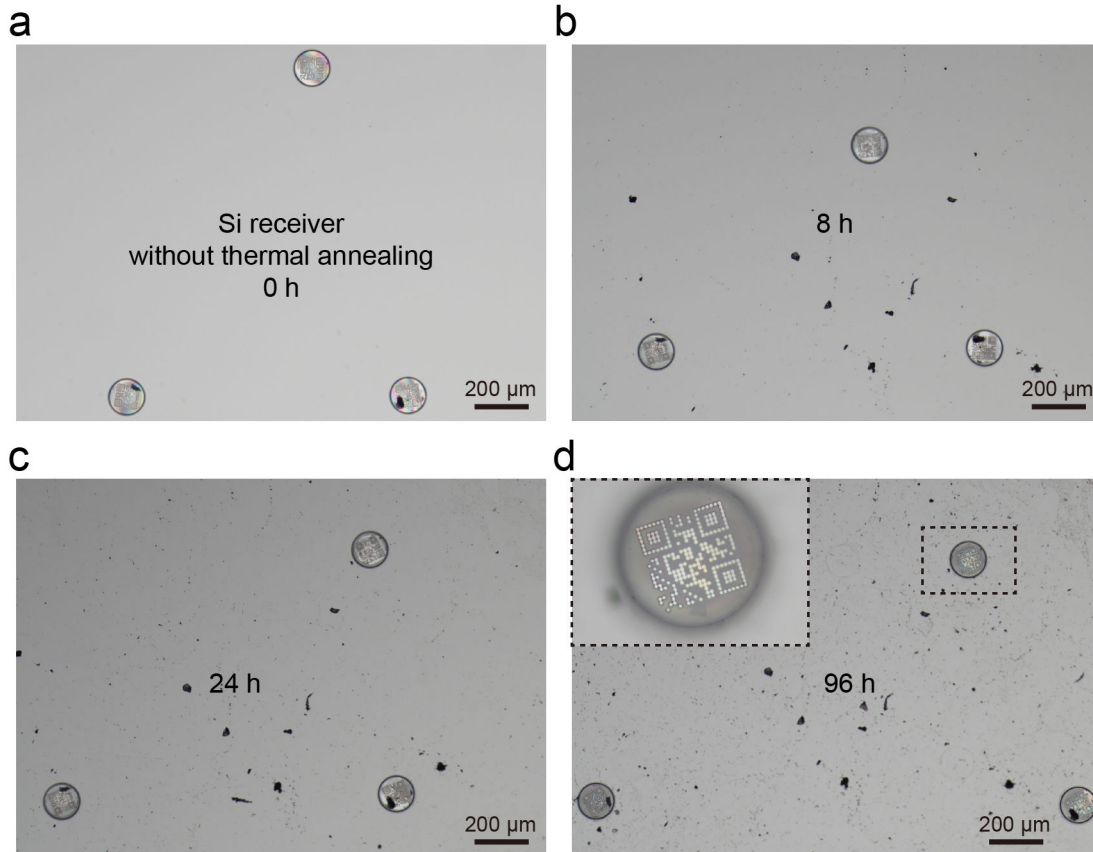


Figure A.30: **Adhesion test in DI water for SU-8 microdisks on Si receiver without thermal annealing in DI water.** (a). Image of three transferred SU-8 microdisks LIFT experiment. (b-d). Images of the SU-8 microdisks after being immersed in DI water for 8, 24, and 96 h. Scale bar in the inset: 50 µm.

**A.31 Adhesion test for SU-8 microdisks on PDMS receiver without thermal annealing in DI water**

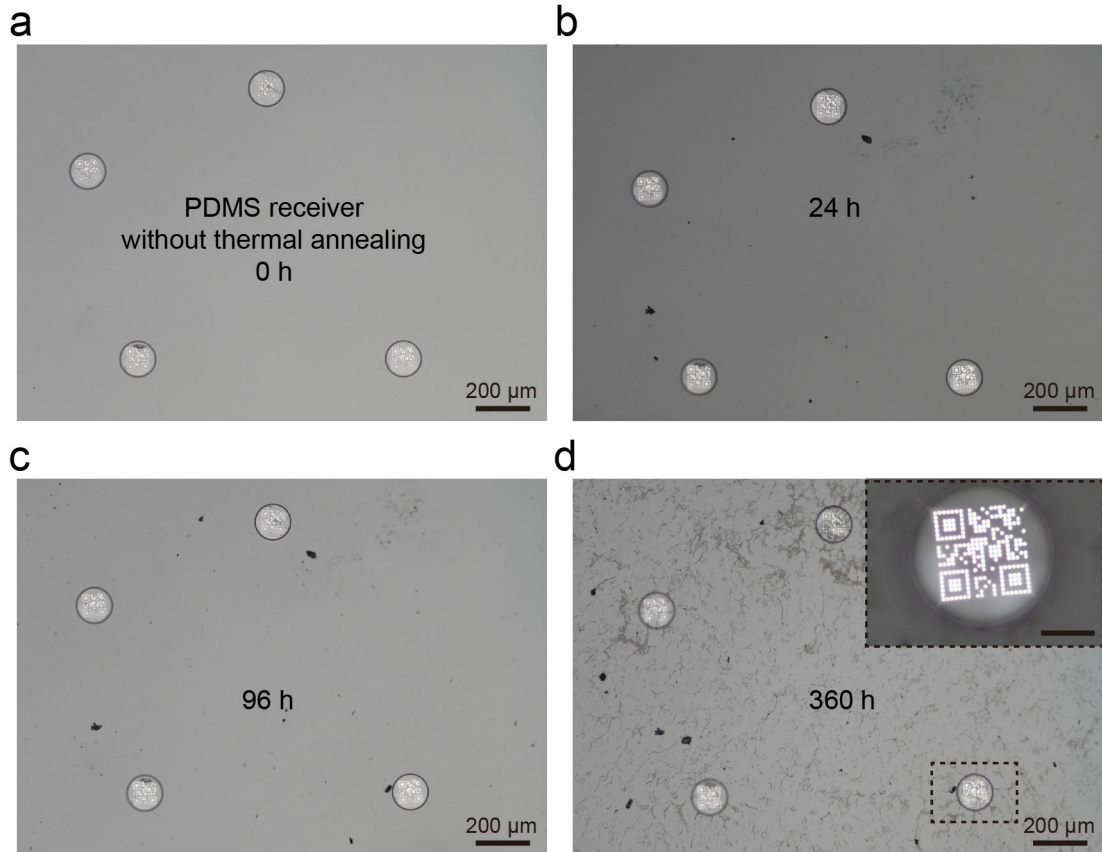


Figure A.31: **Adhesion test for PDMS receiver without thermal annealing in DI water.** (a). Image of three transferred SU-8 microdisks LIFT experiment. (b-d). Images of the SU-8 microdisks after being immersed in DI water for 24, 96, and 360 h. Scale bar in the inset: 50 μm.

### A.32 G-code script for 40×30 SU-8 microdisk array transfer

```

1 ; Name: 40x30 SU8 array on PDMS_Pitch distance 1000um.nc
2 ; Author: Zhiwei Yang
3 ; Created: 2019-07-07
4 ; $LastChangedBy: Zhiwei Yang
5 ; $LastChangedDate: 2022-08-06
6 ; Copyright: c 2022 LMIS1 EPFL
7 ; Purpose: Transfer 40x30 array of SU-8 microdisks with a pitch distance of
1000 μm using 10 μJ laser energy
8
9 ; Some code explanation:
10 ; M101-->laser energy in uJ
11 ; M100-->laser pulse, with laser manual pulse and emission on
12 ; M102-->trigger camera image
13 ; M02-->end program;
14
15
16 G90 G0 ;Absolute Movement, F60 Feedrate 60 mm/min G1 Incremental
Movement
17 X[-38.285] Y[10.777] U[7] V[55] Z[-7.10] ;initial position for the very first
laser spot
18 ; X and Y mean the movement of donor stage along X-/Y-axis; U and V mean the
movement of receiver stage along X-/Y-axis. Z is the height of the focusing lens to
change the focus plane of the laser.
19
20
21 ;2 rows
22 ;2 rows
23 ;2 rows
24
25 G91 G0 ;incremental move
26 M101=10 ;10 uJ
27
28 P1=4 ; here it means the while loop will iterate 4 times
29 $WHILE P1>0 ; P1 is just a variable, you can name it as what you want
30 P2=10 ; here it means the while loop will iterate 10 times
31 $WHILE P2>0
32 G04 0.4 ;dwelling time, increasing the dwelling time from
0 to 0.8 will lead to a more well-aligned array
33 M100
34 U+1
35 Y+0.2 ;find the increment of the movement for the next
spot, in our case, it should be 200 um
36 P2=P2-1
37 $ENDWHILE
38 Y-0.2*10
39 X-0.2
40 P1=P1-1
41 $ENDWHILE
42
43 G90 G0
44 X[-39.085] Y[10.777] U[7] V[54] Z[-7.10]
45 G91 G0
46 M101=10
47
48 P1=4
49 $WHILE P1>0
50 P2=10
51 $WHILE P2>0
52 G04 0.4
53 M100
54 U+1
55 Y+0.2
56 P2=P2-1
57 $ENDWHILE
58 Y-0.2*10
59 X-0.2
60 P1=P1-1
61 $ENDWHILE
62
63
64 ;4 rows
65 ;4 rows
66

```

Figure A.32: G-code script for 40×30 SU-8 microdisk array transfer with pitch distance of 1000 μm. In this g-code script, no coordinate correction is not introduced. The laser fluence is set to 3.2 J/cm<sup>2</sup> with a single laser shot mode. This file only presents a part of the whole code.

## A.33 SU-8 coordinate in the LIFT setup

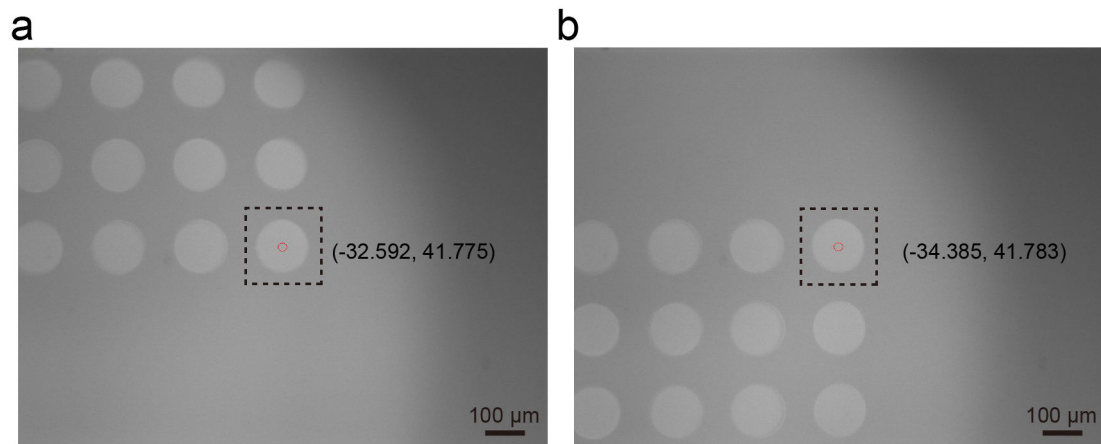


Figure A.33: **SU-8 coordinate in the LIFT setup.** (a). Image of the SU-8 microdisk array, highlighting the first SU-8 microdisk in the first column. The red circle indicates the position of the laser shot. The coordinate of the first SU-8 microdisk is provided. (b). Image of the SU-8 microdisk array, highlighting the tenth SU-8 microdisk in the first column. Its coordinate is shown in the figure.

### A.34 G-code script for 40×40 SU-8 microdisk array transfer

```

1
2 ; Name: 40x40 SU8 array on PDMS_Pitch distance 1000um.nc
3 ; Author: Zhiwei Yang
4 ; Created: 2019-07-07
5 ; $LastChangedBy: Zhiwei Yang
6 ; $LastChangedDate: 2022-08-10
7 ; Copyright: © 2022 LMIS1 EPFL
8 ; Purpose: Transfer 40x40 array of SU-8 microdisks with a pitch distance of
9 ; 1000 µm using 10 µJ laser energy
10 ; Improvements: The dwelling time and X-/Y-axis compensation are introduced and
11 ; optimized to allow more stable and precise transfer
12
13 ; Some code explanation:
14 ; M101-->laser energy in uJ
15 ; M100-->laser pulse, with laser manual pulse and emission on
16 ; M102-->trigger camera image
17 ; M02-->end program;
18
19 ;2rows
20 ;2rows
21 ;2rows
22
23 G90 G0 ;Absolute Movement, F60 Feedrate 60 mm/min G1 Incremental
24 Movement
25 X[-26.876] Y[13.651] U[15] V[50] Z[-7.0] ; initial position for the very first
26 laser spot
27 ; X and Y mean the movement of donor stage along X-/Y-axis; U and V mean the
28 movement of receiver stage along X-/Y-axis. Z is the height of the focusing lens to
29 change the focus plane of the laser.
30
31 G91 G0 ; incremental move
32 M101=10 ; 10 uJ
33
34 P1=4 ; here it means the while loop will iterate 4 times
35 $WHILE P1>0
36 P2=10 ; here it means the while loop will iterate 10 times
37 $WHILE P2>0
38 G04 0.8 ; dwelling time, the dwelling time is kept to be
39 0.8 s. This has been proved to be an optimal value for stable transfer
40 M100
41 U+
42 Y+0.2 ; find the increment of the movement for the next
43 spot, in our case, it should be close to 200 µm
44 X-0.001 ; this compensate for the theta angle on
45 X-direction. For two consecutive SU-8 microdisks along Y-direction, the X-shift is
46 1µm.
47 P2=P2-1
48 $ENDWHILE
49 Y-0.2*10+0.001 ; this compensate for the theta angle on
50 Y-direction. For two consecutive SU-8 microdisks along X-direction, the Y-shift is
51 1µm.
52 X-0.19
53 P1=P1-1
54 $ENDWHILE
55
56 G90 G0
57 X[-27.672] Y[13.654] U[15] V[49] Z[-7.0]
58
59 G91 G0
60 M101=10
61
62 P1=4
63 $WHILE P1>0
64 P2=10
65 $WHILE P2>0
66 G04 0.8
67 M100
68 U+
69 Y+0.2
70 X-0.001

```

Figure A.34: **G-code script for 40×40 SU-8 Microdisk Array Transfer with Pitch Distance of 1000 µm.** In this g-code script, the dwelling time is optimized to be 0.8 s and coordinate correction is introduced (1 µm shift per SU-8 microdisk). The laser fluence is set to 3.2 J/cm<sup>2</sup> with a single laser shot mode. This file only presents a part of the whole code.



A.35 Microscaffold building blocks design

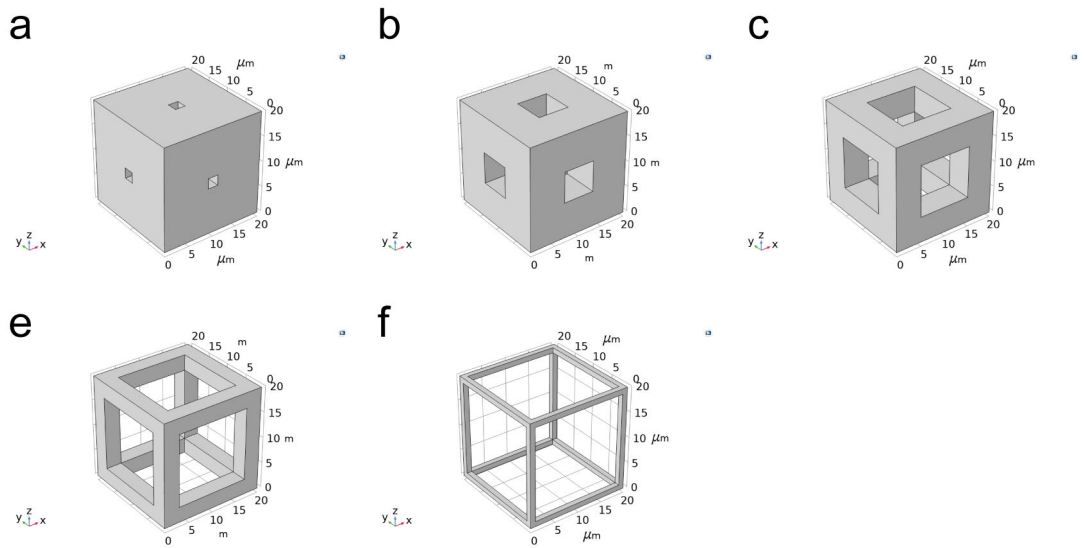


Figure A.35: **Microscaffold building blocks design.** (a)-(e).  $20 \times 20 \times 20 \mu\text{m}^3$  microscaffold building blocks with the pore size of 2, 6, 10, 14, and 18  $\mu\text{m}$ , respectively. The backbone beam size is 9, 7, 5, 3, and 1  $\mu\text{m}$  from (a)-(e).

### A.36 Microscaffolds with different pore sizes

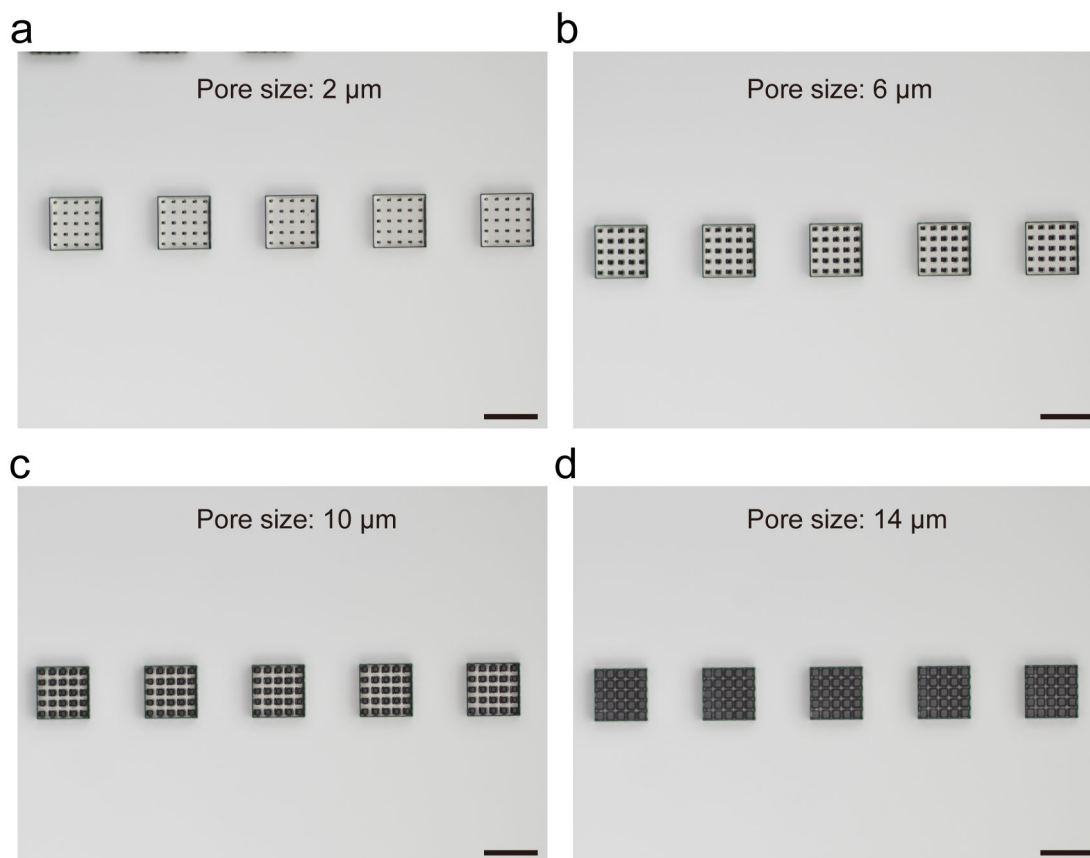


Figure A.36: **Microscaffolds fabricated on PI layer with the size of  $100 \times 100 \times 100 \mu\text{m}^3$ .** (a)-(d). Pore size for these four types of scaffolds increases from 2 to 14  $\mu\text{m}$ , respectively.

**A.37 Microscaffolds with different sizes**

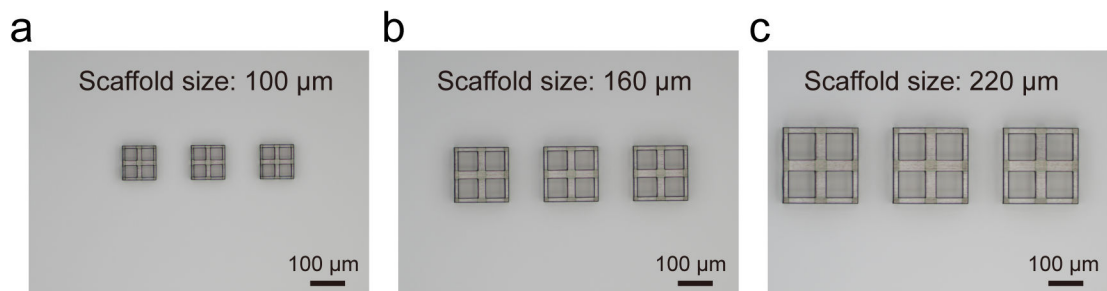


Figure A.37: **Microscaffolds fabricated on PI layer with increasing sizes.** (a)-(c). Scaffold size increases from 100 to 220 μm, respectively.

### A.38 Microscaffolds with the supporting layer

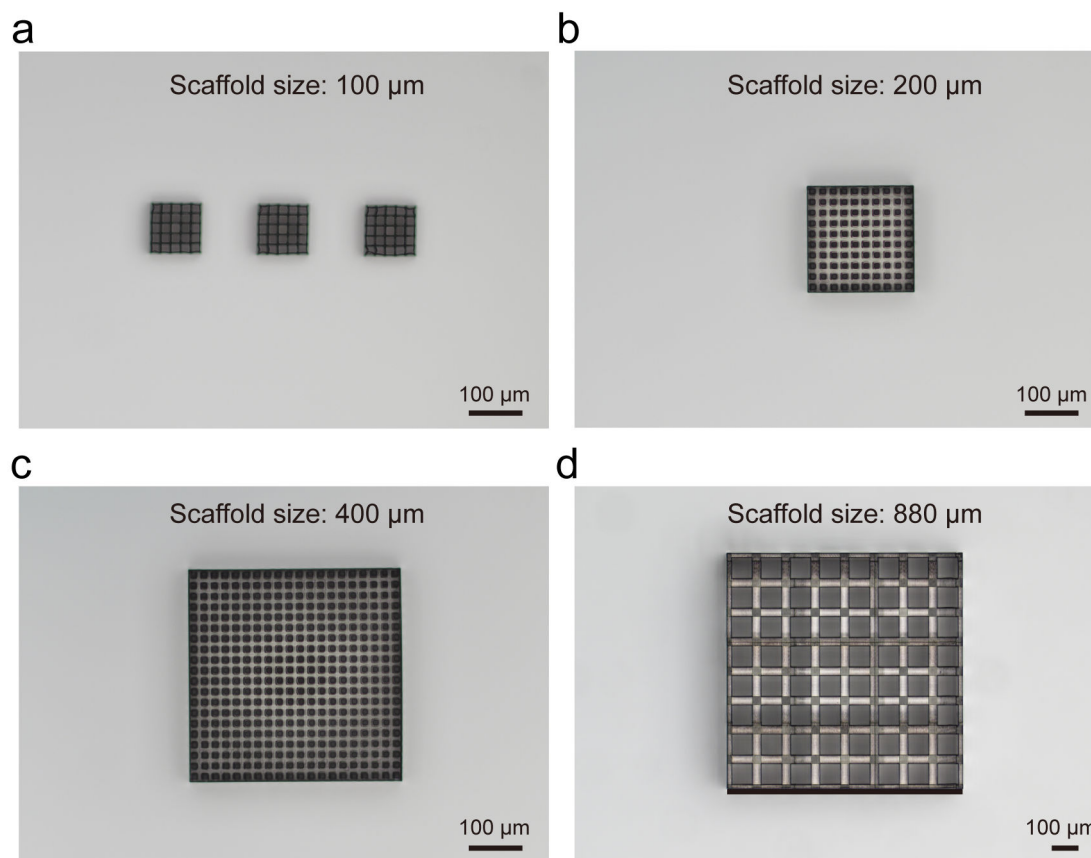


Figure A.38: **Four types of microscaffold with a supporting layer.** (a). Microscaffolds with a size of  $100 \times 100 \times 100 \mu\text{m}^3$ . The pore size is  $18 \mu\text{m}$  (block size is  $20 \mu$ ). A thin supporting layer is between the PI and the scaffold. (b-c). Scaffold size increases from 200 to 880  $\mu\text{m}$  and all have a supporting layer underneath.

**A.39 Transfer result of a T-shape microstructure into PDMS channel with a tilted angle**

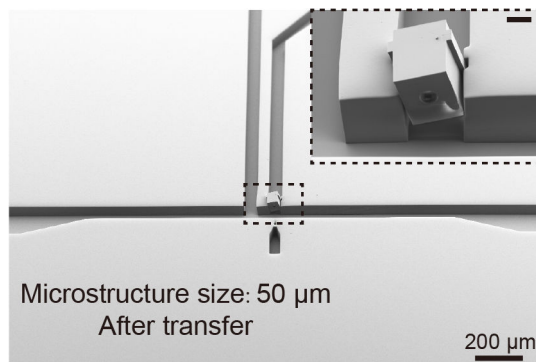


Figure A.39: **Transfer result of a T-shape microstructure into PDMS channel with a tilted angle.** SEM image of the 50  $\mu\text{m}$  large T-shape structure transferred to the targeted position in the channel. The microstructure is tilted against the PDMS wall. Scale bar in the inset: 20  $\mu\text{m}$ .

## A.40 Microscaffold array design

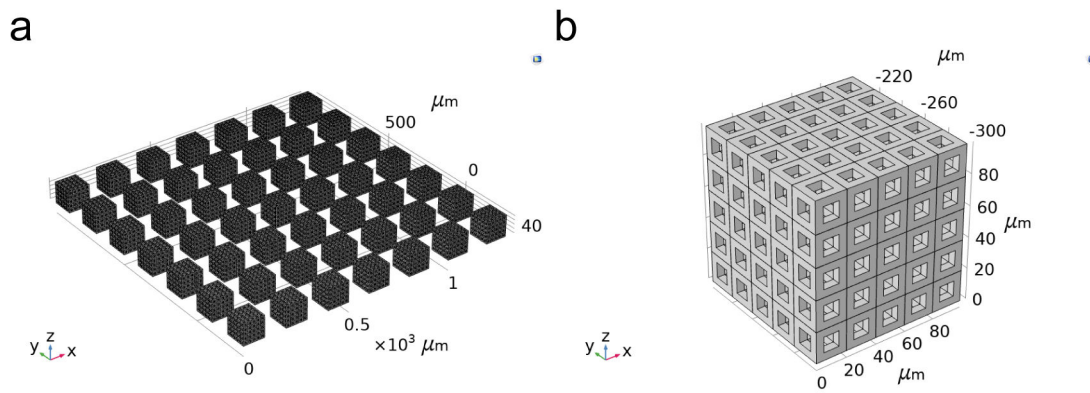


Figure A.40: **Microscaffold array design.** (a). A  $7 \times 7$  scaffold array design. (b). Close-up image of one scaffold.

## A.41 G-code script for 7×7 microsccaffold array transfer with varying pitch distance

```

1
2 ; Name:          40x40 SU8 array on PDMS_Pitch distance 1000um.nc
3 ; Author:       Zhiwei Yang
4 ; Created:      2019-07-07
5 ; $LastChangedBy: Zhiwei Yang
6 ; $LastChangedDate: 2022-08-20
7 ; Copyright:    © 2022 LMIS1 EPFL
8 ; Purpose:      Transfer 7x7 array of TPL fabricated microsccaffolds with varying
9 ;               pitch distance from 2000 μm to 14000 μm using 3 μJ laser energy
10 ; Improvements: The dwelling time and X-/Y-axis compensation are introduced and
11 ;               optimized to allow more stable and precise transfer
12
13 ; Some code explanation:
14 ; M101-->laser energy in uJ
15 ; M100-->laser pulse, with laser manual pulse and emission on
16 ; M102-->trigger camera image
17 ; M02-->end program;
18
19
20 G90 G0          ;Absolute Movement, F60 Feedrate 60 mm/min  G1 Incremental
21 Movement
22 X[11.921] Y[44.003] U[0] V[60] Z[-7.15] ; initial position for the very first
23 laser spot
24 ; X and Y mean the movement of donor stage along X-/Y-axis; U and V mean the
25 movement of receiver stage along X-/Y-axis. Z is the height of the focusing lens to
26 change the focus plane of the laser.
27
28 G91 G0          ; incremental move
29 M101=3          ; 3 uJ
30
31 P1=7            ; here it means the while loop will iterate 7 times
32 SWHILE P1>0
33     P2=7        ; here it means the while loop will iterate 7 times
34     SWHILE P2>0
35         G04 0.8 ; dwelling time, the dwelling time is kept to be
36         0.8 s. This has been proved to be an optimal value for stable transfer
37         M100
38         U*16-2*P2 ; this code helps realize the varying pitch
39         distance along X-direction.
40         Y+0.2     ; find the increment of the movement for the next
41         spot, in our case, it should be close to 200 μm
42         X+0.0105 ; this compensate for the theta angle on
43         X-direction. For two consecutive SU-8 microdisks along Y-direction, the X-shift is
44         10.5um.
45         P2=P2-1
46     SENDWHILE
47     Y-0.2*7+0.012 ; this compensate for the theta angle on
48     Y-direction. For two consecutive SU-8 microdisks along X-direction, the Y-shift is
49     12um.
50     X-0.2-0.062-0.011 ; this compensate for the theta angle on
51     X-direction after transferring the previous column. For two consecutive SU-8
52     microdisks along X-direction, the Y-shift is 11um.
53     U=56 ; Receiver stage moves back to the initial
54     position along X-direction to start the next-row transfer.
55     V=16+2*P1 ; this code helps realize the varying pitch
56     distance along Y-direction.
57     P1=P1-1
58 SENDWHILE
59
60 M02

```

Figure A.41: G-code script for 7×7 microsccaffold array transfer with varying pitch distance. In this g-code file, rotation correction is introduced, and the dwelling time is set to 0.8 s. The laser fluence is set to be 0.96 J/cm<sup>2</sup>, and a single laser shot is applied to each microsccaffold.





# Bibliography

- [1] K. V. Wong and A. Hernandez, "A Review of Additive Manufacturing," *ISRN Mechanical Engineering*, vol. 2012, 2012.
- [2] H. Bikas, P. Stavropoulos, and G. Chryssolouris, "Additive manufacturing methods and modeling approaches: A critical review," *International Journal of Advanced Manufacturing Technology*, vol. 83, no. 1-4, 2016.
- [3] T. D. Ngo, A. Kashani, G. Imbalzano, K. T. Nguyen, and D. Hui, "Additive manufacturing (3D printing): A review of materials, methods, applications and challenges," 2018.
- [4] O. Abdulhameed, A. Al-Ahmari, W. Ameen, and S. H. Mian, "Additive manufacturing: Challenges, trends, and applications," *Advances in Mechanical Engineering*, vol. 11, no. 2, 2019.
- [5] P. Calvert, "Inkjet printing for materials and devices," 2001.
- [6] B. J. De Gans, P. C. Duineveld, and U. S. Schubert, "Inkjet printing of polymers: State of the art and future developments," 2004.
- [7] M. Singh, H. M. Haverinen, P. Dhagat, and G. E. Jabbour, "Inkjet printing-process and its applications," *Advanced Materials*, vol. 22, no. 6, 2010.
- [8] J. U. Park, M. Hardy, S. J. Kang, K. Barton, K. Adair, D. K. Mukhopadhyay, C. Y. Lee, M. S. Strano, A. G. Alleyne, J. G. Georgiadis, P. M. Ferreira, and J. A. Rogers, "High-resolution electrohydrodynamic jet printing," *Nature Materials*, vol. 6, no. 10, 2007.
- [9] M. S. Onses, E. Sutanto, P. M. Ferreira, A. G. Alleyne, and J. A. Rogers, "Mechanisms, Capabilities, and Applications of High-Resolution Electrohydrodynamic Jet Printing," 2015.
- [10] C. Goth, S. Putzo, and J. Franke, "Aerosol Jet printing on rapid prototyping materials for fine pitch electronic applications," in *Proceedings - Electronic Components and Technology Conference*, 2011.

## Bibliography

---

- [11] L. J. Deiner, T. Jenkins, T. Howell, and M. Rottmayer, "Aerosol Jet Printed Polymer Composite Electrolytes for Solid-State Li-Ion Batteries," *Advanced Engineering Materials*, vol. 21, no. 12, 2019.
- [12] B. D. Young, B. Gamboa, A. S. Bhalla, and R. Guo, "Current status of functional and multifunctional materials for 3D microfabrication: An overview," *Ferroelectrics*, vol. 555, no. 1, 2020.
- [13] A. Lee, K. Sudau, K. H. Ahn, S. J. Lee, and N. Willenbacher, "Optimization of experimental parameters to suppress nozzle clogging in inkjet printing," *Industrial and Engineering Chemistry Research*, vol. 51, no. 40, 2012.
- [14] M. Makrygianni, A. Millionis, C. Kryou, I. Trantakis, D. Poulidakos, and I. Zergioti, "On-Demand Laser Printing of Picoliter-Sized, Highly Viscous, Adhesive Fluids: Beyond Inkjet Limitations," *Advanced Materials Interfaces*, vol. 5, no. 18, 2018.
- [15] J. Bohandy, B. F. Kim, and F. J. Adrian, "Metal deposition from a supported metal film using an excimer laser," *Journal of Applied Physics*, vol. 60, no. 4, pp. 1538–1539, 1986.
- [16] E. Jabari, F. Ahmed, F. Liravi, E. B. Secor, L. Lin, and E. Toyserkani, "2D printing of graphene: A review," 2019.
- [17] A. Pique and P. Serra, *Laser Printing of Functional Materials: 3D Microfabrication, Electronics and Biomedicine*, 2018, vol. 39, no. 5.
- [18] P. Serra and A. Piqué, "Laser-Induced Forward Transfer: Fundamentals and Applications," 2019.
- [19] M. Morales, D. Munoz-Martin, A. Marquez, S. Lauzurica, and C. Molpeceres, *Laser-Induced Forward Transfer Techniques and Applications*, second ed. Elsevier Ltd., 2018. [Online]. Available: <http://linkinghub.elsevier.com/retrieve/pii/B9780081012529000133>
- [20] T. Han, A. Nag, N. Afsarimanesh, S. C. Mukhopadhyay, S. Kundu, and Y. Xu, "Laser-Assisted printed flexible sensors: A review," 2019.
- [21] J. Bian, L. Zhou, X. Wan, C. Zhu, B. Yang, and Y. A. Huang, "Laser Transfer, Printing, and Assembly Techniques for Flexible Electronics," 2019.
- [22] B. H. In'T Veld, L. Overmeyer, M. Schmidt, K. Wegener, A. Malshe, and P. Bartolo, "Micro additive manufacturing using ultra short laser pulses," *CIRP Annals - Manufacturing Technology*, vol. 64, no. 2, 2015.
- [23] A. Piqué, R. C. Auyeung, H. Kim, N. A. Charipar, and S. A. Mathews, "Laser 3D micro-manufacturing," *Journal of Physics D: Applied Physics*, vol. 49, no. 22, 2016.

- [24] A. Piqué, "Laser-based microadditive manufacturing technologies," in *Three-Dimensional Microfabrication Using Two-Photon Polymerization*, 2019.
- [25] A. Piqué, D. B. Chrisey, R. C. Auyeung, J. Fitz-Gerald, H. D. Wu, R. A. McGill, S. Lakeou, P. K. Wu, V. Nguyen, and M. Duignan, "A novel laser transfer process for direct writing of electronic and sensor materials," *Applied Physics A: Materials Science and Processing*, vol. 69, no. 7, 1999.
- [26] D. B. Chrisey, A. Pique, R. Modi, H. D. Wu, R. C. Auyeung, and H. D. Young, "Direct writing of conformal mesoscopic electronic devices by MAPLE DW," *Applied Surface Science*, vol. 168, no. 1-4, 2000.
- [27] D. B. Chrisey, A. Pique, J. Fitz-Gerald, R. C. Auyeung, R. A. McGill, H. D. Wu, and M. Duignan, "New approach to laser direct writing active and passive mesoscopic circuit elements," *Applied Surface Science*, vol. 154, pp. 593–600, 2000.
- [28] J. M. Fitz-Gerald, D. B. Chrisey, A. Piqu, R. C. Auyeung, R. Mohdi, H. D. Young, H. D. Wu, S. Lakeou, and R. Chung, "Matrix assisted pulsed laser evaporation direct write (MAPLE DW): A new method to rapidly prototype active and passive electronic circuit elements," in *Materials Research Society Symposium - Proceedings*, vol. 625, 2000.
- [29] D. Young, R. C. Auyeung, A. Piqué, D. B. Chrisey, and D. D. Dlott, "Time-resolved optical microscopy of a laser-based forward transfer process," *Applied Physics Letters*, vol. 78, no. 21, 2001.
- [30] D. Young, R. C. Auyeung, A. Pique, D. B. Chrisey, and D. D. Dlott, "Plume and jetting regimes in a laser based forward transfer process as observed by time-resolved optical microscopy," *Applied Surface Science*, vol. 197-198, 2002.
- [31] A. Pique, D. W. Weir, P. K. Wu, B. Pratap, C. B. Arnold, B. R. Ringeisen, R. A. McGill, R. C. Y. Auyeung, R. A. Kant, and D. B. Chrisey, "Direct-write of sensor devices by a laser forward transfer technique," in *Photon Processing in Microelectronics and Photonics*, vol. 4637, 2002.
- [32] A. Piqué, R. C. Auyeung, J. L. Stepnowski, D. W. Weir, C. B. Arnold, R. A. McGill, and D. B. Chrisey, "Laser processing of polymer thin for chemical sensor applications," *Surface and Coatings Technology*, vol. 163-164, 2003.
- [33] J. A. Barron, B. R. Ringeisen, H. Kim, B. J. Spargo, and D. B. Chrisey, "Application of laser printing to mammalian cells," in *Thin Solid Films*, vol. 453-454, 2004.
- [34] N. R. Schiele, R. A. Koppes, D. T. Corr, K. S. Ellison, D. M. Thompson, L. A. Ligon, T. K. Lippert, and D. B. Chrisey, "Laser direct writing of combinatorial libraries of idealized

## Bibliography

---

- cellular constructs: Biomedical applications,” *Applied Surface Science*, vol. 255, no. 10, pp. 5444–5447, 2009.
- [35] Y. Lin, Y. Huang, G. Wang, T. R. J. Tzeng, and D. B. Chrisey, “Effect of laser fluence on yeast cell viability in laser-assisted cell transfer,” *Journal of Applied Physics*, vol. 106, no. 4, 2009.
- [36] Y. Lin, G. Huang, Y. Huang, T. R. J. Tzeng, and D. Chrisey, “Effect of laser fluence in laser-assisted direct writing of human colon cancer cell,” *Rapid Prototyping Journal*, vol. 16, no. 3, 2010.
- [37] A. Doraiswamy, R. J. Narayan, M. L. Harris, S. B. Qadri, R. Modi, and D. B. Chrisey, “Laser microfabrication of hydroxyapatite-osteoblast-like cell composites,” *Journal of Biomedical Materials Research - Part A*, vol. 80, no. 3, 2007.
- [38] E. C. Kinzel, X. Xu, B. R. Lewis, N. M. Laurendeau, and R. P. Lucht, “Direct writing of conventional thick film inks using MAPLE-DW process,” *Journal of Laser Micro Nanoengineering*, vol. 1, no. 1, 2006.
- [39] I. Nicolae, C. Viespe, and C. Grigoriu, “Nanocomposite sensitive polymeric films for SAW sensors deposited by the MAPLE direct write technique,” *Sensors and Actuators, B: Chemical*, vol. 158, no. 1, 2011.
- [40] A. Piqué, R. C. Y. Auyeung, K. M. Metkus, H. Kim, S. Mathews, T. Bailey, X. Chen, and L. J. Young, “Laser decal transfer of electronic materials with thin film characteristics,” in *Photon Processing in Microelectronics and Photonics VII*, vol. 6879, 2008.
- [41] A. Pique, R. C. Auyeung, H. Kim, K. M. Metkus, and S. A. Mathews, “Digital microfabrication by laser decal transfer,” *Journal of Laser Micro Nanoengineering*, vol. 3, no. 3, 2008.
- [42] E. Breckenfeld, H. Kim, R. C. Auyeung, and A. Piqué, “Laser-induced forward transfer of Ag nanopaste,” *Journal of Visualized Experiments*, vol. 2016, no. 109, 2016.
- [43] S. A. Mathews, R. C. Y. Auyeung, and A. Piqué, “Analysis and characterization of the laser decal transfer process,” in *Laser-based Micro- and Nanopackaging and Assembly VI*, vol. 8244, 2012.
- [44] S. A. Mathews, R. C. Auyeung, H. Kim, N. A. Charipar, and A. Piqué, “High-speed video study of laser-induced forward transfer of silver nano-suspensions,” *Journal of Applied Physics*, vol. 114, no. 6, 2013.
- [45] R. C. Auyeung, H. Kim, N. A. Charipar, A. J. Birnbaum, S. A. Mathews, and A. Piqué, “Laser forward transfer based on a spatial light modulator,” *Applied Physics A: Materials Science and Processing*, vol. 102, no. 1, 2011.

- [46] A. Piqué, R. C. Y. Auyeung, A. T. Smith, H. Kim, S. A. Mathews, N. A. Charipar, and M. A. Kirleis, "Laser transfer of reconfigurable patterns with a spatial light modulator," in *Laser-based Micro- and Nanopackaging and Assembly VII*, vol. 8608, 2013.
- [47] R. C. Y. Auyeung, H. Kim, S. Mathews, and A. Piqué, "Laser forward transfer using structured light," *Optics Express*, vol. 23, no. 1, 2015.
- [48] R. C. Y. Auyeung, H. Kim, S. Mathews, and A. Piqué, "Spatially modulated laser pulses for printing electronics," *Applied Optics*, vol. 54, no. 31, 2015.
- [49] R. C. Auyeung, H. Kim, A. J. Birnbaum, M. Zalalutdinov, S. A. Mathews, and A. Piqué, "Laser decal transfer of freestanding microcantilevers and microbridges," *Applied Physics A: Materials Science and Processing*, vol. 97, no. 3, pp. 513–519, 2009.
- [50] A. J. Birnbaum, R. C. Auyeung, K. J. Wahl, M. Zalalutidnov, A. R. Laracuente, and A. Piqué, "Laser printed micron-scale free standing laminate composites: Process and properties," *Journal of Applied Physics*, vol. 108, no. 8, 2010.
- [51] J. Wang, R. C. Auyeung, H. Kim, N. A. Charipar, and A. Piqué, "Three-dimensional printing of interconnects by laser direct-write of silver nanopastes," *Advanced Materials*, 2010.
- [52] H. Kim, J. S. Melinger, A. Khachatryan, N. A. Charipar, R. C. Y. Auyeung, and A. Piqué, "Fabrication of terahertz metamaterials by laser printing," *Optics Letters*, vol. 35, no. 23, 2010.
- [53] A. T. Smith, D. Simonson, N. A. Charipar, and A. Piqué, "Laser direct write fabrication of meta-antennas for electro-optic conversion," *Journal of Laser Micro Nanoengineering*, vol. 7, no. 3, 2012.
- [54] A. Piqué, N. A. Charipar, H. Kim, M. A. Kirleis, R. C. Y. Auyeung, A. T. Smith, K. M. Metkus, and S. A. Mathews, "Realization of metamaterial structures by non-lithographic processes," in *Metamaterials: Fundamentals and Applications V*, vol. 8455, 2012.
- [55] A. J. Birnbaum, M. K. Zalalutdinov, K. J. Wahl, and A. Piqué, "Fabrication and response of laser-printed cavity-sealing membranes," *Journal of Microelectromechanical Systems*, vol. 20, no. 2, 2011.
- [56] A. Piqué, H. Kim, R. C. Auyeung, and A. T. Smith, "Laser forward transfer of functional materials for digital fabrication of microelectronics," *Journal of Imaging Science and Technology*, vol. 57, no. 4, 2013.
- [57] H. Kim, M. Duocastella, K. M. Charipar, R. C. Auyeung, and A. Piqué, "Laser printing of conformal and multi-level 3D interconnects," *Applied Physics A: Materials Science and Processing*, vol. 113, no. 1, 2013.

## Bibliography

---

- [58] E. Breckenfeld, H. Kim, R. C. Y. Auyeung, N. Charipar, P. Serra, and A. Piqué, “Laser-induced forward transfer of silver nanopaste for microwave interconnects,” *Applied Surface Science*, vol. 331, pp. 254–261, 2015. [Online]. Available: <http://dx.doi.org/10.1016/j.apsusc.2015.01.079>
- [59] M. Duocastella, A. Patrascioiu, J. M. Fernández-Pradas, J. L. Morenza, and P. Serra, “Film-free laser forward printing of transparent and weakly absorbing liquids,” *Optics Express*, vol. 18, no. 21, 2010.
- [60] A. Patrascioiu, M. Duocastella, J. M. Fernández-Pradas, J. L. Morenza, and P. Serra, “Liquids microprinting through a novel film-free femtosecond laser based technique,” in *Applied Surface Science*, vol. 257, no. 12, 2011.
- [61] A. Patrascioiu, J. M. Fernández-Pradas, J. L. Morenza, and P. Serra, “Microdroplet deposition through a film-free laser forward printing technique,” in *Applied Surface Science*, vol. 258, no. 23, 2012.
- [62] P. Serra, A. Patrascioiu, J. M. Fernández-Pradas, and J. L. Morenza, “Film-free laser microprinting of transparent solutions,” in *Laser Applications in Microelectronic and Optoelectronic Manufacturing (LAMOM) XVIII*, vol. 8607, 2013.
- [63] A. Patrascioiu, J. M. Fernández-Pradas, J. L. Morenza, and P. Serra, “Film-free laser printing: Jetting dynamics analyzed through time-resolved imaging,” in *Applied Surface Science*, vol. 302, 2014.
- [64] H. Desrus, B. Chassagne, F. Moizan, R. Devillard, S. Petit, R. Kling, and S. Catros, “Effective parameters for film-free femtosecond laser assisted bioprinting,” *Applied Optics*, vol. 55, no. 14, 2016.
- [65] J. Zhang, P. Byers, A. Erben, C. Frank, L. Schulte-Spechtel, M. Heymann, D. Docheva, H. P. Huber, S. Sudhop, and H. Clausen-Schaumann, “Single Cell Bioprinting with Ultrashort Laser Pulses,” *Advanced Functional Materials*, 2021.
- [66] V. Dinca, E. Kasotakis, J. Catherine, A. Mourka, A. Mitraki, A. Popescu, M. Dinescu, M. Farsari, and C. Fotakis, “Development of peptide-based patterns by laser transfer,” *Applied Surface Science*, vol. 254, no. 4, 2007.
- [67] V. Dinca, A. Ranella, M. Farsari, D. Kafetzopoulos, M. Dinescu, A. Popescu, and C. Fotakis, “Quantification of the activity of biomolecules in microarrays obtained by direct laser transfer,” *Biomedical Microdevices*, vol. 10, no. 5, 2008.
- [68] C. F. Huang, M. M. Colley, L. S. Lu, C. Y. Chang, P. W. Peng, and T. S. Yang, “Performance characterization of continuous-wave laser-induced forward transfer of liquid bioink,” *Applied Physics Express*, vol. 12, no. 11, 2019.

- [69] J. M. Fernández-Pradas, M. Colina, P. Serra, J. Domínguez, and J. L. Morenza, "Laser-induced forward transfer of biomolecules," in *Thin Solid Films*, vol. 453-454, 2004.
- [70] M. Colina, P. Serra, J. M. Fernández-Pradas, L. Sevilla, and J. L. Morenza, "DNA deposition through laser induced forward transfer," in *Biosensors and Bioelectronics*, vol. 20, no. 8 SPEC. ISS., 2005.
- [71] C. Florian, S. Piazza, A. Diaspro, P. Serra, and M. Duocastella, "Direct Laser Printing of Tailored Polymeric Microlenses," *ACS Applied Materials and Interfaces*, vol. 8, no. 27, 2016.
- [72] P. Delrot, S. P. Hauser, J. Krizek, and C. Moser, "Depth-controlled laser-induced jet injection for direct three-dimensional liquid delivery," *Applied Physics A: Materials Science and Processing*, vol. 124, no. 9, 2018.
- [73] Q. Guo, M. Wang, and Z. Zhang, "The dynamics and deposition results of femtosecond laser-induced liquid film forward transfer," in *International Conference on Laser, Optics and Optoelectronic Technology (LOPET 2021)*, vol. 11885. International Society for Optics and Photonics, 2021, p. 118850D.
- [74] B. Hopp, T. Smausz, N. Kresz, N. Barna, Z. Bor, L. Kolozsvári, D. B. Chrisey, A. Szabó, and A. Nógrádi, "Survival and proliferative ability of various living cell types after laser-induced forward transfer," *Tissue Engineering*, vol. 11, no. 11-12, 2005.
- [75] A. Narazaki, A. Oyane, S. Komuro, R. Kurosaki, T. Kameyama, I. Sakamaki, H. Araki, and H. Miyaji, "Bioactive micropatterning of apatite immobilizing cell adhesion protein by laser-induced forward transfer with a shock absorber," *Optical Materials Express*, vol. 9, no. 7, 2019.
- [76] T. Mito, T. Tsujita, H. Masuhara, N. Hayashi, and K. Suzuki, "Hollowing and transfer of polymethyl methacrylate film propelled by laser ablation of triazeno polymer film," *Japanese Journal of Applied Physics, Part 2: Letters*, vol. 40, no. 8 A, 2001.
- [77] A. Doraiswamy, R. J. Narayan, T. Lippert, L. Urech, A. Wokaun, M. Nagel, B. Hopp, M. Dinescu, R. Modi, R. C. Auyeung, and D. B. Chrisey, "Excimer laser forward transfer of mammalian cells using a novel triazene absorbing layer," *Applied Surface Science*, vol. 252, no. 13 SPEC. ISS., 2006.
- [78] R. Fardel, M. Nagel, F. Nüesch, T. Lippert, and A. Wokaun, "Fabrication of organic light-emitting diode pixels by laser-assisted forward transfer," *Applied Physics Letters*, vol. 91, no. 6, 2007.

## Bibliography

---

- [79] J. Xu, J. Liu, D. Cui, M. Gerhold, A. Y. Wang, M. Nagel, and T. K. Lippert, "Laser-assisted forward transfer of multi-spectral nanocrystal quantum dot emitters," *Nanotechnology*, vol. 18, no. 2, 2007.
- [80] R. Fardel, M. Nagel, F. Nüesch, T. Lippert, and A. Wokaun, "Laser forward transfer using a sacrificial layer: Influence of the material properties," *Applied Surface Science*, vol. 254, no. 4, 2007.
- [81] D. P. Banks, K. Kaur, R. Gazia, R. Fardel, M. Nagel, T. Lippert, and R. W. Eason, "Triazene photopolymer dynamic release layer-assisted femtosecond laser-induced forward transfer with an active carrier substrate," *EPL*, vol. 83, no. 3, 2008.
- [82] A. Palla-Papavlu, V. Dinca, I. Paraico, A. Moldovan, J. Shaw-Stewart, C. W. Schneider, E. Kovacs, T. Lippert, and M. Dinescu, "Microfabrication of polystyrene microbead arrays by laser induced forward transfer," *Journal of Applied Physics*, vol. 108, no. 3, 2010.
- [83] V. Dinca, A. Palla-Papavlu, M. Dinescu, J. Shaw Stewart, T. K. Lippert, F. Di Pietrantonio, D. Cannata, M. Benetti, and E. Verona, "Polymer pixel enhancement by laser-induced forward transfer for sensor applications," *Applied Physics A: Materials Science and Processing*, vol. 101, no. 3, 2010.
- [84] A. Palla-Papavlu, I. Paraico, J. Shaw-Stewart, V. Dinca, T. Savopol, E. Kovacs, T. Lippert, A. Wokaun, and M. Dinescu, "Liposome micropatterning based on laser-induced forward transfer," *Applied Physics A: Materials Science and Processing*, vol. 102, no. 3, 2011.
- [85] J. Shaw-Stewart, T. Lippert, M. Nagel, F. Nüesch, and A. Wokaun, "Laser-induced forward transfer of polymer light-emitting diode pixels with increased charge injection," *ACS Applied Materials and Interfaces*, vol. 3, no. 2, 2011.
- [86] J. R. Shaw-Stewart, T. K. Lippert, M. Nagel, F. A. Nüesch, and A. Wokaun, "Sequential printing by laser-induced forward transfer to fabricate a polymer light-emitting diode pixel," *ACS Applied Materials and Interfaces*, vol. 4, no. 7, 2012.
- [87] L. Rapp, C. Cibert, S. Nénon, A. P. Alloncle, M. Nagel, T. Lippert, C. Videlot-Ackermann, F. Fages, and P. Delaporte, "Improvement in semiconductor laser printing using a sacrificial protecting layer for organic thin-film transistors fabrication," in *Applied Surface Science*, vol. 257, no. 12, 2011.
- [88] B. Mitu, A. Matei, M. Filipescu, A. Palla Papavlu, A. Bercea, T. Lippert, and M. Dinescu, "Ferrocene pixels by laser-induced forward transfer: Towards flexible microelectrode printing," *Journal of Physics D: Applied Physics*, vol. 50, no. 11, 2017.



- [89] E. C. Smits, A. Walter, D. M. De Leeuw, and K. Asadi, "Laser induced forward transfer of graphene," *Applied Physics Letters*, vol. 111, no. 17, 2017.
- [90] N. T. Kattamis, P. E. Purnick, R. Weiss, and C. B. Arnold, "Thick film laser induced forward transfer for deposition of thermally and mechanically sensitive materials," *Applied Physics Letters*, vol. 91, no. 17, 2007.
- [91] N. T. Kattamis, N. D. McDaniel, S. Bernhard, and C. B. Arnold, "Laser direct write printing of sensitive and robust light emitting organic molecules," *Applied Physics Letters*, 2009.
- [92] —, "Ambient laser direct-write printing of a patterned organo-metallic electroluminescent device," *Organic Electronics*, vol. 12, no. 7, pp. 1152–1158, 2011.
- [93] L. Hecht, K. Rager, M. Davidonis, P. Weber, G. Gauglitz, and A. Dietzel, "Blister-actuated LIFT printing for multiparametric functionalization of paper-like biosensors," *Micro-machines*, vol. 10, no. 4, 2019.
- [94] A. Marquez, M. Gómez-Fontela, S. Lauzurica, R. Candorcio-Simón, D. Muñoz-Martin, M. Morales, M. Ubago, C. Toledo, P. Lauzurica, and C. Molpeceres, "Fluorescence enhanced BA-LIFT for single cell detection and isolation," *Biofabrication*, vol. 12, no. 2, 2020.
- [95] G. Paris, A. Klinkusch, J. Heidepriem, A. Tsouka, J. Zhang, M. Mende, D. S. Mattes, D. Mager, H. Riegler, S. Eickelmann, and F. F. Loeffler, "Laser-induced forward transfer of soft material nanolayers with millisecond pulses shows contact-based material deposition," *Applied Surface Science*, vol. 508, 2020.
- [96] D. Xu, K. C. Chan, H. Guo, H. Zhong, and L. Lu, "One-step fabrication of a laser-induced forward transfer graphene/Cu: XO nanocomposite-based electrocatalyst to promote hydrogen evolution reaction," *Journal of Materials Chemistry A*, vol. 9, no. 30, 2021.
- [97] N. T. Goodfriend, S. Y. Heng, O. A. Nerushev, A. V. Gromov, A. V. Bulgakov, M. Okada, W. Xu, R. Kitaura, J. Warner, H. Shinohara, and E. E. Campbell, "Blister-based-laser-induced-forward-transfer: A non-contact, dry laser-based transfer method for nanomaterials," *Nanotechnology*, vol. 29, no. 38, 2018.
- [98] N. T. Goodfriend, O. Nerushev, W. Xu, M. Okada, R. Kitaura, J. Warner, H. Shinohara, A. V. Bulgakov, E. Campbell, and N. M. Bulgakova, "Two Dimensional Film Printing by Blister-Based Laser-Induced Forward-Transfer," in *2019 Conference on Lasers and Electro-Optics, CLEO 2019 - Proceedings*, 2019.
- [99] N. R. Arutyunyan, M. S. Komlenok, T. V. Kononenko, M. A. Dezhkina, A. F. Popovich, and V. I. Konov, "Printing of single-wall carbon nanotubes via blister-based laser-induced forward transfer," *Laser Physics*, vol. 29, no. 2, 2019.

## Bibliography

---

- [100] M. S. Komlenok, O. S. Kudryavtsev, D. G. Pasternak, I. I. Vlasov, and V. I. Konov, "Blister-Based Laser-Induced Forward Transfer of Luminescent Diamond Nanoparticles," *Physica Status Solidi (A) Applications and Materials Science*, vol. 218, no. 5, 2021.
- [101] P. Sopeña, J. Arrese, S. González-Torres, J. M. Fernández-Pradas, A. Cirera, and P. Serra, "Low-Cost Fabrication of Printed Electronics Devices through Continuous Wave Laser-Induced Forward Transfer," *ACS Applied Materials and Interfaces*, vol. 9, no. 35, 2017.
- [102] C. C. Liu, J. Cheng, X. Q. Li, Z. J. Gu, and K. Ogino, "Laser-induced silver seeding on filter paper for selective electroless copper plating," *Materials*, vol. 11, no. 8, 2018.
- [103] J. M. Fernández-Pradas, P. Sopeña, S. González-Torres, J. Arrese, A. Cirera, and P. Serra, "Laser-induced forward transfer for printed electronics applications," *Applied Physics A: Materials Science and Processing*, vol. 124, no. 2, 2018.
- [104] R. Molina, M. Ertuğrul, Larrea, R. Navarro, V. Rico, F. Yubero, A. R. González-Elipe, G. F. de la Fuente, and L. A. Angurel, "Laser-induced scanning transfer deposition of silver electrodes on glass surfaces: A green and scalable technology," *Applied Surface Science*, vol. 556, 2021.
- [105] Y. Shan, X. Zhang, H. Li, and Z. Zhan, "Single-step printing of high-resolution, high-aspect ratio silver lines through laser-induced forward transfer," *Optics and Laser Technology*, vol. 133, 2021.
- [106] P. Sopeña, J. Sieiro, J. M. Fernández-Pradas, J. M. López-Villegas, and P. Serra, "Laser-Induced Forward Transfer: A Digital Approach for Printing Devices on Regular Paper," *Advanced Materials Technologies*, vol. 5, no. 6, 2020.
- [107] K. M. Charipar, N. A. Charipar, J. C. Prestigiacomo, N. S. Bingham, and A. Piqué, "Laser printing of flip-chip interconnects for high frequency applications," *Journal of Manufacturing Processes*, vol. 32, 2018.
- [108] K. M. Charipar, N. A. Charipar, R. C. Auyeung, H. Kim, and A. Piqué, "Low-profile interconnects via laser-induced forward transfer," *Journal of Laser Micro Nanoengineering*, vol. 13, no. 2, 2018.
- [109] P. Smyrek, H. Kim, Y. Zheng, H. J. Seifert, A. Piqué, and W. Pfleging, "Laser printing and femtosecond laser structuring of electrode materials for the manufacturing of 3D lithium-ion micro-batteries," in *Laser 3D Manufacturing III*, vol. 9738, 2016.
- [110] S. M. Perinchery, E. C. Smits, A. Sridhar, P. Albert, J. Van Den Brand, R. Mandamparambil, I. Yakimets, and H. F. Schoo, "Investigation of the effects of LIFT printing with a KrF-excimer laser on thermally sensitive electrically conductive adhesives," *Laser Physics*, vol. 24, no. 6, 2014.

- [111] A. Sridhar, S. M. Perinchery, E. C. Smits, R. Mandamparambil, and J. Van Den Brand, "Reliability investigations on LIFT-printed isotropic conductive adhesive joints for system-in-foil applications," in *Microelectronics Reliability*, vol. 55, no. 11, 2015.
- [112] M. Makrygianni, I. Theodorakos, F. Zacharatos, D. Reppas, P. Papadopoulos, N. Oikonomidis, C. Spandonidis, and I. Zergioti, "Laser induced forward transfer of solder paste for microelectronics assembly applications," 2021.
- [113] T. Araki, R. Mandamparambil, D. M. P. Van Bragt, J. Jiu, H. Koga, J. Van Den Brand, T. Sekitani, J. M. Den Toonder, and K. Suganuma, "Stretchable and transparent electrodes based on patterned silver nanowires by laser-induced forward transfer for non-contacted printing techniques," *Nanotechnology*, vol. 27, no. 45, 2016.
- [114] P. Sopena, P. Serra, and J. M. Fernández-Pradas, "Transparent and conductive silver nanowires networks printed by laser-induced forward transfer," *Applied Surface Science*, vol. 476, 2019.
- [115] W. Shou, B. K. Mahajan, B. Ludwig, X. Yu, J. Staggs, X. Huang, and H. Pan, "Low-Cost Manufacturing of Bioresorbable Conductors by Evaporation–Condensation-Mediated Laser Printing and Sintering of Zn Nanoparticles," *Advanced Materials*, vol. 29, no. 26, 2017.
- [116] O. Koritsoglou, I. Theodorakos, F. Zacharatos, M. Makrygianni, D. Kariyapperuma, R. Price, B. Cobb, S. Melamed, A. Kabla, F. de la Vega, and I. Zergioti, "Copper micro-electrode fabrication using laser printing and laser sintering processes for on-chip antennas on flexible integrated circuits," *Optical Materials Express*, vol. 9, no. 7, 2019.
- [117] N. Gorodesky, S. Sedghani-Cohen, M. Altman, O. Fogel, G. Cohen-Taguri, Y. Fleger, Z. Kotler, and Z. Zalevsky, "Concurrent Formation of Metallic Glass During Laser Forward Transfer 3D Printing," *Advanced Functional Materials*, vol. 30, no. 25, 2020.
- [118] C. Sammartino, S. Sedghani Cohen, Z. Kotler, and N. Eliaz, "Direct Writing of High-Resolution, High-Quality Pure Metal Patterns on Smooth Transparent Substrates by Laser-Induced Forward Transfer Followed by a Novel Laser Treatment," *Advanced Engineering Materials*, vol. 23, no. 9, 2021.
- [119] Y. Berg, S. Winter, Z. Kotler, and Y. Shacham-Diamand, "Embedded metal microstructures in glass substrates by a combined laser trenching and printing process," *Journal of Laser Micro Nanoengineering*, vol. 13, no. 2, 2018.
- [120] C. K. P. Vallabh, Y. Xiong, and X. Zhao, "3D printing of liquid metal EGaln through laser induced forward transfer: A proof-of-concept study," *Manufacturing Letters*, vol. 28, 2021.

## Bibliography

---

- [121] S. Papazoglou, Y. S. Raptis, S. Chatzandroulis, and I. Zergioti, "A study on the pulsed laser printing of liquid-phase exfoliated graphene for organic electronics," *Applied Physics A: Materials Science and Processing*, vol. 117, no. 1, 2014.
- [122] K. T. Paula, N. B. Tomazio, O. I. Salas, A. J. Otuka, J. M. Almeida, M. B. Andrade, N. C. Vieira, D. T. Balogh, and C. R. Mendonça, "Femtosecond-laser selective printing of graphene oxide and PPV on polymeric microstructures," *Journal of Materials Science*, vol. 56, no. 19, 2021.
- [123] L. Rapp, C. Constantinescu, Y. Larmande, A. P. Alloncle, and P. Delaporte, "Smart beam shaping for the deposition of solid polymeric material by laser forward transfer," *Applied Physics A: Materials Science and Processing*, vol. 117, no. 1, 2014.
- [124] B. R. Ringeisen, P. K. Wu, H. Kim, A. Piqué, R. Y. Auyeung, H. D. Young, D. B. Chrisey, and D. B. Krizman, "Picoliter-scale protein microarrays by laser direct write," *Biotechnology Progress*, vol. 18, no. 5, 2002.
- [125] A. Karaiskou, I. Zergioti, C. Fotakis, M. Kapsetaki, and D. Kafetzopoulos, "Microfabrication of biomaterials by the sub-ps laser-induced forward transfer process," in *Applied Surface Science*, vol. 208-209, no. 1, 2003.
- [126] P. Serra, M. Colina, J. M. Fernández-Pradas, L. Sevilla, and J. L. Morenza, "Preparation of functional DNA microarrays through laser-induced forward transfer," *Applied Physics Letters*, vol. 85, no. 9, 2004.
- [127] I. Zergioti, A. Karaiskou, D. G. Papazoglou, C. Fotakis, M. Kapsetaki, and D. Kafetzopoulos, "Femtosecond laser microprinting of biomaterials," *Applied Physics Letters*, vol. 86, no. 16, 2005.
- [128] V. Dinca, A. Ranella, A. Popescu, M. Dinescu, M. Farsari, and C. Fotakis, "Parameters optimization for biological molecules patterning using 248-nm ultrafast lasers," *Applied Surface Science*, vol. 254, no. 4, 2007.
- [129] I. N. Katis, J. A. Holloway, J. Madsen, S. N. Faust, S. D. Garbis, P. J. Smith, D. Voegeli, D. L. Bader, R. W. Eason, and C. L. Sones, "Paper-based colorimetric enzyme linked immunosorbent assay fabricated by laser induced forward transfer," *Biomicrofluidics*, vol. 8, no. 3, 2014.
- [130] V. Dinca, A. Ranella, M. Farsari, D. Kafetzopoulos, M. Dinescu, A. Popescu, and C. Fotakis, "Quantification of the activity of biomolecules in microarrays obtained by direct laser transfer," *Biomedical Microdevices*, vol. 10, no. 5, 2008.
- [131] P. K. Wu, B. R. Ringeisen, J. Callahan, M. Brooks, D. M. Bubb, H. D. Wu, A. Piqué, B. Spargo, R. A. McGill, and D. B. Chrisey, "The deposition, structure, pattern deposition, and

- activity of biomaterial thin-films by matrix-assisted pulsed-laser evaporation (MAPLE) and MAPLE direct write," in *Thin Solid Films*, vol. 398-399, 2001.
- [132] J. A. Barron, B. J. Spargo, and B. R. Ringeisen, "Biological laser printing of three dimensional cellular structures," in *Applied Physics A: Materials Science and Processing*, vol. 79, no. 4-6, 2004.
- [133] M. Gruene, M. Pflaum, A. Deiwick, L. Koch, S. Schlie, C. Unger, M. Wilhelmi, A. Haverich, and B. N. Chichkov, "Adipogenic differentiation of laser-printed 3D tissue grafts consisting of human adipose-derived stem cells," *Biofabrication*, vol. 3, no. 1, 2011.
- [134] R. Gaebel, N. Ma, J. Liu, J. Guan, L. Koch, C. Klopsch, M. Gruene, A. Toelk, W. Wang, P. Mark, F. Wang, B. Chichkov, W. Li, and G. Steinhoff, "Patterning human stem cells and endothelial cells with laser printing for cardiac regeneration," *Biomaterials*, vol. 32, no. 35, 2011.
- [135] S. Catros, J. C. Fricain, B. Guillotin, B. Pippenger, R. Bareille, M. Remy, E. Lebraud, B. Desbat, J. Amédée, and F. Guillemot, "Laser-assisted bioprinting for creating on-demand patterns of human osteoprogenitor cells and nano-hydroxyapatite," *Biofabrication*, vol. 3, no. 2, 2011.
- [136] L. Koch, A. Deiwick, S. Schlie, S. Michael, M. Gruene, V. Coger, D. Zychlinski, A. Schambach, K. Reimers, P. M. Vogt, and B. Chichkov, "Skin tissue generation by laser cell printing," *Biotechnology and Bioengineering*, vol. 109, no. 7, 2012.
- [137] Z. Ma, Q. Liu, H. Yang, R. B. Runyan, C. A. Eisenberg, M. Xu, T. K. Borg, R. Markwald, Y. Wang, and B. Z. Gao, "Laser patterning for the study of MSC cardiogenic differentiation at the single-cell level," *Light: Science and Applications*, vol. 2, no. MAY, 2013.
- [138] V. Keriquel, F. Guillemot, I. Arnault, B. Guillotin, S. Miraux, J. Amédée, J. C. Fricain, and S. Catros, "In vivo bioprinting for computer- and robotic-assisted medical intervention: Preliminary study in mice," *Biofabrication*, vol. 2, no. 1, 2010.
- [139] D. A. Willis and V. Grosu, "Evaporation and phase explosion during laser-induced forward transfer of aluminum," in *Photon Processing in Microelectronics and Photonics III*, vol. 5339, 2004.
- [140] L. Yang, C. Y. Wang, X. C. Ni, Z. J. Wang, W. Jia, and L. Chai, "Microdroplet deposition of copper film by femtosecond laser-induced forward transfer," *Applied Physics Letters*, 2006.
- [141] D. P. Banks, C. Grivas, J. D. Mills, R. W. Eason, and I. Zergioti, "Nanodroplets deposited in microarrays by femtosecond Ti:sapphire laser-induced forward transfer," *Applied Physics Letters*, vol. 89, no. 19, 2006.

## Bibliography

---

- [142] R. Pohl, "Laser-induced forward transfer of pure metals," *University of Twente*, 2015.
- [143] M. Zenou, A. Sa'Ar, and Z. Kotler, "Laser Transfer of Metals and Metal Alloys for Digital Microfabrication of 3D Objects," *Small*, vol. 11, no. 33, 2015.
- [144] M. Zenou, A. Sa'ar, and Z. Kotler, "Laser jetting of femto-liter metal droplets for high resolution 3D printed structures," *Scientific Reports*, vol. 5, 2015.
- [145] M. Zenou, A. Sa'Ar, and Z. Kotler, "Digital laser printing of aluminum micro-structure on thermally sensitive substrates," *Journal of Physics D: Applied Physics*, vol. 48, no. 20, 2015.
- [146] M. Zenou and Z. Kotler, "Printing of metallic 3D micro-objects by laser induced forward transfer," *Optics Express*, vol. 24, no. 2, 2016.
- [147] C. W. Visser, R. Pohl, C. Sun, G. W. Römer, B. Huis In 'T Veld, and D. Lohse, "Toward 3D Printing of Pure Metals by Laser-Induced Forward Transfer," *Advanced Materials*, vol. 27, no. 27, 2015.
- [148] O. Fogel, S. S. Cohen, Z. Kotler, and Z. Zalevsky, "Mechanical properties of 3D metallic microstructures printed by laser induced forward transfer," in *Procedia CIRP*, vol. 74, 2018.
- [149] J. Luo, R. Pohl, L. Qi, G. W. Römer, C. Sun, D. Lohse, and C. W. Visser, "Printing Functional 3D Microdevices by Laser-Induced Forward Transfer," *Small*, vol. 13, no. 9, 2017.
- [150] A. S. Holmes and S. M. Saidam, "Sacrificial layer process with laser-driven release for batch assembly operations," *Journal of Microelectromechanical Systems*, vol. 7, no. 4, 1998.
- [151] A. S. Holmes, "Laser processes for MEMS manufacture," in *Second International Symposium on Laser Precision Microfabrication*, vol. 4426, 2002.
- [152] S. A. Mathews, R. C. Auyeung, and A. Piqué, "Use of laser direct-write in microelectronics assembly," *Journal of Laser Micro Nanoengineering*, vol. 2, no. 1, pp. 103–107, 2007.
- [153] K. S. Kaur, M. Feinaeugle, D. P. Banks, J. Y. Ou, F. Di Pietrantonio, E. Verona, C. L. Sones, and R. W. Eason, "Laser-induced forward transfer of focussed ion beam pre-machined donors," *Applied Surface Science*, vol. 257, no. 15, 2011.
- [154] G. Luo, D. Wu, Y. Zhou, Y. Hu, and Z. Yao, "Laser printing of large-scale metal micro/nanoparticle array: Deposition behavior and microstructure," *International Journal of Machine Tools and Manufacture*, vol. 173, 2022.

- [155] R. Saeidpourazar, R. Li, Y. Li, M. D. Sangid, C. Lu, Y. Huang, J. A. Rogers, and P. M. Ferreira, "Laser-driven micro transfer placement of prefabricated microstructures," *Journal of Microelectromechanical Systems*, vol. 21, no. 5, pp. 1049–1058, 2012.
- [156] R. Saeidpourazar, M. D. Sangid, J. A. Rogers, and P. M. Ferreira, "A prototype printer for laser driven micro-transfer printing," in *Journal of Manufacturing Processes*, vol. 14, no. 4, 2012, pp. 416–424.
- [157] N. S. Karlitskaya, D. F. de Lange, R. Sanders, and J. Meijer, "Study of laser die release by Q-switched Nd:YAG laser pulses," in *High-Power Laser Ablation V*, vol. 5448, 2004.
- [158] N. S. Karlitskaya, J. Meijer, D. F. de Lange, and H. Kettelarij, "Laser propulsion of microelectronic components: releasing mechanism investigation," in *High-Power Laser Ablation VI*, vol. 6261, 2006.
- [159] S. A. Mathews, I. Beniam, N. Charipar, and A. Piqué, "Laser induced forward transfer (lift) for direct-write fabrication and assembly of microelectronics," in *International Congress on Applications of Lasers & Electro-Optics*, vol. 2015, no. 1. Laser Institute of America, 2015, pp. 9–13.
- [160] K. M. Charipar, R. C. Auyeung, H. Kim, N. A. Charipar, and A. Piqué, "Use of an elastomeric donor for LIFT of metal foils," *Journal of Laser Micro Nanoengineering*, vol. 13, no. 2, 2018.
- [161] K. M. Charipar, R. E. Diaz-Rivera, N. H. De Jesus-Villanueva, R. C. Y. Auyeung, N. A. Charipar, and A. Piqué, "Reusable laser-absorbing layers for LIFT," in *Laser Applications in Microelectronic and Optoelectronic Manufacturing (LAMOM) XXIV*, 2019.
- [162] Y. Huang, N. Zheng, Z. Cheng, Y. Chen, B. Lu, T. Xie, and X. Feng, "Direct Laser Writing-Based Programmable Transfer Printing via Bioinspired Shape Memory Reversible Adhesive," *ACS Applied Materials and Interfaces*, vol. 8, no. 51, 2016.
- [163] J. Eisenhaure and S. Kim, "Laser-Driven Shape Memory Effect for Transfer Printing Combining Parallelism with Individual Object Control," *Advanced Materials Technologies*, 2016.
- [164] E. E. Kuran, Y. Berg, M. Tichem, and Z. Kotler, "Integration of laser die transfer and magnetic self-assembly for ultra-thin chip placement," *Journal of Micromechanics and Microengineering*, vol. 25, no. 4, 2015.
- [165] M. Springer, J. Düsing, J. Koch, P. Jäschke, S. Kaierle, and L. Overmeyer, "Laser-induced forward transfer as a potential alternative to pick-and-place technology when assembling semiconductor components," *Journal of Laser Applications*, vol. 33, no. 4, 2021.

## Bibliography

---

- [166] L. Overmeyer, S. N. Gottwald, M. Springer, and J. F. Düsing, "On-the-fly bare die bonding based on laser induced forward transfer (lift)," *CIRP Annals*, 2022.
- [167] H. Luo, C. Wang, C. Linghu, K. Yu, C. Wang, and J. Song, "Laser-driven programmable non-contact transfer printing of objects onto arbitrary receivers via an active elastomeric microstructured stamp," *National Science Review*, vol. 7, no. 2, 2020.
- [168] R. Guerre, U. Drechsler, D. Jubin, and M. Despont, "Selective transfer technology for microdevice distribution," *Journal of Microelectromechanical Systems*, vol. 17, no. 1, 2008.
- [169] R. Miller, V. Marinov, O. Swenson, Z. Chen, and M. Semler, "Noncontact selective laser-assisted placement of thinned semiconductor dice," *IEEE Transactions on Components, Packaging and Manufacturing Technology*, 2012.
- [170] V. R. Marinov, O. Swenson, Y. Atanasov, and N. Schneck, "Laser-assisted ultrathin die packaging: Insights from a process study," *Microelectronic Engineering*, vol. 101, 2013.
- [171] V. Marinov, O. Swenson, R. Miller, F. Sarwar, Y. Atanasov, M. Semler, and S. Datta, "Laser-enabled advanced packaging of ultrathin bare dice in flexible substrates," *IEEE Transactions on Components, Packaging and Manufacturing Technology*, vol. 2, no. 4, 2012.
- [172] V. R. Marinov, "52-4: Laser-Enabled Extremely-High Rate Technology for  $\mu$ LED Assembly," *SID Symposium Digest of Technical Papers*, vol. 49, no. 1, 2018.
- [173] W. K. Yung, J. S. Liu, H. C. Man, and T. M. Yue, "355 nm Nd:YAG laser ablation of polyimide and its thermal effect," *Journal of Materials Processing Technology*, vol. 101, no. 1, 2000.
- [174] J. Hong, P. Cheng, W. Chen, J. Guo, Y. Li, and J. Liu, "Theoretical Modeling and Experimental Studies of Ultra-Thin Chip Transfer in Laser-Induced Forward Transfer," *IEEE Transactions on Components, Packaging and Manufacturing Technology*, vol. 12, no. 3, 2022.
- [175] B. Peng, Y. Huang, Z. Yin, and Y. Xiong, "Analysis of interfacial peeling in ic chip pick-up process," *Journal of Applied Physics*, vol. 110, no. 7, p. 073508, 2011.
- [176] M. S. Brown, N. T. Kattamis, and C. B. Arnold, "Time-resolved study of polyimide absorption layers for blister-actuated laser-induced forward transfer," *Journal of Applied Physics*, vol. 107, no. 8, pp. 083–103, 2010.
- [177] N. T. Kattamis, M. S. Brown, and C. B. Arnold, "Finite element analysis of blister formation in laser-induced forward transfer," *Journal of Materials Research*, 2011.



- [178] Y. Hu, H. Cheng, J. Xu, and Z. Yao, "A coupling model to simulate the dynamic process of blister-actuated nanosecond laser-induced forward transfer," *Journal of Physics D: Applied Physics*, vol. 50, no. 32, 2017.
- [179] J. Hong, "Thermo-Mechanical Analysis of Blister Formation on a Rigid Substrate in Blister-Actuated Laser-Induced Forward Transfer," *IEEE Transactions on Components, Packaging and Manufacturing Technology*, vol. 10, no. 4, 2020.
- [180] B. P. Jelle, A. Gustavsen, T. N. Nilsen, and T. Jacobsen, "Solar material protection factor (SMPF) and solar skin protection factor (SSPF) for window panes and other glass structures in buildings," *Solar Energy Materials and Solar Cells*, vol. 91, no. 4, 2007.
- [181] P. E. Dyer and J. Sidhu, "Excimer laser ablation and thermal coupling efficiency to polymer films," *Journal of Applied Physics*, vol. 57, no. 4, 1985.
- [182] R. Dreyfus, "Cn temperatures above laser ablated polyimide," *Applied Physics A*, vol. 55, no. 4, pp. 335–339, 1992.
- [183] C. Han, M. A. Zahid, B. Lee, J.-Y. Oh, Y. Kim, and J. Yi, "Ultraviolet nanosecond laser ablation of polyimide with thermal and nonthermal effects near threshold fluence," *Journal of Laser Applications*, vol. 34, no. 3, p. 032004, 2022.
- [184] L. Peng, M. Li, P. Wang, M. He, C. Zhou, H. Zhang, and S. Chen, "Numerical Simulation of Ultra-Short Pulse Laser Ablation Based on Comsol," *Available at SSRN 4153619*.
- [185] F. Raimondi, S. Abolhassani, R. Brüttsch, F. Geiger, T. Lippert, J. Wambach, J. Wei, and A. Wokaun, "Quantification of polyimide carbonization after laser ablation," *Journal of Applied Physics*, vol. 88, no. 6, pp. 3659–3666, 2000.
- [186] H. Liu, Y. Tang, Y. Xie, L. Lu, Z. Wan, W. Tang, L. Yang, and D. Yang, "Effect of pulsed nd: Yag laser processing parameters on surface properties of polyimide films," *Surface and Coatings Technology*, vol. 361, pp. 102–111, 2019.
- [187] Z. Liu, Y. A. Huang, H. Liu, J. Chen, and Z. Yin, "Reliable peeling of ultrathin die with multineedle ejector," *IEEE Transactions on Components, Packaging and Manufacturing Technology*, vol. 4, no. 9, pp. 1545–1554, 2014.
- [188] Z. Liu, Y. Huang, J. Chen, and Z. Yin, "Tunable peeling technique and mechanism of thin chip from compliant adhesive tapes," *IEEE Transactions on Components, Packaging and Manufacturing Technology*, vol. 4, no. 4, pp. 560–568, 2014.
- [189] N. C. LaBianca and J. D. Gelorme, "High-aspect-ratio resist for thick-film applications," in *Advances in Resist Technology and Processing XII*, vol. 2438. SPIE, 1995, pp. 846–852.

## Bibliography

---

- [190] J. Zhang, K. Tan, G. Hong, L. Yang, and H. Gong, "Polymerization optimization of su-8 photoresist and its applications in microfluidic systems and mems," *Journal of Micromechanics and Microengineering*, vol. 11, no. 1, p. 20, 2001.
- [191] E. H. Conradie and D. F. Moore, "Su-8 thick photoresist processing as a functional material for mems applications," *Journal of Micromechanics and Microengineering*, vol. 12, no. 4, p. 368, 2002.
- [192] A. Mata, A. J. Fleischman, and S. Roy, "Fabrication of multi-layer su-8 microstructures," *Journal of micromechanics and microengineering*, vol. 16, no. 2, p. 276, 2006.
- [193] A. Del Campo and C. Greiner, "SU-8: A photoresist for high-aspect-ratio and 3D sub-micron lithography," *Journal of Micromechanics and Microengineering*, vol. 17, no. 6, 2007.
- [194] M. Tijero, G. Gabriel, J. Caro, A. Altuna, R. Hernández, R. Villa, J. Berganzo, F. Blanco, R. Salido, and L. Fernández, "Su-8 microprobe with microelectrodes for monitoring electrical impedance in living tissues," *Biosensors and Bioelectronics*, vol. 24, no. 8, pp. 2410–2416, 2009.
- [195] M. Holgado, C. Barrios, F. Ortega, F. Sanza, R. Casquel, M. Laguna, M. Bañuls, D. López-Romero, R. Puchades, and A. Maquieira, "Label-free biosensing by means of periodic lattices of high aspect ratio su-8 nano-pillars," *Biosensors and Bioelectronics*, vol. 25, no. 12, pp. 2553–2558, 2010.
- [196] K. V. Nemani, K. L. Moodie, J. B. Brennick, A. Su, and B. Gimi, "In vitro and in vivo evaluation of su-8 biocompatibility," *Materials Science and Engineering: C*, vol. 33, no. 7, pp. 4453–4459, 2013.
- [197] N. Takano, L. M. Doeswijk, M. A. Van Den Boogaart, and J. Brugger, "Application of microstencil lithography on polymer surfaces for microfluidic systems with integrated microelectrodes," in *Proceedings of 2006 International Conference on Microtechnologies in Medicine and Biology*, 2006.
- [198] V. Savu, J. Kivioja, J. Ahopelto, and J. Brugger, "Quick and clean: stencil lithography for wafer-scale fabrication of superconducting tunnel junctions," in *IEEE Transactions on Applied Superconductivity*, vol. 19, no. 3, 2009.
- [199] O. Vazquez-Mena, L. Gross, S. Xie, L. G. Villanueva, and J. Brugger, "Resistless nanofabrication by stencil lithography: A review," *Microelectronic Engineering*, vol. 132, 2015.
- [200] Y.-C. Sun, G. Boero, and J. Brugger, "Stretchable conductors fabricated by stencil lithography and centrifugal force-assisted patterning of liquid metal," *ACS applied electronic materials*, vol. 3, no. 12, pp. 5423–5432, 2021.

- [201] F. Mailly, A. Giani, R. Bonnot, P. Temple-Boyer, F. Pascal-Delannoy, A. Foucaran, and A. Boyer, "Anemometer with hot platinum thin film," *Sensors and Actuators A: Physical*, vol. 94, no. 1-2, pp. 32–38, 2001.
- [202] K. Tsutsumi, A. Yamashita, and H. Ohji, "The experimental study of high tcr pt thin films for thermal sensors," in *SENSORS, 2002 IEEE*, vol. 2. IEEE, 2002, pp. 1002–1005.
- [203] T. W. Lim, Y. Son, Y. J. Jeong, D. Y. Yang, H. J. Kong, K. S. Lee, and D. P. Kim, "Three-dimensionally crossing manifold micro-mixer for fast mixing in a short channel length," *Lab on a Chip*, vol. 11, no. 1, 2011.
- [204] S. Tottori, L. Zhang, F. Qiu, K. K. Krawczyk, A. Franco-Obregón, and B. J. Nelson, "Magnetic helical micromachines: Fabrication, controlled swimming, and cargo transport," *Advanced Materials*, vol. 24, no. 6, 2012.
- [205] B. Richter, V. Hahn, S. Bertels, T. K. Claus, M. Wegener, G. Delaittre, C. Barner-Kowollik, and M. Bastmeyer, "Guiding Cell Attachment in 3D Microscaffolds Selectively Functionalized with Two Distinct Adhesion Proteins," *Advanced Materials*, vol. 29, no. 5, 2017.
- [206] M. Hippler, K. Weißenbruch, K. Richler, E. D. Lemma, M. Nakahata, B. Richter, C. Barner-Kowollik, Y. Takashima, A. Harada, E. Blasco, M. Wegener, M. Tanaka, and M. Bastmeyer, "Mechanical stimulation of single cells by reversible host-guest interactions in 3D microscaffolds," *Science Advances*, vol. 6, no. 39, 2020.
- [207] C. W. Ha, P. Prabhakaran, Y. Son, K. S. Lee, and D. Y. Yang, "Effective direct writing of hierarchical 3D polymer micromeshes by continuous out-of-plane longitudinal scanning," *Macromolecular Research*, vol. 25, no. 11, 2017.
- [208] F. Larramendy, S. Yoshida, D. Maier, Z. Fekete, S. Takeuchi, and O. Paul, "3D arrays of microcages by two-photon lithography for spatial organization of living cells," *Lab on a Chip*, vol. 19, no. 5, 2019.
- [209] D. Li, C. Liu, Y. Yang, L. Wang, and Y. Shen, "Micro-rocket robot with all-optic actuating and tracking in blood," *Light: Science and Applications*, vol. 9, no. 1, 2020.
- [210] X. Wang, J. Zhang, X. Mei, J. Miao, and X. Wang, "Laser-induced forward transfer of graphene oxide," *Applied Physics A: Materials Science and Processing*, vol. 127, no. 3, 2021.
- [211] A. Paris, D. Decanini, and G. Hwang, "Swimming force characterizations of multistaged bi-helical microswimmer and 3D vortex trap manipulation," *Microelectronic Engineering*, vol. 235, 2021.

## Bibliography

---

- [212] T. Tigges and A. Walther, "Hierarchical Self-Assembly of 3D-Printed Lock-and-Key Colloids through Shape Recognition," *Angewandte Chemie - International Edition*, vol. 55, no. 37, 2016.
- [213] O. Stein, Y. Liu, J. Streit, R. Cahayag, Y. Lu, and N. Petta, "Handling and assembling of low-density foam structures fabricated by two-photon polymerization," 2017.
- [214] O. Stein, Y. Liu, J. Streit, J. H. Campbell, Y. F. Lu, Y. Aglitskiy, and N. Petta, "Fabrication of low-Density shock-Propagation targets using two-Photon polymerization," in *Fusion Science and Technology*, vol. 72, no. 2, 2018.
- [215] S. van Kesteren, X. Shen, M. Aldeghi, and L. Isa, "Printing on particles: combining two-photon nanolithography and capillary assembly to fabricate multi-material microstructures," *arXiv preprint arXiv:2208.02635*, 2022.
- [216] G. Hwang, C. David, A. Paris, D. Decanini, A. Mizushima, and Y. Mita, "Manufacturing of 3D Helical Microswimmer by AFM Micromanipulation for Microfluidic Applications," *IEEE Transactions on Semiconductor Manufacturing*, vol. 34, no. 3, 2021.
- [217] P. Tayalia, C. R. Mendonca, T. Baldacchini, D. J. Mooney, and E. Mazur, "3D cell-migration studies using two-photon engineered polymer scaffolds," *Advanced Materials*, vol. 20, no. 23, 2008.
- [218] A. Koroleva, S. Gittard, S. Schlie, A. Deiwick, S. Jockenhoevel, and B. Chichkov, "Fabrication of fibrin scaffolds with controlled microscale architecture by a two-photon polymerization-micromolding technique," *Biofabrication*, vol. 4, no. 1, 2012.
- [219] K. S. Worthington, L. A. Wiley, E. E. Kaalberg, M. M. Collins, R. F. Mullins, E. M. Stone, and B. A. Tucker, "Two-photon polymerization for production of human iPSC-derived retinal cell grafts," *Acta Biomaterialia*, vol. 55, 2017.
- [220] A. Trautmann, M. R uth, H. D. Lemke, T. Walther, and R. Hellmann, "Two-photon polymerization based large scaffolds for adhesion and proliferation studies of human primary fibroblasts," *Optics and Laser Technology*, vol. 106, 2018.
- [221] D. Casari, J. Michler, P. Zysset, and J. Schwiedrzik, "Microtensile properties and failure mechanisms of cortical bone at the lamellar level," *Acta Biomaterialia*, vol. 120, 2021.
- [222] D. Casari, T. Kochetkova, J. Michler, P. Zysset, and J. Schwiedrzik, "Microtensile failure mechanisms in lamellar bone: Influence of fibrillar orientation, specimen size and hydration," *Acta Biomaterialia*, vol. 131, 2021.
- [223] D. W. Yee, M. D. Schulz, R. H. Grubbs, and J. R. Greer, "Functionalized 3D Architected Materials via Thiol-Michael Addition and Two-Photon Lithography," *Advanced Materials*, vol. 29, no. 16, 2017.

- [224] J. Zhang, H. Ding, X. Liu, H. Gu, M. Wei, X. Li, S. Liu, S. Li, X. Du, and Z. Gu, "Facile Surface Functionalization Strategy for Two-Photon Lithography Microstructures," *Small*, vol. 17, no. 34, 2021.
- [225] P. Marizza, S. S. Keller, and A. Boisen, "Inkjet printing as a technique for filling of micro-wells with biocompatible polymers," *Microelectronic Engineering*, vol. 111, 2013.
- [226] A. V. Do, K. S. Worthington, B. A. Tucker, and A. K. Salem, "Controlled drug delivery from 3D printed two-photon polymerized poly(ethylene glycol) dimethacrylate devices," *International Journal of Pharmaceutics*, vol. 552, no. 1-2, 2018.
- [227] F. Zheng, J. Jang, C. Tse, and J. Brugger, "3D Printed Micro-Scaffolds Loaded by Inkjet Printing with  $\mu\text{g}$ -Precise Amount of Drug," in *15th IEEE International Conference on Nano/Micro Engineered and Molecular System, NEMS 2020*, 2020.
- [228] W. Dai, K. Lian, and W. Wang, "A quantitative study on the adhesion property of cured SU-8 on various metallic surfaces," 2005.
- [229] M. Nordström, A. Johansson, E. S. Nogueroń, B. Clausen, M. Calleja, and A. Boisen, "Investigation of the bond strength between the photo-sensitive polymer SU-8 and gold," in *Microelectronic Engineering*, vol. 78-79, no. 1-4, 2005.



## CONTACT

✉ zhiwei.yang@epfl.ch  
in LinkedIn  
☎ +41 07867 63981  
🏠 Route Cantonale 37, 1025,  
Saint-Sulpice, Switzerland

## SKILLS

Micro/Nano-  
Fabrications

UV & E-Beam & Two-  
Photon Lithography

Thin-Film Deposition

Dry & Wet Etching

Metrology (SEM & AFM  
& Profilometer & Probe  
Station, etc.)

Laser Induced Forward  
Transfer Technique

Laser Printing

Inkjet Printing

FEM Simulation (COM-  
SOL & Abaqus)

Python

Latex

# ZHIWEI YANG

Ph.D. candidate - Microsystems & Microelectronics

## EXPERIENCE

Doctoral Assistant

2018 - 2022

LMIS1/École Polytechnique Fédérale de Lausanne  
(EPFL), Lausanne (Switzerland)

1. During my Ph.D., I developed a universal method to fabricate functional **SU-8-based microdevices** by combining conventional SU-8 micropatterning with stencil lithography. The fabricated microdevices are transferred by a nozzle-free additive manufacturing technique named **laser-induced forward transfer (LIFT)**. I quantified several parameters (laser energy, SU-8 thickness, gap distance, etc.) to guarantee the successful transfer of such functional microdevices to targeted receivers.  
2. Besides SU-8-based microdevices, I also transferred **two-photon lithography fabricated microstructures** using LIFT. I extended the LIFT application to print viscous liquids. Two types of liquids were experimented with, which are SU-8 liquid resin and PDMS elastomer. The experimental results proved LIFT is capable of printing liquids having various viscosity without fearing ink formulation and nozzle-clogging issues.

Research assistant

2014 - 2017

Tribotronics lab/University of Chinese Academy of  
Sciences, Beijing (China)

During this period of time, I combined triboelectric nanogenerators (TENGs) with transistors and integrate them into a system to serve as tactile sensors for external stimuli perception. For this project, I conceived the idea, designed and performed the experiments, graphed and analyzed the data, and wrote the paper and patent.

## EDUCATION

Ph. D. - Microsystems & Microelectronics

2018 - 2022

École polytechnique fédérale de Lausanne (EPFL) -  
Lausanne, Switzerland

Current Status: Thesis preparation.

Master of Science - Physics

2014 - 2017

University of Chinese Academy of Sciences - Beijing,  
China

Bachelor of Engineering - Materials Science & Engi-  
neering

2009 - 2013

North China Electric Power University - Beijing,  
China

## LANGUAGES

### Chinese

Native language

### English

Full professional proficiency

### French

Limited working proficiency  
(A2-B1)

## HOBBY

- Football
- Cooking

## PUBLICATIONS

**Laser-induced forward transfer of functional SU-8 microdevices**

2022

Status: In preparation

## WORKSHOPS & CONFERENCES

**Swiss ePrint-The Swiss Conference on Printed Electronics and Functional Materials**  
Poster-"Laser-induced forward transfer of functional SU-8 microdevices"

09.2022

"Best Poster Award" Buchs, Switzerland

**Micro and Nano Engineering Conference**

Oral presentation-"Laser-induced forward transfer of functional SU-8 microparts"

09.2021

Turin, Italy

**Swiss ePrint-The Swiss Conference on Printed Electronics and Functional Materials**  
Poster-"Functional devices transfer by LIFT: preliminary results"

09.2019

Fribourg, Switzerland